A Barkhausen Noise Testing System for CANDU® Feeder Pipes

by

Steven Andrew White

A thesis submitted to the
Department of Physics, Engineering Physics & Astronomy
in conformity with the requirements for
the degree of Doctor of Philosophy

Queen's University
Kingston, Ontario, Canada
July 2009

Abstract

A Barkhausen noise (BN) testing system was developed for the non-destructive evaluation (NDE) of residual stresses in CANDU® reactor feeder pipes. The system consists of a four-channel arbitrary waveform flux control system (FCS), and the spring-loaded tetrapole prototype (SL4P) BN probe. The combination of the FCS and SL4P was shown to provide repeatable BN measurements on feeder pipe samples, with variations in air gaps between the SL4P poles and the sample from 0.43 mm to 1.29 mm, and typical pickup coil coupling uncertainties for the total BN energy from ±2% to ±7%. Precision for elastic strain estimation in feeder pipes was found to be between ±7 MPa and ±9 MPa in tension, depending on the excitation field configuration, and negligible in compression. Modelling of the BN penetration depth as a function of the excitation field was used to estimate the BN penetration depth between 5 µm at 300 kHz to a maximum of 500 µm at 3 kHz. The modelling, engineering, and procedures developed for this BN testing system provide an improved basis for the future advancement of BN testing, and ferromagnetic NDE in general.

Acknowledgments

This work would not have been possible without the generous support and encouragement of my supervisors, Dr. Lynann Clapham and Dr. Thomas Krause. I would like thank my supervisors for initializing the collaboration with Atomic Energy of Canada Ltd. (AECL), and Dr. Krause for his continued interest in the project upon relocation to the Royal Military College (RMC) of Canada.

I am grateful to all members of the AECL Inspection, Monitoring and Dynamics Branch for supporting this work, in particular: Hélène Hébert, Stuart Craig, Jeffrey Olfert, and Joe Renauld. My visits to AECL were of great benefit to the *LabVIEW* implementation of the system, and the *MagNet* modelling work. Joe Renauld's coil winding techniques were critical to the design and implementation of the SL4P.

Thanks are extended to Dirk Bouma for his consultation regarding my various circuit problems, and to Gary Contant and Chuck Hearns for their help and support in the machine shop. Thanks also to Pat Weyman for mounting the strain gauges to the three-point bending rig, and for her years of support during my time at the Applied Magnetics Group. I would also like to thank Thomas Mak, for helping with the initial amplifier circuit testing, and Ben Lucht, for helping wrangle LaTeX.

My first-round editor and father, Bryan White, is owed more thanks than could be fit on this or any page. Similarly, my father-in-law, Peter Andreae, provided

invaluable suggestions for circuit designs and component selection. I owe a great many thanks to my lovely wife, Sylvia, for being a sounding board for my randomized thoughts, and to my mother, Carol, for her continual emotional support.

Financial support for this project through the National Sciences and Engineering Research Council (NSERC), the University Network for Excellence in Nuclear Engineering (UNENE), AECL, the Ontario Graduate Scholarship (OGS) program, and the Queen's Graduate Awards (QGA) program is gratefully acknowledged.

Table of Contents

List of Tables

List of Figures

List of Symbols and Acronyms

$\vec{A}$	Vector normal to a surface with magnitude of the scalar area A (m^2)
A_F	Feedback coil area (m^2)
$\mathcal{A}_{[n]}$	Attenuation of propagating fields with frequency f_{bn} a distance n µm into the sample (unitless)
A_{eq}	Equivalent cross sectional area of the BN NDE circuit (m^2)
$\boldsymbol{AI_n}$	PCI-6229 voltage waveform on analog input n (V)
$\boldsymbol{AI_{0+}}$	Non-inverting input waveform for PCI-6133 analog input channel 0 (V)
$\boldsymbol{AI_{0-}}$	Inverting input waveform for PCI-6133 analog input channel 0 (V)
AI_n	PCI-6229 analog input voltage for channel n (V)
AO_n	PCI-6229 analog output voltage for channel n (V)
$\overline{AI_n}$	Mean (DC) voltage in channel AI_n over one excitation period (V)
$\vec{B}$	Magnetic flux density (T or $\mathrm{Wb} \cdot \mathrm{m}^{-2}$)
BN_E	Barkhausen noise energy ($\mathrm{V}_{\mathrm{rms}}^2 \cdot \mathrm{s}$)
$\boldsymbol{BN_{env}}$	RMS Barkhausen noise envelope ($\mathrm{V}_{\mathrm{rms}}$)
BN_{rms}	RMS Barkhausen noise ($\mathrm{V}_{\mathrm{rms}}$)
B_0	Peak excitation field amplitude at the center of the sample surface (T)
$B_{F(p)rms}$	RMS flux density in feedback coil p ($\mathrm{T}_{\mathrm{rms}}$)
$\bar{\boldsymbol{B}}_{\boldsymbol{F(p)}}$	Mean waveform of $\boldsymbol{B}_{\boldsymbol{F(p)},k}$ for $k = 1 \ldots k_{max}$ (T)
$\boldsymbol{B}_{\boldsymbol{F(p)},j}$	Flux density in feedback coil p waveform for iteration j (T)

B_{FT}	Target peak flux density in the feedback coils (T)
B_{Fpk}	Peak superposition flux density in the feedback coils ($\mathrm{T_{rms}}$)
B_{Frms}	Mean RMS superposition flux density in the feedback coils ($\mathrm{T_{rms}}$)
B_{Fxrms}	Mean RMS flux density in feedback coils 1 and 3 ($\mathrm{T_{rms}}$)
$\boldsymbol{B_{Fx},_k}$	Mean flux density waveform in feedback coils 1 and 3 for cycle k (T)
$\bar{\boldsymbol{B}}_{\boldsymbol{Fx}}$	Mean $\boldsymbol{B_{Fx},_k}$ waveform for $k = 1 \ldots k_{max}$ (T)
B_{Fyrms}	Mean RMS flux density in feedback coils 2 and 4 ($\mathrm{T_{rms}}$)
$\boldsymbol{B_{Fy},_k}$	Mean flux density waveform in feedback coils 2 and 4 for cycle k (T)
$\bar{\boldsymbol{B}}_{\boldsymbol{Fy}}$	Mean $\boldsymbol{B_{Fy},_k}$ waveform for $k = 1 \ldots k_{max}$ (T)
B_{ex}	Excitation field amplitude as a function of depth z and t (T)
B_{jrms}	RMS amplitude of B_j ($\mathrm{T_{rms}}$)
B_j	The j^{th} component of $\vec{B}$ (T)
B_{rms}	RMS amplitude of $\vec{B}$ ($\mathrm{T_{rms}}$)
C	Electric charge capacitance (F)
C_{ID}	Capacitance of pickup coil inner windings to ground (F)
C_{OD}	Capacitance of pickup coil outer windings to ground (F)
C_S	Power supply filtering capacitor (F)
C_c	Cable capacitance (F)
C_{pu}	Pickup coil self-capacitance (F)
C_{ref}	Reference voltage low-pass filter capacitor (F)
C_t	Terminating/tuning capacitor (F)
$\mathcal{C}$	Magnetic flux capacitance ($\Omega \cdot \mathrm{s}^2$)
$\vec{D}$	Electric displacement field ($\mathrm{C} \cdot \mathrm{m}^{-2}$)
$\boldsymbol{\mathcal{D}}\{\boldsymbol{X}\}$	Dynamic power spectrum of waveform $\boldsymbol{X}$ ($\mathrm{X_{rms}^2} \cdot \mathrm{Hz}^{-1}$)

$\bar{\boldsymbol{\mathcal{D}}}\{\boldsymbol{X}\}$	Mean dynamic power spectrum of waveform $\boldsymbol{X}_k$ for k_{max} cycles ($\mathrm{X}^2_{\mathrm{rms}} \cdot \mathrm{Hz}^{-1}$)
$\boldsymbol{\mathcal{D}_{BN}}$	Barkhausen noise dynamic power spectrum ($\mathrm{V}^2_{\mathrm{rms}} \cdot \mathrm{Hz}^{-1}$)
$\vec{E}$	Electric field ($\mathrm{N} \cdot \mathrm{C}^{-1}$ or $\mathrm{V} \cdot \mathrm{m}^{-1}$)
$\mathcal{E}_\lambda$	Magnetoelastic energy (J)
$\mathcal{E}_{ex}$	Exchange energy (J)
$\mathcal{E}_{mca}$	Magnetocrystalline anisotropy energy (J)
$\mathcal{E}_{ms}$	Magnetostatic energy (J)
$\mathcal{E}_p$	Zeeman energy (J)
$\mathcal{E}_t$	Total internal magnetic energy: $\mathcal{E}_{ex} + \mathcal{E}_{mca} + \mathcal{E}_{ms}$ (J)
$\mathcal{E}_{wall}$	Domain wall energy (J)
$\mathscr{E}_{\partial S}$	Electromotive force around the closed path ∂S (V)
$\mathscr{E}_L$	Back electromotive force across an inductor (V)
$\mathcal{F}$	Complex pickup coil to preamplifier input transfer function (unitless)
$\vec{F}$	Force (N)
$\mathcal{F}_G$	Pickup coil to preamplifier input transfer function gain (dB)
$\mathcal{F}_\phi$	Pickup coil to preamplifier input transfer function phase (rad or °)
G_D	Digital gain between 0 and 1 (unitless)
$G_{F(p)}$	Feedback voltage gain for channel p (unitless or dB)
G_{OL}	Open-loop amplifier gain (unitless or dB)
$G_{V(p)}$	Voltage following gain for channel p (unitless or dB)
$G_{\Phi(p)}$	Flux mode analog gain for channel p (unitless or dB)
$\vec{H}$	Auxiliary magnetic field ($\mathrm{A} \cdot \mathrm{turns} \cdot \mathrm{m}^{-1}$)
$\bar{H}_x$	Volume-averaged x component of $\vec{H}$ (A/m)
H_c	Coercive field ($\mathrm{A} \cdot \mathrm{turns} \cdot \mathrm{m}^{-1}$)

$\vec{H}_d$	Demagnetising field ($\mathrm{A} \cdot \mathrm{turns} \cdot \mathrm{m}^{-1}$)
$\mathcal{H}$	Hall coefficient ($\mathrm{V} \cdot \mathrm{Wb}^{-1}$)
I	Electric current (A)
I_S	Electric current through surface S (A)
I_{Xrms}	Mean RMS current in excitation coils 1 and 3 ($\mathrm{A_{rms}}$)
I_{Yrms}	Mean RMS current in excitation coils 2 and 4 ($\mathrm{A_{rms}}$)
$\overline{I_{ex(p),j}}$	Mean (DC) excitation current in channel p for iteration j (A)
$\bar{\boldsymbol{I}}_{\boldsymbol{ex(p)}}$	Mean waveform of $\boldsymbol{I}_{\boldsymbol{ex(p)},k}$ for $k = 1 \ldots k_{max}$ (V)
I_{ex}	Excitation current (A)
$\boldsymbol{I}_{\boldsymbol{ex}}$	Excitation current waveform. Subscripts $(p), j$ denote channel p and iteration j (A)
I_{rms}	RMS electric current ($\mathrm{A_{rms}}$)
$\Im\{\mathrm{Z}\}$	Imaginary component of the complex number Z.
$\vec{J}$	Current density field ($\mathrm{A} \cdot \mathrm{m}^{-2}$)
$\vec{J}_b$	Bound current density field ($\mathrm{A} \cdot \mathrm{m}^{-2}$)
$\vec{J}_f$	Free current density field ($\mathrm{A} \cdot \mathrm{m}^{-2}$)
$\mathcal{J}$	Exchange integral $(\mathrm{J} \cdot \mathrm{s}^2)^{-1}$
L	Inductance or the reciprocal magnetic impedance. May be complex. (H)
L_F	Feedback coil inductance (H)
L_{air}	Inductance of a multi-layer air-cored coil (H)
L_c	Cable inductance (H)
L_{ex}	Excitation coil inductance. Subscript $(p), j$ denotes channel p and iteration j (H)
L_{pu}	Pickup coil inductance (H)
$\mathcal{L}$	Magnetic conductance (Ω^{-1})

$\mathcal{L}_{roi}$	Magnetic conductance of the sample region of interest (Ω^{-1})
$\vec{M}$	Magnetisation field ($\mathrm{A} \cdot \mathrm{turns} \cdot \mathrm{m}^{-1}$)
$\bar{M}_x$	Volume-averaged x component of $\vec{M}$ (A/m)
$\mathcal{M}_p$	Feedback coil matching parameter for channel p (unitless)
M_s	Saturation magnetisation ($\mathrm{A} \cdot \mathrm{turns} \cdot \mathrm{m}^{-1}$)
N	Number of turns (unitless)
N_F	Number of feedback coil turns (unitless)
N_{ex}	Number of excitation coil turns (unitless)
N_{pu}	Number of pickup coil turns (unitless)
$\mathcal{N}$	Number of skin depths in a material with thickness h (unitless)
$\vec{P}$	Polarization density field ($\mathrm{C} \cdot \mathrm{m}^{-2}$)
$\overline{\boldsymbol{PS}}\{\boldsymbol{X}\}$	Mean power spectrum for k_{max} cycles of waveform $\boldsymbol{X}_k$ ($\mathrm{X}^2_{\mathrm{rms}} \cdot \mathrm{Hz}^{-1}$)
$\boldsymbol{PS}\{\boldsymbol{X}\}$	Power spectrum of waveform $\boldsymbol{X}$ ($\mathrm{X}^2_{\mathrm{rms}} \cdot \mathrm{Hz}^{-1}$)
PS_{R_t}	Power spectral density of thermal noise from resistor R_t ($\mathrm{V}^2_{\mathrm{rms}} \cdot \mathrm{Hz}^{-1}$)
$P_{0.n}$	PCI-6229 digital input/output channel n (low= 0 V, high= 5 V)
R	Electrical resistance (Ω)
$\mathrm{RMS}\{\boldsymbol{X}\}$	Root mean square value of waveform $\boldsymbol{X}$. (RMS units of $\boldsymbol{X}$)
R_B	Current balancing resistor (Ω)
R_{F1}	Series feedback coil resistor 1 (Ω)
R_{F2}	Series feedback coil resistor 2 (Ω)
R_F	Feedback coil resistance (Ω)
R_G	Gain-limiting resistor (Ω)
R_{G1}	Analog flux feedback resistor (Ω)
R_{G2}	Voltage following feedback resistor (Ω)

R_H	H11F3 switch resistor (Ω)
R_S	Shunt resistance. Subscript (p) denotes channel number (Ω)
R_{cp}	Parallel cable resistance (Ω)
R_{cs}	Series cable resistance (Ω)
R_{ex}	Excitation circuit resistance. Subscript $(p), j$ denotes channel p and iteration j (Ω)
R_g	Voltage divider resistor (Ω)
R_{load}	Load resistance in Figure 2.10 (Ω)
R_{off}	H11F3 off-state resistance ($300\,\mathrm{M}\Omega$)
R_{on}	H11F3 on-state resistance ($470\,\Omega$)
R_{pu}	Pickup coil resistance (Ω)
R_{ref1}	Reference voltage and low-pass filter resistor (Ω)
R_{ref2}	Reference voltage resistor (Ω)
R_{ref}	Reference voltage resistor (Ω)
R_t	Terminating/damping resistor (Ω)
R_{wire}	Lumped resistance of a wire in Figure 2.10 (Ω)
$RTSI_n$	Real-time system integration channel n (low= $0\,\mathrm{V}$, high= $5\,\mathrm{V}$)
$\Re\{\mathrm{Z}\}$	Real component of the complex number Z.
$\mathcal{R}$	Magnetic reluctance $(\Omega \cdot \mathrm{s})^{-1}$
$\mathcal{R}_c$	Core reluctance in a magnetic circuit $(\Omega \cdot \mathrm{s})^{-1}$
$\mathcal{R}_g$	Air gap reluctance $(\Omega \cdot \mathrm{s})^{-1}$
$\mathcal{R}_p$	Parallel reluctance across a magnetic circuit $(\Omega \cdot \mathrm{s})^{-1}$
$\mathcal{R}_{em}$	The equivalent reluctance of the BN NDE electromagnet $(\Omega \cdot \mathrm{s})^{-1}$
$\mathcal{R}_{g0}$	The reluctance of a fixed air gap $g0$ $(\Omega \cdot \mathrm{s})^{-1}$
$\mathcal{R}_{g1}$	The reluctance of a variable air gap $g1$ $(\Omega \cdot \mathrm{s})^{-1}$

$\mathcal{R}_{g2}$	The reluctance of a variable air gap $g2$ $(\Omega \cdot \mathrm{s})^{-1}$
$\mathcal{R}_{g3}$	The reluctance of a variable air gap $g3$ $(\Omega \cdot \mathrm{s})^{-1}$
$\mathcal{R}_{g4}$	The reluctance of a variable air gap $g4$ $(\Omega \cdot \mathrm{s})^{-1}$
$\mathcal{R}_{jk}$	Reluctance between poles j and k $(\Omega \cdot \mathrm{s})^{-1}$
$\mathcal{R}_{roi}$	Reluctance of the sample region of interest $(\Omega \cdot \mathrm{s})^{-1}$
S	A surface (m^2)
∂S	A stationary closed path that bounds the surface S (m)
$\vec{S}_j$	Spin angular momentum vector at position $\vec{r}_j$ with magnitude S_j $(\mathrm{J} \cdot \mathrm{s})$
$\mathcal{T}$	Temperature (K)
$\mathcal{T}_C$	Curie temperature (K)
T_f	AO glitch filter frequency threshold (Hz)
T_g	AO glitch filter $\boldsymbol{rst\mathcal{D}}$ threshold (unitless)
T_C	Excitation current threshold (A)
T_{err}	Normalized RMS error threshold (unitless)
V	Electric scalar potential difference or voltage (V)
$\bar{\boldsymbol{V}}_{\boldsymbol{(BN+bk)}}$	Mean $\boldsymbol{V}_{\boldsymbol{(BN+bk)},k}$ waveform for $k = 1 \ldots k_{max}$ (V)
$\boldsymbol{V}_{\boldsymbol{(BN+bk)},j}$	Pickup coil voltage waveform for excitation iteration j (or cycle k) (V)
V_{CC}	*Anatek* 25-20 $+25\,\mathrm{V}$ output
V_{EE}	*Anatek* 25-20 $-25\,\mathrm{V}$ output
$V_{F(p)rms}$	RMS voltage across feedback coil p ($\mathrm{V_{rms}}$)
V_{F+}	Electric potential at the positive feedback coil terminal (V)
V_{F-}	Electric potential at the negative feedback coil terminal (V)
V_{FT}	Target feedback coil voltage. Subscript (p) denotes channel number. (V)
V_F	Feedback coil voltage (V)

$\boldsymbol{V_F}$	Feedback coil voltage waveform. Subscripts $(p), j$ denote channel p and iteration j (V)
$\boldsymbol{V_{Gex}}$	Guess excitation voltage waveform. Subscripts $(p), j$ denote channel p and iteration j (V)
V_H	Hall voltage (V)
$V_{OFF(p),j}$	DC voltage offset to $\boldsymbol{V_{ref(p),(j+1)}}$ for channel p and iteration j (V)
$\boldsymbol{V_S}$	Shunt resistor voltage waveform. Subscripts $(p), j$ denote channel p and iteration j (A)
V_{Trms}	Target RMS excitation/feedback voltage (V_{rms})
$\boldsymbol{V_{bk},k}$	Pickup coil voltage waveform with only background noise for cycle k (V)
V_{bn}	Induced voltage across the pickup coil windings (V)
$\bar{\boldsymbol{V}}_{\boldsymbol{ex(p)}}$	Mean waveform of $\boldsymbol{V_{ex(p),k}}$ for $k = 1 \ldots k_{max}$ (V)
V_{exTpk}	Target peak excitation voltage in VF mode (V)
$\boldsymbol{V_{exT}}$	Excitation voltage waveform require to produce $\boldsymbol{\Phi_{FT}}$ (V)
V_{ex}	Excitation voltage (V)
$\boldsymbol{V_{ex}}$	Excitation voltage waveform. Subscripts $(p), j$ denote channel p and iteration j (V)
V_{in}	Voltage across the preamplifier input impedance (V)
$\bar{\boldsymbol{V}}_{\boldsymbol{ref(p)}}$	Mean waveform of $\boldsymbol{V_{ref(p),k}}$ for $k = 1 \ldots k_{max}$ (V)
$\boldsymbol{V_{refT}}$	Reference voltage waveform require to produce $\boldsymbol{\Phi_{FT}}$ (V)
V_{ref}	Reference voltage (V)
$\boldsymbol{V_{ref}}$	Reference voltage waveform. Subscripts $(p), j$ denote channel p and iteration j (V)
$\mathcal{V}$	Magnetic scalar potential (A $\cdot$ turns)
$\mathcal{V}_{roi}$	Magnetic scalar potential difference across the sample region of interest (A $\cdot$ turns)
$\boldsymbol{X}$	An arbitrary sampled waveform

Y	Young's modulus (Pa)
Z	Electrical impedance (Ω)
Z_g	Preamplifier impedance to ground (Ω)
Z_{in}	Preamplifier input impedance (Ω)
Z_{tot}	Total electrical impedance seen by currents in the pickup coil (Ω)
$\mathcal{Z}$	Magnetic impedance $(\Omega \cdot \mathrm{s})^{-1}$
$\mathcal{Z}_{eq}$	The equivalent magnetic impedance for the BN NDE circuit $(\Omega \cdot \mathrm{s})^{-1}$
Λ	Flux linkage (Wb)
Λ_{rms}	RMS flux linkage ($\mathrm{Wb_{rms}}$)
Φ_S	Magnetic flux through surface S (Wb)
Φ_{FT}	Target superposition flux through the feedback coils (Wb)
$\boldsymbol{\Phi_{FT}}$	Target feedback coil flux waveform (Wb)
Φ_F	Magnetic flux through a feedback coil (Wb)
Φ_H	Magnetic flux through a Hall sensor (Wb)
Φ_{em}	The magnetic flux through the BN NDE electromagnet (Wb)
Φ_{ex}	Magnetic flux through an excitation coil (Wb)
Φ_{roi}	Magnetic flux through the sample region of interest (Wb)
α	Angle between adjacent spins (rad or °)
$\boldsymbol{\chi_e}$	Electric susceptibility tensor field (unitless)
$\boldsymbol{\chi_m}$	Magnetic susceptibility tensor field (unitless)
δ	Attenuation length or skin depth for an electromagnetic wave propagating in a conductive medium (m)
δ_{bn}	Attenuation length for Barkhausen noise analysis frequency f_{bn} (Hz)
δ_{ex}	Excitation field attenuation length (m)
$\boldsymbol{\varepsilon}$	Strain tensor field with components ε_{jk} (unitless)

ε_a	Axial strain (unitless)
ε_h	Hoop strain (unitless)
ε_r	Radial strain (unitless)
ϵ_0	Permittivity of free space ($8.8542 \times 10^{-12}\,\mathrm{F \cdot m^{-1}}$)
ϵ_r	Relative permittivity of a dielectric medium (unitless)
κ	Complex wave number for an electromagnetic wave propagating in a conductive medium ($\mathrm{m^{-1}}$)
$\boldsymbol{\lambda}$	Magnetostrictive strain tensor (unitless)
λ_{100}	Saturation magnetostrictive strain along $\langle 100 \rangle$ directions (unitless)
λ_s	Saturation magnetostrictive strain (unitless)
$\mathcal{X}$	The ratio of Φ_{ex} to Φ_F. Subscript p denotes channel number (unitless)
μ_0	Permeability of free space ($4\pi \times 10^{-7}\,\mathrm{H \cdot m^{-1}}$)
μ_c	Relative permeability of the core (unitless)
μ_d	Linear isotropic differential permeability (unitless)
$\boldsymbol{\mu_d}$	Differential permeability tensor field (unitless)
μ_{eq}	Equivalent relative permeability of the BN NDE circuit (unitless)
μ_{ex}	Average differential permeability of the sample for the excitation field propagation (unitless)
μ_{roi}	Relative permeability of the sample region of interest (unitless)
$\boldsymbol{\mu_r}$	Relative permeability tensor field (unitless)
ν	Poisson's ratio (unitless)
ω	Angular frequency ($\mathrm{rad \cdot s^{-1}}$)
$\phi\{\boldsymbol{X}\}$	Phase of waveform $\boldsymbol{X}$ (rad or °)
ϕ_0	Phase of the excitation field at the sample surface (rad or °)
$\phi_{B_{F(p)}}$	Phase of the flux density in feedback coil p (rad or °)

$\phi_{B_{FT}}$	Target phase of the flux density in feedback coils (rad or °)
ϕ_{B_j}	Phase of the j^{th} component of $\vec{B}$ (rad or °)
ϕ_B	Phase of $\vec{B}$ (rad or °)
ϕ_I	Electric current phase (rad or °)
$\phi_{V_{F(p)}}$	Phase of the voltage across feedback coil p (rad or °)
ϕ_Λ	Flux linkage phase (rad or °)
$\phi_{f_{ex}}$	Mean phase of the excitation frequency component of the pickup coil voltage over k_{max} cycles (rad or °)
ρ	Electric charge density ($\mathrm{C} \cdot \mathrm{m}^{-3}$)
$\boldsymbol{\sigma}$	Stress tensor field with components σ_{jk} (Pa)
σ_0	Uniaxial stress (Pa)
σ_a	Axial stress (Pa)
σ_h	Hoop stress (Pa)
σ_e	Isotropic linear electrical conductivity ($\mathrm{S} \cdot \mathrm{m}^{-1}$)
$\boldsymbol{\sigma_e}$	Electrical conductivity tensor field ($\mathrm{S} \cdot \mathrm{m}^{-1}$)
σ_{yield}	Yield stress (Pa)
ϑ	Angle between a given domain orientation and an applied stress.
θ_B	Flux density superposition angle: $\arctan\{B_{yrms}/B_{xrms}\}$ (rad or °)
θ_F	Measured feedback coil superposition angle (rad or °)
θ_T	Target feedback coil superposition angle (rad or °)
a_p	Multiplier for channel p (0 in VF mode, 1 in RTA and DEC modes)
c_{jklm}	Component of the fourth-order stiffness tensor of a material (Pa)
d_0	Unstrained length of a material (m)
d	As-tested length of a material (m)

$(\mathrm{d}\boldsymbol{B}/\mathrm{d}\boldsymbol{t})_{\boldsymbol{F(p)},j}$ Flux density rate through feedback coil p waveform for iteration j ($\mathrm{T}\cdot\mathrm{s}^{-1}$)

$(\overline{\boldsymbol{dB/dt}})_{\boldsymbol{F(p)}}$ Mean waveform of $(\boldsymbol{dB/dt})_{\boldsymbol{F(p)},k}$ for $k = 1 \ldots k_{max}$ (T/s)

$d\ell_g$ Incremental air gap length in the BN NDE circuit (m)

$d\mathcal{L}_{roi}$ Incremental magnetic conductance of the sample region of interest (Ω^{-1})

$d\mathcal{R}_{air}$ Incremental reluctance of distributed air in a magnetic circuit $(\Omega\cdot\mathrm{s})^{-1}$

$d\mathcal{R}_c$ Incremental core reluctance in a magnetic circuit $(\Omega\cdot\mathrm{s})^{-1}$

$d\mathcal{R}_g$ Incremental air gap reluctance in a magnetic circuit $(\Omega\cdot\mathrm{s})^{-1}$

$d\mathcal{R}_{roi}$ Incremental reluctance of the sample region of interest $(\Omega\cdot\mathrm{s})^{-1}$

d_{id} Multi-layer coil inside diameter (m)

d_ℓ Multi-layer coil length (m)

d_{od} Multi-layer coil outside diameter (m)

$erBN_E$ Standard error of the Barkhausen noise energy ($\mathrm{V}^2_{\mathrm{rms}}\cdot\mathrm{s}$)

$erBN_{rms}$ Standard error of the RMS Barkhausen noise ($\mathrm{V}_{\mathrm{rms}}$)

$\boldsymbol{er\mathcal{D}}\{\boldsymbol{X}\}$ Standard error of the mean dynamic power spectrum for k_{max} cycles of waveform $\boldsymbol{X}_k$ ($\mathrm{X}^2_{\mathrm{rms}}\cdot\mathrm{Hz}^{-1}$)

$\boldsymbol{er\mathcal{D}_{BN}}$ Standard error of the Barkhausen noise dynamic power spectrum ($\mathrm{V}^2_{\mathrm{rms}}\cdot\mathrm{Hz}^{-1}$)

err_{rms} Normalized RMS difference between target and measured waveforms. Subscript $(p), j$ denotes channel p and iteration j (unitless)

f_0 Resonant frequency in $\mathcal{F}$ (Hz)

f_{6133AI} PCI-6133 analog input sampling frequency (Hz)

f_{6229AI} PCI-6229 analog input sampling frequency (Hz)

f_{6229AO} PCI-6229 analog output sampling frequency (Hz)

f_{bin} Frequency bin width of the dynamic power spectrum (Hz)

f_{bn} Barkhausen noise analysis frequency (Hz)

f_{ex}	The excitation frequency (Hz)
g_p	Voltage divider ratio for channel p (unitless)
h	The minimum dimension of a magnetic conductive material orthogonal to the direction of propagation of magnetic flux (m)
h_c	Core height in the BN NDE circuit (m)
h_{roi}	Sample thickness in the BN NDE circuit (m)
$[hkl]$	A Miller direction
$\langle hkl \rangle$	The set of Miller directions orthogonal to $[hkl]$
(hkl)	The Miller plane with normal $[hkl]$
$\{hkl\}$	The set of Miller planes with normals along $\langle hkl \rangle$
i	The imaginary unit: $\sqrt{-1}$
k_B	Boltzmann's constant: $1.38 \times 10^{-24}\ \mathrm{J \cdot K^{-1}}$
k_{max}	Total number of excitation cycles sampled during a Barkhausen noise measurement (unitless)
$\vec{\ell}$	Vector along an arbitrary path (m)
ℓ_c	Mean magnetic path length in the electromagnet core (m)
ℓ_{eq}	Equivalent magnetic path length of the BN NDE circuit (m)
ℓ_{g0}	Mean magnetic path length for a constant air gap between the poles and sample (m)
ℓ_{roi}	Mean magnetic path length in the sample region of interest (m)
$m_{yx,k}$	Slope of $\boldsymbol{B_{Fy},_k}$ vs. $\boldsymbol{B_{Fx},_k}$ (unitless)
p	Pole index: takes values of 1, 2, 3, and 4 (unitless)
q	Electric charge of a particle (C)
r	Radial distance from the center of the sample surface (m)
$\vec{r}$	Position vector (m)

r_{90} Radius at which 90% of the field sensed by the pickup coil is detected (m)

r_{ψ} Radius at which ψ percent of the field sensed by the pickup coil is detected (m)

rnd {x} The value of x rounded to the nearest integer (units of x)

$\boldsymbol{rst\mathcal{D}}\{\boldsymbol{X}\}$ Ratio of the standard deviation to the mean of the dynamic power spectrum for k_{max} cycles of waveform $\boldsymbol{X}_k$ ($\mathrm{X}^2_{\mathrm{rms}} \cdot \mathrm{Hz}^{-1}$)

$\boldsymbol{st\mathcal{D}}\{\boldsymbol{X}\}$ Standard deviation for k_{max} dynamic power spectra of waveform $\boldsymbol{X}_k$ ($\mathrm{X}^2_{\mathrm{rms}} \cdot \mathrm{Hz}^{-1}$)

std {X(0 : x)} Standard deviation of scalar parameter X from position 0 to position x (units of X)

t Time (s)

$\boldsymbol{t}$ Time axis for one excitation period (s)

t_{bin} Time bin width of the dynamic power spectrum (s)

$\vec{v}$ Velocity of a particle ($\mathrm{m} \cdot \mathrm{s}^{-1}$)

$\vec{v}_d$ Drift velocity of charged particles in a conductor ($\mathrm{m} \cdot \mathrm{s}^{-1}$)

w_c Core width in the BN NDE circuit (m)

x Cartesian x-axis coordinate, parallel to the sample surface (m)

y Cartesian y-axis coordinate, parallel to the sample surface (m)

z Cartesian z-axis coordinate, normal to the sample surface (m)

3PBR **3**-**P**oint **B**ending **R**ig

AC **A**lternating **C**urrent

AECL **A**tomic **E**nergy of **C**anada **L**td.

AMG **A**pplied **M**agnetics **G**roup

AO **A**nalog **O**utput

AWG **A**merican **W**ire **G**auge

BCC **B**ody **C**entered **C**ubic

BN	**B**arkhausen **N**oise
CANDU	**CAN**adian **D**euterium **U**ranium
CB	**C**ommon **B**acking
CNSC	**C**anadian **N**uclear **S**afety **C**ommission
CSS	**C**ore **S**heath **S**hield
DAC	**D**igital to **A**nalog **C**onverter
DC	**D**irect **C**urrent
DEC	**D**igital **E**rror **C**orrection
EMF	**E**lectro**M**otive **F**orce
EMI	**E**lectro**M**agnetic **I**nterference
FCS	**F**lux **C**ontrol **S**ystem
FEM	**F**inite **E**lement **M**odel
GMR	**G**iant **M**agneto**R**esitance
GUI	**G**raphical **U**ser **I**nterface
HR	**H**igh **R**esolution
IIR	**I**nfinite **I**mpulse **R**esponse
LR	**L**ow **R**esolution
MAE	**M**agneto**A**coustic **E**mission
MAPS	**M**agnetic **A**nisotropy and **P**ermeability **S**ystem
MMF	**M**agneto**M**otive **F**orce
MR	**M**edium **R**esolution
NDE	**N**on-**D**estructive **E**valuation
OUC	**O**rthogonal **U**-**C**ore
PCB	**P**rinted **C**ircuit **B**oard

PSD	**P**ower **S**pectral **D**ensity
PUA	**P**ick**U**p **A**ssembly
RFID	**R**adio-**F**requency **ID**entification
RMS	**R**oot-**M**ean-**S**quare
RTA	**R**eal-**T**ime **A**nalog
SCC	**S**tress **C**orrosion **C**cracking
SFB	**S**mall **F**eeder **B**end
SL4P	**S**pring-**L**oaded **4**[tetra]pole **P**rototype
SSD	**S**teady **S**tate **D**igital
UNENE	**U**niversity **N**etwork for **E**xcellence in **N**uclear **E**ngineering
VF	**V**oltage **F**ollowing

Chapter 1

Introduction

The design of engineered components is constrained by the properties of the materials and the manufacturing methods employed. During their service life, components are subject to processes that change their characteristics and material properties. Such changes can lead to the eventual failure of a system if the components are not repaired or replaced appropriately. Where the cost of repair, replacement, or the consequence of failure of specific components is sufficient, it becomes cost-effective to inspect the components regularly for signs of degradation. Inspections performed using measurement techniques that do not require disassembling or damaging the system are valued. Analysis of the inspection data produces estimates of the component properties. This process is referred to as non-destructive evaluation (NDE). An estimate of risk is derived from the data, and only components identified as requiring repair or replacement are addressed. This reduces the system owner's costs and helps maximise the system availability.

The uncertainties associated with the NDE of material properties in an industrial environment vary widely between measurement technologies and specific components.

Hence the effectiveness of flaw detection and lifetime estimation are limited. The distribution of stress within a material following significant plastic deformation (residual stress) has proven to be a particularly elusive quantity for NDE.

The goal of this thesis was to develop a prototype NDE system capable of measuring residual stresses in ferromagnetic CANDU® (CANadian Deuterium Uranium) feeder pipe bends, with a specific focus on magnetic Barkhausen noise (BN) testing. This chapter presents an introduction to BN testing and residual stress measurement in feeder pipes:

- Section 1.1 presents a description of the stress tensor field.
- Section 1.2 introduces strain as a measurable tensor field that can be related to stress.
- In Section 1.3 the relationship between ferromagnetism, stress and strain is introduced.
- The history of BN NDE and a basic BN testing apparatus are described in Section 1.4.
- Section 1.5 presents an introduction to CANDU® feeder pipes.
- The ideal specifications for residual stress measurement on feeder pipes are presented in Section 1.6.
- Section 1.7 presents a discussion of the known limitations of BN testing with respect to the ideal stress measurement specifications.
- The organisation of the thesis is presented in Section 1.8.

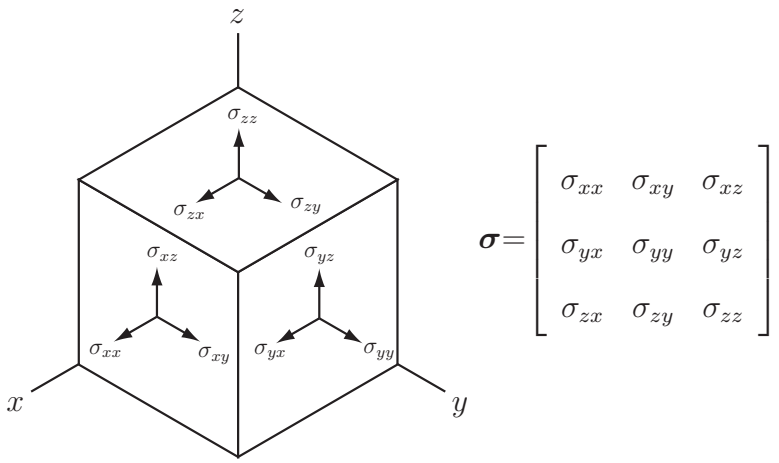

Figure 1.1: Representation of the stress tensor ($\boldsymbol{\sigma}$) in cartesian coordinates.

1.1 Stress

Stress is defined as the force per unit area within a body. Since both force and area* are three-dimensional vectors, stress ($\boldsymbol{\sigma}$) is a second-order tensor with nine components (σ_{jk}) [1], as shown in Figure 1.1. Diagonal elements in the stress tensor ($\sigma_{jk}, j = k$) represent the normal stress components, and off-diagonal elements ($\sigma_{jk}, j \neq k$) are the shear stress components. Stress varies spatially, and is thus a tensor field.

The maximum stress a material can support elastically is its yield stress (σ_{yield}). Once the yield stress is achieved the material undergoes plastic deformation. When an object is in equilibrium, the integral of stress over its volume is zero. All physical measurements of stress are estimates of the average stress within a gauge volume defined by the spatial resolution of the measurement.

The details of the stress field vary as a function of scale [1], as illustrated in Figure

*Area is a vector normal to a surface, with sign defined by the right-hand rule around the perimeter, and magnitude of the scalar area.

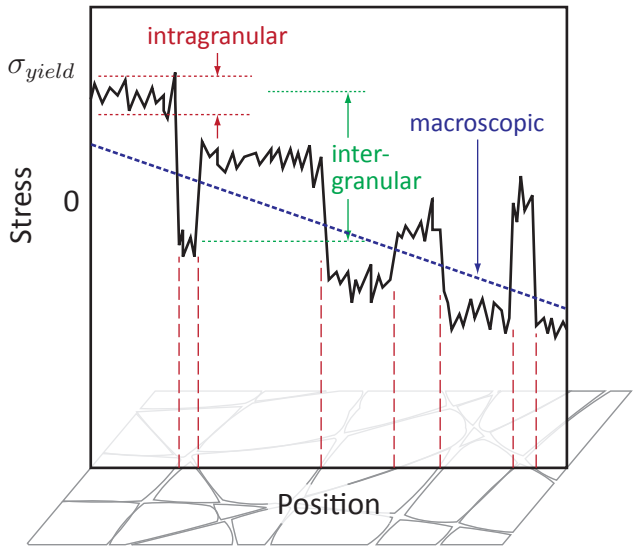

Figure 1.2: An illustration of macrostress, and intergranular and intragranular microstresses as a function of position in a polycrystalline material. Stress cannot exceed σ_{yield} within an object in equilibrium.

1.2. If the gauge volume encloses a significant number of grains in a polycrystalline material, the measured stress is referred to as 'type 1' or the macroscopic stress field. When the gauge volume is on the order of the grain size or less, the measured stresses are referred to as 'microstresses.' 'Type 2' microstresses are classified as the intergranular interactions at grain boundaries, and 'type 3' microstresses are the intragranular variations in the stress field due to dislocations and crystalline defects. Stress gradients are common in engineered components, as are yield stresses at the extremes of these gradients. Gauge volumes must therefore be sufficiently small to resolve gradients in the directions of interest.

Significant stresses are applied to plastically deform many engineered components during manufacturing processes. When these manufacturing stresses are removed, components recover some of their initial shape via elastic deformation and acquire a residual stress distribution. Residual stresses are sometimes desirable, for example in

tempered glass or shot peened components. When undesirable, residual stresses can be removed or modified via additional plastic deformation and annealing processes. While components may be engineered with service life specifications in mind, if the residual stress distribution is insufficiently accounted for in the design, the component may fail earlier than expected.

Early failures of various engineered components due to residual stresses has led to the residual stress field often being cited as a quantity of interest for NDE. As with force, stress cannot be directly measured. Therefore, stress estimates must be inferred from the change in some other measurable tensor phenomena that are influenced by the stress field.

1.2 Strain

The most common parameter used to infer stress is the geometrical deformation, or strain ($\boldsymbol{\varepsilon}$), of the material. Individual components of the strain tensor (ε_{jk}) are typically measured as:

$$\varepsilon_{jk} = \frac{d - d_0}{d_0}, \tag{1.1}$$

where d is the as-tested length of a material and d_0 is the unstrained length in the orientation indicated by j and k.

Conversion between strain and stress requires use of the fourth-order stiffness tensor of the material, with components c_{jklm} [1]:

$$\sigma_{jk} = \sum_{lm} c_{jklm}\varepsilon_{lm}. \tag{1.2}$$

The determination of c_{jklm} requires a full understanding of the effects of elastic and

plastic anisotropy in the material under test, and how these vary throughout the sample.

To simplify the conversion for engineering investigations it is often assumed that materials are isotropic, in which case stress and strain can be related via the generalized Hooke's law equations as [1]:

$$\sigma_{jk} = \frac{Y}{1+\nu}\left[\varepsilon_{jk} + \frac{\nu}{1-2\nu}\left(\varepsilon_{11}+\varepsilon_{22}+\varepsilon_{33}\right)\right], \tag{1.3}$$

where Y is Young's modulus and ν is Poisson's ratio. Note that the appropriate values of Y and ν depend on the details of how strain is measured.

Strain measurements can be performed at a variety of scales, from macroscopic measurements using surface-mounted resistive strain gauges, to measuring the interatomic spacing using X-ray or neutron diffraction. However, strain is not the only measurable phenomenon affected by stress. For example, the magnetic properties of ferromagnetic alloys interact strongly with the stress field, and may be measured with the appropriate instrumentation, calibrated, and used for stress estimation.

1.3 Ferromagnetism and Stress

Two electrons are said to be ferromagnetic when their spins are aligned via the quantum mechanical exchange interaction. Certain materials, such as body-centered cubic (BCC) Fe, have both un-paired valence electrons, and a crystalline lattice spacing that favours ferromagnetic exchange. Ferromagnetism, combined with spin-orbit coupling

and magnetostatics, leads to the unpaired spins throughout these materials spontaneously aligning in groups called domains, bounded by domains walls. This ferromagnetic domain structure was first proposed by Weiss in 1907 [2], as a means of explaining the magnetic behaviour of ferromagnetic alloys.

In BCC Fe, it is the spacing along the $\langle 100 \rangle$ Miller directions[†] that give rise to ferromagnetism. However, the magnetic energies in Fe would be reduced if the $\langle 100 \rangle$ spacing was slightly larger. As a result, the ferromagnetic domain structure exerts stresses on the crystal, and interacts with the stress field.

This interaction between stress and magnetism was discovered in 1841 by Joule, who found that the dimensions of ferromagnetic materials change when magnetised [3]. The inverse was discovered by Villari in 1865; that the magnetic properties of ferromagnets changed when subjected to external stresses [4]. These two phenomena are forms of magnetoelasticity: Joule's discovery being magnetostriction, and Villari's the Villari effect. Ferromagnetic NDE for the purpose of residual stress measurement is primarily concerned with the latter.

In ferromagnetic NDE, domain structures are probed by applying a controlled magnetic excitation field. As the excitation field changes, the domain structure reconfigures to minimize various energies in the system. The excitation field is usually produced by passing electric current through loops of conductive wire, and measuring the change in the electric potential across the wire or in a secondary sensor. The ferromagnetic domain structure is in general anisotropic, with the Villari effect being one of the primary phenomena responsible for the anisotropy. Thus changing the

[†]The following conventions apply: Individual planes are denoted (hkl), such as the six faces of a cube: (100), (010), (001), $(\bar{1}00)$, $(0\bar{1}0)$, $(00\bar{1})$. The set of planes is denoted $\{hkl\}$ where the hkl indices may be any plane in the set. Individual directions are enclosed in square brackets: $[hkl]$, and the set of directions is enclosed in angular brackets: $\langle hkl \rangle$.

orientation of the excitation field allows mapping of the domain structure anisotropy, which can be correlated with stress and strain.

In general, it is difficult to control and localize magnetic fields. However, bulk metallic ferromagnetic alloys are also electrically conductive. When magnetic fields change in conductive materials, eddy currents are produced within the material, which attenuate magnetic fields. Therefore, low frequencies travel further in bulk ferromagnetic alloys than high frequencies, and it is through time and frequency analysis that magnetic fields can be localized. One measurement technique that exploits this phenomenon is Barkhausen noise testing.

1.4 Barkhausen Noise Testing

Barkhausen noise (BN) is attributed to abrupt changes in the domain structure when subjected to a time-varying magnetic field (or other external forces that cause domain reconfiguration, e.g. stress). These abrupt changes occur because non-ferromagnetic interruptions to the domain structure inhibit its motion, until the excitation field is sufficient to overcome the energy potentials involved. The tendency of the domain structure to get 'stuck' on these non-ferromagnetic interruptions has led to them being described as 'pinning sites,' with associated energies.

As a result of the number of pinning sites and the energies involved within bulk ferromagnetic alloys, the power spectrum of BN is typically attributed to frequencies $> 1\,\text{kHz}$. If excitation frequencies are significantly less than 1 kHz, then BN can be isolated from excitation field signals by high-pass filtering. Thus the high frequency BN is local to the BN sensor position, while the low frequency excitation field can be used to uniformly magnetise large regions of the material. Typical excitation

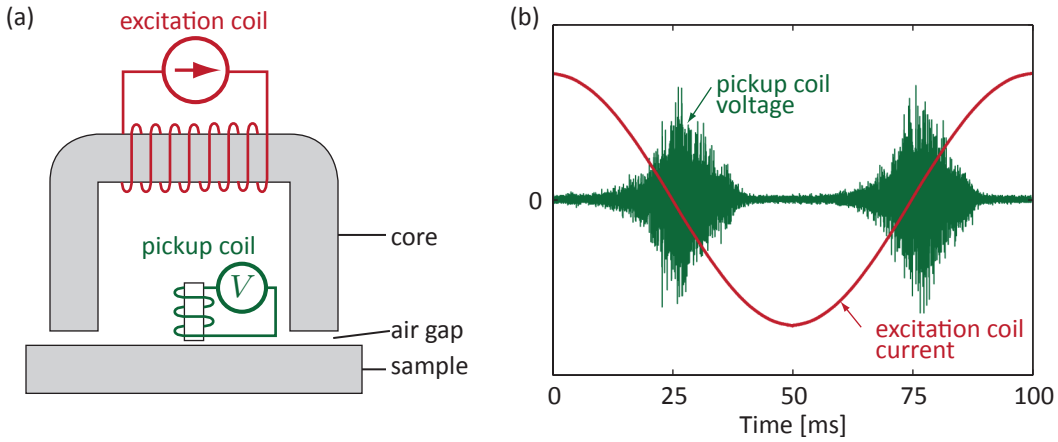

Figure 1.3: (a) A simplified Barkhausen noise apparatus. (b) Excitation coil current and high-pass filtered pickup coil voltage waveforms from a mild steel.

frequencies range from mHz, for fundamental analysis of BN behaviour, up to 100 Hz in NDE studies.

The BN testing methodology uses a large amplitude low frequency excitation field to cycle the sample around the hysteresis loop. As the magnetic configuration of the sample varies, BN emissions are produced within the sample and propagate to the surface. A simplified magnetic circuit for BN measurement is shown in Figure 1.3a. An excitation coil wound on a U-core forms an electromagnet, which is supplied with an alternating current. A pickup coil is placed near the sample, and BN is detected as the domain structure reconfigures in response to the excitation field. Figure 1.3b shows the excitation current waveform and the pickup coil voltage from a mild steel sample with a 10 Hz excitation frequency. Figure 1.3b shows two bursts of BN each excitation cycle, when the derivative of the current is a maximum, and that the frequency content of the BN is significantly higher than that of the excitation current.

BN was discovered by Heinrich Barkhausen in 1919 [5][‡], and was considered the first experimental evidence for the ferromagnetic domain structure. Understanding of BN and domain theory improved throughout the 20$^{\text{th}}$ century. Direct imaging of domain structures was first achieved by Bitter in 1931 [7], and in 1949 Williams and Schockley correlated magnetisation changes with domain wall motion in a single crystal of 3.8% silicon iron [8]. Williams and Shockley's classic experiment also demonstrated rapid domain wall motion around crystal imperfections producing BN.

Barkhausen noise remained a scientific curiousity until 1964, when Leep identified BN as being a "structure-sensitive characteristic of ferromagnetic materials" [9]. The first correlations between BN and stress were demonstrated by Pasley in 1970 [10], and since then BN has been frequently proposed and used for NDE, and in particular for residual stress measurements.

Currently, there are commercial vendors who exploit BN for residual stress measurement, the most prominent of which is the *StressTech* group, whose devices apply a 1987 patent by Tiitto [11]. There is also a competing product dubbed *Introscan* from Vengrinovich in Belarus [12], though engineering details are not found. BN is not the only magnetic technique used for residual stress measurement. For example, the magnetic anisotropy and permeability system (MAPS) [13, 14, 15, 16] measures the excitation field coupling and the magnetic field component orthogonal to the excitation field orientation that results from domain structure anisotropy, and uses various frequencies to retrieve depth information.

While magnetic measurements are sensitive to stress due to magnetostriction, they are also sensitive to a variety of other aspects of the testing system; geometry

[‡]For an English translation see Appendix A in [6]

in particular. Most magnetic NDE applications therefore require a customized sensor design that accommodates the sample geometry. For this project, the specific geometry of interest is that of CANDU® feeder pipe bends. All currently available commercial probes have coupling and/or accessibility restrictions when applied to feeder geometries.

1.5 CANDU® Feeder Pipes

The ferromagnetic SA-106 grade B schedule 80 carbon steel feeder pipes (feeders) in CANDU® nuclear reactors are part of the primary heat transport circuit. A simplified illustration of a CANDU® 6 reactor face is shown in Figure 1.4[§]. Feeders carry heavy water from pump outlet headers to the pressure tube inlet end fittings on the reactor face, and from the pressure tube outlet end fittings to the outlet headers. There are between 760 and 960 feeders per reactor. The feeders must access the matrix of end fittings, which necessitates a variety of bending arrangements with minimum clearances on the order of 20 mm. The feeders have nominal diameters of 50.8 mm (2.0") or 63.5 mm (2.5"), with bend radii of 1.5× the diameter, and bend angles ranging from 32° to 73°. The wall thickness of 63.5 mm diameter feeders can vary between 4 mm and 8 mm, depending on corrosion and the ovality of the pipe due to the bending process. The minimum tensile yield stress for SA-106 grade B steel is 240 MPa [17].

In 1997, an outlet feeder pipe was removed from service following detection of a leak. Cracking in the pipe was analysed with a variety of techniques, and neutron diffraction measurements were used to estimate the residual stress distribution

[§]Adapted from the CANTEACH library, `http://canteach.candu.org/library/19990113.pdf`

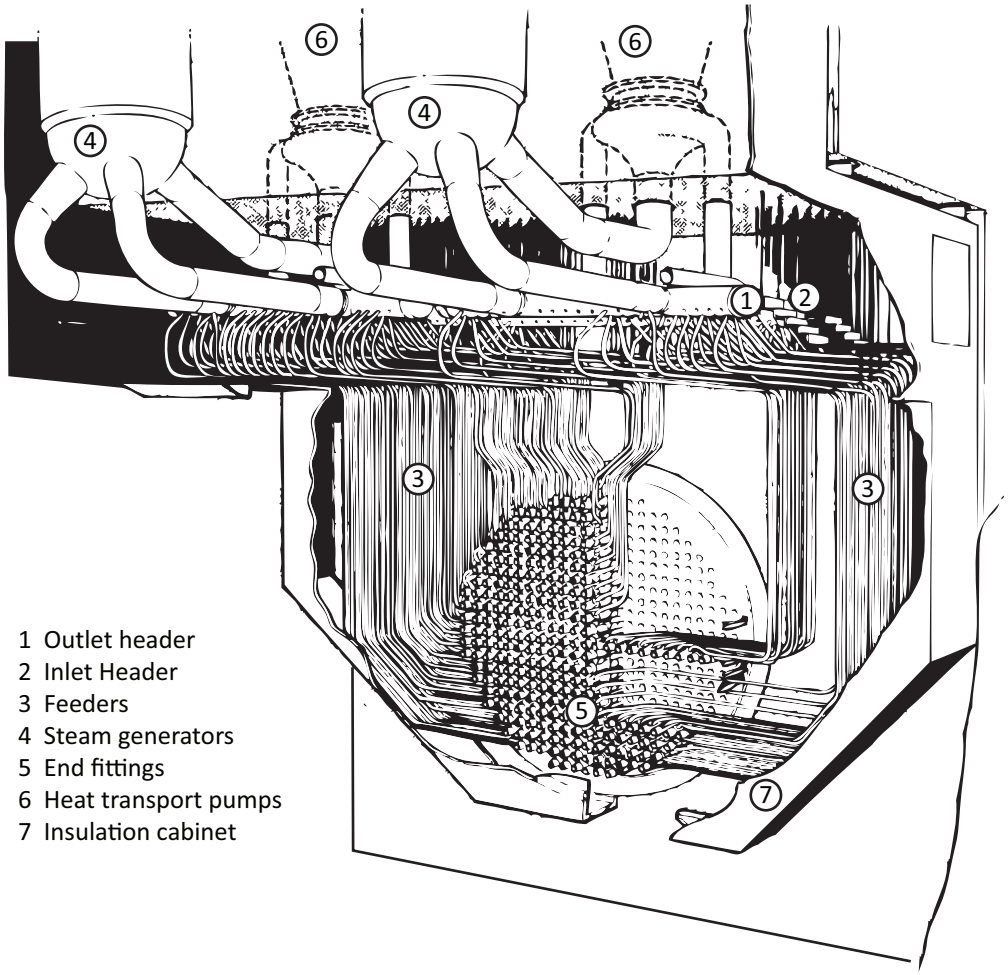

Figure 1.4: Simplified illustration of a CANDU® 6 reactor face.

[18, 19]. It was concluded from the data that a combination of an elevated stress distribution and flow-assisted corrosion led to stress-corrosion cracking (SCC) in the pipe wall along grain boundaries. The SCC was initiated by yield strength tensile stresses on the inner surface of the pipes. Subsequently, SCC has been identified in a number of outlet feeders, both on the inner and the outer surfaces [20].

It is a Canadian regulatory requirement to prevent leakage from the feeder piping

system. When cracking cannot be precluded, the Canadian Nuclear Safety Commission (CNSC) requires a shutdown leakage limit[¶] of $20\,\mathrm{kg}\cdot\mathrm{h}^{-1}$ for feeder piping [20]. Given the high replacement cost of pressure boundary components and the possibility of forced outages[‖], reactor operators are interested in monitoring component status at the reactor face, and deploy NDE teams regularly to inspect their systems. However, there is currently no commercial NDE system, ferromagnetic or otherwise, suitable for measuring stresses in the feeder piping at the reactor face, which are thought to be a primary cause of the SCC observed.

Rather than pursue an industrial research and development initiative with a commercial company, Atomic Energy of Canada Ltd. (AECL) approached the Queen's University Applied Magnetics Group (AMG) through the University Network for Excellence in Nuclear Engineering (UNENE), with regards to adapting a ferromagnetic NDE technique to CANDU® feeders for the purpose of measuring residual stress.

1.6 Specifications & Constraints

An ideal non-destructive stress measurement technology for feeders:

- Provides an estimate of at least three normal components of stress (e.g., the axial, hoop, and radial stress components for a pipe), with a spatial resolution of $1\,\mathrm{mm}^3$ throughout the wall thickness and an accuracy on the order of $\pm 25\,\mathrm{MPa}$.
- Is operational under shut-down conditions at the reactor face, which include feeder pipe temperatures ranging from $35\,^\circ\mathrm{C}$ to $42\,^\circ\mathrm{C}$ and radiation fields on

[¶]If a feeder starts leaking while a reactor is running, operators must shut down the reactor if the leak exceeds the shutdown leakage limit.

[‖]A non-scheduled shut down when unplanned maintenance is required.

the order of $1.5\,\mathrm{mGy}\cdot\mathrm{h}^{-1}$ to $2\,\mathrm{mGy}\cdot\mathrm{h}^{-1}$ [21].

- Fits within the 20 mm minimum clearance between the pipes.
- Accommodates the variable curvature of feeder pipe bends.
- Operates on the outer surface, as direct access to the inner surface is not feasible, due to the closed-loop nature of the primary heat transport circuit.
- Can be adapted to regions where direct access to the outer surface of individual feeders is obscured by the geometry of the feeder lattice.
- Requires minimal training to operate.

The outage schedule, the radiation fields, and the time required to perform a scan limits the number of pipes that can be inspected. The cost of inspection is influenced by the probability of false and missed positives**, the costs associated with extending outages to perform inspections, and the costs of the instruments and performing the inspections themselves.

1.7 BN Limitations

After some preliminary BN [22] and magnetic flux leakage [23] measurements, the two primary magnetic NDE techniques used by the AMG, it was concluded that BN testing was more likely than flux leakage to produce quantitative estimates of stress from feeders. However, the existing technique has some inherent limitations compared with the ideal NDE solution specifications listed in Section 1.6.

**A 'positive' is an inspection result that requires further investigation and expense. A false positive is a mis-identified feature that did not require further investigation. A missed positive is a feature that did require investigation, but was not detected.

While the frequency content of BN is necessary to obtain high resolution measurements of stress, this also means BN is inherently a near-surface measurement. Skin depth considerations typically limit BN penetration depth to between 0.01 mm and 1.5 mm. This is greater than the 5 µm to 10 µm penetration depth of X-ray diffraction (which was ruled out by AECL as being too shallow to resolve the stresses of interest [18]) though not sufficient to resolve stresses through the 4 mm to 8 mm wall thickness.

Due to the near-surface limitation, BN has sensitivity primarily to stress components in the surface plane, which are the axial and hoop stresses for the outer surface of feeder piping. No BN technique has yet been developed to measure the radial stress component, since a radial excitation field is difficult to produce. However, neutron diffraction studies have shown that the residual radial stresses in feeders are small, and are therefore not likely to contribute to SCC [24]. It is unknown if outer surface axial and hoop stresses alone are sufficient for an *in situ* NDE technology to be successful. Despite this limitation, BN was still considered a technology worth exploring.

Historically, BN testing has been performed on samples with well-defined surface geometries and finishes using electromagnets that were geometrically conformed to the surface (usually flat surfaces, with flat bottomed U-core electromagnets). This meant that the magnetic coupling between the electromagnet and the sample would be similar for all measurements, and thus any change in the BN was due to variation in the sample magnetic properties. To measure multiple stress components, the excitation field orientation was rotated in the plane of the sample surface, and the

angular variation of the BN was correlated with the stress components in the surface plane. Often motors were used to mechanically rotate the core for this purpose [13, 14, 16], however some devices employ superposition of fields from two orthogonal electromagnets [12].

On feeders, there is variable surface curvature as a result of the bending process. Thus no fixed-geometry electromagnet can maintain the same coupling at all positions and orientations on the pipe surface. Furthermore, obtaining identical finishes on installed feeder pipes may be problematic. In addition to this electromagnet coupling problem, the 20 mm clearances for the feeder lattice limits the geometry of the electromagnet cores and any additional apparatus used to adjust the electromagnet position.

1.8 Organization of Thesis

The organization of the thesis is as follows:

- Chapter 2 presents a review of the electrodynamic theories used to describe the generation of BN within ferromagnetic materials, and provides an overview of the theories used throughout the thesis to model the BN NDE system.

- In Chapter 3, the BN NDE circuit is evaluated using magnetic circuit theory. Control of the magnetic flux through the circuit is theoretically shown to compensate for electromagnet coupling variations. Models of BN NDE circuits that fit within the feeder clearance are evaluated, which indicate an active flux controller is required to produce repeatable measurements in feeders. Active

flux controller design considerations are provided, and field superposition using a 'tetrapole' electromagnet is then identified as a means of performing BN anisotropy measurements with no moving parts.

- Chapter 4 presents hardware and software implementation details regarding the four channel flux control system (FCS) that was developed to power a tetrapole electromagnet.

- Chapter 5 presents the design process for the spring-loaded tetrapole prototype (SL4P) probe, which included finite element modelling of tetrapole electromagnets and the pickup coil.

- In Chapter 6 the combined performance of the FCS and SL4P is evaluated.

- Chapter 7 presents models for the BN penetration depth in feeder pipe steel, and the transfer function for voltages induced in the pickup coil.

- Chapter 8 presents the BN analysis methodology that was developed in order to parameterize the BN response to the excitation field and strain.

- Chapter 9 presents BN data from three SA-106 Grade B pipes that were used to evaluate the BN excitation field response and strain correlations in feeder pipe steels.

- Chapter 10 presents a summary of the findings of this thesis work.

- Chapter 11 provides suggestions for future measurements and system improvements.

All circuit designs, circuit assembly, models, probe designs, figures, drawings, physical probes and measurements described in this thesis are the work of the author unless otherwise noted. This includes all *MagNet* models, implemented *LabVIEW* code, probe machining, and coil winding. Suppliers for custom and commercial parts are indicated where applicable. The three point bending rig used in Section 9.2 was designed by the author and instrumented by Pat Weyman.

Chapter 2

Theory and Background

This chapter presents a theoretical summary of ferromagnetic behaviour, using magnetic field theory and domain theory, in order to derive the relevant models and approximations for the design work in later chapters.

- The base electrodynamic field theory equations are presented in Section 2.1.
- The classification of magnetic materials is described in 2.2.
- Section 2.3 presents a review of ferromagnetic domain theory, culminating in a description of the Barkhausen effect.
- Field theory equations are used to derive the basic equations for coils and inductors in Section 2.4.
- In Section 2.5 the attenuation of plane wave magnetic fields in conductive materials is presented.
- In Section 2.6 the interaction of multiple permeable and conductive components is presented, drawing analogies from electric circuit theory.

2.1 Electrodynamic Fields

Maxwell's equations describe the general relationships between the electric field ($\vec{E}$) and magnetic flux density ($\vec{B}$) [25, 26]. These four equations* are:

Gauss' law:

$$\nabla \cdot \vec{E} = \frac{1}{\epsilon_0}\rho, \tag{2.1}$$

Faraday's law:

$$\nabla \times \vec{E} = -\frac{\partial \vec{B}}{\partial t}, \tag{2.2}$$

Gauss' law for magnetism:

$$\nabla \cdot \vec{B} = 0, \tag{2.3}$$

and Ampère's law (with Maxwell's correction [25]):

$$\nabla \times \vec{B} = \mu_0 \vec{J} + \mu_0 \epsilon_0 \frac{\partial \vec{E}}{\partial t}, \tag{2.4}$$

where $\epsilon_0 \approx 8.8542 \times 10^{-12}\,\mathrm{F \cdot m^{-1}}$ is the permittivity of free space, $\mu_0 = 4\pi \times 10^{-7}\,\mathrm{H \cdot m^{-1}}$ is the permeability of free space, ρ is the spatial distribution of electric charge, $\vec{J}$ is the current density field, and t is time.

Both $\vec{E}$ and $\vec{B}$ interact with matter by producing forces ($\vec{F}$) on charged particles according to the Lorentz force law:

$$\vec{F} = q\left(\vec{E} + \vec{v} \times \vec{B}\right), \tag{2.5}$$

where q is the charge of a particle, and $\vec{v}$ is the velocity of that particle. To date,

*The following derivations follow the vector notation provided in Griffiths [27], which is attributed to Gibbs, Heaviside and Hertz [28, 29].

there have been no sources of magnetic charge discovered, which would change the form of equations (2.2) and (2.3). Thus $\vec{B}$ is produced by $\vec{J}$ and $\partial\vec{E}/\partial t$, according to Ampère's law (2.4). In most magnetic experiments $\vec{J} \gg \epsilon_0\mu_0 \cdot \partial\vec{E}/\partial t$, and thus the $\partial\vec{E}/\partial t$ term is often dropped. Since $\vec{J}$ is often the primary source of $\vec{B}$, a more detailed understanding of $\vec{J}$ is required to perform magnetic experiments.

$\vec{J}$ describes the motion of electric charge, which includes the intrinsic spin of fundamental charged particles, orbital angular momentum of charged particles within atoms or molecules, and the translation of charged particles. Since the translation of charged particles can be controlled and monitored in the form of electric current, it is considered convenient to differentiate current sources due to spin and angular momentum as the bound current density field ($\vec{J}_b$), and current sources due to translation as the free current density field ($\vec{J}_f$), such that:

$$\vec{J} = \vec{J}_b + \vec{J}_f. \tag{2.6}$$

The magnetisation field ($\vec{M}$) is then attributed to bound currents:

$$\nabla \times \vec{M} = \vec{J}_b, \tag{2.7}$$

and the auxiliary magnetic field ($\vec{H}$) to free currents:

$$\nabla \times \vec{H} = \vec{J}_f + \epsilon_0 \frac{\partial \vec{E}}{\partial t}. \tag{2.8}$$

Rearranging equations (2.4), (2.6), (2.7), and (2.8), $\vec{B}$ can be expressed as:

$$\vec{B} = \mu_0 \left(\vec{M} + \vec{H} \right). \tag{2.9}$$

Since a curl implies gauge freedom, Gauss' law of magnetism (2.3) is required to define $\vec{M}$ and $\vec{H}$ everywhere in space. Combining equations (2.3) and (2.9) gives:

$$\nabla \cdot \vec{H} = -\nabla \cdot \vec{M}. \tag{2.10}$$

Even when there is no free current (i.e., $\vec{J_f} = 0$), the presence of bound currents ($\vec{J_b} \neq 0$), requires that $\vec{H}$ is non-zero. This contribution to $\vec{H}$ is called the demagnetising field ($\vec{H_d}$). In most systems involving ferromagnetic materials, $\vec{J_b} \gg \vec{J_f}$.

2.2 Magnetic Materials

Magnetic materials are classified by characterizing $\vec{B}$ in response to $\vec{H}$, according to either the relative permeability tensor field ($\boldsymbol{\mu_r}$):

$$\vec{B} = \mu_0 \boldsymbol{\mu_r} \vec{H}, \tag{2.11}$$

or the susceptibility tensor field ($\boldsymbol{\chi_m}$):

$$\vec{B} = \mu_0 \left(\mathbf{1} + \boldsymbol{\chi_m}\right) \vec{H}. \tag{2.12}$$

Conceptually, $\boldsymbol{\mu_r}$ and $\boldsymbol{\chi_m}$ are proportionality constants to relate $\vec{B}$ and $\vec{H}$. Both parameters indicate the response of $\vec{J_b}$ to $\vec{J_f}$ and are an alternative means of expressing $\vec{M}$. If the magnetic properties of a material are assumed isotropic and linear, $\boldsymbol{\chi_m}$ can be represented as a scalar and used to differentiate various magnetic materials, as shown in Table 2.1 [30, 31].

Table 2.1: Classification of magnetic materials

χ_m	Classification	Description	Examples
-10^{-5}	Diamagnetic	Atoms/molecules have no net magnetic moment. $\vec{H}$ interacts with orbital electron currents according to Faraday's law, decreasing $\vec{B}$. In the case of superconductors, $\chi_m \approx -1$.	Cu, Ag, Au, Bi
$10^{-5} \ldots 10^{-3}$	Paramagnetic	Atoms/molecules have magnetic moments. $\vec{H}$ produces a torque on the moments causing them to align. When $\vec{H}$ is removed, the alignment disappears.	Al, Pt, Ti
$10 \ldots 10^{6}$	Ferromagnetic	Below the Curie temperature ($\mathcal{T}_C$), spin exchange coupling aligns adjacent atomic moments. Groups of aligned moments form a magnetic domain structure. Above $\mathcal{T}_C$ ferromagnetic materials become paramagnetic.	Fe, Ni, Co
$10 \ldots 10^{4}$	Ferrimagnetic	Similar to ferromagnetism with regards to $\mathcal{T}_C$. Ferrimagnetic materials are alloys or compounds with multiple atomic/molecular species, wherin one or more species are coupled via ferromagnetism, and one or more species are antiferromagnetic.	$BaO \cdot 6Fe_2O_3$, $MO{\cdot}Fe_2O_3$ (M=Fe, Ni, Mg, Mn)

While the isotropic linear approximation is often valid for diamagnetic and paramagnetic materials up to saturation, the response of ferromagnetic and ferrimagnetic materials to any given magnetic field is nonlinear and usually exhibits hysteresis due to irreversible processes. The nonlinear properties of ferromagnetic and ferrimagnetic materials are due to long range ordering of atomic magnetic moments, referred to as the domain structure. The coupling of the domain structure to conditions in material microstructure is the basis for magnetic NDE.

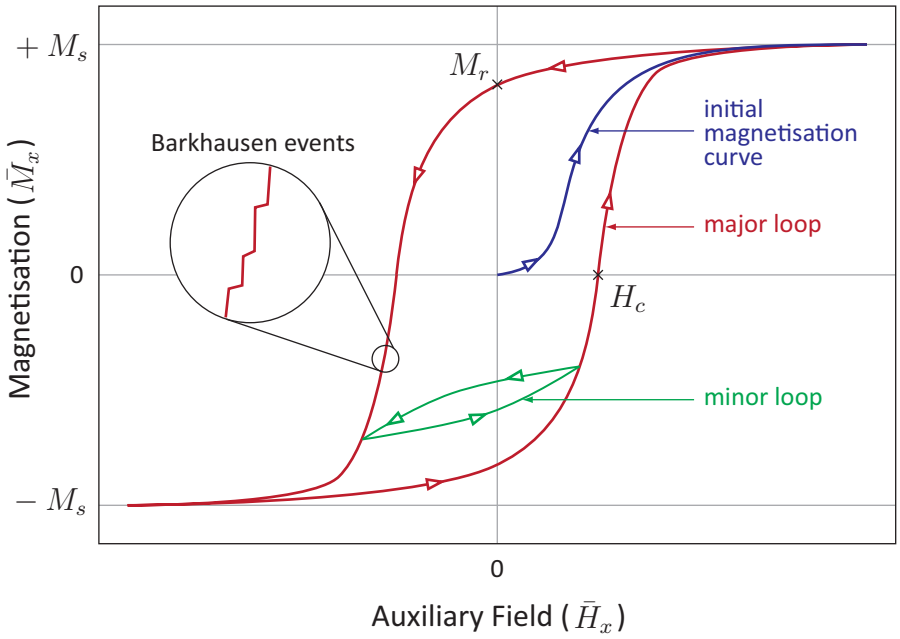

Figure 2.1: An illustration of ferromagnetic hysteresis for volume averaged components of $\vec{H}$ and $\vec{M}$ along the $\hat{x}$ direction ($\bar{H}_x$ and $\bar{M}_x$, respectively). Below the saturation magnetisation (M_s) $\bar{M}_x$ varies in small abrupt changes, referred to as Barkhausen events (inset).

Figure 2.1 illustrates the typical features of a ferromagnetic hysteresis loop, plotting the volume averaged components of $\vec{H}$ and $\vec{M}$ along the $\hat{x}$ direction ($\bar{H}_x$ and $\bar{M}_x$, respectively). Starting at the origin in Figure 2.1, in a demagnetized sample $\bar{H}_x$ and $\bar{M}_x$ are zero. As $\bar{H}_x$ is increased, $\bar{M}_x$ follows the initial magnetisation curve up to the saturation magnetisation M_s. When $\bar{H}_x$ is subsequently varied, $\bar{M}_x$ lags, tracing out the major hysteresis loop, such that when $\bar{H}_x = 0$, $\bar{M}_x$ is the residual magnetisation, M_r. $\bar{M}_x \neq 0$ until $\bar{H}_x$ is the coercive field (H_c). If $\bar{H}_x$ is decreased before M_s is achieved, $\bar{M}_x$ traces out a minor hysteresis loop.

The inset in Figure 2.1 shows that $\bar{M}_x$ varies in relatively small abrupt changes referred to as Barkhausen events. In a macroscopic view, the Barkhausen events are smoothed to give the average slope to the hysteresis loop. When discussing the

changing magnetic fields in non-linear magnetic materials, it is often convenient to define the differential permeability ($\boldsymbol{\mu_d}$):

$$\boldsymbol{\mu_d} = \frac{1}{\mu_0}\frac{\mathrm{d}\vec{B}}{\mathrm{d}\vec{H}}, \tag{2.13}$$

as this parameter indicates the slope of the hysteresis loop within a material.

Note that all free currents, including eddy currents (see Section 2.5), contribute to $\vec{H}$, and must be accounted for in order to determine $\boldsymbol{\mu_r}$, $\boldsymbol{\chi_m}$, and $\boldsymbol{\mu_d}$ for a given material. If materials are anisotropic then nine hysteresis loops are required to completely describe any of the above tensors, as described in [32].

2.3 Domain Theory

In ferromagnetic and ferrimagnetic materials atomic and molecular magnetic moments spontaneously align in groups called domains. Each domain has the saturation magnetisation, M_s, which is a function of temperature. The Curie temperature ($\mathcal{T}_C$) is defined as the temperature above which thermal excitations are sufficient to eliminate the spontaneous alignment. If there is no auxiliary field or residual magnetisation, the domains are oriented such that the sum of all magnetic moments is zero, as illustrated in Figure 2.2a. Between opposing domains there exist transition regions called domain walls, shown in Figures 2.2b and 2.2c, where moments rotate between the orientations of the surrounding domains.

In crystalline ferromagnetic materials, magnetic domains are not randomly oriented, but rather have preferential alignment along specific crystallographic axes. Domain walls are classified according to the relative orientation of the neighbouring

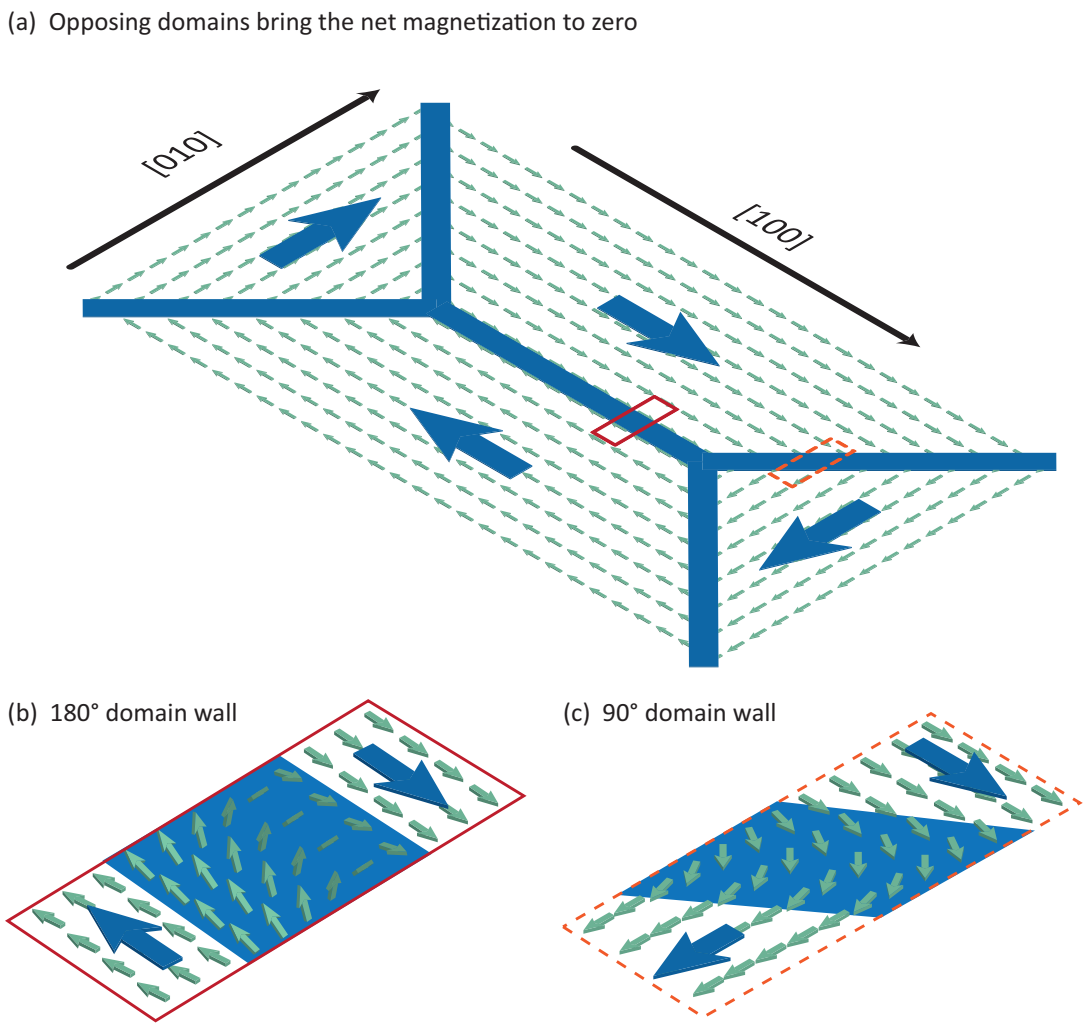

Figure 2.2: (a) Illustration of a 2D Section in a magnetic domain structure showing four domains (blue) consisting of aligned magnetic moments (green), oriented such that the net magnetic moment is zero. Crystalline [100] and [010] axes are indicated to show the preferential domain orientation along these axes, consistent with the behaviour of domains in body-centered cubic Fe. (b) Illustrated magnification of a 180° domain wall. (c) Illustrated magnification of a 90° domain wall.

domains, with 180° walls and 90° walls illustrated in Figures 2.2b and 2.2c respectively. In the case of body-centered cubic (BCC) Fe, domains are oriented primarily along the vectors denoted $\langle 100 \rangle$, and hence domain walls are usually 90° or 180°. More complex domain structures may form at boundaries with non-ferromagnetic materials, such as surfaces and inclusions.

2.3.1 Magnetic Energies

Ferromagnetic domain structures arise from the competition between the exchange energy ($\mathcal{E}_{ex}$), magnetocrystalline anisotropy energy ($\mathcal{E}_{mca}$), and magnetostatic energy ($\mathcal{E}_{ms}$). Competition between $\mathcal{E}_{ex}$ and $\mathcal{E}_{mca}$ results in a characteristic domain wall energy ($\mathcal{E}_{wall}$), and external fields interact with the domain structure via the Zeeman energy ($\mathcal{E}_{p}$). In this section the above energies are individually discussed, with focus on their effects in BCC Fe.

Exchange Energy ($\mathcal{E}_{ex}$)

The alignment of adjacent atomic moments in a ferromagnet is due to the quantum mechanical exchange interaction first described by Heisenberg [33] and Dirac [34]. There is a finite probability that a pair of atomic moments with spins $\vec{S}_j$ and $\vec{S}_k$ will exchange angular momentum, as illustrated in Figure 2.3a. For a group of atoms each with position $\vec{r}_j$, spin angular momentum $\vec{S}_j$ with magnitude S_j, the total exchange energy is [6]:

$$\mathcal{E}_{ex} = \sum_{jk} \mathcal{J}\left(|\vec{r}_j - \vec{r}_k|\right) S_j S_k \cos\alpha. \tag{2.14}$$

where the sum is over all atom pairs (jk), $|\vec{r}_j - \vec{r}_k|$ is the distance between a moment pair, $\mathcal{J}\left(|\vec{r}_j - \vec{r}_k|\right)$ is the exchange integral, and α is the angle between the spins.

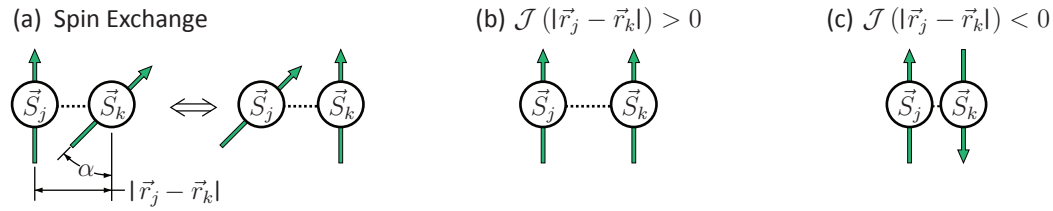

Figure 2.3: (a) A pair of spins $\vec{S}_j$ and $\vec{S}_k$ may exchange angular momentum. (b) If the distance $|\vec{r}_j - \vec{r}_k|$ between the two spins is within a certain range, $\mathcal{J}(|\vec{r}_j - \vec{r}_k|) > 0$ and the spins are aligned. (c) If $\mathcal{J}(|\vec{r}_j - \vec{r}_k|) < 0$, the spins are anti-aligned.

The $\cos\alpha$ term in equation (2.14) is a maximum when $\alpha = 0°$ and a minimum when $\alpha = 180°$, and thus spins are either aligned or anti-aligned depending on the sign of $\mathcal{J}$, as shown in Figure 2.3b and 2.3c, respectively.

The magnitude of $\mathcal{J}\,(|\vec{r}_j - \vec{r}_k|)$ decays rapidly with increasing $|\vec{r}_j - \vec{r}_k|$, and thus it is only the nearest neighbouring spins that contribute significantly to the orientation of a given spin. In BCC Fe, $\mathcal{J}\,(|\vec{r}_j - \vec{r}_k|) > 0$ along the $\langle 100 \rangle$ crystalline axes, and $\mathcal{E}_{ex}$ is minimized when $\alpha = 0°$ between all moments in the crystal. While the minimization of $\mathcal{E}_{ex}$ requires the alignment of magnetic moments in a ferromagnet, $\mathcal{E}_{ex}$ does not specify an orientation for the moments.

Magnetocrystalline Anisotropy Energy ($\mathcal{E}_{mca}$)

The magnetocrystalline anisotropy energy ($\mathcal{E}_{mca}$) is due to spin-orbit coupling between adjacent atoms, and causes the spins to align along defined crystalline axes. In Fe, $\mathcal{E}_{mca}$ is minimized when domain orientations are parallel to the $\langle 100 \rangle$ axes [30]. A phenomenological approach to the derivation of $\mathcal{E}_{mca}$ is described in [30], while a quantum mechanical derivation can be found in [35].

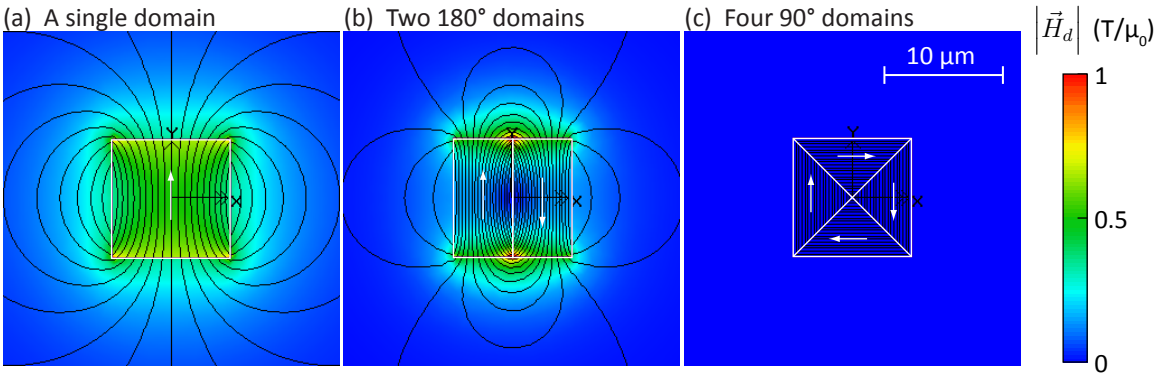

Figure 2.4: 2D static *Infolytica MagNet* models illustrating demagnetising field ($\vec{H}_d$) minimization through domain formation. A 10 µm × 10 µm square of *PM10:Brem 1.0 mur 1.0 MagNet* material is divided into (a) a single domain, (b) two opposing domains, and (c) four domains, with $\mu_0 M_s = 1\,\mathrm{T}$. Domain orientations are indicated by white arrows and flux lines are shown in black. The auxiliary field amplitude ($|\vec{H}|$) is shown in colour, and since $\vec{J}_f = 0$, $\vec{H} = \vec{H}_d$.

Magnetostatic Energy ($\mathcal{E}_{ms}$)

With only the energy contributions from $\mathcal{E}_{ex}$ and $\mathcal{E}_{mca}$, all moments in an Fe crystal would be aligned within a single domain, oriented along one of the $\langle 100 \rangle$ directions. Due to the boundary conditions required by equation (2.3), such a domain structure must produce a demagnetizing field ($\vec{H}_d$). The magnetostatic energy ($\mathcal{E}_{ms}$) is the energy stored in $\vec{H}_d$, which may be written [36, 37]:

$$\mathcal{E}_{ms} = \frac{1}{2}\mu_0 \int_\infty \vec{H}_d^2 \, \mathrm{d}^3 r, \tag{2.15}$$

where the $\int_\infty \mathrm{d}^3 r$ denotes the volume integral over all space.

Figure 2.4 shows how $\vec{H}_d$, and hence $\mathcal{E}_{ms}$, is minimized through domain formation. In Figure 2.4a, $\mathcal{E}_{ex}$ and $\mathcal{E}_{mca}$ are minimized within a single domain crystal, which results in a large $\vec{H}_d$. Figure 2.4b shows that $\vec{H}_d$ can be reduced within the domain structure by the creation of opposing domains, such that for every moment in the

structure there is a moment with the opposite orientation. Figure 2.4c shows $\vec{H}_d$ can be further reduced by ensuring the orientation of all domains is tangential to the surface.

Domain Wall Energy ($\mathcal{E}_{wall}$)

Opposing domains bounded by domain walls are required in order to minimize $\mathcal{E}_{ms}$, as illustrated in Figure 2.4. Within domain walls the exchange interaction acts to minimize α between successive moments which forces moments off the favoured crystalline axes and increases $\mathcal{E}_{mca}$, as illustrated in Figures 2.2b and 2.2c. Minimizing the combination $\mathcal{E}_{ex}$ and $\mathcal{E}_{mca}$ requires domain walls have a finite thickness. The increase in $\mathcal{E}_{ex}$ and $\mathcal{E}_{mca}$ due to domain walls is the total domain wall energy $\mathcal{E}_{wall}$.

In Fe, the energy density required to form a domain wall is on the order of $0.1\,\mathrm{J}\cdot\mathrm{cm}^{-3}$[30]. $\mathcal{E}_{ms}$ is minimized by the formation of opposing domains until it cannot be reduced by more than the energy required to create another wall. Single domain crystals arise when $\mathcal{E}_{wall}$ for one domain wall is larger than $\mathcal{E}_{ms}$.

Zeeman Energy ($\mathcal{E}_p$)

The Zeeman energy ($\mathcal{E}_p$) is due to the interaction between $\vec{H}$ and $\vec{M}$ [30]:

$$\mathcal{E}_p = -\mu_0 \int_{\infty} \vec{M} \cdot \vec{H}\, \mathrm{d}^3 r. \tag{2.16}$$

$\mathcal{E}_p$ is minimized when $\vec{H}$ and $\vec{M}$ are aligned. $\vec{H}$ is usually generated with free currents or permanent magnets, the variation of which changes $\mathcal{E}_p$ and thus the total magnetic energy potential. In these circumstances the domain structure reconfigures until a new minimum system energy is achieved.

2.3.2 Magnetoelasticity

Due to the dependence of the various magnetic energies on the relative configuration of interacting moments, the domain structure interacts with the stress and strain fields within a material. This phenomenon is known as magnetoelasticity. There are two forms of magnetoelasticity: the strain-derivative of $\mathcal{E}_{ms}$, referred to as the form effect, and the strain-derivative of $\mathcal{E}_{ex}$ and $\mathcal{E}_{mca}$, referred to as magnetostriction[†] [31].

The strain tensor field introduced by magnetostriction is $\boldsymbol{\lambda}$. The component of $\boldsymbol{\lambda}$ parallel to $\vec{M}$ is the longitudinal magnetostriction, and at magnetic saturation ($|\vec{M}| = M_s$) is the saturation magnetostriction (λ_s). Magnetostriction is independent of the sign of the magnetisation:

$$\boldsymbol{\lambda}(\vec{M}) = \boldsymbol{\lambda}(-\vec{M}). \tag{2.17}$$

Volume is approximately conserved in magnetostrictive phenomena [30], thus there is also a transverse magnetostriction with sign opposing λ_s.

Magnetostrictive behaviour is anisotropic in crystalline materials. In Fe, the magnetoelastic energy ($\mathcal{E}_\lambda$) is written in terms of the saturation magnetostriction along the $\langle 100 \rangle$ axes (λ_{100}, which is > 0) as:

$$\mathcal{E}_\lambda = -\tfrac{3}{2}\lambda_{100}\sigma_0 \int \left(\cos^2\vartheta - \nu \sin^2\vartheta\right) \mathrm{d}^3 r, \tag{2.18}$$

where σ_0 is a uniaxial stress, ϑ is the angle between domain orientation and the applied stress in the volume $\mathrm{d}^3 r$, and ν is Poisson's ratio [38]. While $\mathcal{E}_\lambda$ is insufficient to rotate domain orientations off the $\langle 100 \rangle$ axes in Fe [30], $\boldsymbol{\sigma}$ may specify which of

[†] $\mathcal{E}_{mca}$ is considered the dominant contributor to magnetostrictive phenomena [30, 31].

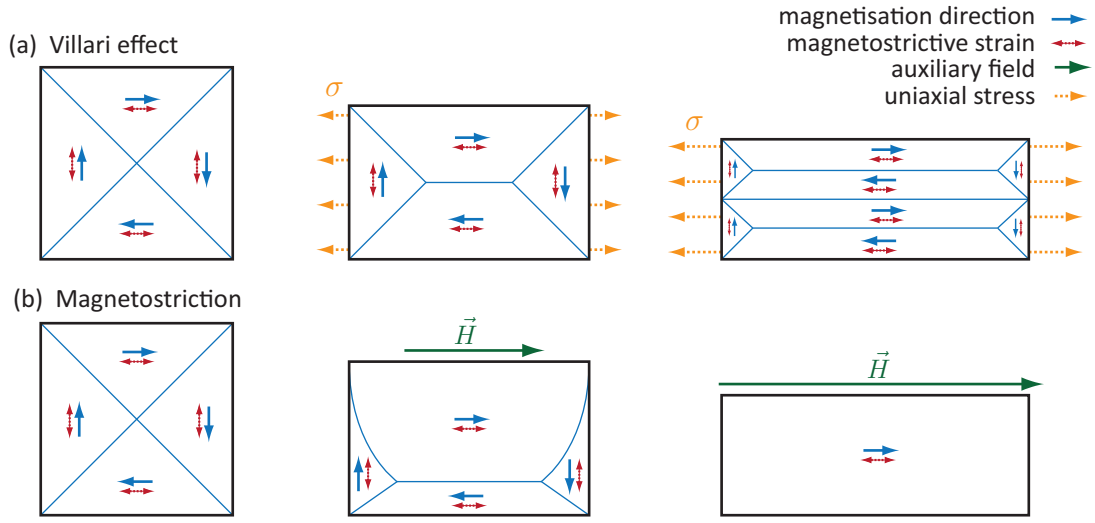

Figure 2.5: Illustration of domain structure anisotropy due to magnetoelasticity. An unstressed material with positive saturation magnetostriction (λ_s) is subjected to: (a) an increasing uniaxial tensile stress (σ), causing elongation and increased population of 180° domains. (b) an increasing auxiliary field ($\vec{H}$), causing an increase in the volume of domains with magnetostrictive strains parallel to $\vec{H}$ and elongation.

the $\langle 100 \rangle$ axes are preferred in an Fe crystal.

Magnetoelasticity implies that each domain has a magnetostrictive strain described by λ_s. The specification of preferred crystal axes due to internal stresses is known as the Villari effect [4], and is illustrated in Figure 2.5a for a material with positive λ_s. Under an applied uniaxial stress there is an increase in 180° domains with magnetostriction parallel to the internal stress field. Magnetostriction [3] is the opposite effect, and is illustrated in Figure 2.5b. As the magnetisation is increased due to an auxiliary field, domains parallel to the field increase in volume and the sample elongates. Magnetostrictive strains are exaggerated in Figure 2.5 for the purpose of illustration.

Magnetoelasticity also has an effect on the domain wall energy. The magnetostrictive strains in the domains on either side of a 90° wall are orthogonal, producing a

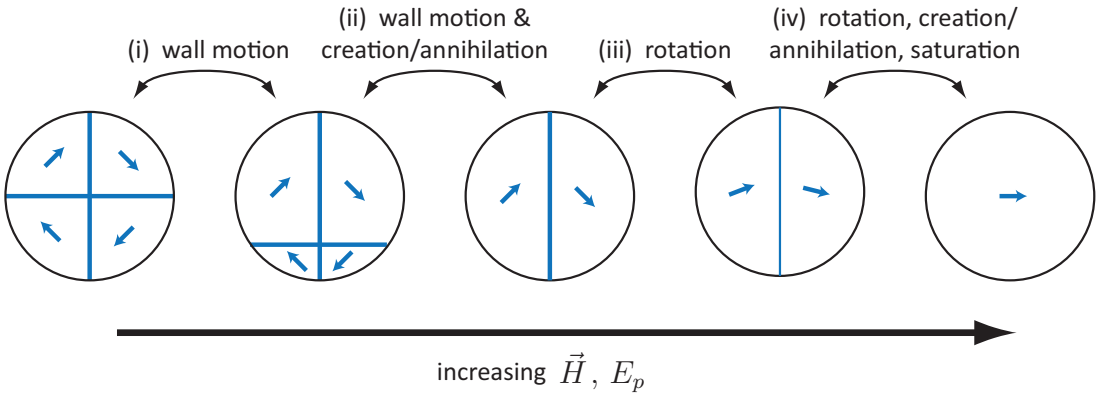

Figure 2.6: Illustration of magnetisation processes in a crystal with orthogonal preferred crystalline axes. As the Zeeman energy ($\mathcal{E}_p$) increases due to an increasing auxiliary field ($\vec{H}$): (i) Domain walls move to increase the volume of domains parallel with $\vec{H}$. (ii) Wall motion continues until the anti-aligned domains are annihilated. (iii) The remaining domains rotate off the preferred crystalline axes. (iv) Rotation continues until the final domain wall is annihilated.

shear stress along the wall and contributing to $\mathcal{E}_\lambda$. Conversely, the magnetostrictions on either side of a 180° wall are equal. Magnetoelastic effects discourage the splitting of 180° walls into two 90° walls, owing to the increased $\mathcal{E}_\lambda$ such a configuration would produce [30].

2.3.3 Magnetisation Processes

Most ferromagnetic NDE applications are based on measuring domain structure response to a changing Zeeman energy ($\mathcal{E}_p$), produced by varying $\vec{H}$. As $\mathcal{E}_p$ increases, the domain structure reconfigures to minimize the total magnetic energy of the system by increasing the average alignment between $\vec{M}$ and $\vec{H}$. This is achieved in three ways, illustrated in Figure 2.6: domain wall movement (i and ii), domain creation and annihilation (ii and iv), and domain orientation rotation (iii and iv).

Domain wall motion occurs when one domain orientation on either side of a domain

wall is more aligned with $\vec{H}$ than its neighbours, and thus may reduce $\mathcal{E}_p$ by increasing in volume. When domain wall motion produces sufficiently small domains that $\mathcal{E}_{wall} > \mathcal{E}_{ms}$, a domain wall is annihilated, decreasing the total number of domains. If $\vec{H}$ is parallel to one of the favoured crystallographic axes, domain wall motion combined with domain annihilation will eventually decrease the total number of domains in a single crystal to one, and the material is saturated. When $\vec{H}$ is not parallel to a favoured crystalline axis, as in Figure 2.6, competition between $\mathcal{E}_p$ and $\mathcal{E}_{mca}$ will result in the domain orientations rotating toward the orientation of $\vec{H}$ until the domain wall disappears, again leaving a single domain.

Since each domain has an associated magnetostrictive strain, as illustrated in Figure 2.5, magnetisation processes have an effect on $\boldsymbol{\lambda}$ (the magnostrictive strain field). For example, $\boldsymbol{\lambda}$ changes orientation across a 90° domain wall, so when a 90° wall moves, the strain associated with the growing domain is increased. If the domain structure was in a potential minimum before the increase in $\mathcal{E}_p$, then it is likely that 90° wall motion also increases $\mathcal{E}_\lambda$. When a 180° wall moves, $\boldsymbol{\lambda}$ only changes within the wall, and there is no net change in $\mathcal{E}_\lambda$ unless the area of the domain wall is significantly increased or decreased. Due to the associated increase in $\mathcal{E}_\lambda$ with 90° motion, 180° walls are theorized to be the first to move, followed by 90° walls at higher magnetisations. As is shown in Figure 2.5b, 180° and 90° wall motion may be correlated.

With the exception of elastic domain wall motion, magnetisation processes are lossy, irreversible and nondeterministic. Due to thermal, radiative, and magnetoelastic effects, magnetisation processes produce electromagnetic and acoustic waves within a material, both of which may be absorbed or scattered such that the energy

cannot be recovered. Thermal excitations produce some randomness to the moment distribution, which makes the reproduction of an exact domain structure following irreversible magnetisation processes unlikely.

2.3.4 Bulk Magnetic Anisotropy

Domain wall motion, creation/annihilation, and orientation rotation are listed in order of the energy required to produce them. Which magnetisation processes occur depends primarily on the relative orientation between $\vec{H}$ and the favoured crystalline directions. When $\vec{H}$ is aligned with the favoured directions, wall motion and creation/annihilation processes are capable of fully magnetising the crystal, hence the single domain state can be reached with the least $\mathcal{E}_p$. The favoured crystalline directions are therefore referred to as the magnetic 'easy' directions. Bulk magnetic anisotropy is associated with materials having easy magnetisation directions, and results from crystallographic texture and/or strain.

Crystallographic texture is defined as the relative orientation of crystalline grains in a polycrystalline material. If the distribution of grain orientations is uniform and random, then the material is said to have no texture. In a non-textured material the average magnetic properties over a sufficient number of grains are isotropic, being the mean magnetic properties over all crystallographic directions. However, if multiple grains are non-randomly aligned with respect to a given crystallographic $\langle hkl \rangle$ set, the material is said to have an $\langle hkl \rangle$ texture. In this case, bulk magnetic properties tend to be anisotropic with respect to the orientation of $\vec{H}$. Multiple $\langle hkl \rangle$ textures are possible simultaneously in a polycrystalline material.

In Fe, the preferred magnetic easy directions are the $\langle 100 \rangle$ set. If a significant

$\langle 100 \rangle$ crystallographic texture is present, then the material tends to have a bulk magnetic easy axis in the direction of this $\langle 100 \rangle$ texture, since a greater proportion of the magnetisation process is domain wall motion. Conversely, in order to saturate Fe along the $\langle 111 \rangle$ direction, a maximum amount of domain rotation must occur. The $\langle 111 \rangle$ directions are therefore referred to as the magnetic 'hard axis.'

Stress may also contribute to the bulk magnetic anisotropy. Consider a stress producing a tensile [100] strain in a single Fe crystal. In this case $\mathcal{E}_\lambda$ is minimized if the domain axes are preferentially aligned to the [100] and $[\bar{1}00]$ directions. This can be achieved by producing a large volume of 180° domains parallel to [100] and $[\bar{1}00]$, such as in Figure 2.5a. It follows that in order to account for a tensile strain in any $[hkl]$ direction, a magnetic easy axis forms along the $\langle 100 \rangle$ axes most closely parallel to the strain. Conversely, when a compressive [100] strain is introduced to the material, Poisson's effect produces tension in the [010] and [001] axes, and domains aligned to the [010], $[0\bar{1}0]$, [001], and $[00\bar{1}]$ are favoured.

When mechanical stresses occur in polycrystalline materials misfitting grains transfer stresses across grain boundaries and stresses accumulate around crystalline defects. Each grain then has magnetic anisotropy governed by its stress state, which sum to give the bulk magnetic properties. When large numbers of grains share a similar stress state, then bulk magnetic anisotropy tends to occur, forming magnetic easy axes along directions of tension in materials with positive λ_s.

2.3.5 Pinning Sites and Barkhausen Events

All the domain theory thus presented has been described in terms of domains in perfect single crystals or highly textured homogeneous materials. In polycrystalline

materials there are a variety of crystalline defects that interrupt ferromagnetic order, including different alloy phases, impurities, dislocations, holes, cracks, and grain boundaries. Strong magnetic energy potential wells and stress potential wells appear around these defects, causing the domain structure to stay invariant around them. Such ferromagnetic interruptions are therefore referred to as pinning sites.

The presence of pinning sites changes the picture of magnetisation processes from the continuous process (excluding domain creation/annihilation) described in Section 2.3.3, to one where the domain structure navigates a spatial distribution of potential wells. In Figure 2.7a the total internal magnetic energy[‡] $\mathcal{E}_t = \mathcal{E}_{ex} + \mathcal{E}_{mca} + \mathcal{E}_{ms}$ is illustrated as having two potential wells as a function of the average magnetisation level ($\bar{M}$). In Figures 2.7b and 2.7c, $\vec{M}$ increases in response to an increasing $\vec{H}$. As $\bar{M}$ and $\bar{H}$ align, $\mathcal{E}_p$ decreases and balances $\mathcal{E}_t$ such that $\mathcal{E}_t = -\mathcal{E}_p$. When $-\mathcal{E}_p$ exceeds the forward edge of the pinning barriers ($\mathcal{E}_{t1}$ and $\mathcal{E}_{t2}$), the magnetisation abruptly crosses the potential well. This abrupt magnetisation change is a Barkhausen event.

2.3.6 Barkhausen Noise

Barkhausen events are abrupt changes in $\vec{M}$ when the domain structure overcomes pinning barriers. Barkhausen events are detectable as abrupt changes in $\vec{B}$, and as pressure waves due to the associated abrupt change in the stress field via magnetostriction [39]. Likewise, Barkhausen events can be produced by either changing $\vec{H}$ or the strain state, $\boldsymbol{\varepsilon}$. Most NDE applications of the Barkhausen effect involve the former.

Pinning site locations in the material are not expected to change due to the AC

[‡]It is assumed that $\mathcal{E}_\lambda$ is included in the $\mathcal{E}_{ex}$, $\mathcal{E}_{mca}$ and $\mathcal{E}_{ms}$ terms.

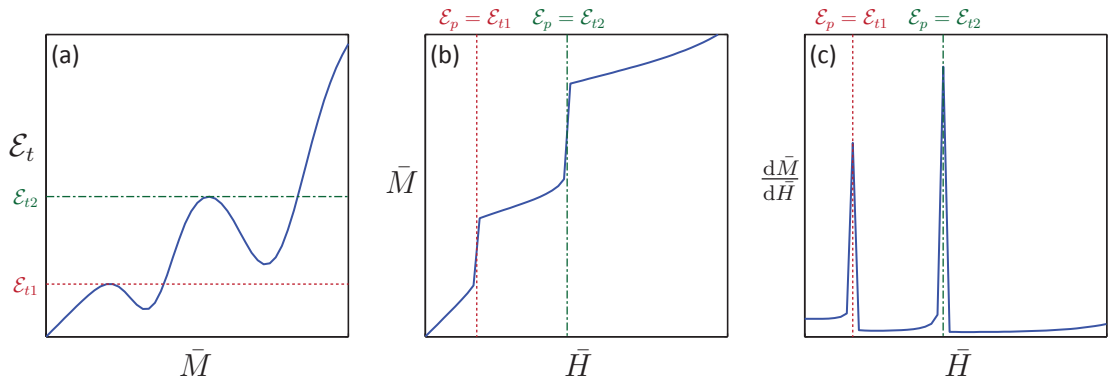

Figure 2.7: Illustration of Barkhausen events. (a) The total internal magnetic energy ($\mathcal{E}_t$) forms a series of potential wells that are a function of the average magnetisation ($\bar{M}$). (b) $\bar{M}$ increases in response to an increasing auxiliary field ($\bar{H}$), which decreases the Zeeman energy ($\mathcal{E}_p$). (c) The derivative of $\bar{M}$ with respect to $\bar{H}$ is shown to increase abruptly when $\mathcal{E}_p$ is equal to the forward edge of the potential wells ($\mathcal{E}_{t1}$ and $\mathcal{E}_{t2}$). Due to the lossy nature of magnetisation processes there is a finite maximum rate at which the domain structure responds.

magnetic excitation. However, due to thermal effects and other sources of noise, domain structures are unlikely form identically each excitation cycle. With sufficiently slow magnetisation conditions, individual Barkhausen events may be detected from thin films and single crystals [6]. The statistical analysis of these pulse distributions can yield fundamental information about the pinning potentials and the domain structure.

When considered for NDE, bulk polycrystalline materials such as steel have sufficiently high pinning site densities that individual Barkhausen events are often not resolved at the excitation frequencies of interest. As a result, Barkhausen events couple to produce broad-band Barkhausen noise (BN) in otherwise low frequency magnetisation waveforms during irreversible magnetisation processes.

BN detected via magnetic means is often called magnetic Barkhausen noise. Any device sensitive to $\vec{B}$ with a suitably wide frequency response, such as pickup coils,

Hall sensors, and giant magnetoresistance (GMR) sensors, can detect BN emissions. Since BN events due to 180° wall motion produce a complete reversal of the magnetisation around a pinning site, they produce larger amplitude electromagnetic waves than 90° events [39]. Thus magnetic sensors are more sensitive to BN emissions due to 180° wall motion than 90° wall motion.

BN is sensitive to strain due to the effects of E_λ on the domain structure. With positive λ_s, tensile uniaxial stresses produce an increased population of 180° domain walls parallel to the tensile axis, as illustrated in Figure 2.5a. When $\vec{H}$ is increased parallel to the tensile axis, the increased domain population moves across the pinning barriers, and since each wall produces a BN event, the net BN emissions increase.

BN detected via acoustic means is referred to as magnetoacoustic emission (MAE). MAE is usually detected by transducers using ultrasonic testing apparatus. The source of MAE is abrupt changes in $\mathcal{E}_\lambda$, which occurs primarily with 90° wall motion and creation/annihilation processes [39, 40]. Domain orientation rotation does produce a change in the stress field, but results in the gradual disappearance of 90° walls, and is not expected to produce significant MAE.

2.4 Coils and Inductors

One of the most common devices used to produce and measure $\vec{B}$ is a coil of conductive wire. The magnetic circuits in this thesis contain as many as nine coupled coils operating under both high and low current conditions over a broad frequency band. This section contains a theoretical description of coils and inductors derived from Maxwell's equations and the Lorentz force law.

2.4.1 Conductors

In conductive materials electromagnetic forces accelerate charged particles to a drift velocity ($\vec{v}_d$), thereby producing a free current density, $\vec{J}_f$, according to Ohm's law [27]:

$$\vec{J}_f = \boldsymbol{\sigma_e}\left(\vec{E} + \vec{v}_d \times \vec{B}\right), \tag{2.19}$$

where $\boldsymbol{\sigma_e}$ is the conductivity tensor with units of $(\Omega \cdot \mathrm{m})^{-1}$. In many cases $\vec{E} \gg \vec{v}_d \times \vec{B}$, and $\boldsymbol{\sigma_e}$ may be treated as isotropic and linear. As such, Ohm's law is often approximated as:

$$\vec{J}_f = \sigma_e \vec{E}. \tag{2.20}$$

where σ_e is the scalar linear isotropic electrical conductivity.

$\vec{J}_f$ describes the flow of charge per unit area through space. Taking the divergence of Ampère's law (2.4) and substituting equation (2.7) produces a continuity equation for $\vec{J}_f$:

$$\nabla \cdot \vec{J}_f = -\frac{\partial \rho}{\partial t}. \tag{2.21}$$

The above is known as Kirchoff's current law, which states that for a given volume, the total current entering the volume is equal to the total current leaving it, provided there is no accumulation of charge within the volume. The electric current through a surface S (I_S) is defined as:

$$I_S = \int_S \vec{J}_f \cdot \mathrm{d}\vec{A}. \tag{2.22}$$

The value of σ_e varies over an extremely large range between materials. For example, at 20 °C in copper $\sigma_e = 5.81 \times 10^7\ (\Omega \cdot \mathrm{m})^{-1}$ [41], while in insulating materials such

as polyvinyl chloride have σ_e values in the range[§] of $10^{-12}\,(\Omega \cdot \mathrm{m})^{-1}$ to $10^{-6}\,(\Omega \cdot \mathrm{m})^{-1}$. Using Ohm's law (2.20) and the above conductivity values, $\vec{J}_f$ inside a conductor may be on the order of 10^{13} to 10^{19} times larger than in a bounding insulator. Therefore, to a good approximation $\vec{J}_f$ is confined to conductors and negligible in insulators.

If the translation of charge is restricted, charge accumulates on boundaries of the conductive device, until $\vec{E} = 0$ inside the conductor. The electric potential difference or voltage (V) between points a and b is:

$$V(a) - V(b) = \int_a^b \vec{E} \cdot \mathrm{d}\vec{\ell}, \tag{2.23}$$

where $\mathrm{d}\vec{\ell}$ is a vector along an arbitrary path between a and b. In linear conductors the voltage across a conductive element is proportional to the current through it. For direct currents (DC), the ratio of the voltage across the device (V) to the current through the device (I) is given by the electrical resistance (R):

$$R = \left| \frac{V}{I} \right|. \tag{2.24}$$

In general, R is a function of the conductor geometry and σ_e.

2.4.2 Electromotive Force

Faraday's law (2.2) states that a changing $\vec{B}$ creates a circulating $\vec{E}$, and can be converted to its integral form using Stokes' theorem:

$$\oint_{\partial S} \vec{E} \cdot \mathrm{d}\vec{\ell} = -\int_S \frac{\partial \vec{B}}{\partial t} \cdot \mathrm{d}\vec{A}, \tag{2.25}$$

[§]From PVC specification sheets, measured by ASTM test D257 [42].

where ∂S is a stationary closed path that bounds the surface S. The electromotive force (EMF) around the closed path ∂S ($\mathscr{E}_{\partial S}$) is defined as:

$$\mathscr{E}_{\partial S} = \oint_{\partial S} \vec{E} \cdot \mathrm{d}\vec{\ell}, \tag{2.26}$$

and the magnetic flux (Φ) through a surface S is defined as:

$$\Phi_S = \int_S \vec{B} \cdot \mathrm{d}\vec{A}. \tag{2.27}$$

Thus, the changing magnetic flux through a surface (S) induces around the surface boundary (∂S) an EMF that opposes the flux change:

$$\mathscr{E}_{\partial S} = -\frac{\mathrm{d}\Phi_S}{\mathrm{d}t}. \tag{2.28}$$

$\mathscr{E}_{\partial S}$ is called the 'back EMF.' In the presence of a conductive material, $\mathscr{E}_{\partial S}$ acts on electrons in the conduction band according to Ohm's law (2.19), and a free current is generated in the conductor that opposes $\mathrm{d}\vec{B}/\mathrm{d}t$. Such opposing currents are called 'eddy currents.'

If a coil of conductive wire with N loops is wound around the path ∂S, through which $\mathrm{d}\Phi_S/\mathrm{d}t \neq 0$, $\mathscr{E}_{\partial S}$ acts along the coil, with each of the N loops contributing to the total electric potential difference across the coil (V). If a current I passes through each turn of the coil, and the coil has a total electrical resistance R, then:

$$V = RI + N\frac{\mathrm{d}\Phi_S}{\mathrm{d}t}, \tag{2.29}$$

assuming negligible build-up of charge between the windings.

The integral form of Faraday's law (2.25) is also known as Kirchoff's voltage law, which states that the sum of the voltage drops around a closed path ∂S is equal to $\mathrm{d}\Phi_S/\mathrm{d}t$. If the back EMF is included in the summation as a voltage source, then the sum of all voltage differences around a closed path is zero.

2.4.3 Magnetomotive Force

Ampère's law (2.4) states that $\vec{J}$ is the primary source of $\vec{B}$. Any available wire can therefore be considered a source of magnetic field if an electrical current is passed through it. Since I_S is related only to $\vec{J}_f$, there is a direct relationship between $\vec{H}$ and I_S, which is determined by applying Stokes' theorem to equation (2.8) and substituting equation (2.22):

$$\oint_{\partial S} \vec{H} \cdot \mathrm{d}\vec{\ell} = \int_S \left(\vec{J}_f + \epsilon_0 \frac{\partial \vec{E}}{\partial t} \right) \cdot \mathrm{d}\vec{A}. \tag{2.30}$$

If it is assumed that $J_f \gg \epsilon_0 \cdot \partial\vec{E}/\partial t$ then equation (2.30) simplifies to:

$$\oint_{\partial S} \vec{H} \cdot \mathrm{d}\vec{\ell} = I_S. \tag{2.31}$$

The left hand side of the above equation is also called the magnetomotive force (MMF). I_S is the total current normal to the surface S, so when the path ∂S encloses conductive materials other than a current-driven wire, eddy currents in the conductive material contribute to the MMF. So long as all free currents are included in the integral, equation (2.31) can be used to calculate the total MMF along any closed path.

Suppose that $\bar{H}$ is the average amplitude of $\vec{H} \cdot \mathrm{d}\vec{\ell}$ along the path ∂S, then:

$$\oint_{\partial S} \vec{H} \cdot \mathrm{d}\vec{\ell} = \bar{H}\ell, \tag{2.32}$$

where ℓ is the total length of path ∂S. Since ∂S bounds the surface S:

$$\bar{H}\ell = I_S. \tag{2.33}$$

Therefore, if the surface S encloses N wires perpendicular to the surface, each with current I, in the absence of any other conducting material, $\bar{H}$ along the path may be calculated as:

$$\bar{H} = \frac{NI}{\ell}. \tag{2.34}$$

There is a mathematical symmetry between equations (2.31) and (2.26), that suggests a magnetic scalar potential difference ($\mathcal{V}$) could be defined similar to V:

$$\mathcal{V}(a) - \mathcal{V}(b) = \int_a^b \vec{H} \cdot \mathrm{d}\vec{\ell}. \tag{2.35}$$

The mathematical symmetry is valid, but while the contribution of the demagnetising field ($\vec{H}_d$) to the MMF around a closed path is zero:

$$\oint_{\partial S} \vec{H}_d \cdot \mathrm{d}\vec{\ell} = 0, \tag{2.36}$$

in general for an open path between a and b:

$$\int_a^b \vec{H}_d \cdot \mathrm{d}\vec{\ell} \neq 0. \tag{2.37}$$

Furthermore, in most situations involving ferromagnetic materials, $\vec{H}_d$ is the dominant contributor to $\vec{H}$.

If there are no bound currents (i.e., $\vec{J}_b = 0$), then $\vec{B} = \mu_0\vec{H}$. If $\vec{J}_b \neq 0$, then $\vec{J}_f$ cannot be assumed to be the dominant contributor to $\vec{H}$, unless geometry is taken into account to ensure $\vec{H}_d = 0$. This is true when $\vec{J}_b \times \vec{J}_f = 0$ at all points along ∂S, which may be achieved by winding a coil around a toroidal or ring core. For this reason, toroidal core geometries and coils are often used to determine fundamental magnetic properties, such as in Appendix B, and in power applications where magnetic field leakage is undesirable. Note however, that eddy currents do contribute to $\vec{H}$ within toroids.

2.4.4 Inductors

It was shown in Section 2.4.3 that I_S can be related to $\vec{H}$. As discussed in Section 2.2, the relationship between $\vec{H}$ and $\vec{B}$ is governed by the coupling of $\vec{H}$ to $\vec{M}$, and may be represented either by the relative permeability ($\boldsymbol{\mu_r} = \mu_0^{-1} \cdot \vec{B}/\vec{H}$) or the differential permeability ($\boldsymbol{\mu_d} = \mu_0^{-1} \cdot \mathrm{d}\vec{B}/\mathrm{d}\vec{H}$). Provided $\boldsymbol{\mu_d} > 0$, then an increase in $\vec{H}$ produces a proportional increase in $\vec{M}$ and $\vec{B}$. The derivative of the flux linkage (Λ) with respect to the current (I) through an inductor is the inductance (L):

$$L = \frac{\mathrm{d}\Lambda}{\mathrm{d}I}, \tag{2.38}$$

where:

$$\Lambda = N\Phi, \tag{2.39}$$

in a coil with N turns. Alternatively, Λ may be considered the total flux through the inductor. Note that L is proportional to $\mathrm{d}\Phi/\mathrm{d}I$ and hence to $\mathrm{d}\vec{B}/\mathrm{d}\vec{H}$ and to $\boldsymbol{\mu_d}$. Thus L varies throughout the hysteresis loop of a non-linear inductor. Combining equations (2.39), (2.38), and (2.28) gives the back EMF across an inductor ($\mathscr{E}_L$) as:

$$-\mathscr{E}_L = L\frac{\mathrm{d}I}{\mathrm{d}t}. \tag{2.40}$$

Most conductors have limited σ_e, and thus inductors are usually modelled as a perfect linear inductor L with a series resistance R. An inductive-resistive (LR) circuit schematic is shown in Figure 2.8a. Adding the voltage across a resistor (2.24) and the inductor (2.40) gives the voltage across the circuit as:

$$V = RI + L\frac{\mathrm{d}I}{\mathrm{d}t}. \tag{2.41}$$

The current in the circuit can be found by solving the above differential equation.

Consider the transient response by a step increase in the voltage from 0 to V at $t = 0$, a situation replicated by closing the switch $s1$ in Figure 2.8a. The solution is:

$$I(t) = \frac{V}{R}\left(1 - e^{-(R/L)t}\right), \tag{2.42}$$

and is pictured in Figure 2.8b, which describes an asymptotic approach to a final DC current V/R with an exponential time constant (L/R). This time constant is an important consideration when driving and measuring inductive circuits.

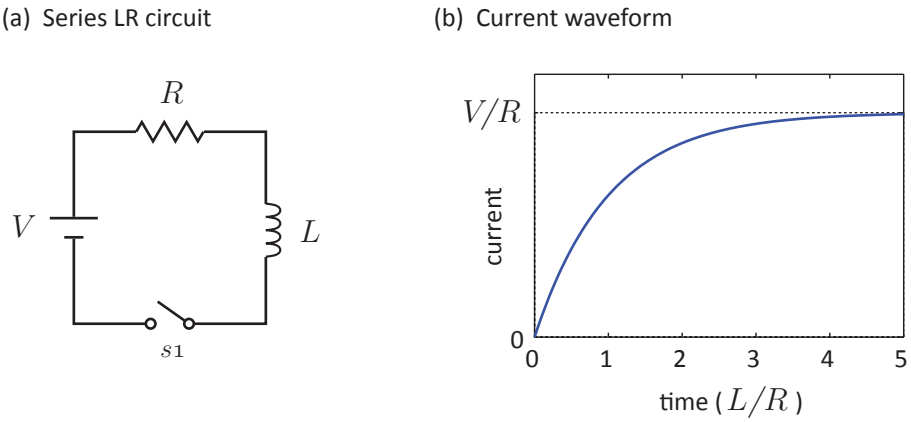

Figure 2.8: LR time constant. (a) A series circuit consisting of resistor R and a perfect linear inductor L, supplied by a DC EMF with voltage V and regulated by switch $s1$. (b) The transient response of the current through the circuit when the $s1$ is closed at time = 0.

2.5 Field Attenuation in Conductive Materials

In addition to being permeable, materials in a magnetic circuit may also be conductive (i.e., $\boldsymbol{\sigma_e} \neq 0$). When $\mathrm{d}\vec{B}/\mathrm{d}t \neq 0$ in a conductive material, eddy currents are produced. In materials with finite conductivity, eddy currents are resistively dissipated, usually producing heat, and are therefore a source of loss in magnetisation processes.

Since eddy current strength is proportional to $-\mathrm{d}\vec{B}/\mathrm{d}t$, conductive materials shield alternating magnetic fields. This attenuation is usually described by considering a plane-wave $\vec{B}$ with normal incidence to the surface of a material with scalar conductivity σ_e. $\vec{B}$ has the solution as a function of depth z into the material [27]:

$$\vec{B}(z,t) = \vec{B}_0 \exp\left(-\Im\{\kappa\}z\right) \cos\left(\Re\{\kappa\}z - \omega t\right), \tag{2.43}$$

where $\vec{B}_0$ is the field at the surface, ω is the angular frequency, and κ is the complex

wave number, with the form:

$$\Re\{\kappa\} = \omega\sqrt{\frac{\epsilon_0\epsilon_r\mu_0\mu_d}{2}}\left[\sqrt{1+\left(\frac{\sigma_e}{\epsilon_0\epsilon_r\omega}\right)^2}+1\right]^{\frac{1}{2}}, \tag{2.44}$$

and:

$$\Im\{\kappa\} = \omega\sqrt{\frac{\epsilon_0\epsilon_r\mu_0\mu_d}{2}}\left[\sqrt{1+\left(\frac{\sigma_e}{\epsilon_0\epsilon_r\omega}\right)^2}-1\right]^{\frac{1}{2}}, \tag{2.45}$$

where ϵ_r is the relative permittivity of the conductive material, and μ_d is the isotropic differential permeability.¶

In the frequency limit that $\sigma_e\left(\epsilon_0\epsilon_r\omega\right)^{-1} \gg 1$ a material is described as a 'good conductor', and (2.44) and (2.45) simplify to:

$$\Re\{\kappa\} \approx \Im\{\kappa\} \approx \sqrt{\frac{\mu_0\mu_d\sigma_e\omega}{2}}. \tag{2.46}$$

In feeder steel, $\sigma_e = 5.15\times10^6\,\mathrm{S/m}$ [43], and $\epsilon_r \approx 1$. Solving $\sigma_e\left(\epsilon_0\epsilon_r\omega\right)^{-1} = 1$ using the preceding values gives $\omega = 5.8\times10^{17}\,{}^{\mathrm{rad}}/_{\mathrm{s}}$ or $93\times10^{15}\,\mathrm{Hz}$. Thus feeder steel (and steels in general) may be characterised as a 'good conductor' below optical frequencies ($\sim 10^{15}\,\mathrm{Hz}$) and for all frequencies considered in this thesis.

When considering time-harmonic magnetic fields in conductive ferromagnetic alloys, the flux density at depth is exponentially attenuated by κ, which has units of m^{-1}. The skin depth (δ) is therefore defined as $\delta \equiv \Im\{\kappa\}^{-1}$. In a good conductor $\Re\{\kappa\}$ is approximately equal to $\Im\{\kappa\}$ and so the magnetic field propagates into the material as a damped oscillation with a wavelength approximately equal to $2\pi\delta$.

¶In Griffiths [27], and most other texts, μ_r is used in place of μ_d here. However, since the fields are changing with time, μ_r is only correct when the magnetic response of the material is linear at all points in its magnetisation cycle.

2.6 Magnetic Circuits

In this section, analogies are drawn between electric and magnetic circuit theory so that electric circuit approximations and schematics can be adapted to the design of magnetic circuits. As part of this thesis work, these analogies were extended beyond those found in standard magnetic text books to illustrate series and parallel aspects of magnetic circuits, and introduce the concept of a magnetic flux source.

2.6.1 Electric-Magnetic Analogs

When designing an instrument to investigate magnetic properties it is useful to consider the analogies between electric and magnetic circuits. Table 2.2 shows some of the mathematical symmetries between electric and magnetic fields.

Passive and Reactive Components

The proportionality constants and tensors that relate electric and magnetic fields have sufficient mathematical symmetry that magnetic equivalents exist for passive resistance, and reactive inductance and capacitance.

The magnetic equivalent to resistance (R) is the magnetic reluctance ($\mathcal{R}$). Consider a linear material magnetised along a path parallel to its length (ℓ), with a scalar permeability μ_r, and a cross Sectional area A. If a uniform $\mathcal{V}_{dc} = H\ell$ is applied along its length, a uniform flux density $B = \Phi_{dc}/A = \mu_0\mu_r H$ is produced. The reluctance may then be calculated as the ratio of $\mathcal{V}_{dc}/\Phi_{dc}$:

$$\mathcal{R} = \frac{\ell}{\mu_0\mu_r A}. \tag{2.47}$$

Table 2.2: Electric-Magnetic Analogs

Electric		**Magnetic**	
Electric Field	$\vec{E}$	Auxiliary Field	$\vec{H}$
Current Density	$\vec{J}_f$	Flux Density	$\vec{B}$
Conductivity	$\boldsymbol{\sigma_e}$	Permeability	$\mu_0\boldsymbol{\mu_r}$
Susceptability	$\boldsymbol{\chi_e}$	Susceptability	$\boldsymbol{\chi_m}$
Polarisation	$\vec{P} = \epsilon_0\boldsymbol{\chi_e}\vec{E}$	Magnetisation	$\vec{M} = \boldsymbol{\chi_m}\vec{H}$
Displacement	$\vec{D} = \epsilon_0\vec{E} + \vec{P}$	Flux Density	$\vec{B} = \mu_0(\vec{H} + \vec{M})$
Current	$I_S = \int_S \vec{J}_f \cdot \mathrm{d}\vec{a}$	Flux	$\Phi_S = \int_S \vec{B} \cdot \mathrm{d}\vec{a}$
EMF	$V(b) = -\int_\infty^b \vec{E} \cdot \mathrm{d}\vec{\ell}$	MMF	$\mathcal{V}(b) = -\int_\infty^b \vec{H} \cdot \mathrm{d}\vec{\ell}$
Ohm's law	$\vec{J}_f = \boldsymbol{\sigma_e}\vec{E}$	Ohm's law	$\vec{B} = \mu_0\boldsymbol{\mu_r}\vec{H}$
Current conservation	$\nabla \cdot \vec{J}_f = 0^*$	Flux conservation	$\nabla \cdot \vec{B} = 0$
Resistance	$R = V_{dc}/I_{dc}$	Reluctance	$\mathcal{R} = \mathcal{V}_{dc}/\Phi_{dc}$
Inductance	$V = L \cdot (\mathrm{d}I/\mathrm{d}t)$	Conductance	$\mathcal{V} = \mathcal{L} \cdot (\mathrm{d}\Phi/\mathrm{d}t)$
Charge Capacitance	$I = C \cdot (\mathrm{d}V/\mathrm{d}t)$	Flux Capacitance	$\Phi = \mathcal{C} \cdot (\mathrm{d}\mathcal{V}/\mathrm{d}t)$
Electrical impedance	$Z = V/I$	Magnetic impedance	$\mathcal{Z} = \mathcal{V}/\Phi$

* For zero charge accumulation within the volume.

If the permeability changes during the magnetisation cycle, then μ_d should replace μ_r in the above equation to calculate the instantaneous reluctance. A similar derivation for the electrical resistance gives:

$$R = \frac{\ell}{\sigma_e A}. \tag{2.48}$$

Just as electric circuit theory requires current to follow the path of least resistance, so too does flux follow the path of least reluctance.

Alternating magnetic fields in good conductors are attenuated according to the equations in Section 2.5. The area of a magnetic material in equation (2.47) is therefore a function of frequency: $A(\omega)$, where ω is the angular frequency of the field. The functional form of $A(\omega)$ depends on the dimensions of the reluctive object orthogonal to the flux path.

Table 2.2 also shows conductance ($\mathcal{L}$) as the magnetic equivalent of inductance (L). Inductors produce a back EMF when subjected to a changing current I. Similarly, conductors produce a back MMF (via eddy currents) when subjected to a changing flux:

$$\mathcal{V} = \mathcal{L}\frac{\mathrm{d}\Phi}{\mathrm{d}t}. \tag{2.49}$$

Calculating $\mathcal{L}$ in a magnetic circuit is analogous to calculating L for an electric circuit. The length and area of a conductor are given by the path length and cross sectional area of an eddy current loop around a line of flux. If a material has a conductivity σ_e, then the total length of the eddy current loop is approximately $\pi\delta$, with a cross sectional area $\ell \cdot \delta/2$, where δ is the skin depth calculated in equation (2.46). The approximate conductance may therefore be calculated as:

$$\mathcal{L} = \frac{\sigma_e \ell}{2\pi\mathcal{N}}, \tag{2.50}$$

where:

$$\mathcal{N} = \begin{cases} 1 & \text{if } \delta > h; \\ h/\delta & \text{if } \delta < h. \end{cases}, \tag{2.51}$$

and h is the minimum dimension of the sample material orthogonal to the flux path (for example, the lamination thickness). Note that ℓ in (2.50) is the length of the

reluctor in (2.47), not the length of the eddy current loop.

The magnetic equivalent to electric charge capacitance is indicated in Table 2.2 to be the flux capacitance. In electric circuits, capacitance represents the storage of energy in the electric field ($\vec{E}$) through the polarization ($\vec{P}$) of a dielectric medium. Similarly, flux capacitance represents the storage of energy in the auxiliary field ($\vec{H}$) through the magnetisation ($\vec{M}$) of a dipolar medium, and has the functional behaviour:

$$\Phi = \mathcal{C}\frac{\mathrm{d}\mathcal{V}}{\mathrm{d}t}. \tag{2.52}$$

The problem with this analogy is that storage of energy in $\vec{H}$ introduces a flux to the circuit, which is already included in the models for $\mathcal{R}$ and $\mathcal{L}$. A flux capacitor must therefore store energy in a closed demagnetising field within the modelled object. Thus, flux capacitance represents the storage of energy in the demagnetising fields around pinning sites in a ferromagnet, and may be useful when attempting to model non-linear effects in the domain structure. No flux capacitors are used in the models in this thesis.

The analysis of electric circuits relies on Kirchoff's current law (2.21) and Kirchoff's voltage law (2.25). These laws facilitate the simplification of linear electric circuits such that any number of discrete resistances (R_j) or inductances between two points add in series ($R_{eq} = \sum_j R_j$) and the reciprocal resistances add in parallel ($1/R_{eq} = \sum_j 1/R_j$). Like resistance, reluctances and conductances add in series ($\mathcal{R}_{eq} = \sum_j \mathcal{R}_j$) and their reciprocals add in parallel ($1/\mathcal{R}_{eq} = \sum_j 1/\mathcal{R}_j$), allowing equivalent magnetic circuits. Charge capacitance and flux capacitance add in parallel and their reciprocals add in series.

Sources

Electrical circuits are usually modelled as being driven by a voltage or current source. Voltage sources are convenient when considering multiple electrical devices in parallel, since the EMF across each device is maintained. Current sources are convenient when considering the behaviour of multiple electrical devices in series, since the same I must pass through each device. Should the electrical properties of any device in a series of components change, the behaviour of the other devices is unaffected when controlled by a current source. It follows from voltage and current sources that magnetic circuits are supplied by MMF and flux sources, with the same parallel and series implications.

These four sources are mathematical constructs, and thus can only be approximated. When required, passive and active sources are designed for the specific loading conditions of the application. Passive sources require the circuit be designed such that maximum variation in the load impedance produces a negligible change in the source characteristics. Active sources use powered circuit elements and some form of feedback to maintain the desired circuit performance.

2.6.2 Circuit Schematics

Using the preceding analogies, magnetic circuits can be drawn with a similar notation to electric circuits, with lines of constant V and $\mathcal{V}$ representing lossless I and Φ paths. Figure 2.9 shows the symbols that are used in this thesis to represent the various circuit components. Symbols for the reactive magnetic circuit components were designed to invoke electric circuit approximations.

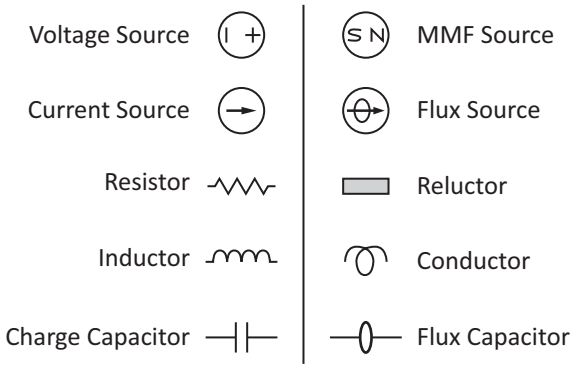

Figure 2.9: Electric (left) and magnetic (right) circuit symbols.

Linear DC Circuits

Figure 2.10 shows analogous DC electric and magnetic circuits. In Figure 2.10a, a battery supplies an EMF V to a load resistor (R_{load}) with a length ℓ and an area A, through which I flows. In Figure 2.10b, a coil with N turns containing a current I supplies a MMF NI to a gapped core and the surrounding air. The accompanying electric circuit schematic to Figure 2.10a is shown in Figure 2.10c. Accompanying magnetic circuit schematics to Figure 2.10b are shown with various approximations and simplifications in Figures 2.10d, 2.10e and 2.10f.

The electric circuit schematic in Figure 2.10c is remarkably simple compared to the magnetic circuit schematic in Figure 2.10d. This is because the ratio of σ_e in the circuit components to σ_e of the surrounding insulator is on the order of 10^{15}. Thus the current in the surrounding insulator is negligible and current paths through the insulator are not included in the schematic. This leaves the current confined to circuit components, and (2.48) can be used to calculate the load and wire resistances R_{load} and R_{wire}, respectively.

In Figure 2.10d, the ratio of the μ_r of the surrounding insulator (usually air, as indicated) and of the core may be as low as 10^2. As such, all paths through the air

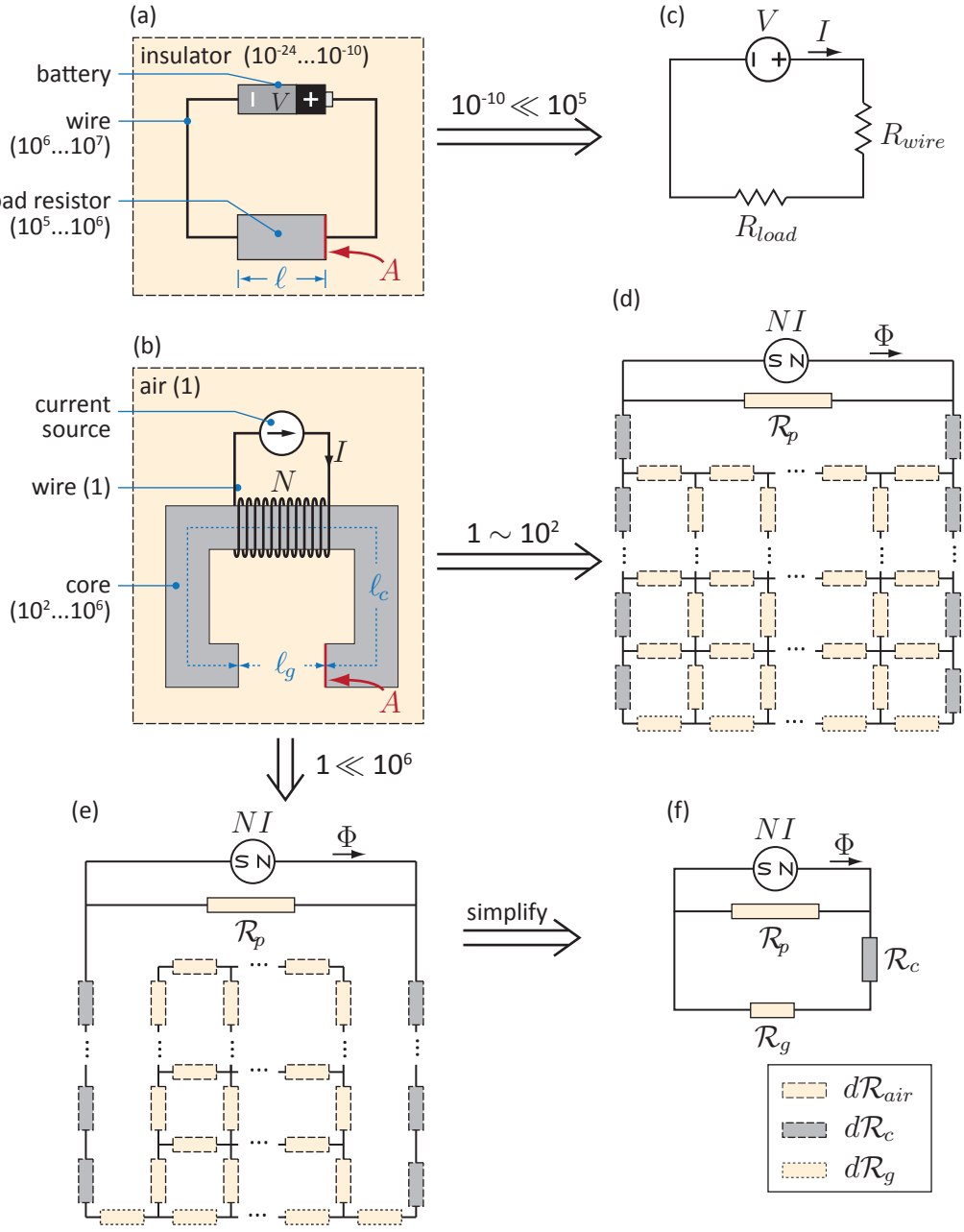

Figure 2.10: Analagous DC (a) electric and (b) magnetic circuits, with associated schematics in (c) and (d, e, f), respectively. Typical ranges of conductivity (σ_e) in (a), and relative permeability (μ_r) in (b), are indicated in brackets for the various materials. Lines in (c) and (d,e,f) represent lossless current (I) and flux (Φ) paths, and regions of constant potential (V or $\mathcal{V}$), respectively. Magnetic schematics (e) and (f) illustrate the simplifications possible when μ_r of the core is much greater than that of the surrounding air.

are considered viable flux paths, and the reluctance of the core and air is modelled as a sum of distributed series and parallel reluctive loads. This is illustrated in Figure 2.10d by dividing the surrounding air, the core, and the air gap into distributed reluctances $d\mathcal{R}_{air}$, $d\mathcal{R}_c$, and $d\mathcal{R}_g$. Since the coil is of finite size, it is also possible for some flux to leak through the windings of the coil and never enter the core. This reluctance is parallel to the whole circuit, and denoted $\mathcal{R}_p$.

Figure 2.10e illustrates the approximation that no flux leaks from the core except at the air gap. This approximation is reasonable when μ_r of the core is much larger than that of the air, and the gap is significantly smaller than the distance between the poles ($d\mathcal{R}_g \ll d\mathcal{R}_{air}$). When the approximation is valid, numerous flux paths into the distributed $d\mathcal{R}_{air}$ are negligible. Figure 2.10f shows further simplification is then possible by lumping the series $d\mathcal{R}_c$ reluctances into $\mathcal{R}_c$ and lumping the remaining $d\mathcal{R}_g$ and $d\mathcal{R}_{air}$ into $\mathcal{R}_g$. In a circuit where $(\mathcal{R}_c+\mathcal{R}_g) \ll \mathcal{R}_p$, $\mathcal{R}_p$ may also be neglected.

Linear AC Circuits

Linear AC magnetic circuits require the addition of conductance to DC magnetic circuits[‖]. The frequency dependence of the conductor MMF necessitates the introduction of the complex magnetic impedance ($\mathcal{Z}$):

$$\mathcal{Z} = \frac{\mathcal{V}}{\Phi} \tag{2.53}$$

where $\mathcal{Z} = \mathcal{R}$ for a reluctor, and $\mathcal{Z} = i\omega\mathcal{L}$ for a conductor, where $i = \sqrt{-1}$ and ω is the angular frequency of the magnetic field. Conductors therefore impede flux at

[‖]While flux capacitance may also be added, with $\mathcal{Z}_\mathcal{C} = (i\omega\mathcal{C})^{-1}$, no models that use it are presented in this thesis.

high frequencies.

Using equations (2.38), (2.39) and (2.53), if a coil with N turns is wound around a magnetic circuit with a total magnetic impedance $\mathcal{Z} = \mathcal{R} + i\omega\mathcal{L}$, then the inductance of the device L is given as:

$$L = \frac{N^2}{\mathcal{Z}} = N^2 \left(\frac{\mathcal{R}}{\mathcal{R}^2 + \omega^2\mathcal{L}^2} - i\frac{\omega\mathcal{L}}{\mathcal{R}^2 + \omega^2\mathcal{L}^2} \right). \tag{2.54}$$

Eddy currents therefore manifest as a negative imaginary component of the inductance ($\Im\{L\}$), which behave as an effective electrical resistance. Due to eddy currents, more current is required to obtain the same Φ with increasing ω in conductive materials. The imaginary component of L may increase significantly when δ is less than the characteristic dimensions of the domain structure. These effects are usually modelled by substituting a complex permeability as a function of ω into equations (2.47) and (2.46).

Non-linear Magnetic Circuits

Linear magnetic circuits can only describe a limited range of magnetic phenomena. Saturation effects require modelling reluctances as a function of the flux through them. Other effects, such as hysteresis and BN require magnetic analogs of amplifiers, transistors and diodes. As such, analysis of non-linear circuits rapidly becomes an exercise in numerical computing, and since linear AC circuits are sufficient to describe the control issues associated with BN circuits, these models are not presented.

Chapter 3

Electromagnet Coupling

In traditional BN instrumentation, the magnetic field is produced via control of the current through or the voltage across an electromagnet excitation coil. These measurements, while demonstrating stress sensitivity, also have strong sensitivity to variations in the magnetic coupling between the electromagnet and sample. As a result, measurements are limited to situations where the electromagnet geometry can be precisely conformed to the sample surface. This electromagnet coupling problem needs to be addressed in order to compensate for the variable geometry of feeder pipe surfaces.

In this chapter magnetic circuit theory is used to describe and propose a solution for the BN NDE electromagnet coupling problem.

- In Section 3.1, the typical magnetic circuit for BN NDE is presented along with its schematic. Approximations are made in order to simplify the schematic, revealing the BN NDE coupling problem to be one of serial reluctive and conductive loads. The theoretical construct of a flux source is shown to solve this problem.

- In Section 3.2 it is shown that a passive flux source cannot meet the design criteria for BN NDE on feeders, and that an active flux source design is required.
- Section 3.3 presents design considerations for an active flux source.
- In Section 3.4 the superposition of the fields from four independent flux sources is proposed as an alternative to mechanical rotation of a U-core electromagnet probe.

3.1 The BN NDE Circuit

The purpose of the electromagnet in BN instruments is to produce a repeatable, time-varying MMF ($\mathcal{V}_{roi}$) across, or flux (Φ_{roi}) through, the region of interest in the sample where the BN measurement is to be performed. In order to estimate magnetic anisotropy in the sample material, the average orientation of $\vec{B}$ in the sensed region must be variable through 180°. The typical solution for BN NDE has been to use a U-core electromagnet and mechanically rotate its orientation with respect to the sample surface normal.

The geometry of a typical BN NDE testing magnet is shown in Figure 3.1a, where the magnetic flux in a U-core and a bulk steel sample is driven by an excitation coil with N_{ex} turns and an alternating current I_{ex} with frequency f_{ex}. In order to magnetise the sample, flux must pass through the series air gaps $g1$ and $g2$. Eddy currents are induced in the sample by the changing magnetic field.

Figure 3.1b shows the accompanying magnetic circuit schematic. In order to simplify the schematic, horizontal flux paths are represented by the sum of three

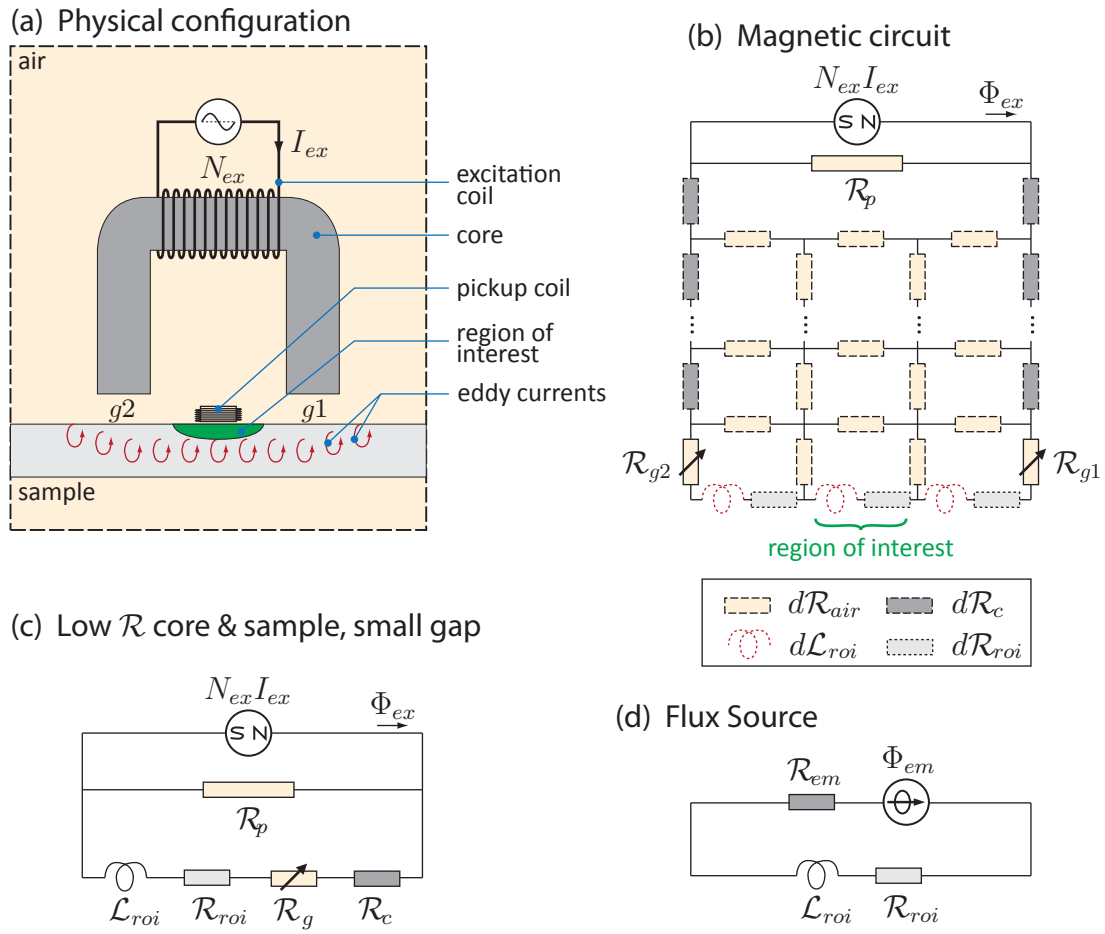

Figure 3.1: A typical BN NDE (a) magnetic circuit and (b) its accompanying schematic, showing the most relevant flux paths, reluctances ($\mathcal{R}$) and conductances ($\mathcal{L}$). The circuit is supplied by an alternating current source with frequency f_{ex}, which produces a MMF $N_{ex}I_{ex}$. (c) The circuit is simplified assuming $d\mathcal{R}_c$, $\mathcal{R}_{g1}$, $\mathcal{R}_{g2}$, $d\mathcal{R}_{roi}$, and $2\pi f_{ex} d\mathcal{L}_{roi}$ are much less than $d\mathcal{R}_{air}$. (d) The excitation coil, $\mathcal{R}_{c1}$, $\mathcal{R}_{c2}$ and $\mathcal{R}_p$ are replaced by a flux source Φ_{em} and its associated impedance $\mathcal{R}_{em}$.

distributed components across Figure 3.1b, with the middle sample component specified as the region of interest for BN measurement. The gaps $g1$ and $g2$ are drawn as unknown variable reluctors $\mathcal{R}_{g1}$ and $\mathcal{R}_{g2}$. It is assumed that the core is non-conductive, while series distributed conductivity ($d\mathcal{L}_{roi}$) is modelled for the sample material. The parallel reluctance $\mathcal{R}_p$ is included, since flux through the excitation coil (Φ_{ex}) is divided into $\mathcal{R}_p$ and the rest of the circuit.

In the context of Figure 3.1b, reproducing a BN measurement requires that either the MMF across or the flux through the center $d\mathcal{R}_{roi}$ is controlled. In order to simplify the circuit, the complications posed by the distributed air gap are removed by approximating that $d\mathcal{R}_c$, $d\mathcal{R}_{roi}$, $2\pi f_{ex} d\mathcal{L}_{roi}$, $\mathcal{R}_{g1}$ and $\mathcal{R}_{g2}$ are small compared to $d\mathcal{R}_{air}$. This removes the distributed air gap, and allows lumping of the core, gap and sample reluctances and conductances into $\mathcal{R}_c$, $\mathcal{R}_g$, $\mathcal{R}_{roi}$ and $\mathcal{L}_{roi}$, as shown in Figure 3.1c.

Figure 3.1c illustrates a fundamental problem with the typical BN NDE circuit. Using a current source, the MMF $N_{ex}I_{ex}$ is applied across the series of reluctances and conductances, giving $\mathcal{V}_{roi}$ as:

$$\mathcal{V}_{roi} = \frac{\mathcal{R}_{roi} + i2\pi f_{ex}\mathcal{L}_{roi}}{\mathcal{R}_c + \mathcal{R}_g + \mathcal{R}_{roi} + i2\pi f_{ex}\mathcal{L}_{roi}} \cdot N_{ex}I_{ex}. \tag{3.1}$$

Since $\mathcal{V}_{roi}$ is a function of $\mathcal{R}_g$, and $\mathcal{R}_g$ is often greater than $\mathcal{R}_c + \mathcal{R}_{roi}$, any change in the gap dimensions between measurements results in a significant change in $\mathcal{V}_{roi}$, and thus reduces the repeatability of the experiment.

As can be seen in Figure 3.1c, the BN NDE excitation magnet control problem is primarily one of series loads. If I_{ex}, the excitation voltage (V_{ex}), and the DC resistance

of the excitation coil (R_{ex}) were used to calculate Φ_{ex} as:

$$\Phi_{ex}(t) = \Phi_{ex}(0) + \frac{1}{N_{ex}} \int_0^t [V_{ex}(t') - R_{ex} I_{ex}(t')] \cdot dt', \tag{3.2}$$

then Φ_{roi} can be calculated as:

$$\Phi_{roi} = \Phi_{ex} \left(1 + \frac{\mathcal{R}_c + \mathcal{R}_g + \mathcal{R}_{roi} + i2\pi f_{ex} \mathcal{L}_{roi}}{\mathcal{R}_p} \right)^{-1}. \tag{3.3}$$

Using the simplified circuit in Figure 3.1c, in the limit that $\mathcal{R}_p \to \infty$ $\Phi_{ex} = \Phi_{roi}$ and the measurement is repeatable.

If the flux in the core closer to the sample (Φ_{em}) is controlled, rather than Φ_{ex}, then $\mathcal{R}_c$ and $\mathcal{R}_p$ can be lumped into $\mathcal{R}_{em}$, and the electromagnet can be replaced by a theoretical flux source, as shown in Figure 3.1d. In such a circuit the flux through $\mathcal{R}_{roi}$ is exactly known and the measurement is repeatable. In the subsequent sections, passive and active flux source designs are presented in the context of feeder pipe BN NDE.

3.2 Passive Flux Source Design

When applied to the BN NDE circuit, the passive flux source design criteria is that any change in the reluctance of a variable air gap ($d\mathcal{R}_g$) is negligible compared to the total impedance of the circuit ($\mathcal{Z}_{eq}$). This is expressed mathematically using the

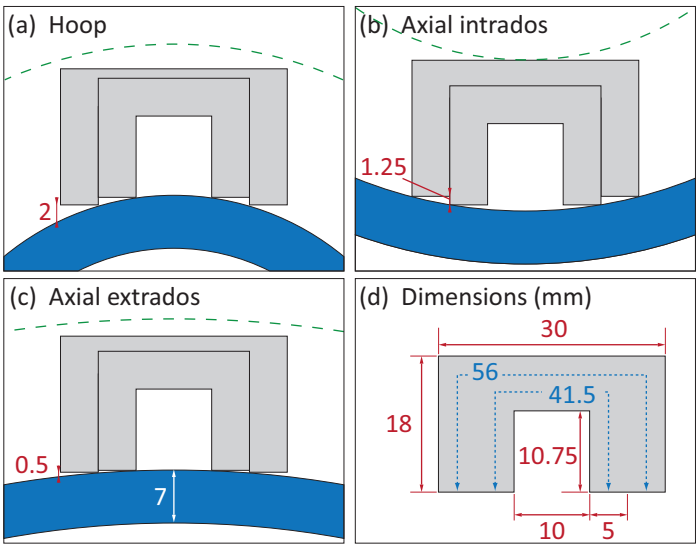

Figure 3.2: A range of fixed U-core excitation circuit dimensions (grey) that fit within the 20 mm clearance (green dashed lines) of the feeder pipe bends (blue), shown along the (a) hoop, (b) axial intrados, and (c) axial extrados of a type 6 feeder bend. (d) The outer dimensions of the potential cores. In (a), (b) and (c), maximum air gaps are indicated in red. Diagrams are to scale.

components labeled in Figure 3.1c:

$$\frac{d\mathcal{R}_g}{|\mathcal{Z}_{eq}|} = \frac{d\mathcal{R}_g}{\left[\left(\mathcal{R}_c + \mathcal{R}_{g0} + d\mathcal{R}_g + \mathcal{R}_{roi}\right)^2 + \left(2\pi f_{ex}\mathcal{L}_{roi}\right)^2\right]^{\frac{1}{2}}} \ll 1, \tag{3.4}$$

where $\mathcal{R}_g = \mathcal{R}_{g0} + d\mathcal{R}_g$, and $\mathcal{R}_{g0}$ is any fixed air gap within the circuit. For the above equation to be valid, it must also be true that the total equivalent permeability of the circuit (μ_{eq}) is much greater than one:

$$\mu_{eq} = \frac{\ell_{eq}}{\mu_0 A_{eq} |\mathcal{Z}_{eq}|} \gg 1, \tag{3.5}$$

where ℓ_{eq} and A_{eq} are equivalent circuit length and area, respectively.

In Figure 3.2 a range of cores $h_c = 5$ mm thick are shown that fit within the 20 mm

clearance at the extremes of feeder pipe curvature. A minimum inner dimension of 10 mm × 10 mm is chosen to accommodate the pickup coil and excitation windings, which results in an inner vertical limit of 10.75 mm to accommodate the hoop curvature. The dimensions in Figure 3.2 indicate that the average air gap in the circuit may range from 0.5 mm to 2 mm between the hoop and axial extrados on a feeder bend. If measurements are also performed on straight sections of pipe, then the total variable gap length ($d\ell_g$) is $\sim$ 2 mm. Core lengths (ℓ_c) are indicated in Figure 3.2d from 41.5 mm to 56 mm. The sample length is defined as the distance between the poles ℓ_{roi}, which ranges from 15 mm to 25 mm in Figure 3.2d, in addition to the penetration depth of the excitation field into the sample (δ_{ex}):

$$\delta_{ex} \approx \frac{1}{\sqrt{\mu_0 \mu_{roi} \sigma_e \pi f_{ex}}}, \tag{3.6}$$

where μ_{roi} is the sample relative permeability, and σ_e is the sample conductivity. The total length of the circuit ℓ_{eq} is therefore defined as:

$$\ell_{eq} = \ell_c + \ell_{roi} + \delta_{ex} + d\ell_g + \ell_{g0}, \tag{3.7}$$

where ℓ_{g0} is the mean magnetic path length for a constant air gap between the poles and sample, produced by coating or non-magnetic spacers.

In order to calculate $\mathcal{Z}_{eq}$, estimates are required for the core and sample permeabilities (μ_c and μ_{roi}), the sample conductivity (σ_e), and f_{ex}. For BN NDE, 10 Hz $\leq f_{ex} \leq$ 100 Hz, and f_{ex} is sufficiently small that real (not complex) permeabilities may be used for all materials. Typical core materials may be either ferrites or laminated ferromagnetic alloys with μ_c values of 2000 or higher. From Appendix B,

the maximum μ_{roi} measured for the SA-106 Grade B steel is 830 ± 60, and σ_e was measured and supplied by AECL [43] as $5.15 \times 10^6\,(\Omega \cdot \mathrm{m})^{-1}$.

If the total width of the core (w_c - the dimension into the page in Figure 3.2) is estimated to be 1 cm, then the core area is $w_c h_c = 0.5\,\mathrm{cm}^2$. Flux is not confined along a specific path in the sample, so its width was increased over that of the core to: $w_s = 2w_c$. The sample thickness (h_{roi}) is 7 mm, but since the sample is conductive, its effective thickness is approximated as the skin depth (δ_{ex}). The sample area is therefore calculated as $2w_c\delta_{ex}$.

Using equations (2.47) and (2.50) $\mathcal{Z}_{eq}$ may then be calculated as:

$$\mathcal{Z}_{eq} = \frac{\ell_c}{\mu_0\mu_c w_c h_c} + \frac{\ell_{g0} + d\ell_g}{\mu_0 w_c \left[\frac{\ell_c h_c + 2\delta_{ex}(\ell_{roi}+\delta_{ex})}{\ell_c + \ell_{roi} + \delta_{ex}}\right]} + \frac{\ell_{roi} + \delta_{ex}}{2\mu_0\mu_{roi} w_c \delta_{ex}} + i f_{ex} \frac{\sigma_e \delta_{ex}(\ell_{roi} + \delta_{ex})}{h_{roi}}, \tag{3.8}$$

with the terms corresponding to $\mathcal{R}_c$, $\mathcal{R}_g$, $\mathcal{R}_{roi}$, and $i2\pi f_{ex}\mathcal{L}_{roi}$ from left to right. The calculation for $\mathcal{R}_g$ uses the weighted average area of the circuit. A_{eq} is then calculated as:

$$A_{eq} = \frac{w_c}{\ell_{eq}} \left(\frac{h_c}{\ell_c} + \frac{2\delta_{ex}}{\ell_{roi} + \delta_{ex}} + \frac{\ell_c h_c + 2\delta_{ex}(\ell_{roi} + \delta_{ex})}{(\ell_{g0} + d\ell_g)(\ell_c + \ell_{roi} + \delta_{ex})} \right). \tag{3.9}$$

The resulting values for $d\mathcal{R}_g / |\mathcal{Z}_{eq}|$ and μ_{eq} are presented in Table 3.1, in addition to the complex excitation coil inductance L_{ex} (as calculated using (2.54)) with and without air gaps for $N_{ex} = 500$ turns. L_{ex} values give useful information as to the electrical characteristics of the electromagnet, and are used for reference in later analysis.

Table 3.1 indicates that $d\mathcal{R}_g / |\mathcal{Z}_{eq}|$ varies from 0.98 to 0.95 with the specified circuit dimensions. Since anywhere from 0% (no gaps) to 98% (2 mm gap) of the equivalent magnetic circuit impedance $|\mathcal{Z}_{eq}|$ is attributable to the variable air gaps

Table 3.1: Passive flux source calculations for the BN NDE circuit. Inductance values L_{ex} are for $N_{ex} = 500$ turns.

	$\ell_c = 41.5$ mm		$\ell_c = 56$ mm	
	10 Hz	100 Hz	10 Hz	100 Hz
$d\mathcal{R}_g / \lvert\mathcal{Z}_{eq}\rvert$	0.98	0.97	0.97	0.95
μ_{eq}	30	29	41	40
L_{ex} with gaps (mH)	$7.6 - 0.1i$	$6.1 - 0.1i$	$7.6 - 0.1i$	$5.8 - 0.2i$
L_{ex} no gaps (mH)	$306 - 141i$	$130 - 89i$	$203 - 101i$	$81 - 58i$

of the BN NDE circuit, no current-controlled U-core electromagnet that fits within the feeder clearances can be considered a viable passive flux source. An active flux source design that makes adjustments to V_{ex} or I_{ex} according to changes in the flux measured somewhere in the circuit is therefore necessary to ensure BN measurement repeatability in feeders.

3.3 Active Flux Source Design

An active flux source operates by measuring a signal related to the amplitude and orientation of the magnetic flux somewhere in the magnetic circuit. The measured signal is then fed back into a device that compares a reference signal with the feedback signal, and eliminates the difference by adjusting the MMF across or the flux into the circuit. Such a device could also be referred to as a magnetic flux servo.

- In Section 3.3.1 encircling coils and Hall probes are discussed as magnetic flux sensors. Engineering considerations for both sensor types are provided.

- Since the BN NDE circuit in Figure 3.1c is only an approximation of the true magnetic circuit, the placement of feedback sensors may have a significant effect

on flux source performance. Excitation coil and feedback sensor placement considerations are presented in Section 3.3.2.

- In Section 3.3.3 methods for adjusting the circuit MMF are presented, as are their relative merits with respect to stability and efficiency.

3.3.1 Feedback Sensors

An active flux source requires that both the amplitude and orientation of the magnetic flux be measured somewhere in the magnetic circuit. This limits the available sensing technologies to Hall sensors and encircling coils in the flux path.

Encircling Coils

The voltage difference across a physical coil is given by (2.29). In the limit that $I = 0$ through the coil, each loop of the coil has a similar cross-sectional area (A_F), and the coil has N_F turns, then the voltage across the coil (V_F) is:

$$V_F = V_{F+} - V_{F-} = N_F \frac{\mathrm{d}\Phi_F}{\mathrm{d}t}, \tag{3.10}$$

where V_{F+} and V_{F-} are the potentials at the positive and negative feedback coil terminals, respectively, and Φ_F is the total magnetic flux through the coil. Thus the open-circuit voltage across a coil provides a passive measurement of $\mathrm{d}\Phi_F/\mathrm{d}t$, with sensitivity determined by N_F. In order to estimate $\Phi_F(t)$, V_F must be integrated with respect to time, and an initial condition for $\Phi_F(0)$ must be known:

$$\Phi_F(t) = \Phi_F(0) + \frac{1}{N_F} \int_0^t V_F(t') \cdot \mathrm{d}t'. \tag{3.11}$$

In practice, all encircling coils form an LR circuit with the voltmeter, and have an associated time constant. To ensure adequate time resolution, the pickup coil inductance (L_F) must be in series with sufficient resistance that the feedback coil time constant is negligible compared to f_{ex}^{-1} (or the circuit bandwidth in an analog feedback configuration). For any given electromagnet, the incremental monetary cost of producing encircling coils for feedback is small, since similar capability is required in order to wind excitation coils.

Hall Sensors

Hall sensors are semi-conducting devices driven by a constant current source. When immersed in a magnetic field, the Hall effect produces a voltage (V_H) across the device given by:

$$V_H = \mathcal{H}\Phi_H, \tag{3.12}$$

where $\mathcal{H}$ is the Hall coefficient and Φ_H is the flux through the sensor. Since Φ_H is measured internal to the semiconductor, Hall sensors must be placed in air gaps somewhere in the magnetic circuit.

Hall sensors have a limited range of flux sensitivity and linearity. Calibrated Hall sensors that are capable of measuring flux densities on the order of 1.5 T cost on the order of $10 to $200 each [44]. Since they are semiconducting, Hall sensors also exhibit some sensitivity to ionizing radiation, which should be considered in nuclear industry applications [45, 46, 47, 48]. Hall sensors are available within a limited range of sizes.

Sensor Selection

In both Hall sensor and encircling coil-based feedback circuits, $\vec{B}$ is produced by supplying voltage (V_{ex}) and current (I_{ex}) to an excitation coil with N_{ex} turns. In general, $\Phi_{ex} \propto I_{ex}$, and $\mathrm{d}\Phi_{ex}/\mathrm{d}t \propto V_{ex}$. Therefore, Hall sensors are best coupled with current controllers, while encircling coils are best coupled with voltage controllers.

While the Hall probe and current controller configuration is conceptually simpler and offers DC flux control, BN excitation fields are normally meant to be purely AC, such that the BN has similar characteristics for each half-cycle. Thus the lack of DC flux feedback from encircling coils is an engineering issue, but not a measurement requirement. Voltage controllers are also considerably easier to implement for large L_{ex} than current controllers. In the specific case of feeder pipes, the limited clearances and significant wall thickness make the added air gaps required for a Hall sensor undesirable. For these reasons, all fully-developed designs in this thesis use encircling coils and voltage controllers.

3.3.2 Coil and Feedback Sensor Placement

The placement of excitation coils and feedback sensors in the magnetic circuit is critical to the performance of the active flux source. For BN measurements, it is desirable to have a uniform field amplitude in the sample region between the two poles where the pickup coil* is located.

For fundamental studies of BN behaviour, the appropriate magnetic field sensing location is inside the sample, preferably in the region of interest. This can only be accomplished by winding a feedback coil around the sample with the coil axis

*Typical pickup coil diameters range from 3 mm to 10 mm.

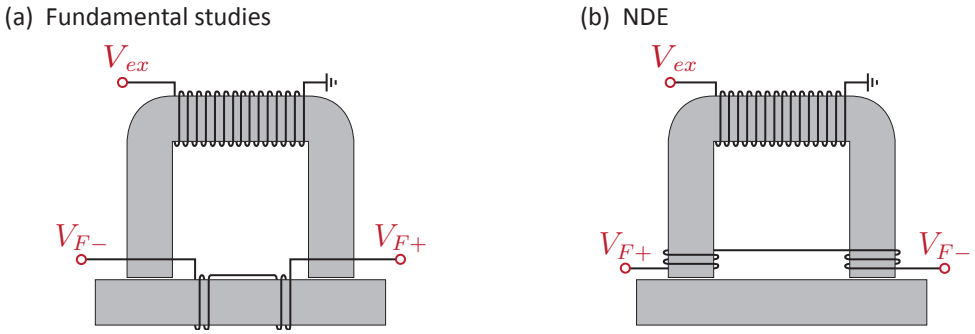

Figure 3.3: Feedback coil positioning for (a) fundamental studies and (b) NDE.

parallel to the field component being measured, as illustrated in Figure 3.3a. The requirement that the sample be wound with a feedback coil limits repositioning of the electromagnet-feedback coil system, and is therefore inappropriate for most NDE applications. Furthermore, unless the sample has rotational symmetry, the geometry in Figure 3.3a is unsuitable for BN anisotropy measurements.

Without measuring the flux directly in the sample, field consistency can only be approximated by measuring the flux in the core via a feedback coil (or in the air gap via a Hall sensor), as shown in Figure 3.3b. The preferred location of the sensors is at the ends of the poles, as this best represents the flux entering and leaving the sample. In both Figures 3.3a and 3.3b, the feedback coil is split to ensure the controlled flux best represents the flux at the mid-point of the sample.

3.3.3 Waveform Compensation

Once an electromagnet is equipped with appropriate excitation and feedback coils, there are several valid approaches to implement feedback and correct the excitation coil waveforms. In this section, three approaches to feedback implementation are discussed: steady state digital feedback, real-time analog feedback, and an approach

that uses digital error-correction to improve analog circuit performance.

Steady State Digital Feedback (SSD)

To use digital feedback, the excitation coil is driven by a computer-controlled digital to analog converter (DAC) coupled with a voltage or current follower. If the magnetic circuit is in a steady state, the feedback signal can be used to iteratively adjust the excitation waveform in a digital environment until the desired feedback signal is produced. This approach has the advantage that the excitation amplifiers have low gains and direct feedback from the excitation circuit, both of which lead to increased stability.

The performance of a SSD controller is limited by the efficiency of the feedback algorithm. For example, the robust algorithm proposed by Zurek in 2005 converges on the order of 60 to 100 iterations [49]. However, as f_{ex} decreases, the number of calculations for Zurek's algorithm increases exponentially, increasing the number of excitation cycles required to perform the calculation. For f_{ex} values on the order of 50 Hz, Zurek's algorithm converges in < 60 s, suggesting approximately 50 excitation cycles are required to compute a single iteration.

A SSD solution was briefly investigated for this project before switching to an analog feedback approach. The algorithm was not developed to the point of being robust, and is not presented in this thesis, though a version can be found in a paper published early in the project [50].

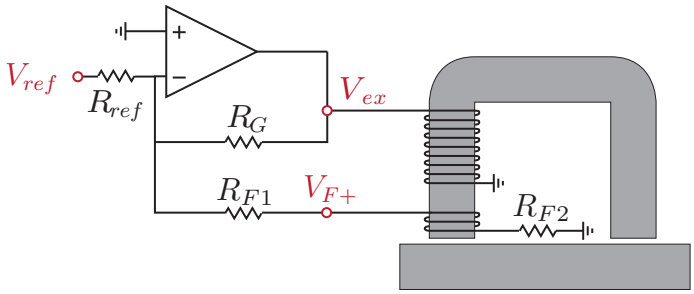

Figure 3.4: Schematic for a real-time analog flux source, using a feedback coil and a gain-limiting resistor R_G.

Real-Time Analog Feedback (RTA)

The disadvantage of SSD feedback is that it requires a steady state over the convergence time of the algorithm, which may be many excitation periods. A more appealing solution is an analog feedback system that achieves the desired result in real time, or a real-time analog (RTA) approach.

An electric circuit schematic for a RTA system that employs an ideal operational amplifier (op-amp) and a feedback coil is shown in Figure 3.4. V_{ref} is an arbitrary reference voltage and V_{ex}, and V_{F+} are ground-referenced voltage measurements. The op-amp is configured as a current-adder, such that the potential at the inverting input is held to a virtual ground, and the sum of the currents through R_{F1}, R_G and R_{ref} is zero:

$$\frac{V_{ref}}{R_{ref}} + \frac{V_{F+}}{R_{F1}} + \frac{V_{ex}}{R_G} = 0. \tag{3.13}$$

The resistors R_{F1} and R_{F2} are much greater than the feedback coil resistance R_F, which limits the current through R_F to ensure that equation (3.10) is a good approximation. Since the same current passes through R_{F1} and R_{F2}, V_F is given by:

$$V_F = \left(1 + \frac{R_{F2}}{R_{F1}}\right) V_{F+}. \tag{3.14}$$

Substituting equation (3.14) into equation (3.13), and solving for V_{ref} gives:

$$V_{ref} = -\left(\frac{R_{ref}}{R_{F1} + R_{F2}}\right) V_F - \left(\frac{R_{ref}}{R_G}\right) V_{ex}. \tag{3.15}$$

The contribution of V_{ex} to V_{ref} in equation (3.15) is problematic, since V_{ex} is unknown. However, in the limit that $R_G \to \infty$ (achieved by removing R_G from the circuit) the gain of the circuit is increased to the open-loop gain of the amplifier (G_{OL}[†]), and to a good approximation V_F follows V_{ref}:

$$\lim_{R_G \to \infty} (V_{ref}) = -\left(\frac{R_{ref}}{R_{F1} + R_{F2}}\right) V_F. \tag{3.16}$$

In this open-loop configuration, any offset between the amplifier terminals is multiplied by G_{OL} and increases V_{ex}. Since there is no feedback to compensate for these offsets, eventually V_{ex} will migrate to the amplifier rails, which indicates the open-loop system with only encircling coil feedback is inherently unstable. Maximum performance for an RTA circuit is therefore obtained by decreasing R_G from ∞ until the circuit stabilizes.

To achieve a target feedback coil voltage (V_{FT}):

$$V_{FT} = N_F \frac{\mathrm{d}\Phi_{FT}}{\mathrm{d}t}, \tag{3.17}$$

where Φ_{FT} is the target flux through the feedback coil, V_{FT} is substituted for V_F in equation (3.15), which is substituted for V_{ref} in equation (3.15). Solving for V_F gives:

$$V_F = V_{FT} - \left(\frac{R_{F1} + R_{F2}}{R_G}\right) V_{ex}. \tag{3.18}$$

[†]For an ideal op-amp, $G_{OL} = \infty$. In practice, G_{OL} is usually between 10^5 and 10^6.

The V_{ex} term above therefore represents an error in the circuit performance, which is minimized as $R_G \to \infty$. It follows that the ideal value for R_G is the highest value that provides an acceptable stability margin.

Digital Error Correction (DEC) for RTA Circuits

If the error introduced by gain limiting is sufficiently small for design requirements, the RTA circuit in Figure 3.4 may be adequate. However, in a system where the target flux waveform ($\boldsymbol{\Phi_{FT}}$) is periodic and the reference voltage waveform ($\boldsymbol{V_{ref}}$) is provided by a computer-controlled DAC, $\boldsymbol{V_{ref}}$ can be modified digitally to reduce the error, i.e., digital error correction (DEC).

Let $\boldsymbol{V_{exT}}$ be the excitation voltage waveform required to produce the target feedback coil voltage waveform ($\boldsymbol{V_{FT}}$). Substituting the corresponding waveforms into equation (3.15) gives the ideal reference voltage waveform ($\boldsymbol{V_{refT}}$) as:

$$\boldsymbol{V_{refT}} = -\left(\frac{R_{ref}}{R_{F1}+R_{F2}}\right)\boldsymbol{V_{FT}} - \left(\frac{R_{ref}}{R_G}\right)\boldsymbol{V_{exT}}. \tag{3.19}$$

Since $\boldsymbol{V_{exT}}$ is unknown, a guess at the target excitation voltage waveform $\boldsymbol{V_{Gex}}$ is substituted for $\boldsymbol{V_{exT}}$ and iteratively modified along with $\boldsymbol{V_{ref}}$ according to:

$$\boldsymbol{V_{ref},_j} = -\left(\frac{R_{ref}}{R_{F1}+R_{F2}}\right)\boldsymbol{V_{FT}} - \left(\frac{R_{ref}}{R_G}\right)\boldsymbol{V_{Gex},_{(j-1)}}, \tag{3.20}$$

with j corresponding to the iteration number, $j = 1$ being the first iteration, and $\boldsymbol{V_{Gex},_0}$ being the initial guess.

The problem of determining $\boldsymbol{V_{Gex},_j}$ is the same as that of purely digital feedback solutions. However, if the RTA circuit shown in Figure 3.4 is used with large R_G, to a

good approximation the measured excitation voltage waveform for iteration j ($\boldsymbol{V_{ex},_j}$) is approximately equal to $\boldsymbol{V_{exT}}$, even with $\boldsymbol{V_{Gex},_j} = 0$. Therefore, if $\boldsymbol{V_{ex},_j}$ is measured and used to calculate $\boldsymbol{V_{Gex},_j}$ according to:

$$\boldsymbol{V_{Gex},_j} = G_D \cdot \boldsymbol{V_{ex},_j} + (1 - G_D) \cdot \boldsymbol{V_{Gex},_{(j-1)}}, \tag{3.21}$$

where G_D is a digital gain between 0 and 1, as j increases $\boldsymbol{V_{Gex},_j}$ will converge toward a solution for $\boldsymbol{V_{exT}}$, and the error will be reduced.

In order to initialize the algorithm the form of $\boldsymbol{V_{Gex},_0}$ is required. When R_G is sufficiently large, setting $\boldsymbol{V_{Gex},_0} = 0$ is an acceptable solution. However, a better initial guess can be calculated with additional knowledge of the system. For example, it is known that V_{ex} has the form of (2.29). For a given $\boldsymbol{\Phi_{FT}}$, the specific waveforms of I_{ex} and Φ_{ex} are unknown. However, if it is approximated that $L_{ex}I_{ex} = N_{ex}\Phi_{ex}$, that the coil has a resistance R_{ex}, and that $\Phi_{ex} = \mathcal{X}\Phi_F$, where $\mathcal{X}$ is a proportionality constant, then a reasonable solution for $\boldsymbol{V_{Gex},_0}$ is:

$$\boldsymbol{V_{Gex},_0} = N_{ex}\left(\frac{R_{ex}}{L_{ex}} + \frac{\mathrm{d}}{\mathrm{d}t}\right)\mathcal{X}\boldsymbol{\Phi_{FT}}. \tag{3.22}$$

If the circuit has sufficiently low hysteresis and eddy current effects, L_{ex} and $\mathcal{X}$ may be considered constants.

A flow chart for the above algorithm that saves k_{max} cycles of data when the root-mean-square difference between the measured feedback voltage for iteration j ($\boldsymbol{V_F},_j$) and $\boldsymbol{V_{FT}}$ is less than a threshold T_{err} is presented in Figure 3.5, where:

$$\mathrm{RMS}\left\{\boldsymbol{X}\right\} = \left(\frac{1}{n_{max}}\sum_{n=1}^{n_{max}}\left(X_{[n]}\right)^2\right)^{\frac{1}{2}} \tag{3.23}$$

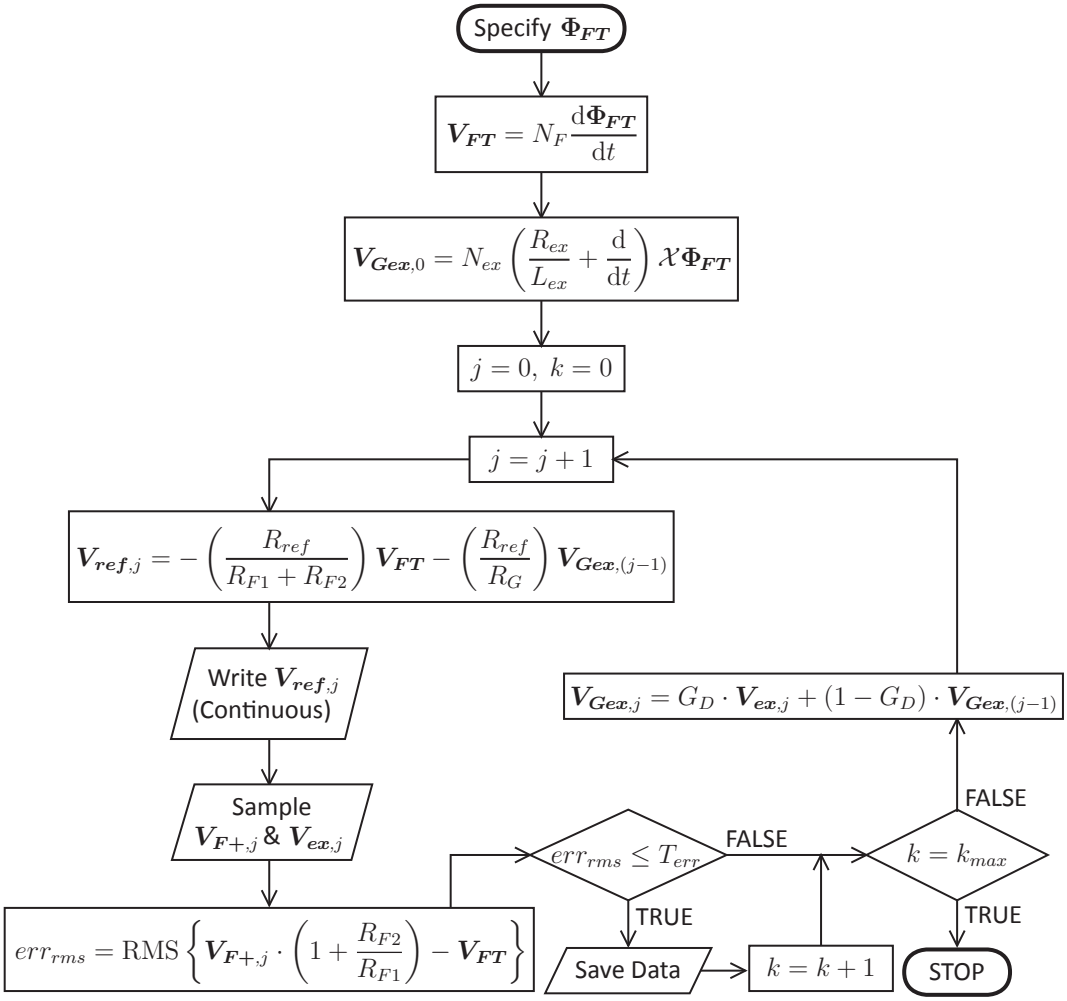

Figure 3.5: Flow chart for the digital error correction algorithm when using a closed-loop steady state analog feedback flux source.

and $X_{[n]}$ denotes the n^{th} time sample of waveform $\boldsymbol{X}$ with a total of n_{max} samples.

The settling time of this DEC algorithm is dependent on R_G, the initialization of $\boldsymbol{V_{Gex},0}$, and how closely the amplifier replicates the behaviour of an ideal op-amp. The algorithm makes use of the assumption that the error is directly proportional to V_{ex}/R_G. Errors in the measurement of V_{ex} and variation of R_G violate this assumption. Furthermore, the algorithm does not account for the limited gain of a real op-amp,

and thus there is some phase delay associated with the amplifier response time. If the minimum error due to these contributions is too large to meet design specifications, then a more sophisticated algorithm is required.

3.4 Flux Superposition

The gain-limiting and error correction approaches described in the previous section can be used to control multiple coupled excitation coils in a magnetic circuit. Using the principles of flux conservation, such configurations can be used to drive flux into sample elements from multiple directions, and use vector addition to compute the resultant magnetic fields.

One application of multiple channels is to use superposition to achieve the field orientation rotation necessary for BN anisotropy measurements in a target region of the sample with no moving parts. This superposition approach eliminates the need for motors or similar mechanical devices within a BN measurement system. Air gaps are fixed once the magnet is attached to the sample, and various magnetisation schemes are achieved by changing the target flux waveforms. The success of this approach relies on linear superposition in an non-linear medium, which is a reasonable approximation for irreversible magnetisation processes below saturation.

Rotational field superposition can be achieved with as few as three independent poles, though a four independent pole (tetrapole) system has advantages in terms of manufacturing and symmetry. Two tetrapole core geometries proposed by the author for feeder pipe testing that can be used to achieve field rotation are shown in Figure 3.6. In Figure 3.6a, four cylindrical poles share a common backing to complete the magnetic circuit. In Figure 3.6b, two orthogonal U-cores are used.

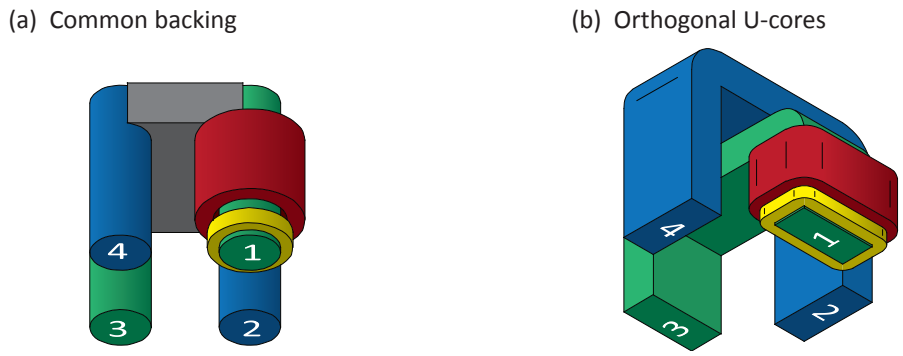

Figure 3.6: Tetrapole core configurations using (a) four cylindrical poles with a common backing, and (b) two orthogonal U-cores. Poles are labeled in a clockwise fashion, with pairs 1,3 and 2,4 forming orthogonal dipoles. In reality, an excitation and feedback coil is present on each of the four poles, but only one excitation coil (in red) and feedback coil (in yellow) is shown here on pole 1 to clarify core geometries.

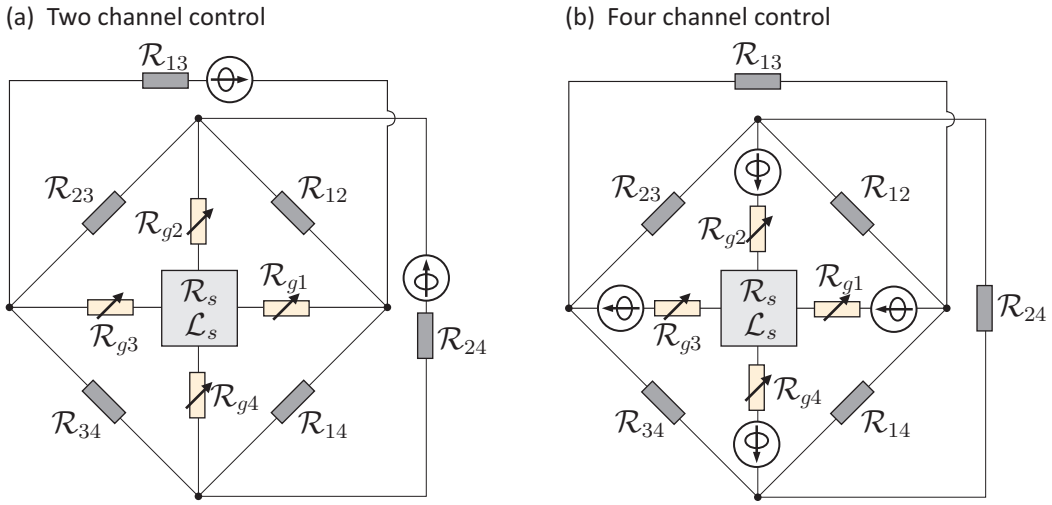

Figure 3.7: Simplified tetrapole magnetic circuit schematics coupled to a reluctive and conductive sample ($\mathcal{R}_{roi}$ $\mathcal{L}_{roi}$), with coupling between poles j and k is expressed as single reluctances $\mathcal{R}_{jk}$. In (a) poles 1 and 3 and poles 2 and 4 are driven each with a single flux source. In (b) all four poles driven independently.

Figure 3.7 shows equivalent magnetic circuit schematics for tetrapoles, with the coupling between each set of poles j and k represented by reluctances $\mathcal{R}_{jk}$. The conductance of the sample is combined with its reluctance for simplicity. In Figure 3.7a, only two flux sources are used across poles 1 and 3 and poles 2 and 4. In Figure 3.7b, four flux sources are used and each pole is driven independently.

Figure 3.7a shows that the flux through the sample is indeterminate when only two flux sources are used, since the flux is free to travel between adjacent poles outside the sample. In the common backing core shown in Figure 3.6a, coupling between adjacent poles is strong due to the permeable backing plate. With the orthogonal U-cores separated by air gaps, as shown in Figure 3.6b, coupling between adjacent poles is weak.

Using four flux sources as shown in Figure 3.7b, the flux through the sample appears over-determined. However, since flux is poorly confined to the magnetic circuit, mismatched flux sources lead to flux along paths that are not indicated in the schematic. Moreover, due to poor flux confinement, the use of four flux sources more precisely defines the flux through the sample.

The classical BN anisotropy measurement is achieved by mechanically rotating a U-core electromagnet with a sinusoidal excitation field about the sample surface normal. To imitate this measurement with a tetrapole, p is defined as the pole index, and poles $p = 1, 3$ and $p = 2, 4$ are paired as dipoles. If the excitation field makes an angle θ_T with the path between poles 1 and 3, and the target feedback coil flux waveform is $\boldsymbol{\Phi_{FT}}$, then a general expression for the target feedback coil voltage

waveform on pole p ($\boldsymbol{V_{FT(p)}}$) is given by:

$$\boldsymbol{V_{FT(p)}} = N_F \, \Re \left\{ i^{(p-1)} e^{-i\,\theta_T} \right\} \frac{\mathrm{d}}{\mathrm{d}t} \boldsymbol{\Phi_{FT}}, \tag{3.24}$$

where $i = \sqrt{-1}$, and $\Re\{\mathrm{Z}\}$ is the real part of the complex number Z.

Substituting $\boldsymbol{\Phi_{FT}} = A_F \cdot B_{FT} \sin(2\pi f_{ex} \boldsymbol{t})$ into equation (3.24), where A_F is the feedback coil area and B_{FT} is the target peak flux density in the feedback coils, and $\boldsymbol{t}$ is the time axis for one excitation period, the target feedback coil waveforms are:

$$\boldsymbol{V_{FT(p)}} = 2\pi f_{ex} \cdot N_F A_F \cdot B_{FT} \cdot \cos(2\pi f_{ex} \boldsymbol{t}) \cdot \Re \left\{ i^{(p-1)} e^{-i\theta_T} \right\}. \tag{3.25}$$

Varying θ_T in equation (3.25) rotates the orientation of the field at the mid-point of the tetrapole. This method differs from a mechanically rotated U-core, since the pole pair orthogonal to the driving direction compensates for any flux produced by anisotropy.

To further investigate the theoretical validity of flux source notation and the tetrapole superposition, the two geometries shown in Figure 3.6 were modelled in 3D using the *Infolytica MagNet® 6.25.0* time harmonic magnetic field solver. The details, results and design implications of these models are presented in Chapter 5.

Chapter 4

Flux Control System

In Chapter 3 a tetrapole electromagnet design was proposed that requires four matched flux sources to compensate for feeder pipe curvature. This chapter presents the design of a flux control system (FCS), capable of driving up to four strongly coupled excitation and feedback coil pairs while sampling BN from a pickup coil.

- Section 4.1 presents the hardware implementation of the FCS.
- Section 4.2 presents the software implementation of the FCS.

The performance of the FCS is dependent on the load electromagnet, and is therefore estimated in Chapter 6, following the tetrapole probe design procedure in Chapter 5.

4.1 Hardware Implementation

The SSD (steady state digital), RTA (real-time analog) and DEC (digital error correction) excitation waveform compensation methods described in Section 3.3 all require

a computer-controlled DAC, time-based voltage measurements, and a power amplifier. All three feedback configurations share similar hardware cost, and thus the FCS hardware implementation was designed such that the system could be configured in any of the three modes via software. The base computer platform for the FCS is a 2.66 GHz *Intel® Pentium® D* with 960 MB of RAM, running *Microsoft® Windows® XP**, and *National Instruments® LabVIEW® 8.2 Full Development Kit*. Additional component selection considerations are presented in Section 4.1.1, and the flux source circuit is presented in Section 4.1.2.

4.1.1 Component Selection

Data Acquisition Boards

For each excitation and feedback coil pair (p) a computer-controlled DAC is required to generate the reference voltage waveform ($\boldsymbol{V_{ref(p)}}$). The SSD and DEC algorithms also require the excitation voltage waveform ($\boldsymbol{V_{ex(p)}}$) and the feedback voltage waveform ($\boldsymbol{V_{F(p)}}$) to be measured. A measurement of the excitation current waveform ($\boldsymbol{I_{ex(p)}}$) via a shunt voltage waveform ($\boldsymbol{V_{S(p)}}$) is optional, though useful for permeability and inductance estimation. A *National Instruments®* PCI-6229 Multifunction DAQ (PCI-6229), was selected to meet these requirements for four channels (i.e., $p = 1 \ldots 4$).

The PCI-6229 features 4 analog output ($AO_{(0\ldots3)}$) channels with ± 10 V range and 16 bit resolution. Each AO channel supports a maximum update rate of 625 kHz. The PCI-6229 features up to 32 single-ended multiplexed analog input ($AI_{(0\ldots31)}$) channels for voltage measurement, with a maximum sampling rate of 250 kHz aggregate over

*No service packs were installed.

all channels. The analog to digital converter has 16 bit resolution over each of four selectable voltage ranges up to ±10 V. Other relevant features include 32 digital input/output channels ($P_{0.(0...31)}$), digital triggering, and support for 8 real-time system integration channels ($RTSI_{(0...7)}$). For a complete list of specifications, see [51].

Typical BN emissions have frequency content up to or exceeding 300 kHz, and a sampling frequency greater than the Nyquist criterion of 600 kHz is required. Since the 253 kHz maximum sampling rate of the PCI-6229 is insufficient, a *National Instruments*® PCI-6133 Multifunction DAQ (PCI-6133), with a maximum sampling frequency of 2.5 MHz, was selected to meet the BN sampling requirements [52].

Amplifier

The excitation coils in the flux source circuit may be modelled by a series resistance R_{ex} and inductance L_{ex} that changes with the excitation frequency f_{ex}. Using the values calculated in Chapter 3 with $L_{ex} = 130 - 89i$ mH at $f_{ex} = 100$ Hz[†] and $R_{ex} = 26\,\Omega$[‡], the excitation coil power amplifier must drive a variable load impedance from 26 Ω to 120 Ω.

Due to the prevalence of audio equipment, there is an abundance of low-cost solid state power amplifiers. The LM4701 amplifier from *National Semiconductor*® [53] was selected. The amplifier has a gain-bandwidth product of 7.5 MHz, is rated for 30 W into 8 Ω from 20 Hz to 20 kHz with total harmonic distortion + noise of 0.08% with appropriate heat-sinking. The LM4701 can accept rail voltages up to ±32 V. In the circuit implemented in this work, the amplifiers have passive heat sinks and are capable of supplying up to 3.5 W of continuous power. The amplifier also features

[†]From Table 3.1.
[‡]Calculated in Section 3.3.1.

SPiKe^{TM} protection circuitry, which protects the output stages from voltage and thermal overload conditions.

Power Supply

An *Anatek* 25-20 dual regulated DC power supply with variable floating voltage outputs up to $\pm 25\,\mathrm{V}$ and current limiting up to 2 A was selected to power the LM4701 amplifiers.

4.1.2 Flux Source Circuit

A schematic for a single channel of the implemented control circuit is shown in Figure 4.1, with functional details of the various components found in Table 4.1. Red open circles in Figure 4.1 correspond to pins on the PCI-6229, with p denoting the pole/channel number ($p = 1 \ldots 4$). Black filled circles are banana jacks[§] used to connect the various magnetic circuits. V_{CC} and V_{EE} are respectively the $+25\,\mathrm{V}$ and $-25\,\mathrm{V}$ outputs of the *Anatek* 25-20 supply. The amplifier rails are therefore $\pm 25\,\mathrm{V}$, and the PCI-6229 $AI_{(0\ldots31)}$ channels have a maximum voltage range of $\pm 10\,\mathrm{V}$. In order to measure the full range of V_{ex} (which is necessary for the DEC algorithm), a voltage divider consisting of resistors $(g-1)\cdot R_g$ and R_g is used, with $g \approx 10$.

Two H11F3 photo FET optocouplers from *Fairchild Semiconductor*® combined with resistors R_H and digital output $P_{0.(p-1)}$ are used to create a digital switch. The off-state resistance (R_{off}) and on-state resistance (R_{on}) of the detector in the H11F3 are $300\,\mathrm{M}\Omega$ and $470\,\Omega$, respectively [54]. When $P_{0.(p-1)} = 0\,\mathrm{V}$ the top H11F3 in Figure

[§]The banana jacks pass directly through the sheet steel FCS chassis. This implementation results in some inductive loading for currents through the chassis. In future designs, banana connector pairs should be housed in non-ferromagnetic material, or an alternative connector should be used.

Table 4.1: Component Descriptions

Component	Functional Description
C_S	Power supply filtering capacitor. Consists of a 22 µF tantalum capacitor in parallel with a 0.1 µF ceramic capacitor.
C_{ref}	Low-pass (23 kHz) filtering capacitor with R_{ref1} to reduce DAC aliasing and glitches from the PCI-6229 *AO* channels.
$(g-1)\cdot R_g$, R_g	Form a voltage divider on the amplifier output to facilitate PCI-6229 sampling of $V_{ex(p)}$.
R_{ref1}, R_{ref2}	Specify the gain of the reference voltage. R_{ref1} also forms a low-pass filter with C_{ref}.
R_{G1}	Analog flux feedback resistor.
R_{G2}	Voltage following feedback resistor.
R_{F1}, R_{F2}	Specifies feedback coil gain and time constant. Must be increased if the circuit is unstable.
R_H	Current limiting resistor for H11F3 operation. The forward current for the H11F3 is 16 mA to 60 mA with 1.5 V across the emitter. $P_{0.(p-1)}$ channels supply 5 V up to 20 mA, thus $R_H < (5-1.5)/0.02$.
R_S	Shunt resistor. Resistance should be low compared to the R_{ex}. *Ohmite*® 13FR200, $0.2 \pm 1\%\,\Omega$, 3 W current sensing resistors were used.
F	Excitation coil protection fuse. Preferably non-inductive.
L_{ex}	Excitation coil inductance with N_{ex} turns. May be modelled as complex to account for hysteresis/eddy currents. Typically > 1 mH.
R_{ex}	Excitation coil resistance. May include eddy current resistance.
L_F	Feedback coil inductance. Value is usually $L_{ex}\cdot(N_F/N_{ex})^2$, where N_F is the number of feedback coil turns. Feedback coil resistance is negligible compared to the added series resistors R_F.
R_F	Feedback coil resistance. Negligible compared to R_{F1} and R_{F2}.
R_B	Optional current balancing resistor. R_B is not included in the present implementation, since its value differs for the two operating modes. For the VF mode: $R_B = (R_{G1}^{-1} + R_{G2}^{-1} + (R_{ref1}+R_{ref2})^{-1} + R_{F1}^{-1})^{-1}$. For the RTA and DEC modes: $R_B = (R_{G1}^{-1} + (R_{ref1}+R_{ref2})^{-1} + R_{F1}^{-1})^{-1}$.

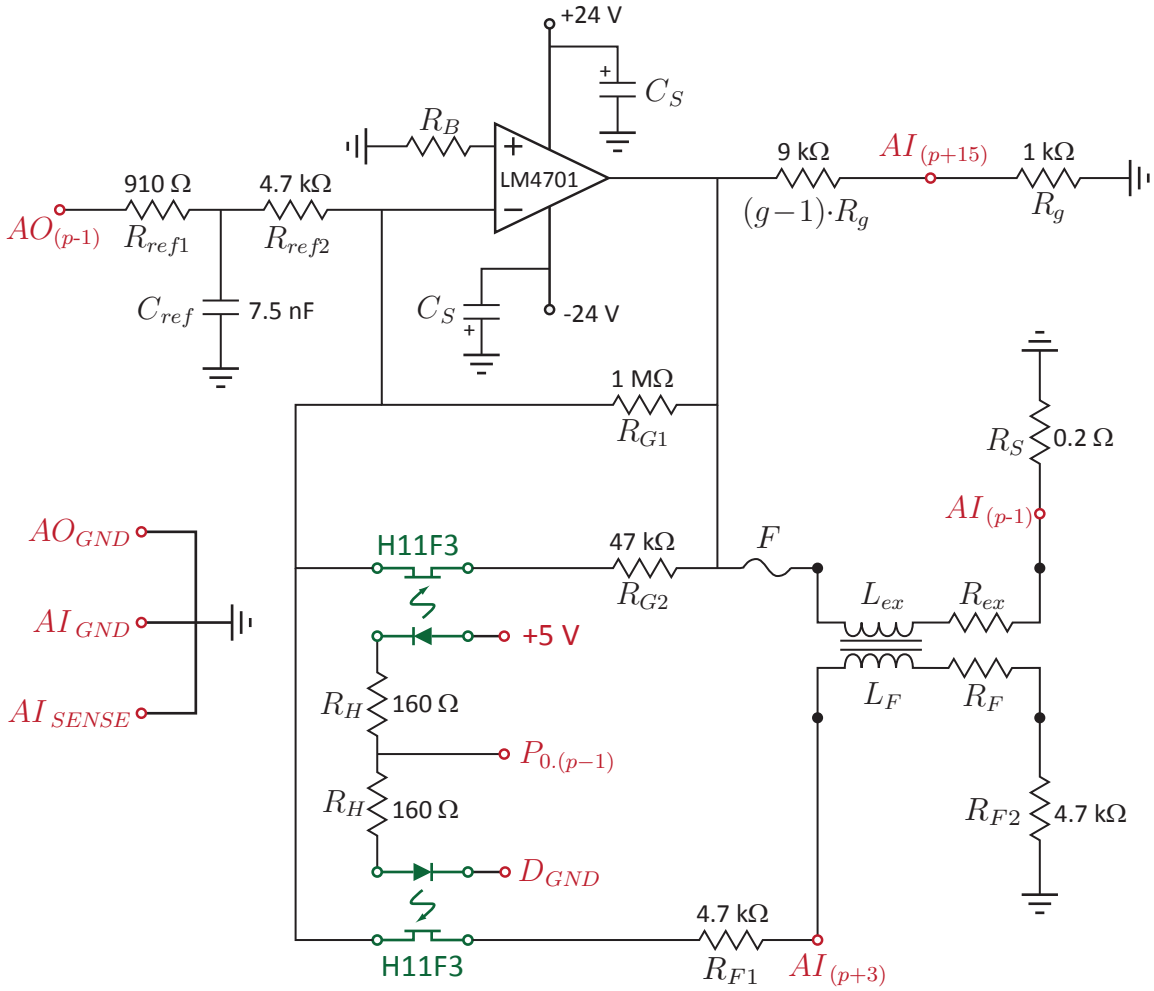

Figure 4.1: LM4701 based electromagnet control circuit with digital switching between voltage follower and analog flux feedback modes.

4.1 is active, and the amplifier receives current though R_{ref}, R_{G1} and R_{G2}. When $P_{0.(p-1)} = 5\,\mathrm{V}$, the bottom H11F3 is active, and the amplifier receives current through R_{ref}, R_{G1}, and R_{F1}.

Using the digital switch, the circuit shown in Figure 4.1 is designed to operate in

both a voltage following (VF) mode when $P_{0.(p-1)} = 0\,\mathrm{V}$ with a gain ($G_{V(p)}$) of:

$$G_{V(p)} \approx \frac{R_{G1} \cdot (R_{G2} + R_{on})}{(R_{G1} + R_{G2} + R_{on}) \cdot (R_{ref1} + R_{ref2})} = 8.1, \tag{4.1}$$

and a real-time analog (RTA) flux feedback mode when $P_{0.(p-1)} = 5\,\mathrm{V}$ with a gain ($G_{\Phi(p)}$) of:

$$G_{\Phi(p)} \approx \frac{R_{G1}}{R_{ref1} + R_{ref2}} = 178. \tag{4.2}$$

Due to limited amplifier bandwidth and filtering on the *AO* channels, $G_{V(p)}$ and $G_{\Phi(p)}$ have some effective frequency dependence, and must be optimized experimentally to maximize system performance.

4.2 Software Implementation

The interface and control software for the FCS was implemented in *LabVIEW® 8.2*. Through use of the H11F3s and PCI-6229 $P_{0.(p-1)}$ digital output channels, the FCS can be switched from VF mode to a RTA flux feedback mode, with or without DEC. The software can be configured to drive either one channel (keeping the other three channels inactive in VF mode) or four channels simultaneously. The utility and basic operation of the three control modes is described in section 4.2.1. A description of the data stored is presented in section 4.2.2. Detailed flow charts, timing diagrams and channel matching procedures for the FCS are presented in Appendix A.

4.2.1 Feedback Modes

Only purely AC excitation fields are explored in this work. To compensate for voltage offsets in the system, all feedback modes were implemented with an iterative digital DC excitation current correction with a digital gain (G_D). In VF mode, only DC current corrections are applied, while in RTA and DEC modes, further corrections are applied to optimize system performance.

VF Mode

VF mode is implemented as a sinusoidal excitation voltage generator, for which the user can specify the target peak excitation voltage (V_{exTpk}), the excitation frequency (f_{ex}), and the target tetrapole angle (θ_T). VF mode is used during degaussing processes, circuit testing, excitation circuit impedance measurement, and calibration. The circuit also operates in VF mode by default when no measurements are being performed. Data are saved in VF mode for iterations j where the DC excitation current in all channels ($\overline{I_{ex(p),m}}$) are less than or equal to the DC current threshold T_C, with $m = (j-1), j$.

In principle, VF mode could be used with a SSD algorithm for flux feedback, though this has not been implemented. It can also be used to power electromagnets without feedback coils, replicating the behaviour of previous BN electromagnet power amplifiers.

RTA Mode

RTA mode is implemented as a sinusoidal feedback coil flux controller, for which the user can specify the target peak flux density in the feedback coils (B_{FT}), the

excitation frequency (f_{ex}), and the target tetrapole angle (θ_T). In RTA mode, the circuit uses analog flux feedback with gain limiting to $G_{\Phi(p)} \approx 178$. To compensate for the gain-limiting error, the reference voltage waveform for channel p and iteration j ($\boldsymbol{V_{ref(p),j}}$) is given by:

$$\boldsymbol{V_{ref(p),j}} = -\frac{\boldsymbol{V_{FT(p)}}}{G_{F(p)}} - \frac{\boldsymbol{V_{Gex(p),0}}}{G_{\Phi(p)}} \tag{4.3}$$

where:

$$G_{F(p)} \approx \frac{R_{F1} + R_{F2} + R_{on}}{R_{ref1} + R_{ref2}} \approx 1.76 \tag{4.4}$$

is the feedback voltage gain, and $\boldsymbol{V_{Gex(p),0}}$ is calculated using equation (3.22), but with $\mathcal{X}$, R_{ex} and L_{ex} specified for each excitation channel as $\mathcal{X}_p$, $R_{ex(p)}$ and $L_{ex(p)}$, respectively. Like VF mode, data are saved in RTA mode for iterations j where $\overline{I_{ex(p),m}} \leq T_C$, with $m = (j-1), j$.

Maximum performance in RTA mode is achieved through optimization of $\mathcal{X}_p$, $R_{ex(p)}/L_{ex(p)}$, $G_{\Phi(p)}$ and $G_{F(p)}$. The software implementation allows the user to modify $R_{ex(p)}$, $L_{ex(p)}$, $\mathcal{X}_p$, $G_{\Phi(p)}$ and $G_{F(p)}$ during excitation iterations, in order to optimize RTA performance. Setting $T_C = 0$ puts RTA mode into an infinite loop, which is useful for optimization. Setting $\mathcal{X}_p = 0$ forces the circuit to operate as a purely real-time circuit with $\boldsymbol{V_{Gex},0} = 0$.

RTA mode is primarily used to optimize $\mathcal{X}_p$, $R_{ex(p)}/L_{ex(p)}$, $G_{\Phi(p)}$ and $G_{F(p)}$. As is shown in Chapter 6, the optimization of these 16 parameters (4 parameters across 4 channels) significantly reduces the convergence time in DEC mode. Such optimization is useful when performing a long series of BN measurements with the electromagnet at a fixed position, as the aggregate time savings may exceed the time required for

manual optimization.

DEC Mode

In DEC mode, the software operates in RTA mode until $\overline{I_{ex(p),j}} \leq T_C$. Once the DC current is below T_C, the measured excitation voltage waveform $\boldsymbol{V_{ex(p),(j-1)}}$ is used to modify $\boldsymbol{V_{ref(p),j}}$ according to the algorithm presented in Figure 3.5. The normalized RMS difference between the measured feedback coil voltage waveforms ($\boldsymbol{V_{F(p),j}}$) and the target feedback coil voltage ($\boldsymbol{V_{FT}}$) for iteration j ($err_{rms,j}$) is then compared to an error threshold T_{err}. Data are saved when both $\overline{I_{ex(p),m}} \leq T_C$ and $err_{rms,m} \leq T_{err}$ for $m = (j-1), j$.

DEC mode was used to drive the excitation coils for all the BN measurements presented in this work. Maximum performance in DEC mode is achieved through optimization of $G_{F(p)}$ and $G_{\Phi(p)}$.

4.2.2 Raw Data

The software implementation is designed such that each BN measurement represents the average BN emissions from a user-specified number of excitation cycles (k_{max}). Prior to each measurement, the sample is degaussed to minimise residual magnetisation effets. The background noise in the pickup coil ($\boldsymbol{V_{bk,k}}$) is then sampled for $k = 1 \ldots k_{max}$ using the PCI-6133 at $f_{6133AI} = 2.5\,\text{MHz}$. Once the background noise is sampled, the excitation field is initialized in the specified feedback mode.

During each excitation iteration j, the pickup coil voltage $\boldsymbol{V_{(BN+bk),j}}$ is sampled at f_{6133AI} using the PCI-6133, followed by the PCI-6229 analog input voltages

($\boldsymbol{AI_{(0...7,16...19)}}$), sampled at f_{6229AI}. The pickup and excitation voltages are not sampled simultaneously, as this has been observed to produce cross-talk at harmonics of f_{6229AI} in the $\boldsymbol{V_{(BN+bk),j}}$ waveforms.

The excitation voltage waveform for channel p and iteration j is then calculated as:

$$\boldsymbol{V_{ex(p),j}} = g_p \cdot \boldsymbol{AI_{(p+15)}}. \tag{4.5}$$

The excitation currents:

$$\boldsymbol{I_{ex(p),j}} = \frac{\boldsymbol{AI_{(p-1)}}}{R_{S(p)}}, \tag{4.6}$$

flux rate through the feedback coils:

$$\left(\frac{\boldsymbol{dB}}{\boldsymbol{dt}}\right)_{\boldsymbol{F(p),j}} = \frac{\mathcal{M}_p}{N_F A_F} \cdot \left(\boldsymbol{AI_{(p+3)}} - \overline{AI_{(p+3)}}\right)\left(1 + a_p \frac{R_{F2}}{R_{F1} + R_{on}}\right), \tag{4.7}$$

where $a_p = 1$ in RTA and DEC modes and $a_p = 0$ in VF mode, flux density within the feedback coils:

$$\boldsymbol{B_{F(p),j}} = \int_0^{1/f_{ex}} \left(\frac{\boldsymbol{dB}}{\boldsymbol{dt}}\right)_{\boldsymbol{F(p),j}} \cdot \mathrm{d}t' - \overline{\int_0^{1/f_{ex}} \left(\frac{dB}{dt}\right)_{F(p),j} \cdot \mathrm{d}t'}, \tag{4.8}$$

and reference voltage waveforms ($\boldsymbol{V_{ref(p),j}}$) are also calculated. If data from iteration j meets the current and error thresholds, all 20 of the excitation waveforms are stored in a data cluster with iteration index k.

In the above equations, the voltage divider gains (g_p) and shunt resistances ($R_{S(p)}$) were calibrated for each channel (p) of the FCS, using the procedures described in Appendix A. The number of turns (N_F), area (A_F) and matching parameter ($\mathcal{M}_p$)

must be measured for the feedback coils of the attached electromagnet[¶]. The $\overline{AI_{(p+3)}}$ term in equation (4.7) represents the mean value of $AI_{(p+3)}$ over one excitation period (i.e., the DC offset), and is subtracted since a DC value in the feedback coil voltage is non-physical.

Since waveforms are digitally sampled, integration in equation (4.8) is a numerical calculation. The subtracted integral is the mean flux density over one excitation period. This subtraction assumes that the flux waveform has no DC component, and eliminates the requirement that $\boldsymbol{B_{F(p),j}}$ at $t = 0$ be known.

[¶]The matching procedure for $\mathcal{M}_p$ compensates for variations in R_{F1} and R_{F2} as well as pickup coil alignment errors and errors in N_F. See Appendix D.4

Chapter 5

Tetrapole Probe Design

In Chapter 3, flux superposition from a tetrapole electromagnet, combined with a flux control system (FCS), was proposed as a means of achieving BN anisotropy measurements with no moving parts. This chapter presents the design process for a prototype BN probe, consisting of a tetrapole electromagnet and a BN sensor.

- In order to visualize and quantify the excitation field produced by a tetrapole, finite element models (FEM) of both the common backing (CB) and orthogonal U-core (OUC) designs shown in Figure 3.6 were developed and are presented in section 5.1. The OUC design is shown to be better suited for BN measurements on feeders, and to have a maximally uniform superposition region for a radius $< 2.5\,\text{mm}$ from the center of the sample surface.

- Section 5.2 presents a model for a BN sensor, consisting of a pickup coil with optional permeable and conductive components. The model is solved at several frequencies in the BN band, and a model configuration that uses a permeable core, permeable sheath, and conductive shield (the CSS configuration) is shown

to have a sensing radius of $\leq 2.4\,\text{mm}$ at frequencies $\geq 30\,\text{kHz}$. The field penetration in the CSS configuration is shown to follow the skin depth equations, and the complex inductance of the pickup assembly is evaluated between 1 kHz and 10 MHz.

- In Section 5.3, the OUC tetrapole and pickup assembly in the CSS configuration are combined to produce the spring-loaded tetrapole prototype (SL4P). The electrical properties of the SL4P are measured and compared with the model results.

5.1 Tetrapole FEM

This section presents results from *Infolytica MagNet® 6.25.0* finite element models (FEM) of the CB and OUC tetrapole geometries shown in Figure 3.6. The objective of the modelling was to visualize and quantify the excitation field in feeder steel produced by a tetrapole, and thereby inform tetrapole design. Flat samples were initially used to investigate tetrapole coupling without the added complexity introduced by feeder pipe curvature.

The CB design was the first design proposed, and was modelled on a 5 mm thick flat plate (CB-P model). CB-P model results are presented in Section 5.1.1. Due to the complexity and small dimensions of the CB design, the CB cores were modelled using ferrite, which is shown to have too low a saturation flux density to maximize the BN response in feeders. The CB model also shows that tetrapole field uniformity is improved by introducing fixed lift-off to all poles.

The OUC design was proposed to facilitate core manufacturing from high saturation flux laminated alloys and overcome the limitations of ferrite. The OUC design was modelled using Supermendur* cores on a 5 mm plate (OUC-P model), and on a 7 mm thick sample matching the extrados curvature of a nominal 63.5 mm feeder pipe with a 95.25 mm bend radius (OUC-F model). The OUC-P and OUC-F models are presented in Sections 5.1.2 and 5.1.3, respectively. Lift-off effects, superposition, and penetration of the excitation field are evaluated. A region of maximum field uniformity centered between the poles with a radius of 2.5 mm is identified.

In order to approximate the response of feeder pipe steel, SA-106 grade B magnetic properties were estimated experimentally in Appendix B, and used to create a user-defined *MagNet* material. *MagNet* materials were also defined for the ferrite and Supermendur cores of the CB and OUC tetrapoles, respectively. Custom *MagNet* material definitions are provided in Appendix C.1.

The FCS circuit was modelled in *MagNet* by driving the feedback coils (F(p)) with null-current sources, and the excitation coils (ex(p)) with voltage and/or current sources. Models were run using the time harmonic field solver with solution frequency f_{ex}. Since the time harmonic solver produces pure AC fields, the RMS voltage across F(p) ($V_{F(p)rms}$) is related to the RMS flux density in F(p) ($B_{F(p)rms}$) by:

$$B_{F(p)rms} = \frac{V_{F(p)rms}}{2\pi f_{ex} N_F A_F}, \tag{5.1}$$

*'Supermendur' is the discontinued product name from *Carpenter Technologies* for a 49% Co - 49% Fe - 2% V alloy with a 2.4 T staturation flux density.

and the voltage phase ($\phi_{V_{F(p)}}$) is related to the flux density phase ($\phi_{B_{F(p)}}$) by:

$$\phi_{V_{F(p)}} = \phi_{B_{F(p)}} + \frac{\pi}{2}. \tag{5.2}$$

FCS operation was emulated by specifying $B_{F(p)rms}$ and $\phi_{B_{F(p)}}$, solving the model, and iteratively adjusting the excitation voltage (or current) amplitude and phase until the appropriate $V_{F(p)rms}$ and $\phi_{V_{F(p)}}$ were produced. Meshing requirements were relaxed to speed model convergence between iterations, and then increased once an approximate solution was achieved.

5.1.1 Common Backing on Plate (CB-P)

The geometry of the CB-P finite element model is shown in Figure 5.1a. The CB-P model consists of four 5 mm diameter ferrite poles magnetically coupled through a 4 mm thick ferrite backing. On each pole there is a 300 turn multi-terminal copper excitation coil, and a 50 turn copper feedback coil. The tetrapole magnet is placed above a 5 mm thick circular SA-106 grade B plate, and surrounded by air. Both the sample and air box are divided into high resolution (HR) and low resolution (LR) sections to allow mesh refinement in the regions of interest. Exact CB-P model dimensions are provided in Appendix C.2.

Figure 5.1b shows a typical CB-P solution mesh. Meshing was refined in the cores and HR air box by setting maximum element sizes of 1 mm and 0.5 mm, respectively. The HR sample volume was meshed in ten 0.25 mm layers to a depth of 2.5 mm, followed by three 0.5 mm layers and one 1 mm layer. No mesh restrictions were placed on the LR sample, the backing plate, or the LR air box.

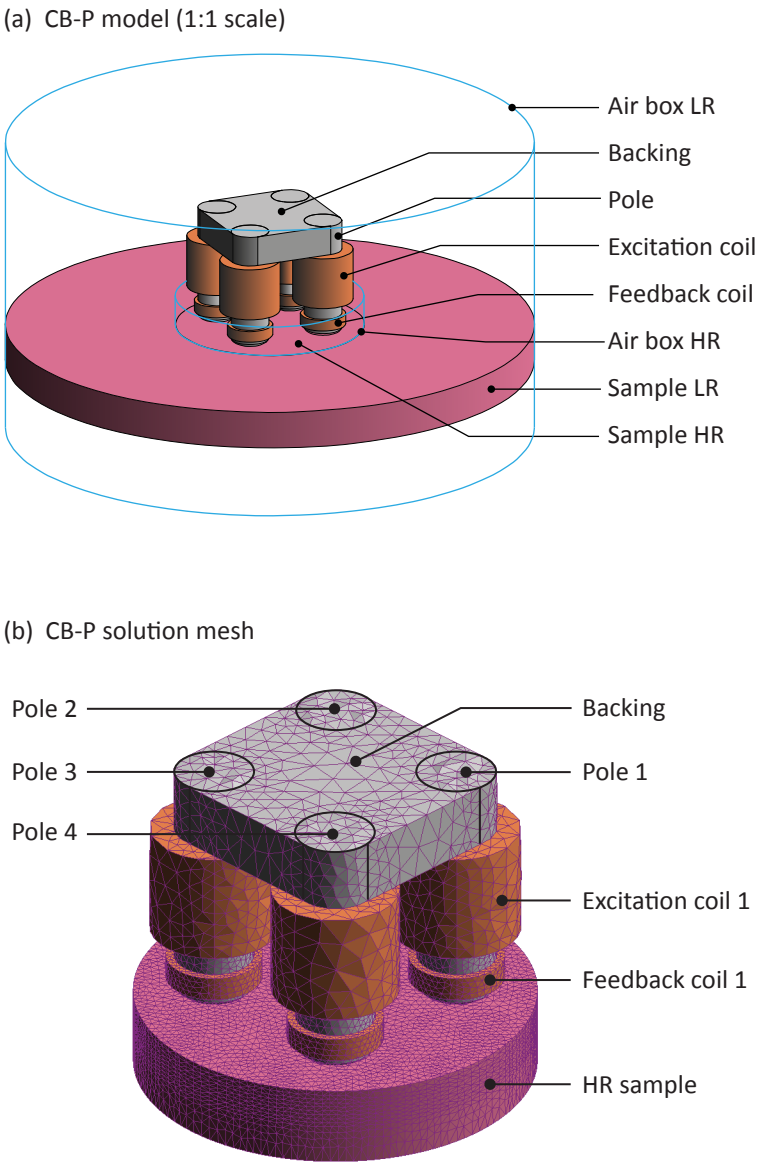

Figure 5.1: CB-P (a) model configuration and (b) typical solution mesh. Air boxes and LR sample are not shown in (b).

CB-P Air Gap Effects

Using $f_{ex} = 30\,\text{Hz}$, the CB-P model was solved for a variety of air gap configurations. In all cases, the feedback coil was considered fixed to the poles. For example, if an air gap of 0.1 mm is introduced between a pole and the sample, the feedback coil is also raised 0.1 mm. The position of the excitation coils and backing plate was not changed with respect to the sample. Target feedback coil voltages were specified as $39.4\,\text{mV}_{\text{rms}}$ across F1 and F3, and $0\,\text{mV}_{\text{rms}}$ across F2 and F4. This was intended to produce a sample field similar to that of a single U-core, with a peak flux density of 301 mT through the feedback coils.

Figure 5.2 shows the RMS flux density (B_{rms}) at the sample surface for the different air gap configurations, with B_{rms} calculated as:

$$B_{rms} = \left(\sum_{j=x,y,z} B_{jrms}^2 \right)^{\frac{1}{2}}, \tag{5.3}$$

where B_{jrms} is the rms amplitude of the j^{th} component of $\vec{B}$. For completeness, the voltage across and current through the excitation and feedback coils for each solution in Figure 5.2 are presented in Tables C.4 and C.5 in Appendix C.2.

Figure 5.2a shows the surface excitation field solution with all poles in direct contact with the sample. As is expected from the dipole-type excitation field, the field orientation in the center of the sample is aligned along the $\hat{x}$ direction between poles 1 and 3. B_{rms} has maxima at the interfaces between poles 1 and 3 and the sample. Between poles 1 and 3, the flux diverges in the $\hat{y}$ direction. While no flux passes through F2 and F4 due to the FCS operation, Figure 5.2a shows that the field couples into the bottom of poles 2 and 4, leaking out of the sample and producing a

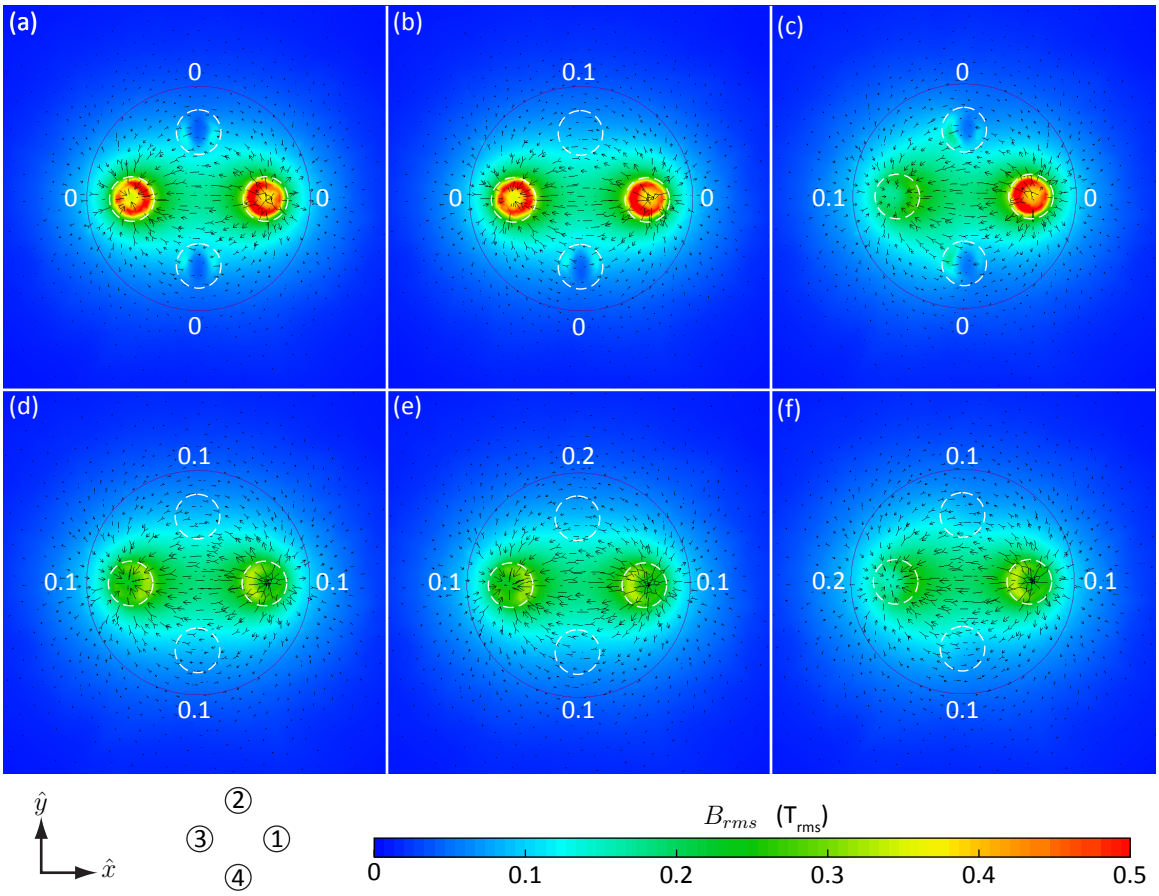

Figure 5.2: CB-P sample surface flux density (B_{rms}) plots for different air gap configurations. Pole locations are indicated by dashed white circles, and corresponding air gaps are indicated in mm.

perturbation to the field that would not be present with a single U-core electromagnet.

Figure 5.2b shows the surface excitation field solution with a 0.1 mm air gap between pole 2 and the sample surface, and the other three poles in direct contact. Comparing Figures 5.2a and 5.2b shows that the air gap under pole 2 in 5.2b reduces the flux leakage and improves the field uniformity in the pole 2 region.

Figure 5.2c shows the surface excitation field solution with a 0.1 mm air gap introduced between pole 3, one of the driving poles, and the sample. In this configuration,

the coupling of pole 3 is significantly reduced from the model configurations in Figures 5.2a and 5.2b, and several flux feedback iterations were required. Referring to Table C.4c in Appendix C.2, the voltages across F1 and F3 were matched to within $0.4\,\mathrm{mV_{rms}}$ and 0.6°, while there was a non-negligible voltage of $3.7\,\mathrm{mV_{rms}}$ across F2 and F4. A non-zero voltage across $ex2$ and $ex4$ would have been required to zero the flux through F2 and F4 and replicate the FCS operation. Even though the FCS operation was not exactly replicated, it can be seen in Figure 5.2c that the field at the sample center is similar to that in Figures 5.2a and 5.2b.

Figure 5.2d shows the surface excitation field solution with 0.1 mm air gaps under each pole. Comparing Figure 5.2d to Figure 5.2a shows that the flux concentration at the sample pole-interface is significantly reduced by the air gaps, as are the flux leakage effects at poles 2 and 4. Due to the FCS operation, the flux at the sample center is similar between Figures 5.2a and 5.2d.

In Figure 5.2e, a 0.2 mm air gap is introduced under pole 2 while 0.1 mm gaps are present under the other three poles. The larger gap on pole 2 in Figure 5.2e has no notable effects when compared to Figure 5.2d. This indicates that a uniform air gap between all the poles is desirable for tetrapole applications, as this will improve measurement repeatability even when the coupling of non-driving poles is varied.

In Figure 5.2f, a 0.2 mm air gap is introduced under the driving pole 3, while 0.1 mm gaps are present under the other three poles. Figure 5.2f does show some decrease in the surface field under pole 3 when compared with Figure 5.2d, however this difference is smaller than that shown between Figures 5.2a and 5.2c. Figure 5.2f also shows significantly less coupling into poles 2 and 4 when compared to Figure 5.2c, which is confirmed in Table C.5f, where only $1.8\,\mathrm{mV_{rms}}$ is across F2 and F4. This

indicates that decoupling of poles by the introduction of uniform air gaps reduces the requirements on the FCS operation, and may also allow for higher FCS gains, leading to smaller errors and convergence times.

CB-P BN Performance

The full BN response of a material is produced by taking a sample from a saturated single domain state, through the domain wall creation, rotation, wall movement, and annihilation processes, and then back to a single domain state in the opposite orientation. The fraction of the total BN response a given electromagnet can produce can therefore be estimated from the peak flux density the magnet can induce in the sample. Under time harmonic conditions, the peak flux density is equal to $\sqrt{2}B_{rms}$.

In SA-106 grade B steel, saturation effects begin to dominate the magnetic response at $\sim 1.5\,\mathrm{T}$. Ferrite saturates at 0.5 T. The CB-P model solutions in Figure 5.2 produced a peak flux density in F1 and F3 of 301 mT. Thus the model magnet is operating at $\sim 60\%$ of saturation. In the uniform 0.1 mm air gap solution in Figure 5.2d, the peak flux density at the center of the sample surface was 261 mT, only 17% of the sample's total BN response assuming 1.5 T saturation.

Let it be assumed that the field at the sample center is linearly proportional to the flux in the feedback coils. Under this assumption, if the ferrite CB tetrapole cores were magnetised to full saturation at 0.5 T, then the peak field at the sample center would be 0.44 T, or 29% of the flux density required to saturate the sample surface. It may therefore be concluded that ferrite cores in the CB geometry can produce up to 29% of the total BN response in a 5 mm thick plate with $f_{ex} = 30\,\mathrm{Hz}$.

CB-P Results Summary

In summary, the CB-P model solutions in Figure 5.2 show that the deliberate introduction of air gaps under all poles improves field uniformity, reduces FCS errors, and is therefore recommended for all tetrapole implementations. However, the CB tetrapole design is limited by the saturation flux density ferrite. In order to increase the measurable BN response from the sample, switching from ferrite to a laminated ferromagnetic alloy with a saturation flux density $> 0.5\,\mathrm{T}$ is required.

5.1.2 Orthogonal U-cores on Plate (OUC-P)

Since the CB tetrapole design cannot be feasibly constructed from laminated ferromagnetic alloys, the orthogonal U-core (OUC) tetrapole design was proposed. In this section, the OUC geometry is modelled using Supermendur cores on 5 mm thick plate (OUC-P model), with the configuration shown in Figure 5.3a.

Figure 5.3a shows that the OUC-P model consists of two orthogonal Supermendur U-cores with a cross sectional area of $4.25\,\mathrm{mm} \times 9.75\,\mathrm{mm}$. The taller of the two cores is parallel to $\hat{x}$, while the shorter core is parallel to $\hat{y}$. On each pole there is a 600 turn multi-terminal excitation coil, and a 50 turn feedback coil, both modelled as copper. The tetrapole magnet is placed 0.25 mm above a 5 mm thick circular plate of SA-106 grade B material, and surrounded by air. Both the sample and air box are divided into high resolution (HR) and low resolution (LR) sections to allow mesh refinement in the regions of interest. Exact OUC-P model dimensions are provided in Appendix C.3.

Figure 5.3b shows a solution mesh for the UCP model. Meshing was refined in the cores and HR air box by setting maximum element sizes of 1.5 mm and 0.75 mm

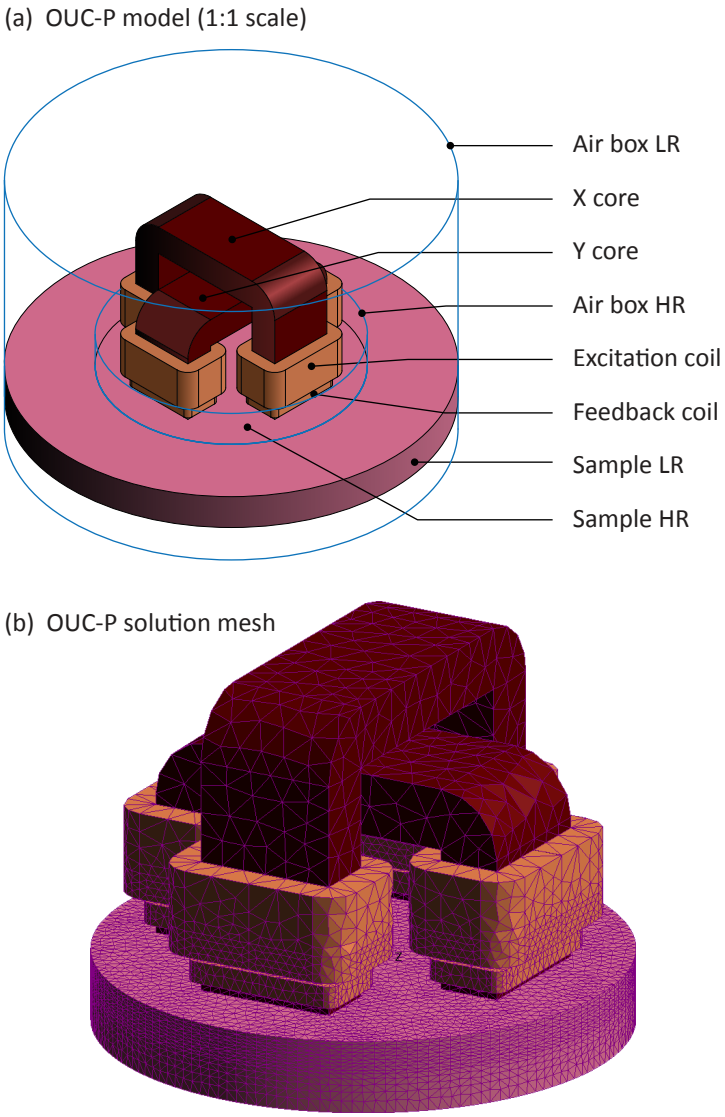

Figure 5.3: OUC-P (a) model configuration and (b) example solution mesh.

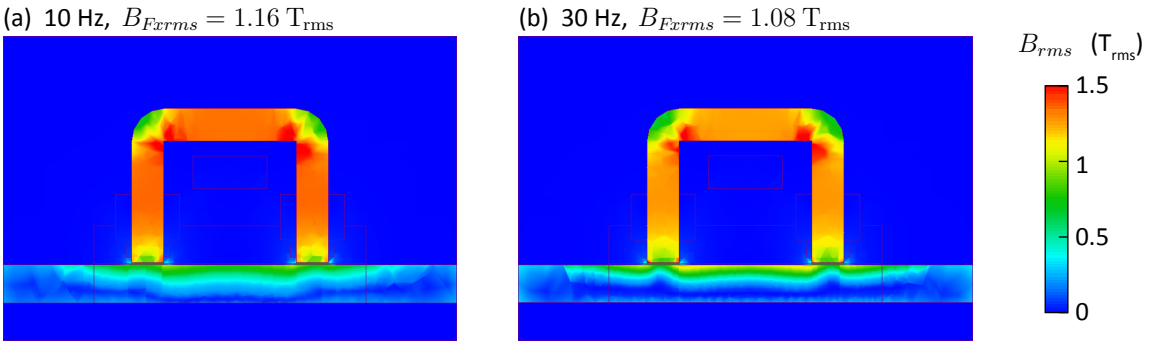

Figure 5.4: OUC-P model solution B_{rms} plots for f_{ex} values of (a) 10 Hz and (b) 30 Hz.

respectively. The HR sample was meshed in ten 0.25 mm layers to a depth of 2.5 mm, followed by three 0.5 mm layers and one 1 mm layer. No mesh restrictions were placed on the LR sample, the backing plate, or the LR air box.

OUC-P Excitation Frequency Effects

The effect of the excitation frequency (f_{ex}) on the sample field distribution was estimated by solving the OUC-P model at 10 Hz and 30 Hz. In order to produce comparable fields at both frequencies, excitation coil voltages were chosen to set the average RMS flux density through F1 and F3 (B_{Fxrms}) equal to 1.16 $\mathrm{T_{rms}}$ at 10 Hz, and 1.08 $\mathrm{T_{rms}}$ at 30 Hz, with an average RMS flux density through F2 and F4 (B_{Fyrms}) equal to $\sim 0\ \mathrm{T_{rms}}$. Figures 5.4a and 5.4b show model solution B_{rms} plots for slices at $y = 0$. For completeness, coil currents and voltages are presented in Table C.6 in Appendix C.3.

Comparison between Figures 5.4a and 5.4b shows that the increased B_{Fxrms} at 10 Hz produced higher B_{rms} in the X core, and that the field penetration into the sample is deeper for 10 Hz than for 30 Hz. Despite the increased core B_{rms} at 10 Hz, Figure 5.4 shows a higher sample surface B_{rms} at 30 Hz. This behaviour is explained

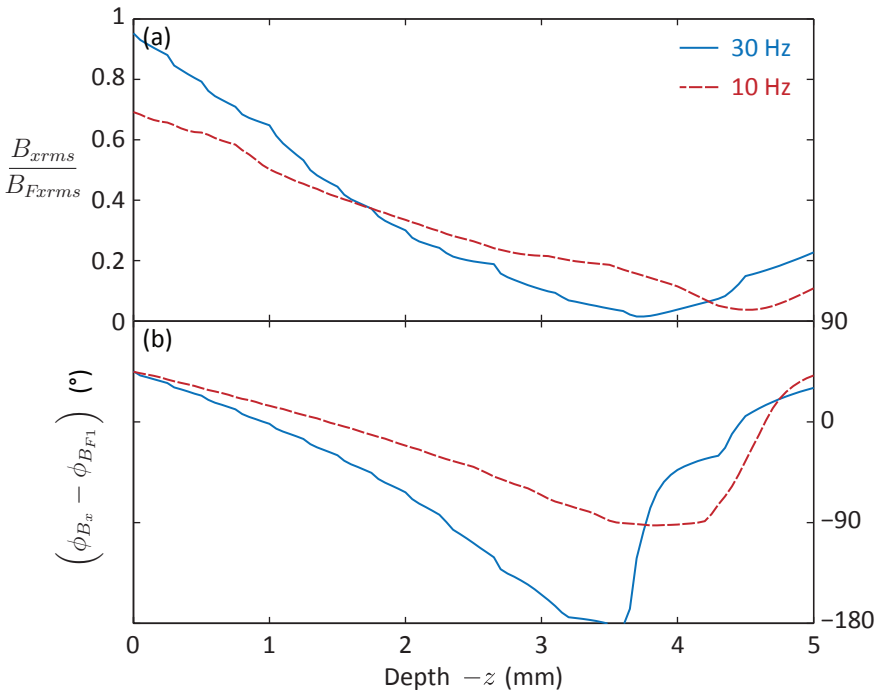

Figure 5.5: OUC-P model solution B_x (a) RMS magnitude normalized with respect to B_{Fxrms} and (b) phase relative to $\phi_{B_{F1}}$ as a function of z for f_{ex} values of 10 Hz and 30 Hz.

with the field attenuation solutions for good conductors, which require the skin depth (δ_{ex}) to decrease with increasing f_{ex}. Since total flux in the sample is approximately equal to the flux through the feedback coils (in this case $B_{Fxrms}A_F$), as f_{ex} increases the same flux passes through a smaller volume, driving the surface flux density higher.

To illustrate the time dependence of the field, Figure 5.5 shows the model solutions for B_x (the x component of $\vec{B}$) as a function of depth ($-z$) at the center of the sample surface for f_{ex} values of 10 Hz and 30 Hz. Figure 5.5a shows the RMS magnitude of B_x (B_{xrms}) normalized with respect to B_{Fxrms}, while Figure 5.5b shows the phase of B_x (ϕ_{B_x}) relative to $\phi_{B_{F1}}$.

Figure 5.5a shows that the normalized field at the sample surface is $\sim 30\%$ higher at 30 Hz than at 10 Hz, and attenuates at depth. The attenuation is not exponential,

as would be predicted by the skin depth equations, due to the non-linearity of sample magnetisation curve. Figure 5.5a also shows that B_{xrms} increases for $-z > 4\,\text{mm}$. This increase in B_{xrms} at depth is due to boundary effects and the limited spatial extent of the model, and is not likely to occur in feeder geometries.

Figure 5.5b shows that ϕ_{B_x} at the sample surface leads $\phi_{B_{F1}}$ by $\sim 45°$ at both f_{ex} values, and decreases at depth. Since the excitation field propagates from the surface into the sample, ϕ_{B_x} at the sample surface must lead $\phi_{B_{F1}}$, which is the average phase of the directly coupled field. The rate of the phase decrease with depth is higher for 30 Hz than at 10 Hz, indicating the increase in the phase velocity with f_{ex}.

OUC-P Field Uniformity

The sample field uniformity was examined using the OUC-P with four excitation field configurations at $f_{ex} = 30\,\text{Hz}$:

- driving along the X core,
- driving along the Y core,
- driving along the X core with different air gaps under poles 1 and 3, achieved by tilting the X core 1° about $\hat{y}$,
- and driving along both X and Y cores to create a superposition field with a target orientation $\theta_F = \arctan\left(B_{Fyrms}/B_{Fxrms}\right) = 30.9°$.

Figure 5.6 shows the OUC-P model solutions for B_{rms} at the sample surface for the four excitation field configurations. Figure 5.6a is the surface field solution for the 30 Hz model presented in Figure 5.4b, with corresponding coil voltages and currents

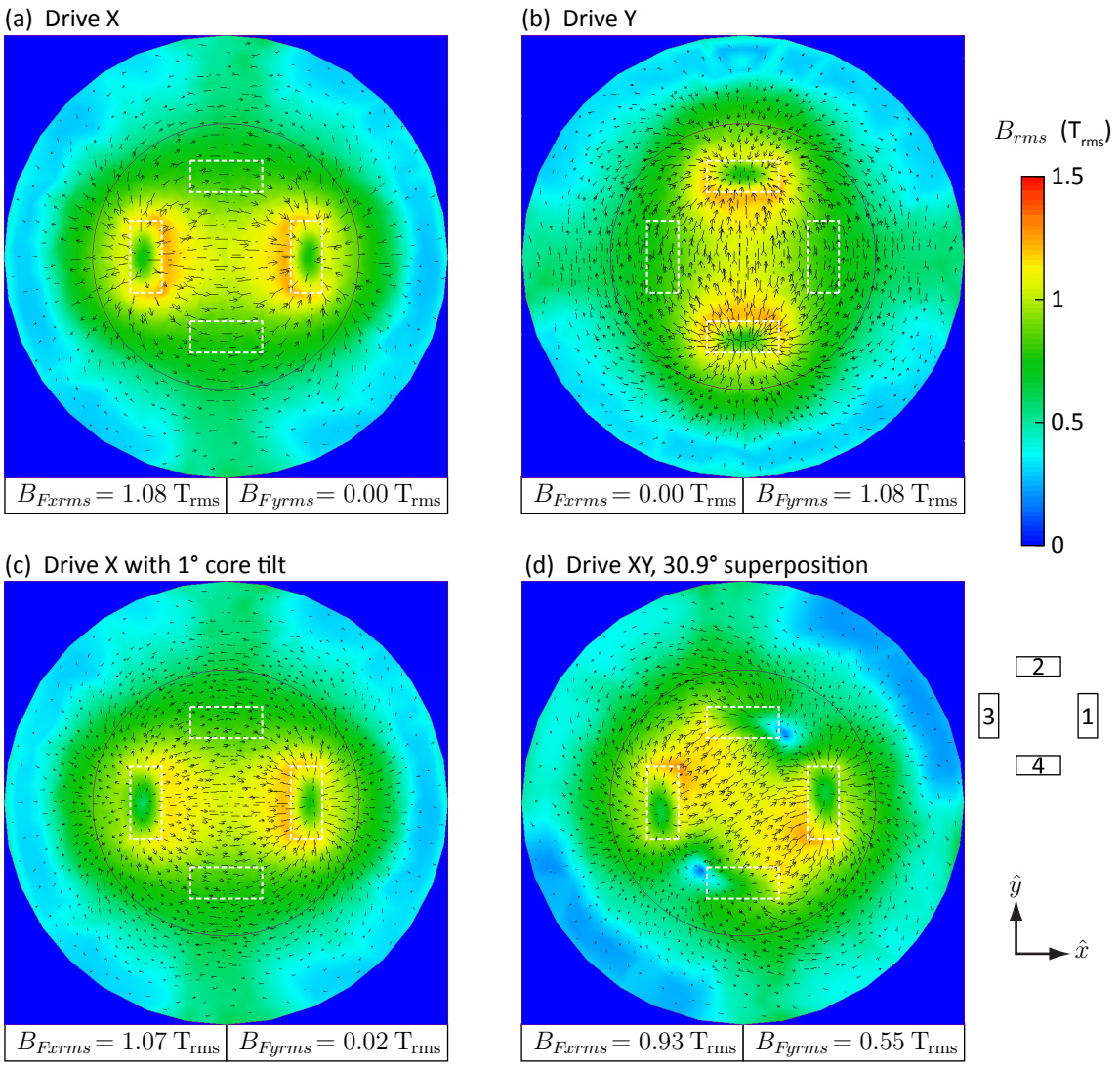

Figure 5.6: OUC-P model surface field solutions driving along the (a) X axis, (b) Y-axis, (c) X-axis with 1° core tilt, and (d) X and Y axes with $\theta_F = 30.9°$. B_{Fxrms} and B_{Fyrms} are indicated for each plot.

in Table C.6b. Coil currents and voltages for the other three excitation configurations are provided in Table C.7.

To assess field uniformity in the sample for the OUC-P model, the area-weighted mean and standard deviation of B_{rms} at the sample surface were estimated within

a radial distance (r) from the center of the sample surface. The same was done for the flux density phase (ϕ_B). B_{rms} values were then normalized with respect to the RMS flux density through the feedback coils ($B_{Frms} = \sqrt{B_{Fxrms}^2 + B_{Fyrms}^2}$), while ϕ_B values were referenced to the flux phase through the dominant feedback coil ($\phi_{B_{F1}}$ when driving the X core, $\phi_{B_{F2}}$ when driving the Y core). Figure 5.7 shows the area-weighted mean and standard deviation of the normalized B_{rms} and referenced ϕ_B for the four excitation configurations in Figure 5.6.

Figure 5.7 shows that the normalized B_{rms} and referenced ϕ_B are consistent between the 'drive X' and 'drive Y' models. This indicates that, provided feedback coils are identically matched and aligned with the cores, FCS operation compensates for difference in length of the X and Y cores for the OUC tetrapole design. Figure 5.7aii shows that the field is maximally uniform for $r < 2.5\,\text{mm}$, and decreases in uniformity toward the poles. For all the OUC-P excitation configurations in Figure 5.6, Figure 5.7b shows that ϕ_B consistently leads the flux in the feedback coils by 45° at the sample surface for $r < 7\,\text{mm}$, and diverges at the poles.

Figure 5.7ai shows that the introduction of asymmetric air gaps by tilting the X core resulted in a systematic increase in the normalized B_{rms} by $\sim 2\%$. Table C.7d indicates that there was a 1.4% mismatch between B_{F1rms} and B_{F3rms}, as well as a $0.02\,\text{T}_{\text{rms}}$ flux through F2 and F4. Since these are effectively errors in FCS operation on the order of 2%, these results cannot provide significant insight into whether perfect FCS operation would match the 'drive X' and 'drive Y' model solutions. Moreover, if the standard deviations in Figure 5.7aii are taken as uncertainties on the mean B_{rms}/B_{Frms} in Figure 5.7ai, then the fields for the 'drive X,' 'drive Y,' and 'drive X with 1° core tilt' are consistent.

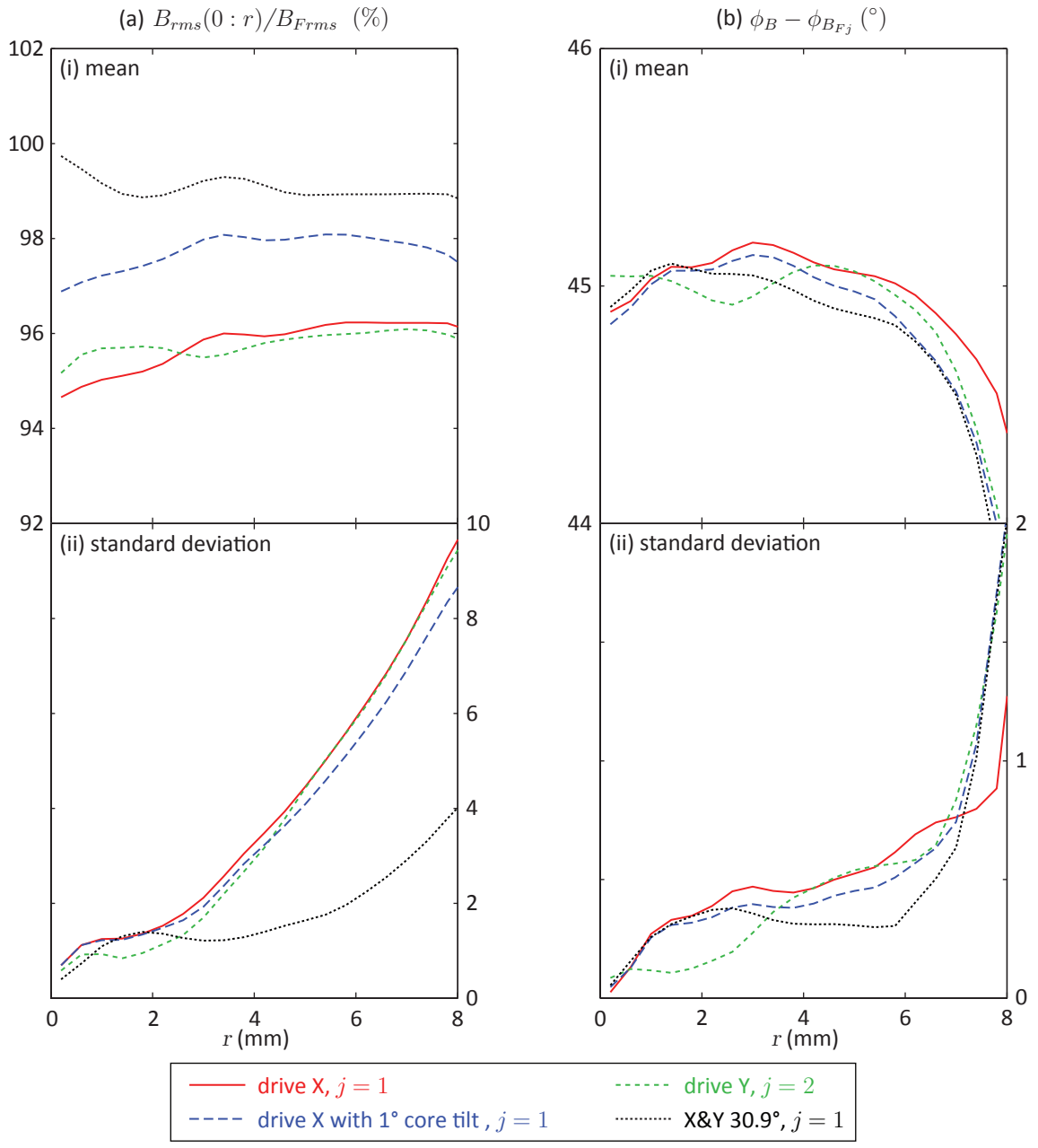

Figure 5.7: OUC-P model solution (a) normalized B_{rms} and (b) referenced ϕ_B area-weighted (i) means and (ii) standard deviations within a radius r from the center of the sample surface.

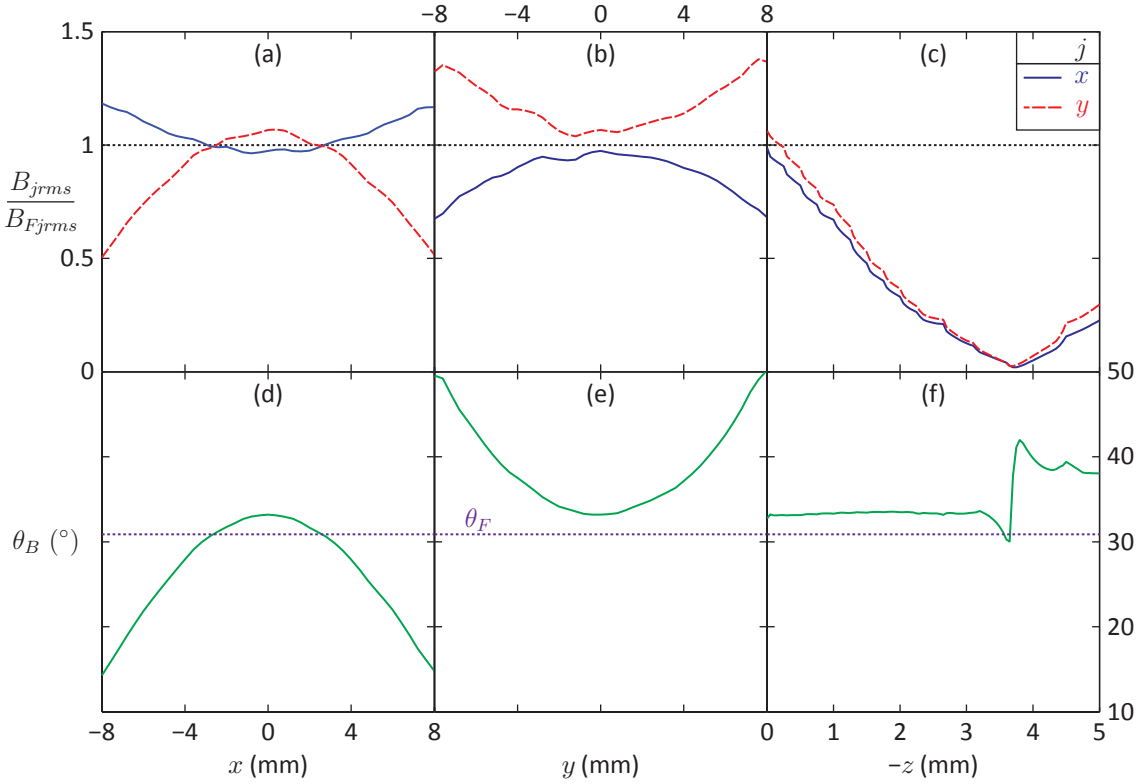

Figure 5.8: OUC-P $\theta_F = 30.9°$ model solution normalized B_{xrms} and B_{yrms}, and θ_B along (a,d) $\hat{x}$, (b,e) $\hat{y}$ and (c,d) $\hat{z}$ with $(x, y, z) = (0, 0, 0)$ being the center of the sample surface.

Figure 5.7ai also shows a $\sim 4\%$ increase in the normalized B_{rms} under the 30.9° superposition conditions corresponding to the model solution in Figure 5.6d. This is a result of non-linear superposition, and is discussed below.

OUC-P Superposition Effects

To assist in further interpretation of the $\theta_F = 30.9°$ superposition OUC-P model solution, Figure 5.8 shows the solutions for B_{xrms} and B_{yrms}, normalized with respect to B_{Fxrms} and B_{Fyrms}, and $\theta_B = \arctan(B_{yrms}/B_{xrms})$ along $\hat{x}$, $\hat{y}$, and $\hat{z}$, with $(x, y, z) = (0, 0, 0)$ defined as the center of the sample surface.

Since the X core induces flux primarily in the $\hat{x}$ direction, B_{xrms} is maximum

near the X core poles, and Figure 5.8a shows B_{xrms}/B_{Fxrms} increasing with $|x|$. The flux induced by the X core diverges in the $\hat{y}$ direction, and Figure 5.8b shows B_{xrms}/B_{Fxrms} decreasing with $|y|$. This 'saddle' pattern is typical of the flux distribution introduced by a dipole electromagnet. Similarly, Figures 5.8b and 5.8a show B_{yrms}/B_{Fyrms} increasing with $|y|$ and decreasing with $|x|$, respectively. This superposition of two dipole patterns leads to larger B_{xrms}/B_{Fxrms} near poles 1 and 3, and larger B_{yrms}/B_{Fyrms} near poles 2 and 4. As a result of the superposition, Figures 5.8d and 5.8e respectively show θ_B decreasing toward the X core poles and increasing toward the Y core poles.

Figures 5.8a, 5.8b, and 5.8c show that $B_{yrms}/B_{Fyrms} > B_{xrms}/B_{Fxrms}$ at the center of the sample surface. This leads to θ_B being larger than θ_F near the model origin, as shown in Figures 5.8d, 5.8e, and 5.8f. This is a nonlinear superposition effect that occurs because the sample is more saturated along $\hat{x}$. As the sample saturates in a given orientation, the reluctance increases along that orientation and additional flux is diverted elsewhere. Thus the ratio of B_{jrms} to B_{Fjrms} decreases for increasing B_{Fjrms}. Both B_{Fxrms} and B_{Fyrms} for the $\theta_F = 30.9°$ solution are less than B_{Fxrms} and B_{Fyrms} for the other three model solutions in Figure 5.6. Thus nonlinear superposition results in the elevated mean B_{rms}/B_{Frms} for $\theta_F = 30.9°$ solution, shown in Figure 5.7ai.

Figures 5.8c and 5.8f show that θ_B is approximately constant as a function of depth, up to $-z \approx 3\,\text{mm}$. This indicates that while the superposition is nonlinear due to saturation effects at the surface, the orientation at the surface is preserved as the field propagates into the sample. Variation in θ_B for $-z > 3\,\text{mm}$ is attributed to model boundary effects.

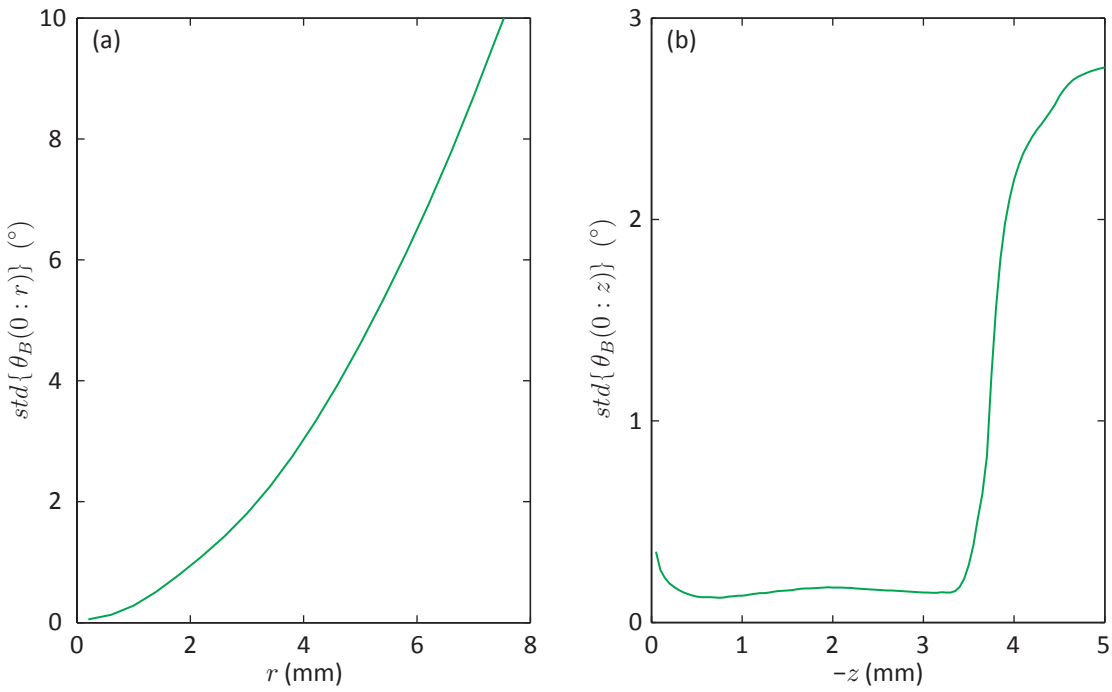

Figure 5.9: UCP model θ uniformity (a) at the sample surface and (b) at depth for $\theta_F = 30.8°$.

In order to estimate the uniformity of θ_B in the sample, the standard deviation of θ_B from the model origin to r (std $\{\theta_B(0:r))\}$) and z (std $\{\theta_B(0:z))\}$) is plotted in Figures 5.9a and 5.9b, respectively. Figure 5.9a shows that std $\{\theta_B(0:r))\}$ increases toward the poles, and is on the order of 1.4° for $r < 2.5\,\text{mm}$. Figure 5.9b shows that std $\{\theta_B(0:z)\}$ is approximately 0.2° for $-z < 3\,\text{mm}$. Boundary effects dominate Figure 5.9b for $-z > 3\,\text{mm}$.

OUC-P Results Summary

The OUC-P model showed that increasing f_{ex} while keeping B_{Frms} constant leads to increased sample surface flux densities and shallower excitation field penetration. The OUC-P model was tested to B_{Frms} values of $1.16\,\text{T}_{\text{rms}}$ and $1.08\,\text{T}_{\text{rms}}$ for f_{ex} values

of 10 Hz and 30 Hz, respectively. OUC-P solutions showed peak flux densities at the center of the sample surface of 1.16 T at 10 Hz and 1.52 T at 30 Hz. Therefore, the Supermendur cores in the OUC-P model are sufficient to produce the full BN response from the surface region of feeder pipe samples, provided f_{ex} is sufficiently large.

Solving the OUC-P model for different excitation configurations showed that FCS operation effectively compensates for the different core lengths of the OUC tetrapole, producing consistent sample fields when driving along either the X or Y core. FCS operation also produces consistent sample fields under 1° core tilt conditions, within the uncertainties of the OUC-P model solutions.

The OUC-P 30.9° superposition model showed that the ratio of B_{jrms}/B_{Fjrms} in the sample is a function of B_{Fjrms} due to saturation effects. For the $f_{ex} = 30$ Hz OUC-P model solutions, this resulted in a $\sim 4\%$ increase in B_{rms}/B_{Frms} in the $\theta_F = 30.9°$ superposition model compared to models where only one core was driven. Nonlinear superposition also produced a systematic deviation in θ_B from θ_F by $+2.5°$. To correct these errors, a mapping between B_{Fjrms} and B_{jrms} at the center of the sample surface may be required.

5.1.3 Orthogonal U-Cores on Feeder (OUC-F)

This section presents FEM solutions for the OUC tetrapole fields induced in a 7 mm thick sample with curvature matching that of a nominal 63.6 mm diameter feeder pipe with a 95.25 mm bend radius (the OUC-F model). Exact dimensions for the OUC-F model are provided in Appendix C.4.

As in previous models, both the sample and air box were divided into high resolution (HR) and low resolution (LR) sections to allow mesh refinement in the regions of

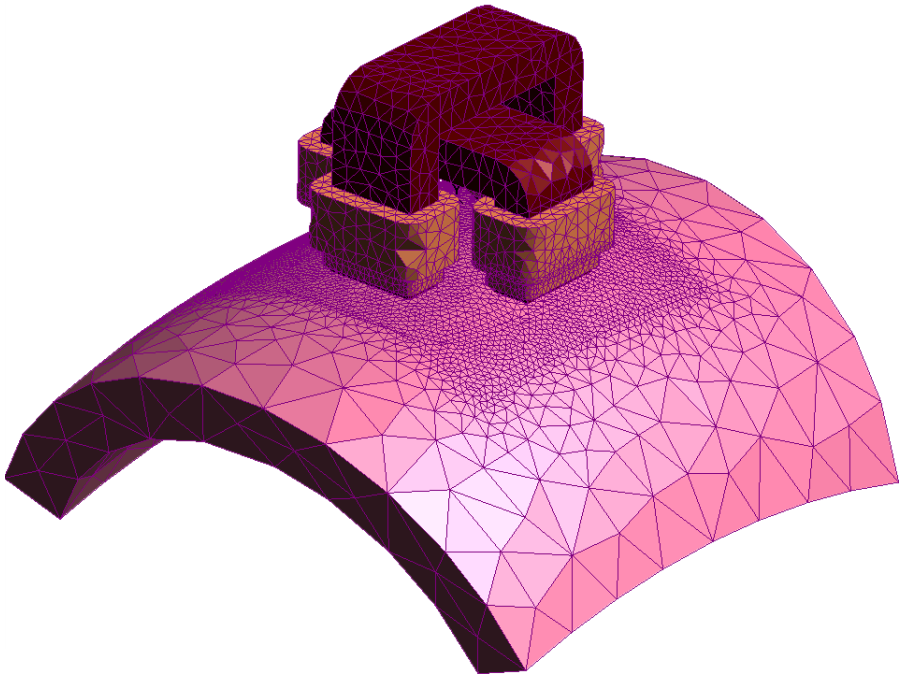

Figure 5.10: Example solution mesh for the UCF model, showing mesh refinement around the HR sample and poles. Air boxes are not shown.

interest. Figure 5.10 shows a solution mesh for the OUC-P model with the air boxes hidden. Meshing was refined in the cores, HR air box, and HR sample by setting maximum element sizes of 1.5 mm, 0.75 mm, and 0.75 mm, respectively.

Superposition in Feeders

In order to study field uniformity and superposition in the feeder geometry, the OUC-F model was solved with θ_F equal to 0°, 90° and 45°, with $B_{Frms} = 0.93\,\mathrm{T_{rms}}$. Figure 5.11 shows the resulting B_{rms} solutions at the sample surface. Corresponding coil voltages and currents are presented in Table C.8, in Appendix C.4.

Comparing Figures 5.11a and 5.11b shows that the X-core (aligned with the axial direction) couples more strongly to the sample than the Y-core (aligned with the hoop

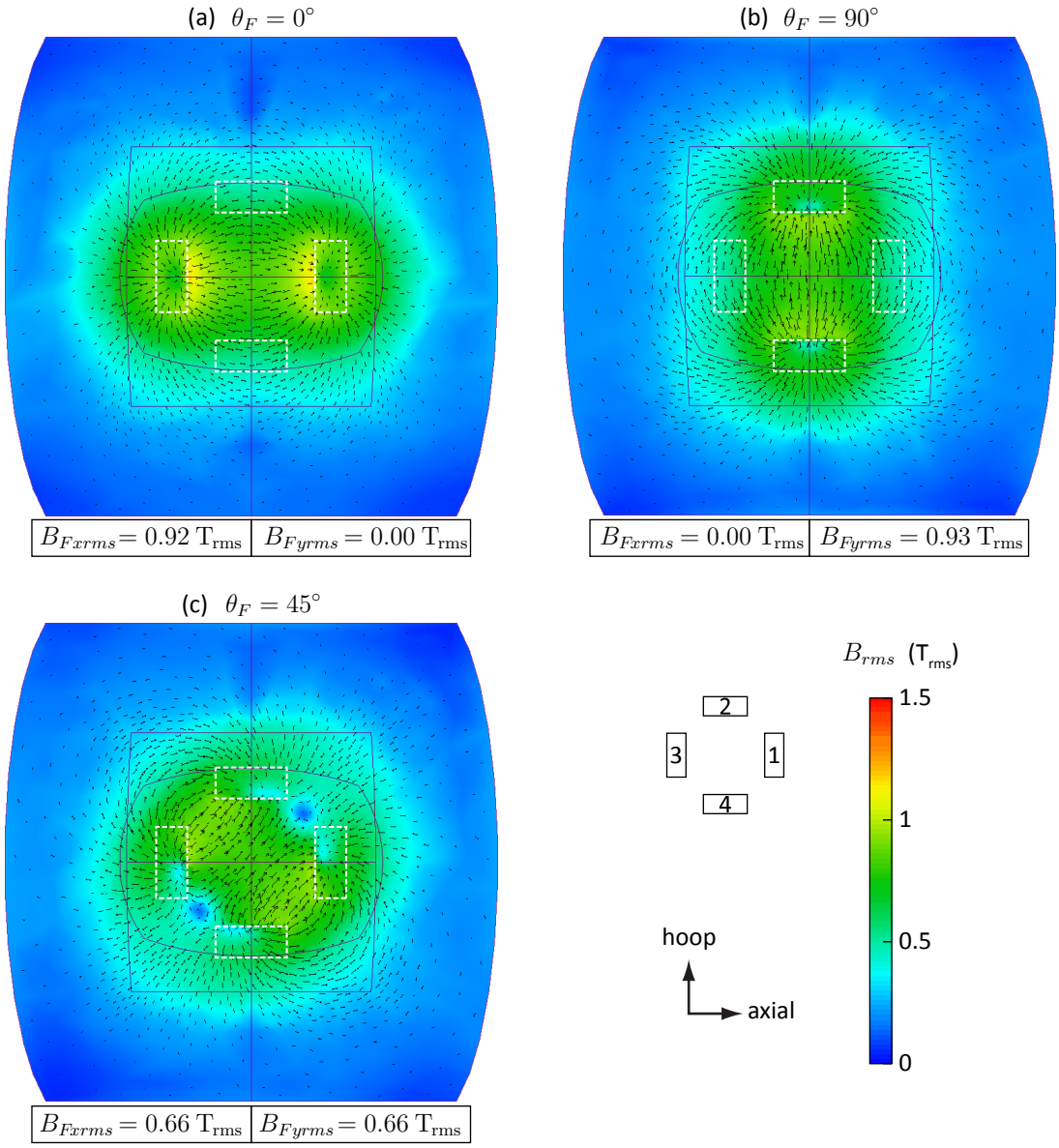

Figure 5.11: OUC-F solution B_{rms} plots for θ_F values of (a) 0°, (b) 90° and (c) 45°.

direction). However, in Figure 5.11c, stronger X core coupling is not apparent.

To assess field uniformity, B_{rms}/B_{Frms} and $\theta_B = \arctan\left(B_{hrms}/B_{arms}\right)$ were measured from the OUC-F solutions along the axial and hoop axes at the sample surface, where B_{arms} and B_{hrms} are respectively the RMS flux density of the axial and hoop components of $\vec{B}$. The area-weighted mean and standard deviation of B_{rms} and θ_B were then estimated as a function of distance from the center of the sample surface, and are presented in Figure 5.12.

Figure 5.12ai shows that the increased coupling of the X core results in a mean B_{rms}/B_{Frms} that is $\sim 4\%$ larger for $\theta_F = 0°$ than for the other two model solutions. Figure 5.12aii also shows increased field variation for $\theta_F = 0°$. However, Figure 5.12aii shows that the standard deviation of B_{rms}/B_{Frms} for $r < 3\,\text{mm}$ is approximately 2% and thus all solutions have consistent normalized field amplitudes.

Figure 5.12bi shows that there is a variation of the mean θ_B for θ_F values of 0° and 90°. Through symmetry of the OUC-F model, the mean $\theta_B(0:r)$ should be exactly 0° or 90° for θ_F values of 0° and 90°, respectively. Therefore the $\sim 1°$ standard deviation of θ_B shown in Figure 5.12bii is a result of meshing noise in the 3D finite element model.

Figure 5.12bi shows that the mean $\theta_B(0:r) - \theta_F$ is $\sim +2.5°$ for $\theta_F = 45°$. This is surprising, as the increased coupling of the X core would be expected to drive the mean $(\theta_B(0:r) - \theta_F)$ for small r to negative values. If the meshing noise is assumed to cause variations in θ_B by $\pm 1°$, then the superposition field is consistent with θ_F for all θ_F values modelled. Figure 5.12bii shows that the standard deviation of $\theta_B(0:r)$ increases significantly for $r > 2.5\,\text{mm}$ for $\theta_F = 45°$.

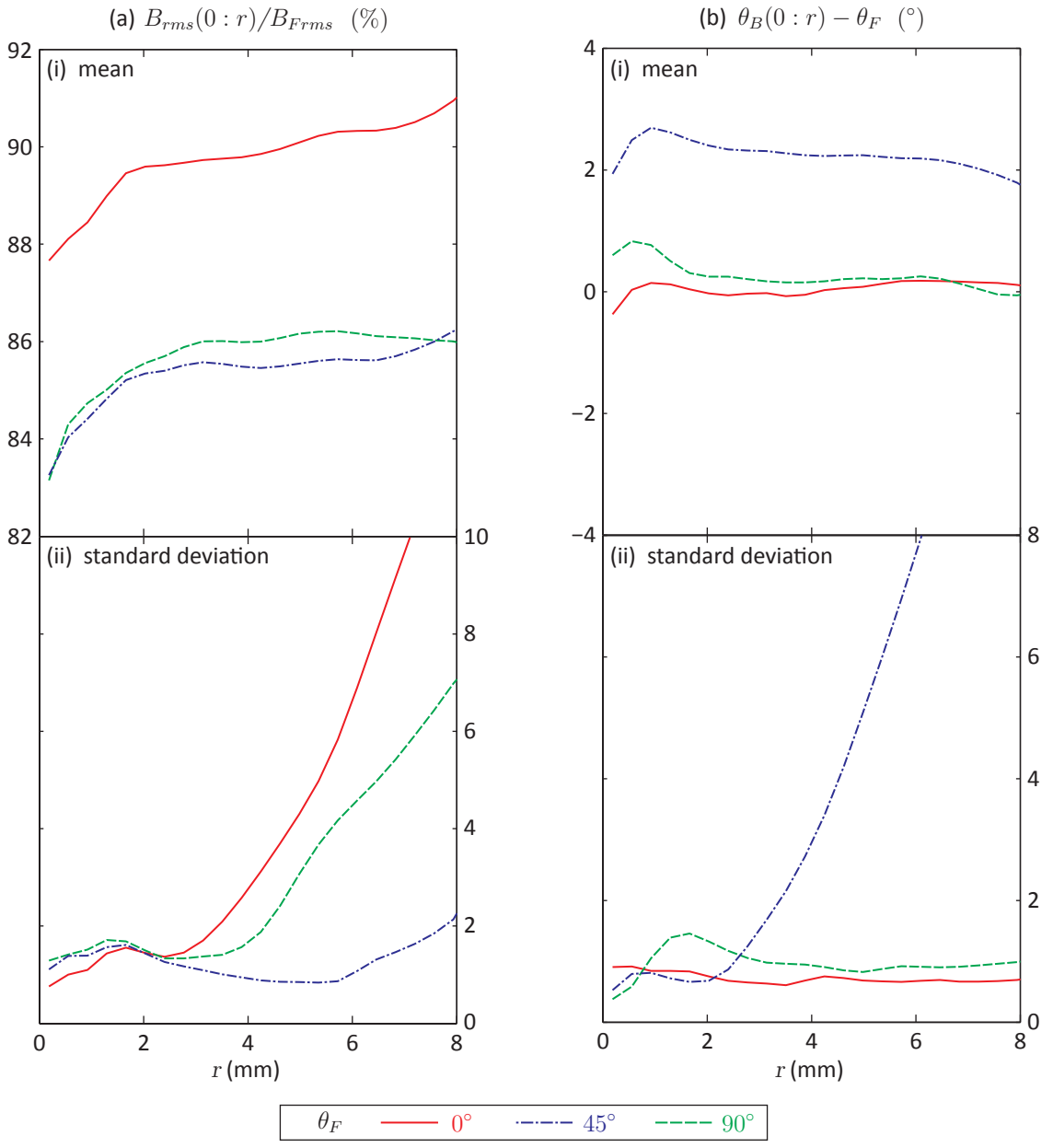

Figure 5.12: OUC-F model solution normalized (a) surface field magnitude (B_{rms}/B_{Frms}) and (b) orientation ($\theta_B - \theta_F$) area weighted (i) mean and (ii) standard deviation as a function of distance along the surface ($\sqrt{axial^2 + hoop^2}$) from the sample center for θ_F values of 0°, 45° and 90° with $B_{Frms} \approx 0.93\,\mathrm{T_{rms}}$.

OUC-F Results Summary

Surface field amplitudes in the OUC-F model solutions with $B_{Frms} = 0.93\,\mathrm{T_{rms}}$ and $f_{ex} = 30\,\mathrm{Hz}$ were self-consistent for varying θ_F. Surface field orientations in the OUC-F model solutions were consistent with θ_F. This indicates that a OUC tetrapole combined with a FCS sufficiently compensates for feeder curvature that BN measurements for varying θ_F can be compared with confidence that the magnetisation conditions are reproduced.

OUC-F model solutions showed maximum field amplitude uniformity ($\pm 2\%$) for $r < 3\,\mathrm{mm}$, and orientation uniformity ($\pm 1^\circ$) for $r < 2.5\,\mathrm{mm}$. This sets the desired sensing radius to $< 2.5\,\mathrm{mm}$ for a BN pickup coil coupled with the modelled OUC geometry, in order to avoid sampling BN events from the regions where the excitation field is not sufficiently uniform.

5.2 Pickup Assembly FEM

While numerous sensors may be used to detect BN, in order to have equal sensitivity to BN emissions from all field orientations, sensors coupled with tetrapoles must have cylindrical symmetry about the normal to the sample surface. This is achieved when using a multi-layer solenoid with the winding axis normal to the sample surface (henceforth 'pickup coil'). The sensing characteristics of a pickup coil depend on the coil geometry, the distribution of permeable and conductive material, and the frequency of the detected field. This section presents finite element modelling results from *Infolyitca MagNet*® that were used to inform the design a BN pickup assembly (PUA).

- Section 5.2.1 describes the PUA model configuration.
- In Section 5.2.2 the sensing area of the PUA model is evaluated for various combinations of a pickup coil with a permeable core, a permeable sheath, and a conductive shield. The combination of the core, sheath and shield (the CSS configuration) is shown to provide a sensing radius < 2.5 mm at 30 kHz for use with an OUC tetrapole.
- Section 5.2.2 presents field penentration profiles for the PUA in the CSS configuration for a variety of solution frequencies and sample permeabilities. It is shown that the field penetration follows the skin depth equations.
- In Section 5.2.4 the PUA model is used to evaluate the complex inductance of the pickup coil from 1 kHz to 10 MHz, taking eddy currents in the sample and shield, and the complex permeability of the core and sheath, into account.

In the time span between the modelling work done in Sections 5.2.3 and 5.2.4, *MagNet* went through a version change from *MagNet 6.25.0* to *MagNet 6.26.1*. To the author's knowledge, the version change had no effect on the model solutions.

5.2.1 PUA Model Configuration

Figure 5.13 shows the components of the PUA model. Targeting a 2.5 mm sensing radius, the PUA model was based on a 100 turn 1 mm ID, 3 mm OD copper coil. The coil was placed 0.1 mm above a 7 mm thick sample. To shape the field, an optional permeable core, permeable sheath, and conductive brass shield were added to the model. To precisely model the shallow penetration of high frequency fields, the sample was subdivided into high resolution (HR), medium resolution (MR) and

Table 5.1: PUA model user-defined *MagNet* materials. All materials have a relative permittivity equal to 1.

Material	Permeability (μ_0)	Conductivity (S/m)	PUA Component
SA106 μ_d 100	100	5.15×10^6	sample
SA106 μ_d 500	500	5.15×10^6	sample
SA106 μ_d 1500	1500	5.15×10^6	sample
SA106 μ_d 3000	3000	5.15×10^6	sample
Linear μ_d 2500	2500	0	core & sheath
Brass	0	1.25×10^7	shield

low resolution (LR) components. The air box was also subdivided into HR and LR components.

Invoking cylindrical symmetry would allow the PUA model in Figure 5.13 to be solved in 2D. However, since no 2D time-harmonic or transient solver was present in the licensed version of *MagNet*, the model had to be solved in 3D. To minimize computation time, the profile of Figure 5.13 was swept $\pm 1^\circ$ about the axis of cylindrical symmetry, and an even periodic boundary condition was applied.

It was assumed in the PUA model that the bulk differential permeability (μ_d) of all modelled materials does not significantly change due to a single Barkhausen event. This approximation allows the PUA to be modelled from linear materials. To model the sample properties at different magnetisations, several user-defined sample materials were created using the 5.15×10^6 S/m conductivity of SA-106 grade B and various linear permeabilities, which are given in Table 5.1. Additional user-defined materials included brass and the linear core and sheath material with $\mu_d = 2500$.

The time-harmonic solver was used to estimate the sample fields induced by a variety of PUA configurations and frequencies. Using the principle of reciprocity, the model field solutions were taken as a mapping of the PUA sensitivity at the solution frequency (f_{bn}). Solution frequencies were varied in the range between 3 kHz and

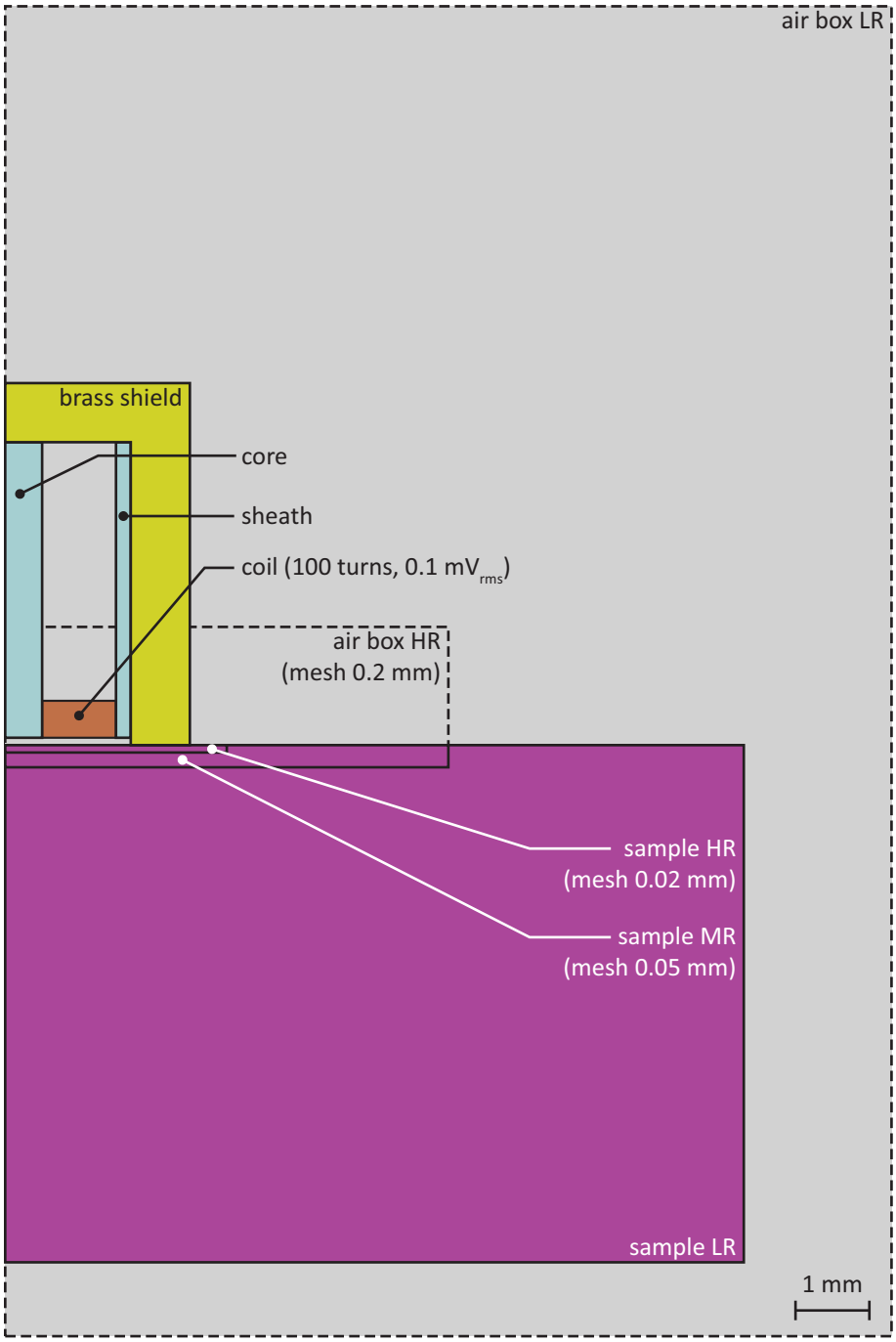

Figure 5.13: Drawing of the PUA model components, 10:1 scale. Maximum element sizes are indicated on component labels in which mesh refinement was used.

300 kHz, which is shown in Chapter 8 to represent the majority of the detected BN power spectrum.

5.2.2 PUA Area Sensitivity

The sensing radius of the PUA model can be varied by changing f_{bn}, enabling or disabling the permeable core, permeable sheath, and the conductive shield, and changing the sample permeability. To converge on a model configuration with the smallest sensing radius, $f_{bn} = 30\,\text{kHz}$ was chosen as a center frequency in the BN power spectrum, and the sample material was set to SA106 μ_d 3000, which corresponds to SA-106 grade B with a flux density of $\sim 0.2\,\text{T}$. All PUA model configurations were then solved with $0.1\,\text{mV}_{\text{rms}}$ across the pickup coil.

In order to quantify the sensing radius for the model solutions, $r \cdot B_{rms}$ at the sample surface was integrated with respect to r and normalized within 10 mm (the extent of the sample surface in the model) according to:

$$\psi = 100 \frac{\int_0^{r_\psi} (r' \cdot B_{rms})\,\mathrm{d}r'}{\int_0^{10} (r' \cdot B_{rms})\,\mathrm{d}r'}, \tag{5.4}$$

where r_ψ is the radius at which ψ percent of the total sensed field has been detected.

Figure 5.14 shows the surface B_{rms} solutions for the various combinations of the model components with $f_{bn} = 30\,\text{kHz}$. The radius at which 90% of the sensed field has been detected (r_{90}), is indicated in red for each of the plots.

Figure 5.14a shows the solution for the bare coil without any additional permeable or conductive material. The surface B_{rms} is zero at the center of the coil, maximized directly under the windings, and rolls off with increasing radius outside the coils

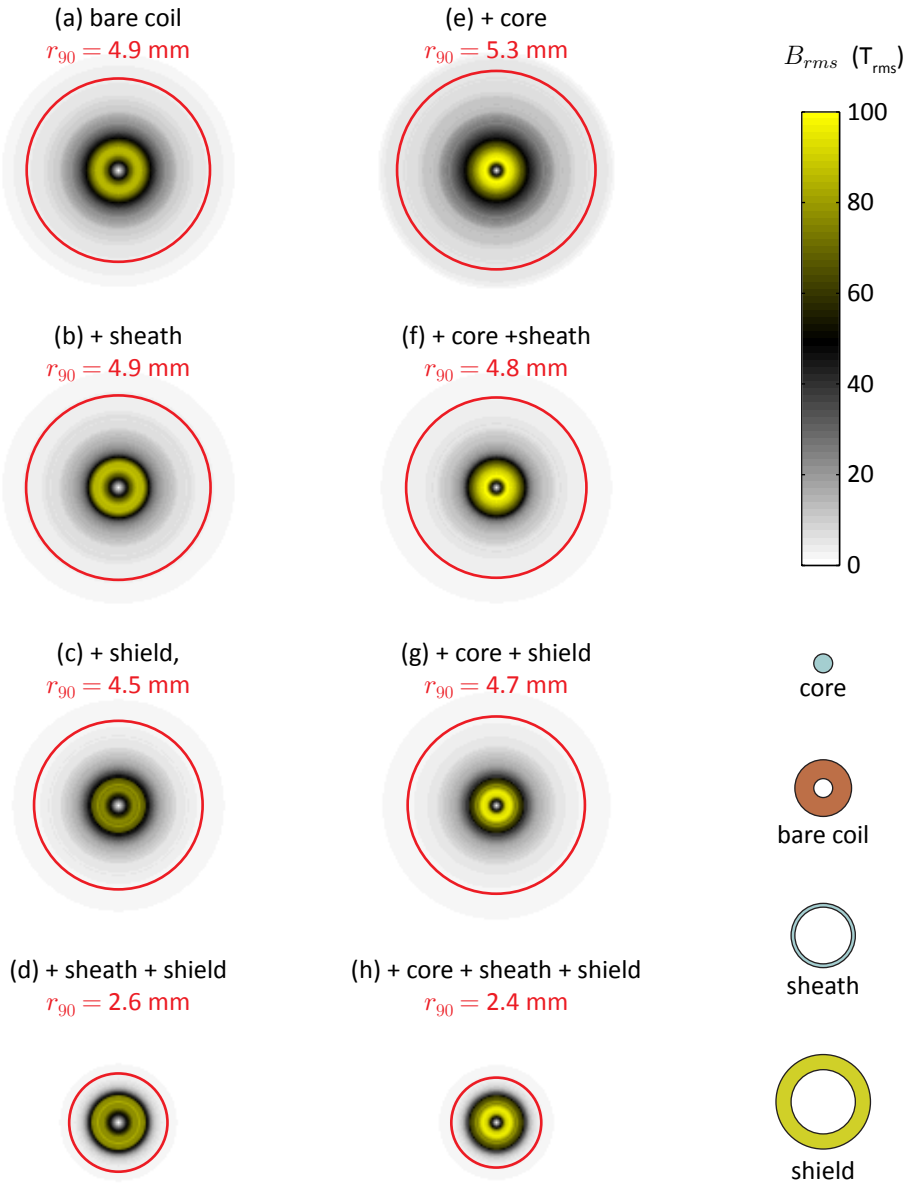

Figure 5.14: PUA model solution B_{rms} plots for different model configurations with $0.1\,\mathrm{mV_{rms}}$ across the coil and $f_{bn} = 30\,\mathrm{kHz}$. The 90% sensing radius (r_{90}) for each configuration is indicated in red. 2.5:1 scale.

physical diameter. The bare coil solution gives $r_{90} = 4.9\,\text{mm}$, which is 3.3× larger than the 1.5 mm outer radius of the coil windings. To produce a bare coil with $r_{90} = 2.5\,\text{mm}$ would require a coil with an outer radius of $\sim 0.77\,\text{mm}$.

In order to reduce the sensing radius without shrinking the coil size, the magnetic impedance for $r < 2.5\,\text{mm}$ must be reduced, and increased for $r > 2.5\,\text{mm}$. Figure 5.14b shows that the introduction of a permeable sheath at $r = 1.6\,\text{mm}$ increases B_{rms} underneath the outer windings of the coil by introducing a low impedance path at the sheath position. Figure 5.14c shows that the introduction of a brass shield decreases B_{rms} everywhere by attenuating flux both inside the shield propagating to larger radii, and flux outside the shield propagating to smaller radii. In Figure 5.14d, the combination of a permeable sheath and the brass shield reduces r_{90} to 2.6 mm.

In order to reduce r_{90} further requires concentration of the flux at small radii. This is achieved in Figure 5.14e by the introduction of a permeable core, which offers a low impedance path to the flux near the center of the coil. The introduction of a core increases r_{90} from the bare coil by effectively making the magnetic circuit taller. Figure 5.14f shows that the combination of a permeable core and permeable sheath makes a more closed magnetic circuit, while Figure 5.14g shows the combination of a permeable core and brass shield attenuates the fields at higher radii. Figure 5.14h shows the combination of the core, sheath and shield (the CSS configuration) closes the magnetic circuit, attenuates fields at larger radii, and has the smallest sensing radius of the available model configurations with $r_{90} = 2.4\,\text{mm}$.

Since the $r_{90} = 2.4\,\text{mm}$ produced by the CSS configuration was less than 2.5 mm, the CSS configuration was considered a good candidate for integration with a Supermendur orthogonal U-core tetrapole electromagnet. In addition to the solution at

30 kHz, the model was solved in the CSS configuration at 3 kHz and 300 kHz, and r_{90} was estimated for these frequencies to be 5.1 mm and 1.53 mm, respectively. Further design optimization, including shrinking the core and coil, making the sheath thicker, and using a higher conductivity shield (i.e., copper instead of brass) may reduce the sensing radius at all frequencies.

While the CSS configuration offers a smaller sensing radius in comparison to the bare coil, the use of permeable material in BN sensors comes with caveats:

- Due to the high frequencies of the BN power spectrum, only low-conductivity permeable materials, such as distributed-air-gap powdered cores and ferrites, can be used. Neither of these materials can be machined to the sizes used in the PUA model, thus such components must be molded and pressed/sintered. Costs for small runs of molded components are prohibitive, which limits core and sheath geometries to standard commercial sizes. The core and sheath geometries used in the model respectively correspond to commercially available RFID antenna rods and EMI suppression beads/sleeves that are readily available in ferrite.

- Due to interactions between the domain structure and microscopic eddy currents, the permeability of ferrites and powder cores becomes complex above $\sim$ 200 kHz and rolls off (-3 dB) at $\sim$ 3 MHz[†] [55, 57, 56]. The complex permeabilities of the core and sheath materials may distort BN power spectrum if they roll off at comparable frequency to the sample permeability. These effects

[†]The frequency response of ferrite and powdered core permeability can be kept real and flat up to $\sim$ 20 MHz [55, 56] by the inclusion of distributed non-magnetic material in the ceramic/powder mix. Adding such material decreases the effective permeability of the bulk material, so powdered cores with bandwidth $\geq$ 1 MHz tend to have $\mu_r \leq 100$, which is significantly less than the modelled $\mu_r = 2500$.

are modelled in Section 5.2.4.

- The introduction of permeable and free conductive materials alters the magnetic impedance near the PUA and may distort the excitation field. If sufficient flux couples into the ferrite in the PUA, it may generate its own BN. The degree of distortion and ferrite flux densities are expected to be small due to the 0.1 mm lift-off of the core and shield in the CSS configuration, but can be investigated by including the pickup assembly in future tetrapole models.

5.2.3 PUA Depth Sensitivity

To estimate the depth sensitivity of the pickup coil model in the CSS configuration, the sample material was varied through the SA106 μ_d materials in Table 5.1. For each sample material, the model was solved at frequencies (f_{bn}) of 3 kHz, 30 kHz and 300 kHz.

In Figure 5.15 B_{rms} is normalized with respect to B_{rms} at the sample surface and plotted as a function of depth at a position of $r = 0.6$ mm (these are shown as data points). For comparison, the solid lines in Figure 5.15 are $\exp\{-z/\delta_{bn}\}$ plotted with $\delta_{bn} = (\mu_0 \mu_d \sigma_e \pi f_{bn})^{-1/2}$ using the SA106 μ_d material values. It can be seen from the plots in Figure 5.15 that the signal attenuation is in good agreement with equations (2.43) and (2.46) for most f_{bn}. Discrepancies exist particularly for low μ_d at 3 kHz in Figure 5.15a and high μ_d at 300 kHz Figure 5.15c.

The discrepancy at 3 kHz and $\mu_d = 100$ is attributed to reduced field attenuation. Since the flux is less confined, the field orientation is no longer parallel to the surface plane and the field propagates at an angle to the surface normal. This results in lower fields at depth than are predicted using equation (2.43). The discrepancy at 300 kHz

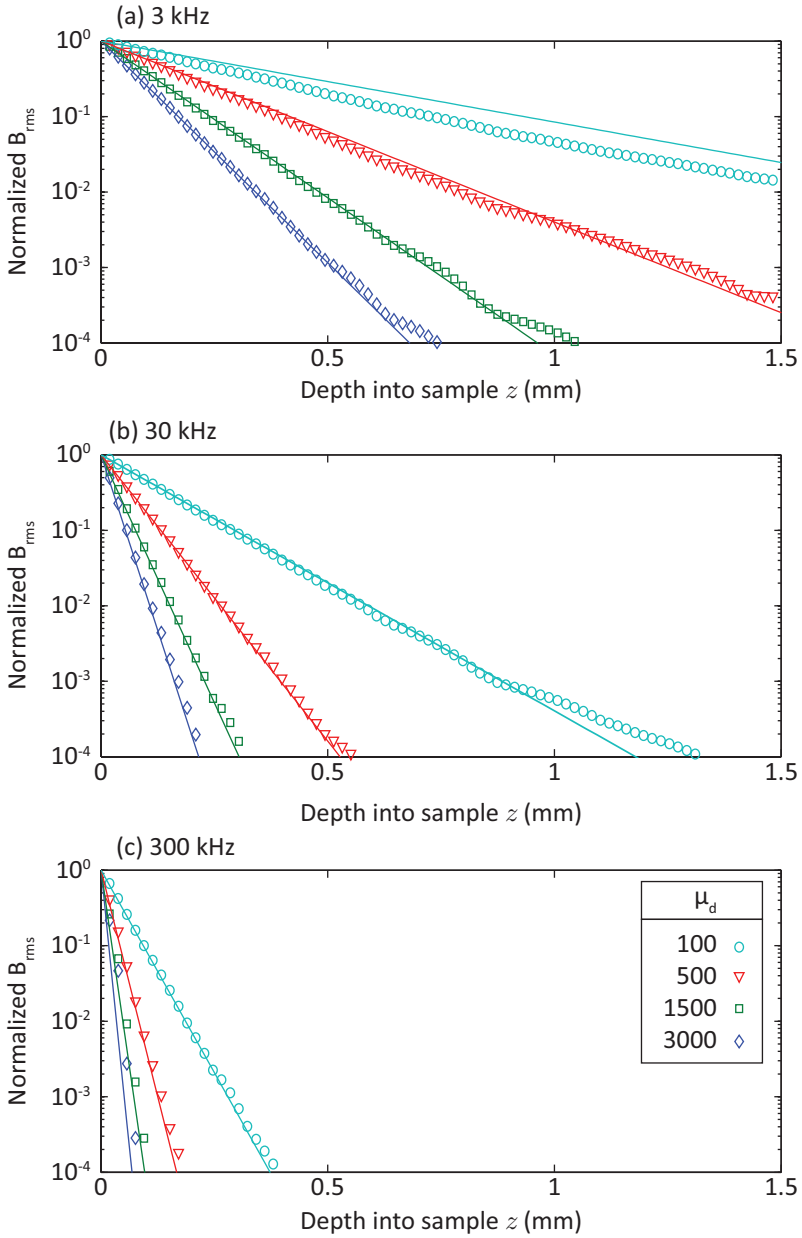

Figure 5.15: Data points are normalized B_{rms} depth profiles for the PUA model in the CSS configuration solved at frequencies (f_{bn}) of (a) 3 kHz, (b) 30 kHz and (c) 300 kHz. At each f_{bn} the sample material was modelled with μ_d values of 100, 500, 1500 and 3000. Lines are $\exp\{-z/\delta_{bn}\}$ with $\delta_{bn} = (\mu_0 \mu_d \sigma_e \pi f_{bn})^{-1/2}$ and $\sigma_e = 5.15 \times 10^6$ S/m.

and $\mu_d = 3000$ is attributed to meshing noise. According to equation (2.46), the skin depth is 7.4 µm, which is less than the minimum mesh element size of 0.2 mm.

The PUA model results in Figure 5.15 indicate that the depth sensitivity of the PUA across the BN frequency range can be treated using the plane-wave skin depth equations, provided that the sample has a uniform value of μ_d. At frequencies near the lower end of the BN power spectrum and near-saturation values of μ_d, coil geometry becomes a complicating factor in the skin depth analysis.

5.2.4 PUA Complex Inductance

As will be shown in Chapter 7, the pickup assembly inductance (L_{pu}) contributes significantly to the transfer function of the detected BN. To sample BN up to 300 kHz, the maximum sampling frequency of the BN must be several times greater. Thus, a estimate of L_{pu} up to $\sim$ 10 MHz was desired. Due to eddy current effects in the sample and shield, and the complex permeability of the sample, core and sheath above $\sim$ 200 kHz, L_{pu} is complex.

To model the complex permeabilities of the core, sheath and sample in the CSS configuration, user-specified *MagNet* materials were created. The core material complex permeability was set to match *Fair-Rite Corp.*'s 'Material 78', corresponding to their 1 mm in diameter RFID core, part 3078990831 with $\sigma_e = 0.2$ S/m. Similarly, the sheath material was set to match *National Magnetics* 'M20 material', corresponding to their EMI sleeve SB-1487-M20 with $\sigma_e = 1$ S/m. These are the parts used in the prototype tetrapole probe detailed in Section 5.3.

L_{pu} is expected to change with the sample μ_d, and the complex μ_d of SA-106 Grade B was not estimated in Appendix B. To model a scenario where the sample μ_d changes

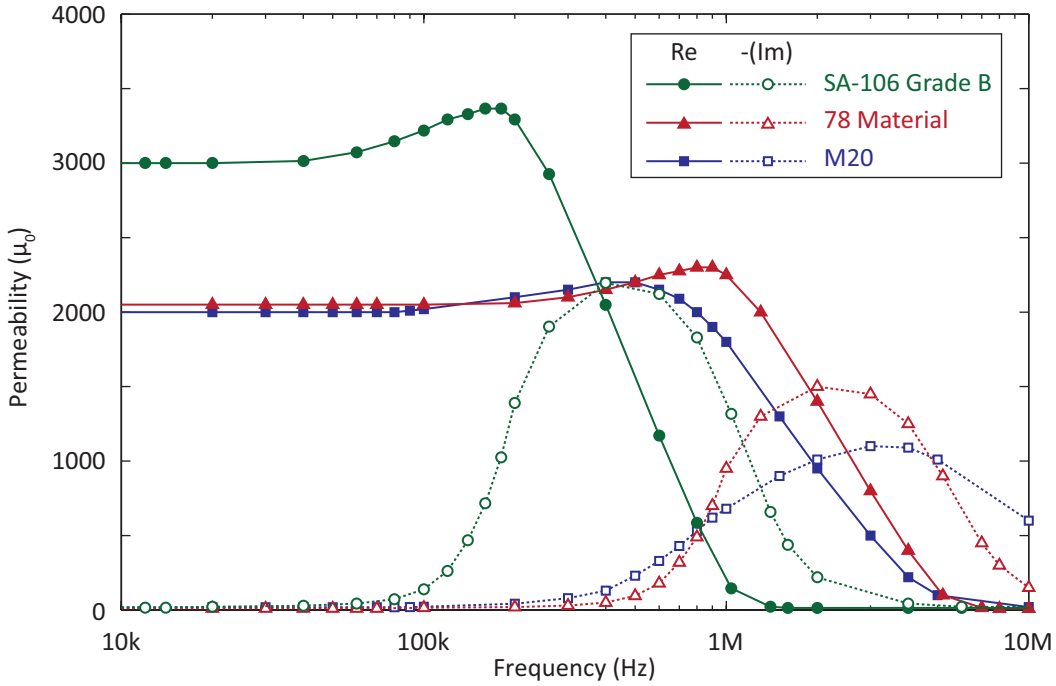

Figure 5.16: Complex permeability values entered into *MagNet*® for SA-106 Grade B 3000, Material 78, and M20. Lines are to guide the eye.

within the sampled frequency range, the sample material was approximated using the 'Material 78' curves, logarithmically shifted such that the maximum complex permeability occurs at 600 kHz. The DC permeability of the material was scaled to 3000, and the sample material conductivity was left unchanged at 5.15×10^6 S/m.

Plots of the complex material permeabilities entered into *MagNet* are shown in Figure 5.16. Note that the imaginary component of the complex permeability is negative. Since *MagNet 6.26.1* only accepts complex permeability as a function of temperature, frequency values in kHz were entered as temperatures in °C. The pickup coil model in the CSS configuration was then solved for temperature/frequency values from 1 kHz to 10 MHz with 1 mA_{rms} driven through the coil. To speed calculation, meshing requirements for the sample HR and sample MR were relaxed to those of

the sample LR.

For each model solution the complex flux linkage ($\Lambda = \sqrt{2}\Lambda_{rms}e^{i\phi_\Lambda}$) and current ($I = \sqrt{2}I_{rms}e^{i\phi_I}$) values were recorded from *MagNet*. Since the PUA model represents 2° of the full pickup coil, in order to obtain the total inductance, Λ was multiplied by 180 to give:

$$L_{pu} = 180\frac{\Lambda_{rms}}{I_{rms}}e^{i(\phi_\Lambda - \phi_I)}. \tag{5.5}$$

Inductance values from *MagNet* can be compared to the Wheeler formula for a multi-layer air-cored coil [58]:

$$L_{air} = 3.94 \times 10^{-6}\frac{(d_{od} + d_{id})^2 N^2}{13d_{od} - 7d_{id} + 18d_\ell}, \tag{5.6}$$

where d_{od}, d_{id} and d_ℓ are the outside diameter, inner diameter and length of the coil in meters, and L_{air} is the inductance in Henrys. Equation (5.6) gives 15.4 µH for the bare coil dimensions in the PUA model.

With the core, sheath, shield and sample disabled, *MagNet* gives $L_{air} = 20.7\,\mu H$ (at all frequencies). Disabling the air box HR and setting the smallest element size of the air box LR and coil to 0.1 mm gives $L_{air} = 15.8\,\mu H$, which is in good agreement with the Wheeler formula. In general it was observed that increasing meshing requirements decreased the *MagNet* real inductance values in all configurations by $\sim 5\,\mu H$, but substantially increased computing time. *MagNet* calculated L_{pu} values for the CSS configuration are shown in Figure 5.17, along with similar values for the bare coil on the sample, and the coil in air with $L_{air} = (20.7 + 0i)\,\mu H$. Fits to L_{pu} in the CSS configuration below 1 MHz are shown in red.

For the bare coil configuration, Figure 5.17 indicates that the sample increases

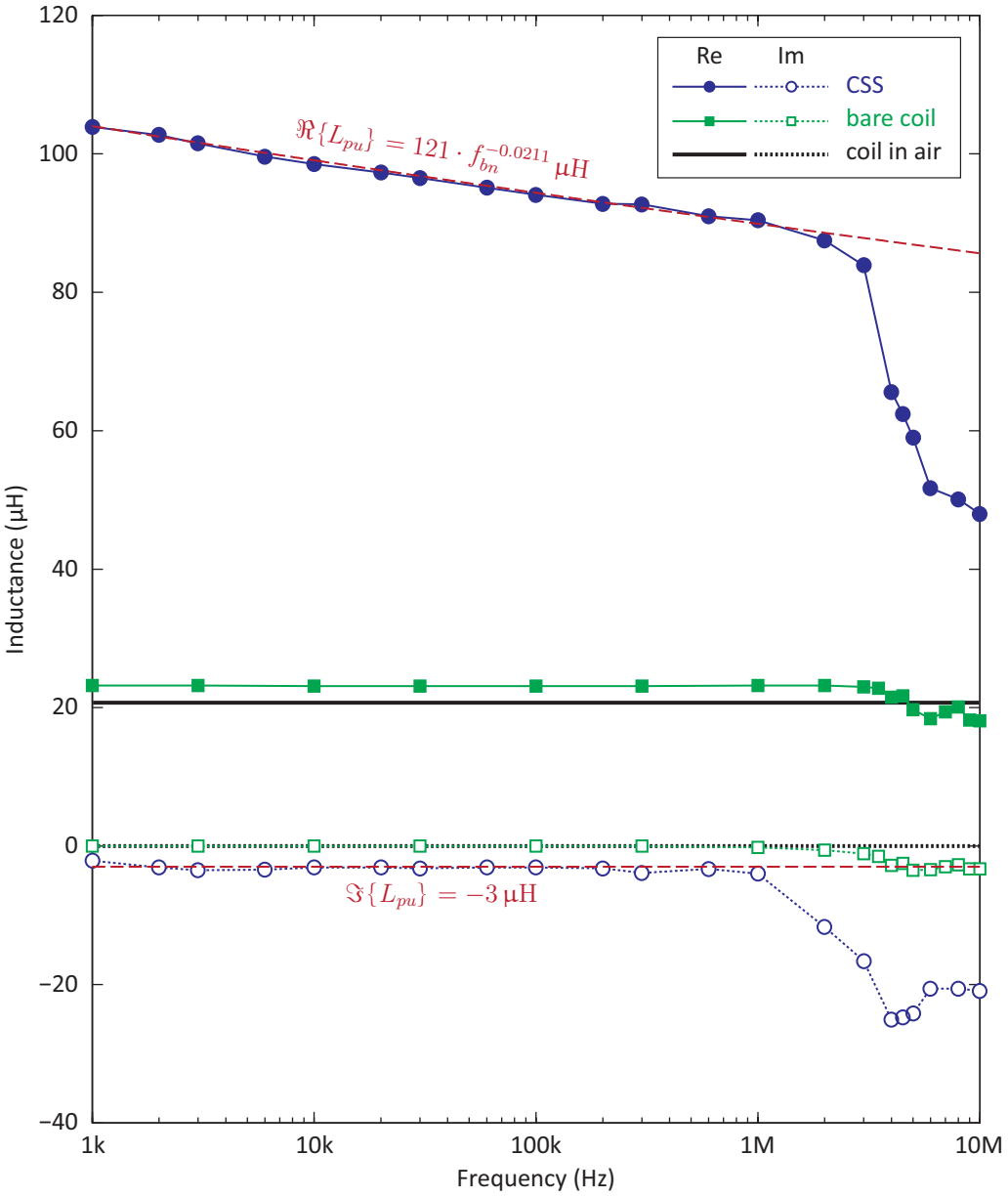

Figure 5.17: Complex inductance values from the PUA model in the CSS configuration and as a bare coil. Data points are connected to guide the eye. The inductance for the coil in air (no sample) is indicated in black as $20.7 + 0i\,\mu H$. Fits to the CSS configuration below 1 MHz are shown as red dashed lines.

$\Re\{L_{pu}\}$ by 2.5 µH (or 11%) over L_{air}. Due to the air gap between the sample and the coil, coupling of the eddy currents is weak, resulting in a negligble complex inductance $\Im\{L_{pu}\}$. For frequencies above 1 MHz the sample permeability decreases significantly in the model, resulting in an increased skin depth and eddy currents. The increased eddy currents decrease both $\Re\{L_{pu}\}$ and $\Im\{L_{pu}\}$ in Figure 5.17.

In the CSS configuration coupling to the core and sheath increases $\Re\{L_{pu}\}$ to 104 µH at 1 kHz. Eddy currents in the shield and sample decrease $\Im\{L_{pu}\}$ from the bare coil value of 0 µH to −3 µH. For increasing frequency, $\Re\{L_{pu}\}$ decreases as $121 \cdot f_{bn}^{-0.0211}$ up to $\sim$ 1 MHz. Above 1 MHz the sample permeability decreases rapidly, resulting in a rapid decrease of both $\Re\{L_{pu}\}$ and $\Im\{L_{pu}\}$.

Similarities between the high frequency roll-off of the bare coil case and the CSS configuration in Figure 5.17 indicate that high frequency roll-off of the Material 78 and M20 materials does not have a significant effect on L_{pu} below 10 MHz. Between 1 kHz and 1 MHz the $\Re\{L_{pu}\}$ decreases due to eddy current effects, while $\Im\{L_{pu}\}$ remains approximately constant and negative. Above 1 MHz variation in L_{pu} appears primarily due to sample permeability change, which may or may not roll-off as indicated in Figure 5.16. The fits to L_{pu} below 1 MHz in Figure 5.17 should therefore be a reasonable approximation to L_{pu} in electric circuit models up to 1 MHz, and higher if the sample permeability roll-off occurs at frequencies higher than 600 kHz.

5.3 Spring-Loaded Tetrapole Prototype (SL4P)

Based upon the modelling results in Sections 5.1 and 5.2, an orthogonal Supermendur U-core tetrapole electromagnet coupled with a pickup assembly in the CSS configuration was constructed for BN anisotropy measurement on feeder pipes. In order to

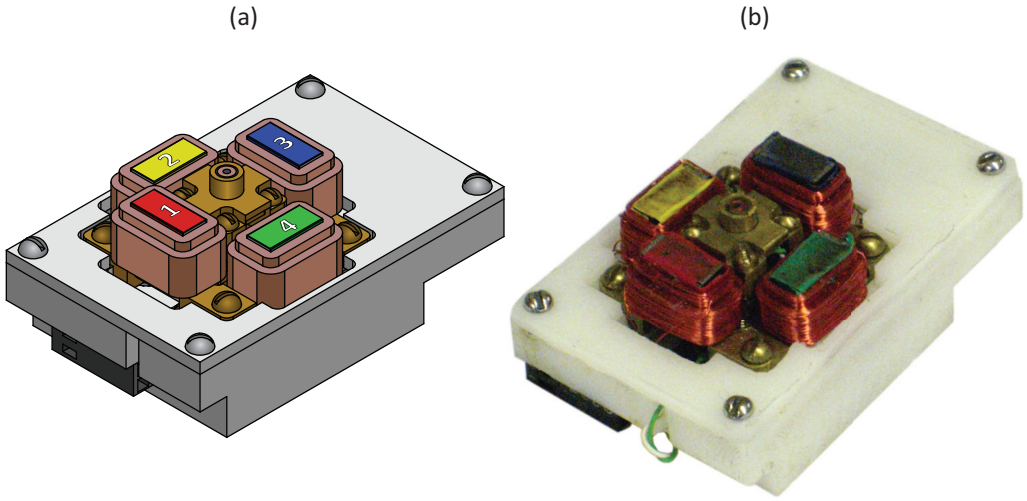

Figure 5.18: (a) SL4P assembly drawing at 1:1 scale. (b) A photograph of the completed SL4P.

ensure pickup coil coupling is repeatable between measurements, the spring-loaded tetrapole prototype (SL4P) was designed to keep both the pickup coil and the electromagnet poles in contact with the sample. Pole and pickup coil travel in the SL4P were designed to allow measurements on both feeder pipe curvatures and flat plates.

The SL4P was modelled in *Solid Edge*, and was designed to be non-destructively disassembled, with exception of the CSS pickup assembly, which held together with epoxy. The excitation and feedback coils are held to the poles by friction and rubber cement, and may typically be removed without damaging the windings. SL4P assembly drawings, along with drawings for all custom SL4P parts are presented in Appendix D. The full SL4P assembly with numbered poles is shown in Figure 5.18a, along with a photograph of the prototype in Figure 5.18b.

The *Tyco Electronics* connectors used for all coils were selected for their density and size, and are rated for 3 A. Since there is no active cooling for the excitation coils, fast-blow 2 A protection fuses (as shown in Figure 4.1) were selected to protect

Table 5.2: SL4P excitation coil DC resistances and impedances at 100 Hz and 1 V when attached to a straight section of feeder pipe.

Coil	R_{ex} (Ω)	$\lvert Z\rvert$ (Ω)	θ ($^\circ$)	L_{ex} (mH)
ex1	25.12	32.84	34.27	$29.43 - 0.32i$
ex2	25.42	38.74	40.05	$39.67 - 0.67i$
ex3	25.36	33.73	34.97	$30.77 - 0.36i$
ex4	25.39	37.97	39.32	$38.29 - 0.35i$

the AWG 36 excitation windings. When excitation currents > 1 A were required to generate the maximum excitation fields used in this thesis, duty cycling between measurements was implemented to allow heat dissipation.

The SL4P design features a significant amount of brass (in the frame and the pickup housing) that was not included in the tetrapole models in Section 5.1. The brass is expected to increase the AC magnetic impedance between the poles (i.e., add conductance to $d\mathcal{R}_{air}$ in Figure 3.1), and improve the approximation that the flux through the feedback coils is the only flux entering and leaving the sample. Care was taken in the SL4P tetrapole design to ensure that no closed conducting loops around the electromagnet cores were present, as these would significantly decrease the electromagnet performance.

Following construction, the SL4P was attached to the small feeder bend (see Section 9.1) with the short core aligned to the hoop axis, and the coil impedances were measured using a *BK Precision*® Model 885 LCR/ESR meter. Results for the excitation coils, feedback coils, and the pickup coil are in Tables 5.2, 5.3, and 5.4, respectively. Excitation coil inductances may be compared to those calculated using magnetic circuit theory and in Table 3.1. Pickup coil inductances may be compared with those calculated in *MagNet*, which are presented in Figure 5.17.

Table 5.3: SL4P feedback coil DC resistances and impedances at 100 Hz and 1 V when attached to a straight section of feeder pipe.

Coil	R_F (Ω)	$\lvert Z\rvert$ (Ω)	θ ($^\circ$)	L_F (μH)
F1	2.537	2.550	3.722	$264 - 1i$
F2	2.493	2.534	5.152	$363 - 5i$
F3	2.422	2.460	4.038	$276 - 5i$
F4	2.482	2.520	4.987	$349 - 5i$

Table 5.4: SL4P pickup coil impedance as measured at 50 mV when attached to a straight section of feeder pipe.

Frequency (Hz)	$\lvert Z\rvert$ (Ω)	θ ($^\circ$)	L_{pu} (μH)
DC	4.559	-	-
100	4.556	0.961	$121.6 + 5.8i$
1k	4.658	8.979	$115.7 - 6.7i$
10k	8.298	51.41	$103.2 - 9.8i$

The mean of the R_{ex} values in Table 5.2 is 25.3 Ω. The mean L_{ex} value for excitation coils 1 and 3 at $(30.1 - 0.3i)$ mH is lower than those of excitation coils 2 and 4 at $(39.0 - 0.7i)$ mH due to the increased air gap along the hoop axis. Both real and imaginary L_{ex} values are within the maximum and minimum inductance ranges specified in Table 3.1 at 100 Hz.

The mean of the R_F values in Table 5.3 is 2.48 Ω, which is $\sim 0.98 \cdot (N_F/N_{ex})$ times the mean R_{ex} value, with the 2% decrease attributed to the smaller coil thickness. Mean L_F values are $0.9 \cdot (N_F/N_{ex})^2$ times the mean L_{ex} values. Successful operation of the SL4P with the FCS requires the flux through each of the four feedback coils to be matched. Using the matching procedure described in Appendix D.4, feedback coils were matched via the $\mathcal{M}_p$ parameter to within $\pm 0.3\%$, with a systematic uncertainty of 2%.

Pickup coil inductance values (L_{pu}) in Table 5.4 are in good agreement with the

decreasing $\Re\{L_{pu}\}$ in Figure 5.17. The $\Im\{L_{pu}\}$ for 100 Hz is positive, which is the result of the LCR meter measuring $|Z|$ less than the DC resistance at this frequency, and likely a discrepancy between the LCR meter calculation of DC resistance and $|Z|$. $\Im\{L_{pu}\}$ values are less than the $-3i\,\mu$H predicted by *MagNet*, though within the correct order of magnitude. Discrepancies between LCR meter and *MagNet* are attributed primarily to the relatively coarse sample meshing compared to the skin depth in the *MagNet* models.

Inductance values provided in Tables 5.2, 5.3, and 5.4 are only considered approximate, since coupling to the sample through the air gaps strongly affect the observed values. While air gaps may be fixed for a given BN measurement, sample permeability changes due to saturation during the measurement will alter all inductance values as a function of the excitation waveform phase.

Chapter 6

FCS and SL4P Performance

The flux control system (FCS) from Chapter 4, combined with the spring-loaded tetrapole prototype (SL4P) from Chapter 5, comprise an electromagnet system capable driving the excitation coils using three distinct control algorithms, while recording 21 waveforms during each excitation iteration. In this chapter, the combined performance of the FCS and SL4P is evaluated.

- Section 6.1 presents an optimization procedure for the digital feedback gain G_D, and a comparison of error performance for the three control algorithms.
- Section 6.2 presents the waveform analysis methodology that was developed in order to parameterize the excitation field. Experimental data from the SL4P mounted on a feeder pipe sample are used to illustrate typical waveform characteristics and parameters.

6.1 Control System Performance

This section presents performance specifications for the VF (voltage following), RTA (real time analog) flux, and RTA flux with DEC (digital error correction) modes. Convergence data for the DC current correction algorithm in RTA and DEC modes is presented in Section 6.1.1, while convergence data for the DEC algorithm is presented in Section 6.1.2. RMS error and timing performance comparisons between the three control modes are presented in Section 6.1.3.

6.1.1 DC Current Convergence

Any voltage offsets at the amplifier input terminals, due to noise, matching errors, or input current requirements, are multiplied by the amplifier gains ($G_{V(p)}$ in VF mode, $G_{\Phi(p)}$ in RTA and DEC modes) to produce DC excitation currents ($\overline{I_{ex(p)}}$) for $p = 1 \ldots 4$. All three FCS modes include a digital feedback loop with proportional gain G_D that apply a DC voltage offset ($V_{OFF(p),(j-1)}$) to the reference voltage ($\boldsymbol{V_{ref(p),j}}$) ito iteratively converge toward $\overline{I_{ex(p)}} = 0$. Data are collected when $\left|\overline{I_{ex(p)}}\right| \leq T_C$ for two sequential iterations, with typical threshold current values of $T_C = 500\,\mu\text{A}$. This ensures that the sample excitation field follows a major hysteresis loop, and that the two BN pulses per excitation cycle are statistically similar.

With $V_{OFF(p),j} = 0$, $\left|\overline{I_{ex(p)}}\right|$ values in VF mode are typically $(20 \pm 20)\,\mu\text{A}$. Thus all cycles in VF mode are usually below T_C, and convergence times are negligible for any value of $G_D < 1$. This is not the case in the RTA and DEC modes, where the product of the voltage offsets and $G_{\Phi(p)}$ cause $\left|\overline{I_{ex(p)}}\right| > T_C$ for $V_{OFF(p),j} = 0$. Optimization of G_D in RTA and DEC modes improves stability and reduces convergence times.

To optimize G_D, the SL4P was mounted on a straight section of the small feeder

bend (see Section 9.1 for details), and the system was run in RTA mode with $V_{OFF(p),0} = 0$, $f_{ex} = 50\,\text{Hz}$, $B_{FT} = 477\,\text{mT}$ and $\theta_T = 45°$ for G_D values from 0.1 to 1. For each iteration the time and DC currents ($\overline{I_{ex(p),j}}$) were recorded. Figure 6.1 shows the effect of different G_D values. The average current offset for the first iteration across all channels is $(-18 \pm 6)\,\text{mA}$, and is consistent between G_D values in Figure 6.1.

For $G_D < 0.3$, Figure 6.1 shows that the current correction is under-driven. While the current never over-shoots the target DC current of 0 mA, it takes longer to converge than is achieved with $G_D = 0.3$. For $G_D \geq 0.4$, the system is over-driven, and is shown to over-shoot 0 mA. Oscillations are seen for $G_D > 0.4$. The critical value of G_D is therefore between 0.3 and 0.4. For all subsequent measurements, G_D was set to 0.35.

Since initial DC offset currents are consistent for various G_D values in Figure 6.1, it is a reasonable assumption that the offset voltages in the system are constant or vary slowly with time. As such, convergence times can be significantly reduced by setting $V_{OFF(p),0}$ to the final voltage offsets from the previous measurement. This is implemented in the software, though $V_{OFF(p),j}$ can be reset to 0 V, during and outside the control loop, if desired. Using offset values from previous measurements usually reduces the convergence time for DC current correction to 1 iteration in RTA and DEC modes.

6.1.2 DEC Mode Convergence

Maximum performance in DEC mode is achieved when $G_{\Phi(p)}$ and $G_{F(p)}$ are optimized for f_{ex}. This is accomplished by setting T_{err} to 0, and manually adjusting $G_{\Phi(p)}$ and

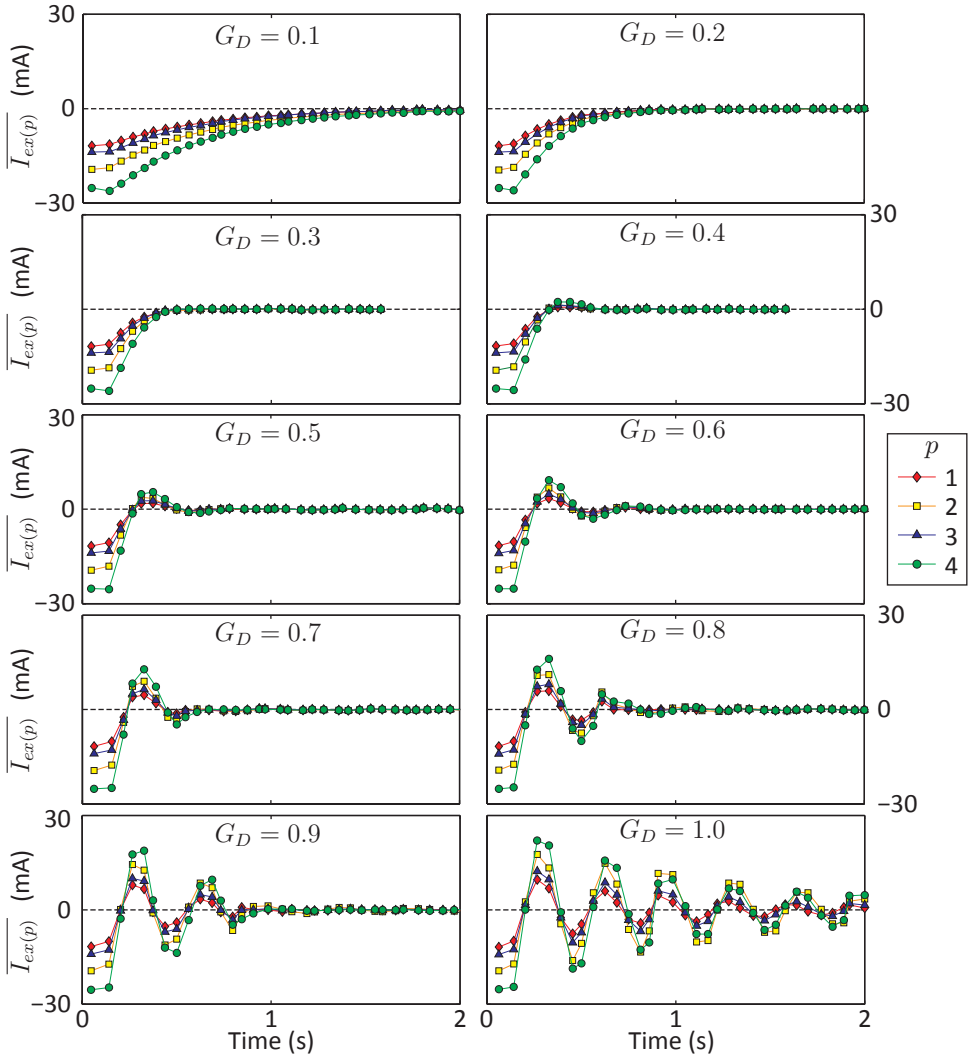

Figure 6.1: SL4P DC current ($\overline{I_{ex(p)}}$) convergence for various G_D values in real time flux mode, with $V_{OFF(p),0} = 0$, $f_{ex} = 50\,\text{Hz}$, $B_{FT} = 477\,\text{mT}$ and $\theta_T = 45°$ on the small feeder bend. Points correspond to the values measured during each excitation iteration and are connected to guide the eye.

$G_{F(p)}$ while the feedback loop is running until the RMS difference between the measured and target feedback coil voltages (err_{rms}) is minimized. This section presents convergence data for the DEC algorithm using $G_D = 0.35$, and $G_{F(p)}$ and $G_{\Phi(p)}$ values optimized for $f_{ex} = 50\,\text{Hz}$ and $B_{FT} = 477\,\text{mT}^*$. Figure 6.2 shows the err_{rms} values for each iteration in DEC mode for various f_{ex} values from 10 Hz to 100 Hz. To ensure a consistent initial error with which to estimate convergence time, $\boldsymbol{V_{Gex(p),0}}$ was set to 0 V for each measurement.

Values of err_{rms} for iteration 1 in Figure 6.2 represent RTA mode errors with $\boldsymbol{V_{Gex(p),0}} = 0$. The initial err_{rms} is seen to decrease from 72% at 10 Hz to 8.4% at 100 Hz. This decrease in initial error with f_{ex} is due to the phase shift in $V_{ex(p)}$ associated with the $L_{ex(p)}/R_{ex(p)}$ time constant. After the second iteration, the DC current threshold is met, and the DEC algorithm is initialized.

For iterations greater than 2, Figure 6.2 shows the err_{rms} values converging toward a final frequency-dependent value. Convergence rates are shown to be dependent on f_{ex}. Data sets for f_{ex} values of 75 Hz and 100 Hz reach a minimum err_{rms} value at iterations 7 and 10 respectively. This indicates that $G_D = 0.35$ is not optimal at these f_{ex} values, resulting in an over-shoot of the reference waveform correction. The occurrence of over-shoot suggests that $G_{F(p)}$ and $G_{\Phi(p)}$ may be further optimized at these frequencies.

Figure 6.2 shows that the DEC algorithm requires between 15 and 25 iterations to converge with $\boldsymbol{V_{Gex(p),0}} = 0\,\text{V}$. Any improved guess for $\boldsymbol{V_{Gex(p),0}}$ substantially reduces the initial error and hence reduces the number of convergence iterations.

*While the data in this thesis was being collected, the $(1 + a_p R_{F2}/(R_{F1} + R_{on})) = 1.91$ term in equation (4.7) was overlooked. Hence many flux density values are not as aesthetically round as one might prefer.

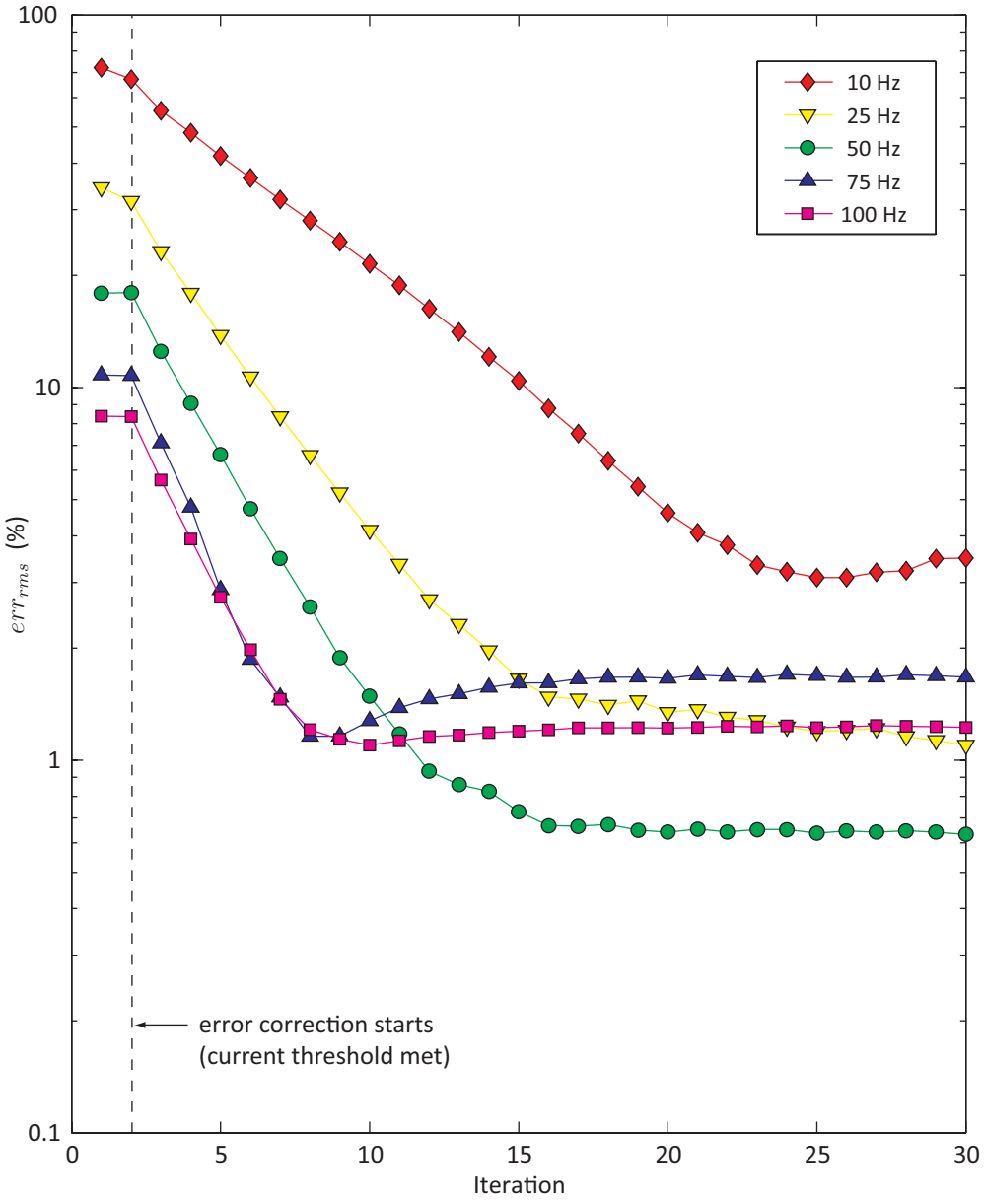

Figure 6.2: SL4P err_{rms} convergence in DEC mode with $G_D = 0.35$, $B_{FT} = 477\,\text{mT}$, $\theta_T = 45°$, $\boldsymbol{V_{Gex(p),0}} = 0$ and f_{ex} values from 10 Hz to 100 Hz on a the small feeder bend. Points are connected to guide the eye.

6.1.3 RMS Errors and Iteration Times

In this section VF, RTA, and DEC modes are compared in terms of their ability to match the target waveforms, and the number of cycles required between iterations.

In VF mode, the amplifier circuit for each channel operates as a voltage follower with gain $G_{V(p)}$. The limitations of the LM4701 amplifiers, timing delays associated with triggering processes, and the low pass filtering of the $AO_{(p-1)}$ channels all contribute some frequency dependence to $G_{V(p)}$, and introduce error between the target and measured excitation voltages (err_{rms})[†]. In VF mode, err_{rms} is minimized by optimizing $G_{V(p)}$ in the software interface to match that of the physical circuit at a given f_{ex}.

In RTA mode, the control algorithm relies on a large gain $G_{\Phi(p)} \approx 178$ to match $V_{ref(p)}$ and $V_{F(p)}$, and uses the form of $\boldsymbol{V_{Gex(p),0}}$ in equation (3.22) to further reduce the error. Minimizing err_{rms} in RTA mode requires optimization of $G_{F(p)}$, $G_{\Phi(p)}$, $L_{ex(p)}/R_{ex(p)}$, and $\mathcal{X}_p$. All 16 of these parameters (for $p = 1 \ldots 4$) have some dependence on f_{ex}, while $L_{ex(p)}/R_{ex(p)}$ and $\mathcal{X}_p$ also vary with B_{FT} due to eddy current and saturation effects. The system also has the same amplifier and reference voltage filtering limitations as VF mode.

In DEC mode, optimization requirements for $L_{ex(p)}/R_{ex(p)}$ and $\mathcal{X}_p$ are eliminated by using the measured excitation voltage from one iteration to calculate the guess excitation voltage for the subsequent iteration. Thus, only $G_{F(p)}$ and $G_{\Phi(p)}$ require optimization to minimize err_{rms}.

To compare err_{rms} between modes, the SL4P was mounted on a straight section of the small feeder bend. In VF mode, $G_{V(p)}$ values were manually optimized for

[†]Calculation of err_{rms} differs between VF mode and RTA and DEC modes. See the flow charts in Appendix A.1 for details.

$V_{exTpk} = 5\,\mathrm{V}$, $\theta_T = 45°$, and $f_{ex} = 50\,\mathrm{Hz}$. In RTA mode, $R_{ex(p)}$ were set to the values in Table 5.2, and $G_{F(p)}$, $G_{\Phi(p)}$, $L_{ex(p)}$ and $\mathcal{X}_p$ were optimized for $f_{ex} = 50\,\mathrm{Hz}$, $B_{FT} = 477\,\mathrm{mT}$ and $\theta_T = 45°$. The RTA values for $G_{F(p)}$ and $G_{\Phi(p)}$ were kept in DEC mode.

With $f_{ex} = 50\,\mathrm{Hz}$ and $\theta_T = 45°$, V_{exTpk} was varied from 10 mV to 24 V in VF mode, and B_{FT} was varied from 19 mT to 1.53 T in the RTA and DEC modes. Then, with $\theta_T = 45°$, $V_{exTpk} = 5\,\mathrm{V}$ in VF mode, and $B_{FT} = 477\,\mathrm{mT}$ in the RTA and DEC modes, f_{ex} was varied from 10 Hz to 100 Hz. For each iteration, the time and err_{rms} values were recorded. Time values were used to calculate the number of cycles for each iteration. The resulting data are shown in Figure 6.3. Note that in DEC mode, err_{rms} values are the steady state values following convergence of the DEC algorithm.

Figure 6.3a shows the dependence of err_{rms} on V_{exTpk} and B_{FT} for $f_{ex} = 50\,\mathrm{Hz}$. In VF mode, the average value of err_{rms} is 0.64% for $V_{exTpk} > 5\,\mathrm{V}$. Values of err_{rms} less than 0.6% are primarily attributed to phase lags associated with analog output filtering and triggering delays. An increase in err_{rms} is seen for $V_{exTpk} < 1\,\mathrm{V}$, as noise in the $V_{ex(p)}$ waveforms become significant relative to V_{exTpk}.

In RTA mode, Figure 6.3a shows err_{rms} values are consistently larger than those in VF mode. A minimum err_{rms} value of 0.77% is observed for $B_{FT} = 0.86\,\mathrm{T}$. Error increases for $B_{FT} > 0.86\,\mathrm{T}$ are attributed to magnetic saturation effects in the sample. Error increases for $B_{FT} < 0.86\,\mathrm{T}$ are attributed to the decreasing signal-to-noise ratio for $\boldsymbol{V_{F(p),j}}$ due to decreasing $\mathrm{d}\Phi_{F(p)}/\mathrm{d}t$.

In DEC mode, Figure 6.3a shows err_{rms} values converge to a value of 0.63% for $B_{FT} > 0.5\,\mathrm{T}$. For $B_{FT} < 0.5\,\mathrm{T}$, increased err_{rms} values over VF mode are attributed to noise in $\boldsymbol{V_{F(p)}}$. Since err_{rms} does not increase for $B_{FT} > 0.5\,\mathrm{mT}$, it

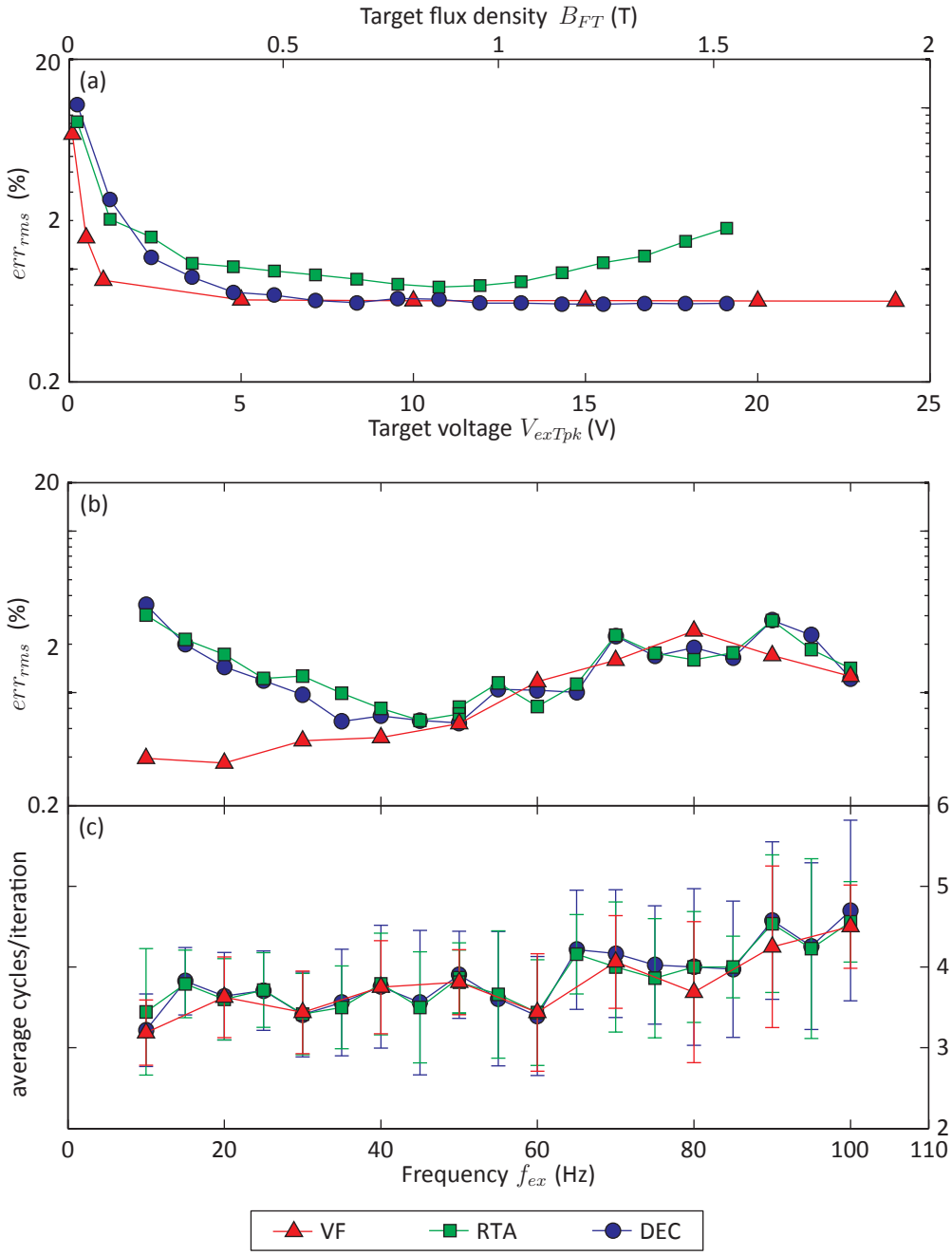

Figure 6.3: VF, RTA, and DEC mode (a) err_{rms} values for varying V_{exTpk} and B_{FT} at $f_{ex} = 50\,\text{Hz}$, (b) err_{rms} values for varying f_{ex}, and (c) average cycles per iteration for varying f_{ex}. Lines are to guide the eye.

may be concluded that the DEC algorithm is effectively compensating for magnetic saturation effects. As with VF mode, the minimum err_{rms} value of 0.63% in DEC mode is attributed to phase lags.

Figure 6.3b shows the frequency dependence of err_{rms} with $V_{exTpk} = 5\,\mathrm{V}$ and $B_{FT} = 477\,\mathrm{mT}$. In VF mode, the value of err_{rms} is shown to increase with f_{ex}. This is attributed to the phase lags from analog output filtering and triggering delays. In the RTA and DEC modes, err_{rms} decreases up to the optimized frequency of 50 Hz and then increases similarly to VF mode. The decreasing err_{rms} in RTA and DEC modes with increasing f_{ex} is a result of increasing signal-to-noise ratios in $\boldsymbol{V_{F(p)}}$.

Figure 6.3c shows that the average number of cycles per iteration is consistent between modes, and increases with f_{ex}. For the measured frequency range, the average number of cycles per iteration is between 3 and 5. Appendix A.2 shows that theoretical minimum number of cycles per iteration in the present FCS implementation is 3, but may increase if the number of computations per iteration take longer than $3/(4f_{ex})$. Since all modes are consistent, it may be concluded that DEC is sufficiently computationally efficient that it does not significantly affect the number of cycles per iteration when compared to the present implementation of the VF or RTA modes.

Overall, Figure 6.3 shows that values of err_{rms} are lower in DEC mode than in RTA mode, both as a function of B_{FT} and f_{ex}, and that the number of cycles per iteration are consistent between the two modes. Performance in RTA mode is only adequate following optimization of $L_{ex(p)}/R_{ex(p)}$ and $\mathcal{X}_p$, which typically requires hundreds of iterations when done manually. Furthermore, any error reduction obtained via optimization in RTA mode similarly decreases the initial error in DEC mode. It may therefore be concluded that DEC mode is effective both at compensating for

time-varying magnetic circuit properties and at reducing optimization times. Only when a large number of measurements are being performed at the same location might it be advantageous to optimize $L_{ex(p)}/R_{ex(p)}$ and $\mathcal{X}_p$, in order to reduce convergence times.

6.2 Excitation Waveform Analysis Methodology

Once a user-specified number of cycles (k_{max}) below current and error thresholds are sampled, the stored reference voltage ($\boldsymbol{V_{ref(p),k}}$), excitation voltage ($\boldsymbol{V_{ex(p),k}}$), excitation current ($\boldsymbol{I_{ex(p),k}}$), feedback coil flux rate ($\boldsymbol{(dB/dt)_{F(p),k}}$), feedback coil flux density ($\boldsymbol{B_{F(p),k}}$), BN waveforms ($\boldsymbol{V_{(BN+bk),k}}$) and background noise waveforms ($\boldsymbol{V_{bk,k}}$) are analyzed in order to parameterize the excitation field and BN properties. This section presents the analysis methodology for the excitation waveforms implemented in the software GUI. The analysis methodology for $\boldsymbol{V_{(BN+bk),k}}$ and $\boldsymbol{V_{bk,k}}$ is presented in Chapter 8.

6.2.1 Averaged Waveforms

In order to analyse the timing and phase relationships between the various waveforms, the $\boldsymbol{V_{ref(p),k}}$ waveforms are resampled from f_{6229AO} to f_{6229AI}, and the mean and standard deviation of each time sample for the 20 stored waveforms is computed. This reduces the $20 \cdot k_{max}$ excitation waveforms to 20 waveforms: $\boldsymbol{\bar{V}_{ref(p)}}$, $\boldsymbol{\bar{V}_{ex(p)}}$, $\boldsymbol{\bar{I}_{ex(p)}}$, $\boldsymbol{(\overline{dB/dt})_{F(p)}}$ and $\boldsymbol{\bar{B}_{F(p)}}$ with a mean and standard deviation for each time sample.

Typical mean waveforms from the SL4P on the small feeder bend in DEC mode

with $B_{FT} = 477\,\text{mT}$, $\theta_T = 45°$ and f_{ex} values of 10 Hz, 50 Hz and 100 Hz are shown in Figures 6.4a, 6.4b and 6.4c, respectively. Figures 6.4av, 6.4bv, and 6.4cv show the flux control to be effective, with the magnitude and phase of $\bar{\boldsymbol{B}}_{\boldsymbol{F(p)}}$ consistent for all three f_{ex} values.

A comparison of Figures 6.4i to Figures 6.4iv indicates that magnitudes of $\bar{\boldsymbol{V}}_{\boldsymbol{ref(p)}}$ and $\overline{(\boldsymbol{dB/dt})}_{\boldsymbol{F(p)}}$ are approximately proportional, though $\bar{\boldsymbol{V}}_{\boldsymbol{ref(p)}}$ lags $\overline{(\boldsymbol{dB/dt})}_{\boldsymbol{F(p)}}$ more at low f_{ex} due to gain limiting. Were the system operating in RTA mode with $G_{\Phi(p)} = \infty$, the phase of $\bar{\boldsymbol{V}}_{\boldsymbol{ref(p)}}$ and $\overline{(\boldsymbol{dB/dt})}_{\boldsymbol{F(p)}}$ would be matched.

Figures 6.4iii indicate that the current required to induce the desired flux does not change significantly with f_{ex}, and that the phase of $\bar{\boldsymbol{I}}_{\boldsymbol{ex(p)}}$ is similar to $\bar{\boldsymbol{B}}_{\boldsymbol{F(p)}}$ in Figures 6.4v. This indicates that $I_{ex(p)} \propto B_{F(p)}$, and therefore that current controlled electromagnets are capable of producing repeatable flux waveforms when driving a constant inductance. Note that $\bar{\boldsymbol{I}}_{\boldsymbol{ex1}}$ and $\bar{\boldsymbol{I}}_{\boldsymbol{ex3}}$ are significantly greater $\bar{\boldsymbol{I}}_{\boldsymbol{ex2}}$ and $\bar{\boldsymbol{I}}_{\boldsymbol{ex4}}$ as there are larger air gaps between poles 1 and 3 and the sample (along the hoop direction).

Figures 6.4ii indicate that the magnitudes and phases of $\bar{\boldsymbol{V}}_{\boldsymbol{ex(p)}}$ change significantly with f_{ex}. As f_{ex} increases, greater $\bar{\boldsymbol{V}}_{\boldsymbol{ex(p)}}$ amplitudes are required to compensate for the back EMF across the excitation coils, and the phase of $\bar{\boldsymbol{V}}_{\boldsymbol{ex(p)}}$ shifts toward matching the phase of $\overline{(\boldsymbol{dB/dt})}_{\boldsymbol{F(p)}}$. For low f_{ex} values, such as in Figures 6.4a, $\bar{\boldsymbol{V}}_{\boldsymbol{ex(p)}}$ is approximately in phase with $\bar{\boldsymbol{I}}_{\boldsymbol{ex(p)}}$, and indicates the voltage required to drive current through $R_{ex(p)}$.

Standard deviations for each time sample are sufficiently small that they are not visible in Figure 6.4. The average standard deviation across all channels and time samples was calculated for each subplot in Figure 6.4, and are given in Table 6.1.

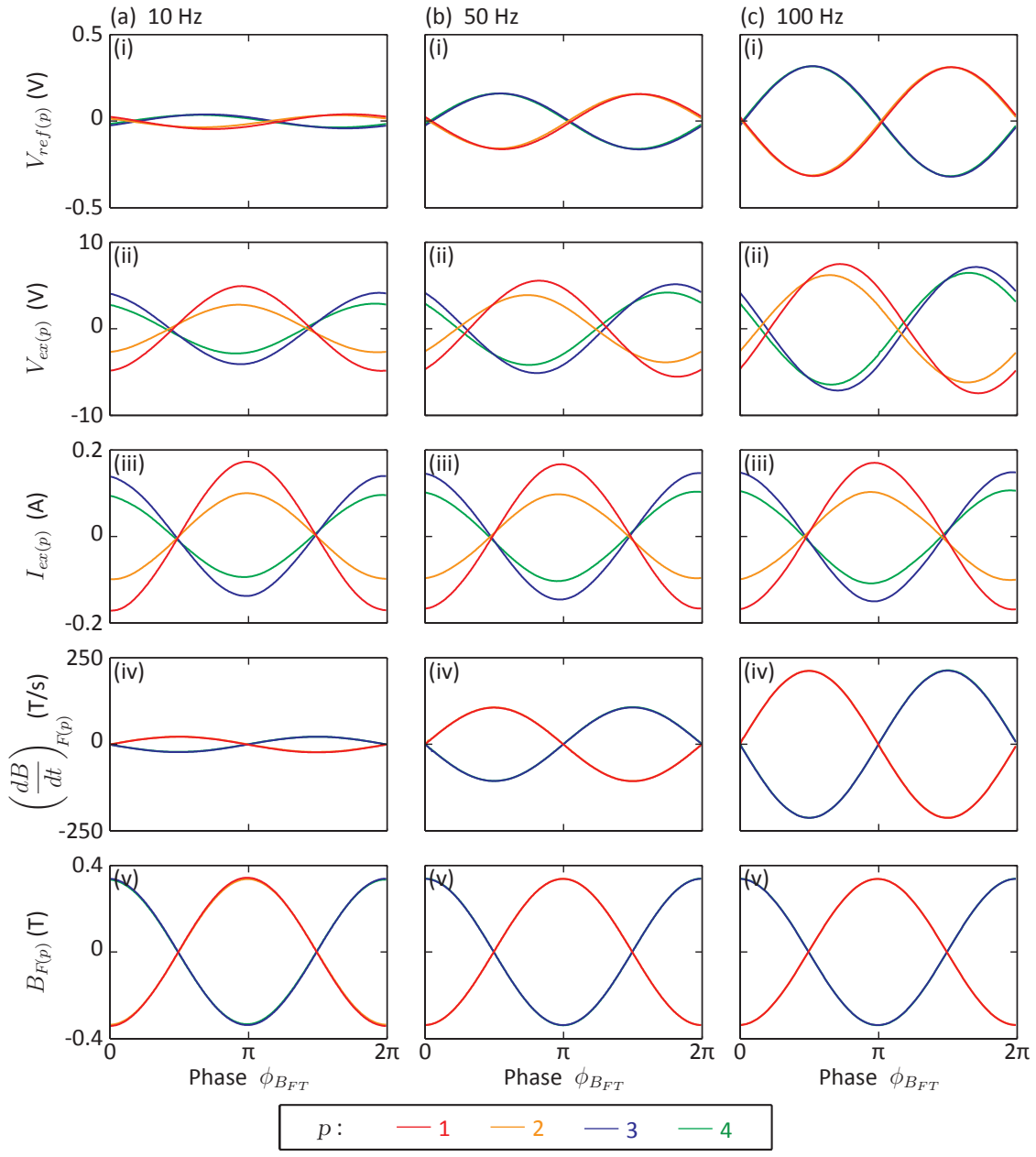

Figure 6.4: Mean (i) reference voltage, (ii) excitation voltage, (iii) excitation current, (iv) feedback coil flux rate, and (iv) feedback coil flux density waveform data in DEC mode with $B_{FT} = 477\,\text{mT}$ and $\theta_T = 45°$ for f_{ex} values of (a) 10 Hz, (b) 50 Hz and (c) 100 Hz.

Table 6.1: Average precision of the waveforms in Figure 6.4.

	f_{ex} (Hz)		
Waveform	10	50	100
$\bar{\boldsymbol{V}}_{\boldsymbol{ref(p)}}$ (μV)	360 ± 140	49 ± 15	27 ± 5
$\bar{\boldsymbol{V}}_{\boldsymbol{ex(p)}}$ (mV)	60 ± 20	7 ± 2	6.7 ± 1.4
$\bar{\boldsymbol{I}}_{\boldsymbol{ex(p)}}$ (mA)	2.6 ± 1.0	0.37 ± 0.09	0.33 ± 0.06
$(\overline{\boldsymbol{dB/dt}})_{\boldsymbol{F(p)}}$ (mT/s)	120 ± 60	100 ± 40	100 ± 40
$\bar{\boldsymbol{B}}_{\boldsymbol{F(p)}}$ (mT)	1.3 ± 0.4	0.18 ± 0.02	0.074 ± 0.015

Values in Table 6.1 therefore correspond to vertical error bars for the corresponding plots in Figure 6.4, and the precision to which waveforms were repeatable.

The precision of the $(\overline{\boldsymbol{dB/dt}})_{\boldsymbol{F(p)}}$ and $\bar{\boldsymbol{B}}_{\boldsymbol{F(p)}}$ waveforms are of primary interest, as this is the precision to which the FCS produced consistent magnetisation conditions within the SL4P. Table 6.1 shows that $(\overline{\boldsymbol{dB/dt}})_{\boldsymbol{F(p)}}$ precision is better than $\pm 180\,\mathrm{mT/s}$. $\bar{\boldsymbol{B}}_{\boldsymbol{F(p)}}$ waveform precision is better than $\pm 1.7\,\mathrm{mT}$ at 10 Hz and better than $\pm 0.20\,\mathrm{mT}$ above 50 Hz. Frequency dependence of flux waveform precision is attributed to signal-to-noise levels in the feedback coils, which decrease with f_{ex}.

A plot of $\bar{\boldsymbol{B}}_{\boldsymbol{F(p)}}$ versus $\bar{\boldsymbol{I}}_{\boldsymbol{ex(p)}}$ gives the magnetic hysteresis loop for each channel. In the present implementation, hysteresis loops are plotted in the GUI for each iteration, and are useful for checking how effectively the different poles are coupling to the sample. Note that sample permeability measurements cannot be extracted from this data since air gaps and core permeability are not accounted for. If the excitation coil and feedback coil are wound around a toroid, as in Appendix B, these waveforms may be used for permeability and eddy current loss measurements.

6.2.2 Single Parameter Analysis

While thorough examination of the averaged waveforms is useful, the resulting waveforms require large files and are inconvenient to transport and manually analyze. Thus a number of single parameters are derived for each waveform and each channel in order to simplify plotting and parameterization of system performance. These single parameters are described in this section.

For $k = 1 \ldots k_{max}$ the RMS magnitude of each excitation waveform is calculated. The mean and standard deviation of the RMS magnitude over all k are then stored. The phase ($\phi\{\boldsymbol{X}_k\}$) of each waveform $\boldsymbol{X}_k$ is calculated by taking the discrete Fourier transform of $\boldsymbol{X}_k$, and extracting the phase sample corresponding to f_{ex}. Phase values are expressed relative to the target phase of the feedback coil flux density ($\phi_{B_{FT}}$). The mean and standard deviation of the phases over all k are then stored. The RMS and phase values of $\boldsymbol{V_{ex(p)}}_{,k}$ and $\boldsymbol{I_{ex(p)}}_{,k}$ waveforms are also used to calculate the effective resistance ($R_{ex(p),k}$) and inductance ($L_{ex(p),k}$) of each channel according to:

$$R_{ex(p),k} = \frac{\mathrm{RMS}\left\{\boldsymbol{V_{ex(p)}}_{,k}\right\}}{\mathrm{RMS}\left\{\boldsymbol{I_{ex(p)}}_{,k}\right\}} \cos\left(\phi\left\{\boldsymbol{V_{ex(p)}}_{,k}\right\} - \phi\left\{\boldsymbol{I_{ex(p)}}_{,k}\right\}\right) \tag{6.1}$$

and

$$L_{ex(p),k} = \frac{\mathrm{RMS}\left\{\boldsymbol{V_{ex(p)}}_{,k}\right\}}{2\pi f_{ex}\mathrm{RMS}\left\{\boldsymbol{I_{ex(p)}}_{,k}\right\}} \sin\left(\phi\left\{\boldsymbol{V_{ex(p)}}_{,k}\right\} - \phi\left\{\boldsymbol{I_{ex(p)}}_{,k}\right\}\right). \tag{6.2}$$

The mean and standard deviation of $R_{ex(p),k}$ and $L_{ex(p),k}$ for all k are then stored. These values for $R_{ex(p)}$ and $L_{ex(p)}$ include the resistance of cabling, fuses, saturation effects, and eddy currents, and are suitable for substitution into equation (3.22) for the calculation of $\boldsymbol{V_{Gex(p)}}_{,0}$. Table 6.2 shows the RMS, phase, $R_{ex(p)}$ and $L_{ex(p)}$ values for the $f_{ex} = 50\,\mathrm{Hz}$ data in Figure 6.4.

Table 6.2: Excitation waveform RMS and phase values from for $f_{ex} = 50\,\mathrm{Hz}$ in DEC mode with $B_{FT} = 477\,\mathrm{mT}$ and $\theta_T = 45°$.

		Pole p			
		1	2	3	4
$V_{ex(p)}$	($\mathrm{V_{rms}}$)	3.906 ± 0.006	2.741 ± 0.004	3.613 ± 0.006	2.953 ± 0.005
	(°)	32.431 ± 0.006	48.157 ± 0.004	216.453 ± 0.006	226.350 ± 0.005
$I_{ex(p)}$	($\mathrm{mA_{rms}}$)	117.4 ± 0.3	68.1 ± 0.2	101.9 ± 0.3	72.0 ± 0.2
	(°)	2.65 ± 0.07	5.67 ± 0.10	184.57 ± 0.06	187.45 ± 0.08
$(dB/dt)_{F(p)}$	$(\mathrm{T/s})_{\mathrm{rms}}$	75.05 ± 0.06	75.10 ± 0.04	75.08 ± 0.03	75.32 ± 0.03
	(°)	90.23 ± 0.04	90.17 ± 0.04	270.214 ± 0.016	270.128 ± 0.018
$B_{F(p)}$	($\mathrm{T_{rms}}$)	238.81 ± 0.17	239.04 ± 0.15	238.94 ± 0.10	239.69 ± 0.10
	(°)	0.73 ± 0.04	0.67 ± 0.04	180.714 ± 0.016	180.628 ± 0.018
$R_{ex(p)}$	(Ω)	28.89 ± 0.03	29.69 ± 0.05	30.12 ± 0.02	31.95 ± 0.04
$L_{ex(p)}$	(mH)	52.61 ± 0.12	86.5 ± 0.3	59.65 ± 0.13	82.0 ± 0.2

To estimate the performance of the system to reproduce the target flux waveforms, consider the $B_{F(p)}$ data in Table 6.2. The target RMS value for $\boldsymbol{B_{F(p),k}}$ is $238.6\,\mathrm{mT_{rms}}$ for $B_{FT} = 477\,\mathrm{mT}$ and $\theta_T = 45°$. RMS values of $B_{F(p)}$ in Table 6.2 average to $(239.2 \pm 0.4)\,\mathrm{mT_{rms}}$. The system therefore over-shoots the target flux density by 0.25%. This overshoot was reproduced to within ±0.17% across the four poles. Similarly, phase values for $B_{F(p)}$ in Table 6.2 systematically deviate from the target values of 0° and 180° by $(0.69 \pm 0.05)°$. Phases were therefore consistent to within ±0.05°, though a systematic offset of all flux waveform phases by 0.69° was observed. This offset is expected to be influenced by the relative magnitude of timing delays for different f_{ex} values.

6.2.3 Superposition Field

To parameterize the superposition field, the $\boldsymbol{B_{F(p),k}}$ waveforms are combined to give:

$$\boldsymbol{B_{Fx},_k} = \frac{\boldsymbol{B_{F1},_k} - \boldsymbol{B_{F3},_k}}{2} \tag{6.3}$$

and

$$\boldsymbol{B_{Fy},_k} = \frac{\boldsymbol{B_{F2},_k} - \boldsymbol{B_{F4},_k}}{2}. \tag{6.4}$$

The mean and standard deviation over k of the RMS amplitude (B_{Fxrms}, B_{Fyrms}) and phase ($\phi_{B_{Fx}}$, $\phi_{B_{Fy}}$) of $\boldsymbol{B_{Fx},_k}$ and $\boldsymbol{B_{Fy},_k}$ are then calculated and stored. The RMS amplitude of the superposition field ($B_{Frms,k}$) is then estimated as:

$$B_{Frms,k} = \text{RMS}\left\{\sqrt{\boldsymbol{B}^2_{\boldsymbol{Fx},k} + \boldsymbol{B}^2_{\boldsymbol{Fy},k}}\right\}, \tag{6.5}$$

and the peak flux density ($B_{Fpk,k}$) is estimated as:

$$B_{Fpk,k} = \max\left\{\sqrt{\boldsymbol{B}^2_{\boldsymbol{Fx},k} + \boldsymbol{B}^2_{\boldsymbol{Fy},k}}\right\}, \tag{6.6}$$

where $\boldsymbol{X}^2$ indicates each time sample in waveform $\boldsymbol{X}$ is squared, and $\max\{\boldsymbol{X}\}$ yields the value of the largest time sample in waveform $\boldsymbol{X}$. The mean and standard deviation of $B_{Frms,k}$ and $B_{Fpk,k}$ over k are then stored.

To estimate the feedback superposition angle ($\theta_{F,k}$), a linear regression is performed on a plot of $\boldsymbol{B_{Fy},_k}$ versus $\boldsymbol{B_{Fx},_k}$. The slope of the fit ($m_{yx,k}$) is then used to calculate $\theta_{F,k}$ according to $\theta_{F,k} = \arctan(m_{yx,k})$. Figure 6.5 shows plots of $\bar{\boldsymbol{B}}_{\boldsymbol{Fy}}$ versus $\bar{\boldsymbol{B}}_{\boldsymbol{Fx}}$ for $k_{max} = 16$ and various θ_T values. The mean and standard deviation of $\theta_{F,k}$ over $k = 1 \ldots 16$ are indicated in Figure 6.5 for each data series. Comparison

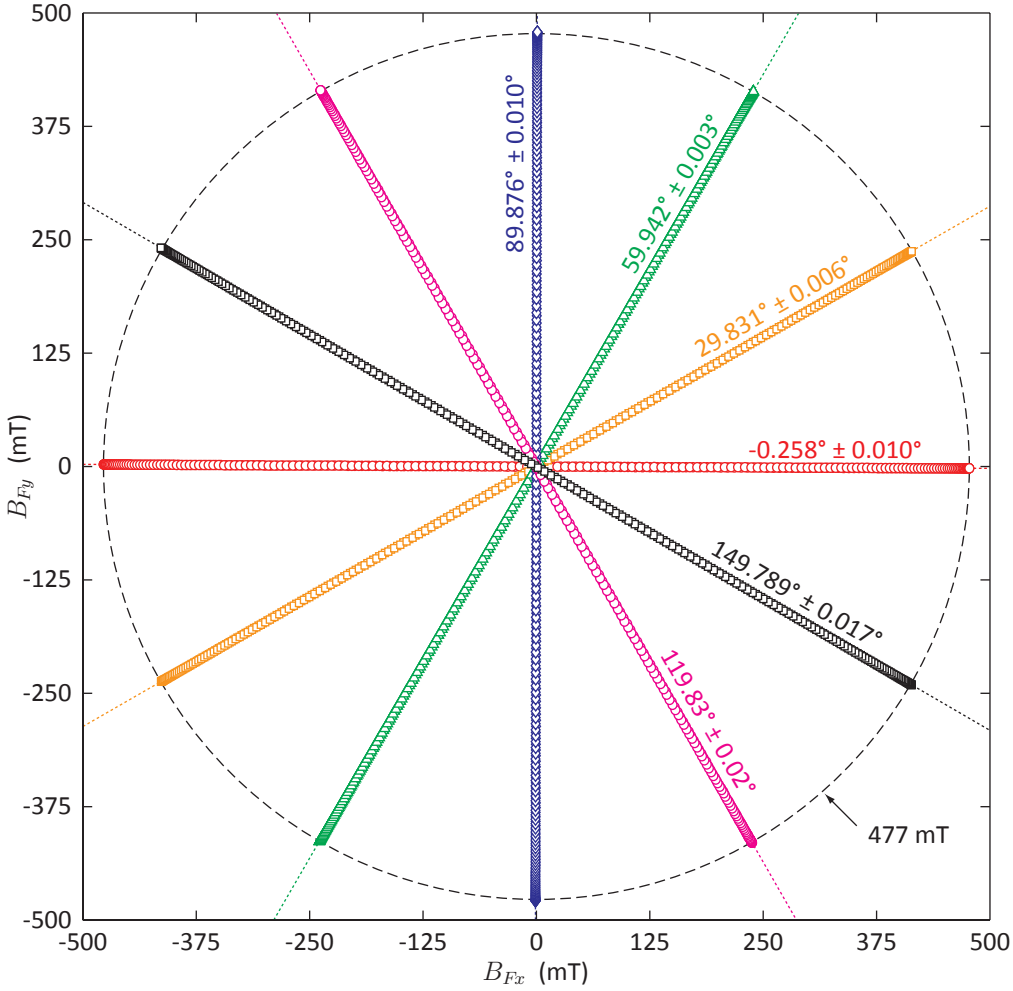

Figure 6.5: Plots of $\bar{\boldsymbol{B}}_{\boldsymbol{Fy}}$ vs $\bar{\boldsymbol{B}}_{\boldsymbol{Fx}}$ for $k_{max} = 16$ and θ_T values from 0° to 150° in increments of 30° with $B_{FT} = 477\,\mathrm{mT}$ at $f_{ex} = 50\,\mathrm{Hz}$ for the SL4P mounted on a feeder pipe sample. Linear fits to $\bar{\boldsymbol{B}}_{\boldsymbol{Fy}}$ vs $\bar{\boldsymbol{B}}_{\boldsymbol{Fx}}$ are shown as dotted lines. Slope values of $\boldsymbol{B}_{\boldsymbol{Fy},k}$ vs. $\boldsymbol{B}_{\boldsymbol{Fx},k}$ for $k = 1 \ldots k_{max}$ are used to calculate $\theta_{F,k}$, and the mean and standard deviation of $\theta_{F,k}$ over k are indicated next to each data series.

of θ_T and θ_F for the values in Figure 6.5 gives $(\theta_F - \theta_T) = -0.17° \pm 0.07°$.

Mean values of $B_{Fpk,k}$ and $B_{Frms,k}$ for the data in Figure 6.5 are $B_{Fpk} = (478 \pm 1)\,\mathrm{mT}$ and $B_{Frms} = (338.1 \pm 0.6)\,\mathrm{mT_{rms}}$, respectively. Since B_{FT} was set to 477 mT, excitation field levels were systematically larger than target values by 0.2%, with a relative precision of ±0.2%.

Chapter 7

BN Modelling

To produce the measured BN waveform, BN emitted at depth in the sample must propagate to the surface and induce a voltage in the pickup coil windings. This voltage drives a current through the pickup coil, its associated cabling, and a preamplifier input impedance before being isolated, amplified, and sampled by a analog to digital converter (ADC). To better understand this process, this Chapter presents two models that examine the propagation of single frequencies in the BN power spectrum through the system.

- Section 7.1 presents a model of the pickup coil sensing depth, as modulated by the excitation field, and estimates the detected BN depth using a simple model for BN emissions.
- In Section 7.2 the transfer function between the pickup coil and preamplifier input is modelled using electric circuit theory, and calculations for the various circuit components are provided.

7.1 BN Depth Penetration

The penetration depth of BN in feeders is required to determine the volume over which stress effects are measured. This section presents a multi-frequency model used to estimate the BN penetration depth and other aspects of the BN response as a function of the excitation field.

The model applies the solutions for plane electromagnetic waves with normal incidence on conducting materials, described in Section 2.5. In a good conductor with a linear isotropic differential permeability (μ_d) and conductivity (σ_e), electromagnetic waves with frequency (f) propagate as damped harmonic oscillations with an exponential attenuation length [27]:

$$\delta\{f, \mu_d\} = \sqrt{\frac{1}{\mu_0 \mu_d \sigma_e \pi f}}, \tag{7.1}$$

a phase velocity $2\pi f\delta$, and a wavelength $2\pi\delta$. However, in most ferromagnetic materials, μ_d is an nonlinear function of $\vec{B}$, and may be anisotropic.

Let B_{ex} be the excitation field propagating into the sample, with amplitude B_0 at the sample surface and frequency f_{ex}. In SA-106 grade B steel, with $\sigma_e = 5.15 \times 10^6\,\mathrm{S/m}$ and $\mu_d \gg 1$, the 7 mm feeder thickness is significantly larger than $\delta\{f_{ex}, \mu_d\}$ for f_{ex} values between 10 Hz and 100 Hz. However, since B_{ex} changes μ_d as it propagates, the attenuation characteristics of the excitation field are not the pure exponential decay described by equation (2.43). In general, magnetic fields propagate further as the sample saturates, due to the decrease in μ_d associated with saturation, and must be modelled numerically (such as in the tetrapole finite element models in Chapter 5). Rather than solve a finite element model for every configuration of the

excitation field, in this model B_{ex} is approximated as:

$$B_{ex}\{z,t\} = B_0 \exp\left\{-\frac{z}{\delta_{ex}}\right\} \cos\left\{\frac{z}{\delta_{ex}} - 2\pi f_{ex} t\right\}, \tag{7.2}$$

where $\delta_{ex} = \delta\{f_{ex}, \mu_{ex}\}$, and μ_{ex} is an average permeability that varies with B_0.

To calculate μ_{ex}, and later μ_d throughout the sample, a relationship between μ_d and $\vec{B}$ is required. Figure 7.1 shows μ_d for the SA-106 Grade B *MagNet* material plotted as a function of $|\vec{B}|$. An exponential fit*:

$$\mu_d\left\{\vec{B}\right\} = 4985 \exp\left\{-2.596|\vec{B}|\right\}. \tag{7.3}$$

is shown to approximately follow the data. Equation (7.3) was then integrated from 0 to B_0 to calculate μ_{ex} as:

$$\mu_{ex} = 4985 \cdot \frac{1 - \exp\{-2.596 B_0\}}{2.586 B_0}. \tag{7.4}$$

Using B_0 and f_{ex} to calculate μ_{ex} and δ_{ex}, equation (7.2) can be used to model B_{ex}. For example, Figure 7.2a shows B_{ex} in the first 1 mm of the sample surface as a function of the phase at the sample surface ($\phi_0 = 2\pi f_{ex} t$) for $B_0 = 1.5$ T and $f_{ex} = 30$ Hz. The excitation field is seen to vary at the surface from $+1.5$ T to -1.5 T and propagates into the sample (shifting to the right of the page) as z increases. Substituting B_{ex} from Figure 7.2a into equation (7.3) gives $\mu_d\{B_{ex}\}$, shown in Figure 7.2b. As is expected, μ_d is a maximum when $B_{ex} = 0$, and decreases with $|B_{ex}|$.

As B_{ex} propagates into the sample the domain structure reconfigures and BN is emitted. BN emissions can be treated as broad-band plane wave sources at the depth

*There is no physical argument for choosing an exponential, other than the quality of the fit.

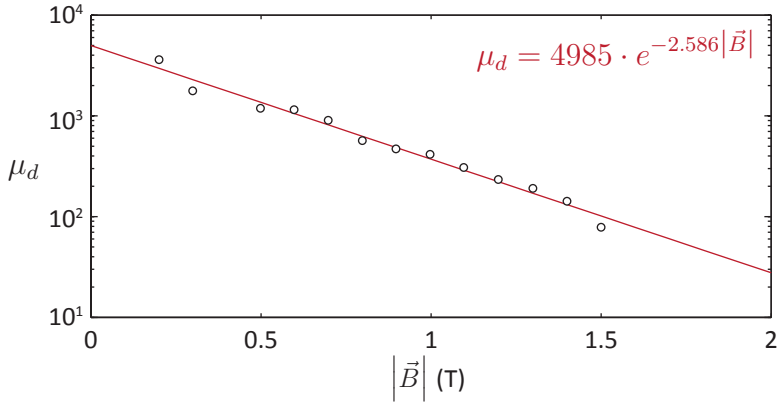

Figure 7.1: Differential permeability (μ_d) as a function of flux density (B) for the *MagNet* SA-106 Grade B material. The line is an exponential fit to the data.

where they are produced. This is because BN field perturbations share the orientation of the excitation field (on average), and the excitation field is approximately uniform over the sensing area of the pickup coil. Each frequency in the BN power spectrum (f_{bn}) has a characteristic phase velocity that is proportional to $(f_{bn}/\mu_d)^{1/2}$. If $f_{bn} \gg f_{ex}$, the phase velocity of the BN is much larger than that of the excitation field, and it may be approximated that BN is detected instantaneously on excitation field time scales. It is assumed in this model that the BN fields are sufficiently small that they do not change μ_d as they propagate through material.

As the BN propagates back to the sample surface it is attenuated according to $\delta\{f_{bn}, \mu_d\{B_{ex}\{z,t\}\}\}$. The detected fraction of BN emissions n µm into the sample ($\mathcal{A}_{[n]}$) was calculated as:

$$\mathcal{A}_{[n]} = \prod_{j=1}^{n} \exp\left\{\frac{-1\,\mu\text{m}}{\delta\{f_{bn}, \mu_d\{B_{ex}\{j \cdot 1\,\mu\text{m}, t\}\}\}}\right\}, \tag{7.5}$$

and is shown for $f_{bn} = 3\,\text{kHz}$ in Figure 7.2c. $\mathcal{A}$ can also be interpreted as the modulation of the pickup coil sensing depth by B_{ex}. Figure 7.2c shows that the mean

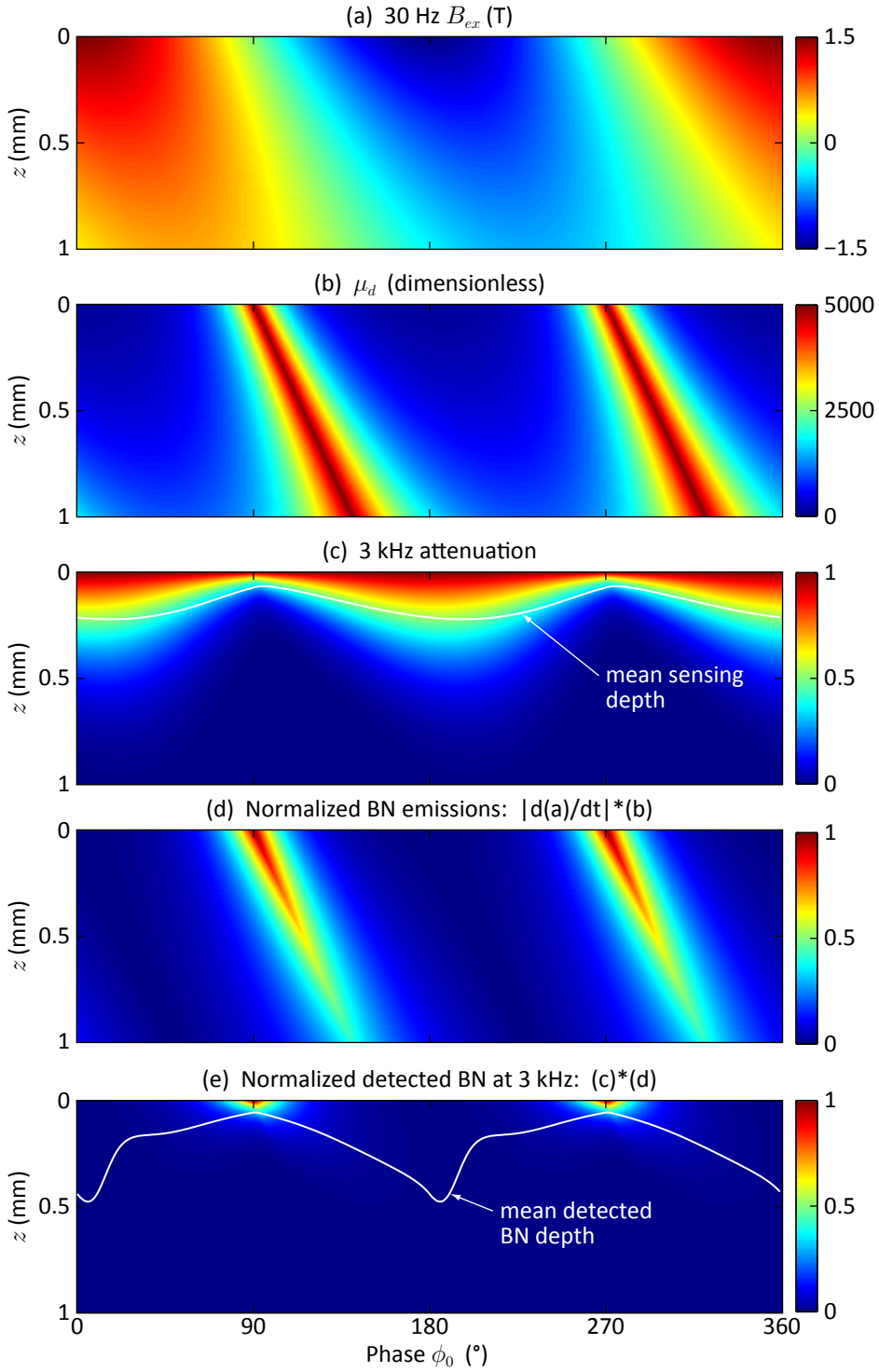

Figure 7.2: BN depth model results for $B_0 = 1.5\,\mathrm{T}$, $f_{ex} = 30\,\mathrm{Hz}$, and $f_{bn} = 3\,\mathrm{kHz}$.

sensing depth for $B_0 = 1.5\,\mathrm{T}$, $f_{ex} = 30\,\mathrm{Hz}$, and $f_{bn} = 3\,\mathrm{kHz}$ varies between 60 µm and 220 µm.

While Figure 7.2c represents the sensing depth for the pickup coil, to estimate the emission depth of the detected BN requires a model for the BN emission intensity. The intensity of BN emissions from a given volume depends on the domain configuration and the direction and speed at which the flux through the volume is changing. A simple model was constructed by assuming $\mu_d\{B_{ex}\}$ is proportional to the number of domains in a given volume, since it is maximum at $B_{ex} = 0$ and minimum at saturation, and the product of $\mu_d\{B_{ex}\}$ and $|\mathrm{d}B_{ex}/\mathrm{d}t|$ was taken as an estimate for the BN emissions from a given depth and time, which is shown in Figure 7.2d. This model shows BN emissions are produced primarily when $B_{ex} \approx 0$ (maxima of $|\mathrm{d}B_{ex}/\mathrm{d}t|$), and decrease in amplitude with depth, due to the attenuation of B_{ex}.

The product of $\mathcal{A}$, $\mu_d\{B_{ex}\}$ and $|\mathrm{d}B_{ex}/\mathrm{d}t|$ (i.e., the product of Figures 7.2c and 7.2d), shown in Figure 7.2e, was taken as the depth and time distribution of the detected BN. Figure 7.2e indicates that peak BN emissions are detected when B_{ex} at the sample surface is a minimum. The sum of the detected BN over z was taken as the BN envelope, and the mean and standard deviation of the detected BN depth were estimated. The mean detected BN depth is indicated on Figure 7.2e, and is a minimum during peak detected BN emissions at ϕ_0 values of 90° and 270°.

Figure 7.3 shows the mean sensing depth, BN envelope and mean detected BN depth using the above model for B_0 values from 0.25 T to 1.5 T. Figure 7.3a shows that B_{ex} modulates the mean sensing depth for $f_{bn} = 3\,\mathrm{kHz}$, with a minimum sensing depth of 60 µm to a maximum sensing depth of 220 µm at $B_0 = 1.5\,\mathrm{T}$. In Figure 7.3b, the BN envelope is shown to be a maximum at the minimum sensing depth, which

corresponds to ϕ_0 values when B_{ex} at the sample surface is ≈ 0. As B_0 increases, the same BN emissions occur in less time (i.e., $|\mathrm{d}B_{ex}/\mathrm{d}t|$ increases), and the envelope peak increases in amplitude. Figure 7.3c shows that the mean detected BN depth is actually larger than the mean sensing depth in Figure 7.3a, because the peak BN emissions are being generated deeper in the sample than the pickup coil sensing depth.

Using this particular model for BN emissions, BN occurs primarily when $B_{ex} \approx 0$. While the peak of the BN envelope coincides with the BN emissions from the sample surface, as ϕ_0 varies from 90° and 270°, the BN envelope represents BN from increasing depth in the sample. Figure 7.3c shows that mean detected BN depths at $f_{bn} = 3\,\mathrm{kHz}$ may approach $480\,\mu\mathrm{m}$ with $B_0 = 1.5\,\mathrm{T}$, though these emissions will be strongly attenuated. Weighting the mean detected BN depth by the BN envelope, the BN power at 3 kHz with $B_0 = 1.5\,\mathrm{T}$ has a mean depth of $120\,\mu\mathrm{m}$ over one excitation cycle. As B_0 decreases to 0 T, this average sensing depth over the cycle decreases to $\sim 50\,\mu\mathrm{m}$ for $f_{bn} = 3\,\mathrm{kHz}$.

Figure 7.4 shows how the mean sensing depth, BN envelope and mean detected BN depth vary with f_{bn} for $f_{ex} = 30\,\mathrm{Hz}$ and $B_0 = 1.5\,\mathrm{T}$. Figure 7.4a shows that the mean sensing depth decreases as approximately $f_{bn}^{-1/2}$, with a minimum sensing depths for f_{bn} values of 3 kHz, 30 kHz and 300 kHz of $60\,\mu\mathrm{m}$, $20\,\mu\mathrm{m}$ and $5.3\,\mu\mathrm{m}$, respectively, and maximum sensing depths of $220\,\mu\mathrm{m}$, $100\,\mu\mathrm{m}$ and $35\,\mu\mathrm{m}$, respectively. In Figure 7.4b, the BN envelope is shown to scale between the three f_{bn} values, with deviations occurring near ϕ_0 values of 0° and 180° where detected BN emissions are a minimum. This indicates that the BN power spectrum is not expected to vary strongly with ϕ_0. Comparison between Figures 7.4a and 7.4c shows that for f_{bn} values of 30 kHz and 300 kHz, there is little difference between the sensing depth and detected depths.

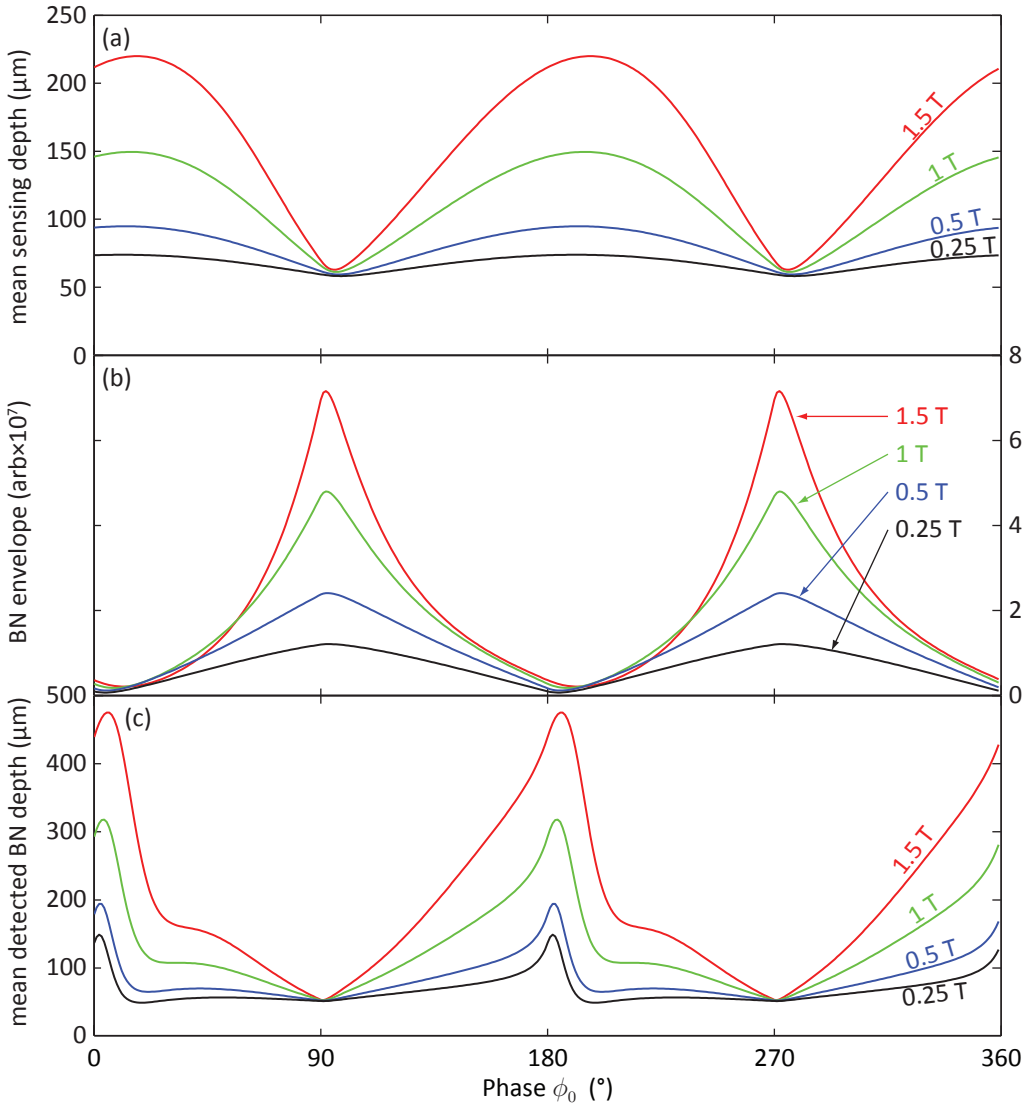

Figure 7.3: BN depth model results for (a) the mean pickup coil sensing depth, (b) the BN envelope, and (c) the mean detected BN depth with $f_{ex} = 30\,\text{Hz}$, $f_{bn} = 3\,\text{kHz}$, and B_0 values from 0.25 T to 1.5 T.

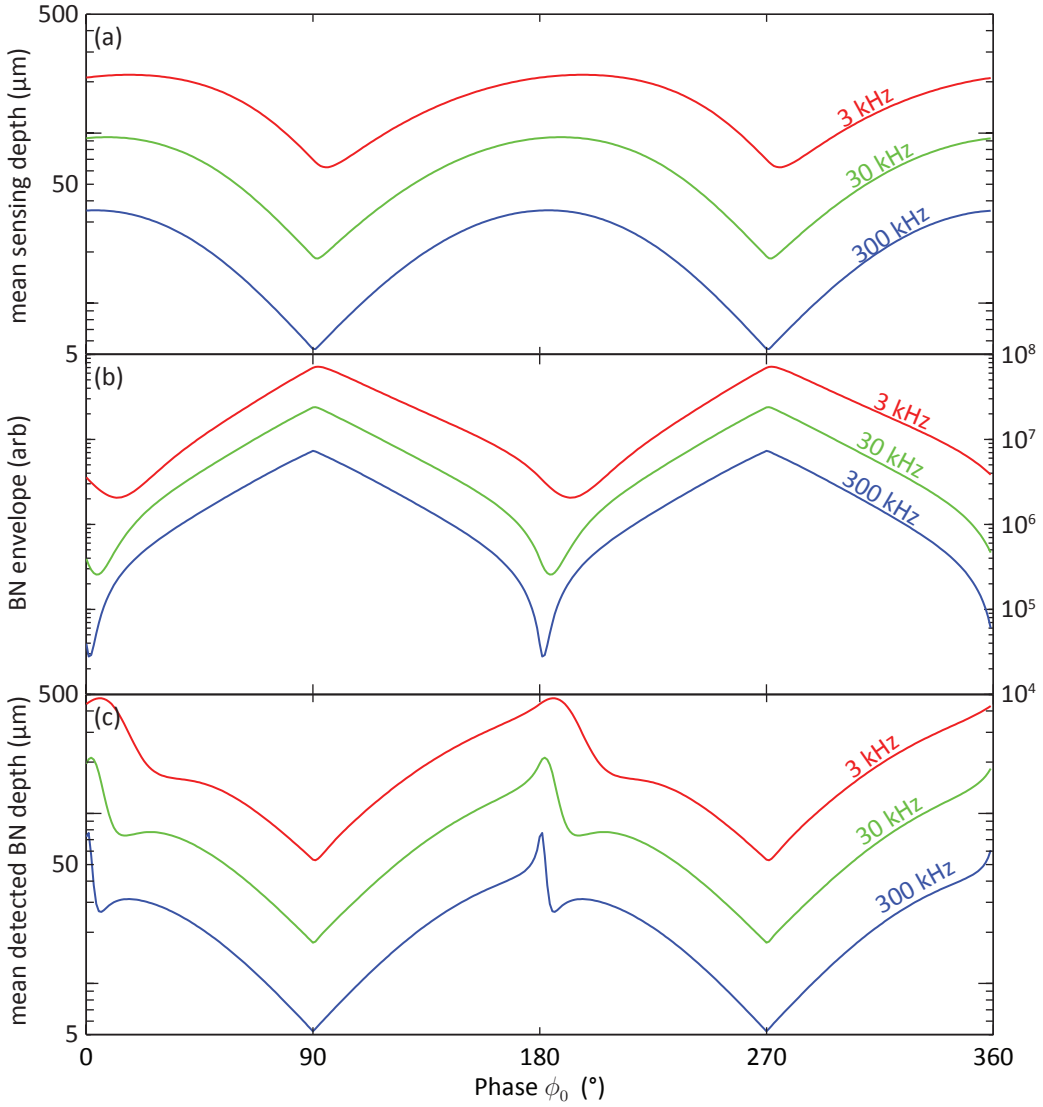

Figure 7.4: BN depth model results for (a) the mean pickup coil sensing depth, (b) the BN envelope, and (c) the mean detected BN depth with $f_{ex} = 30\,\text{Hz}$, $B_0 = 1.5\,\text{T}$, and f_{bn} values of 3 kHz, 30 kHz and 300 kHz.

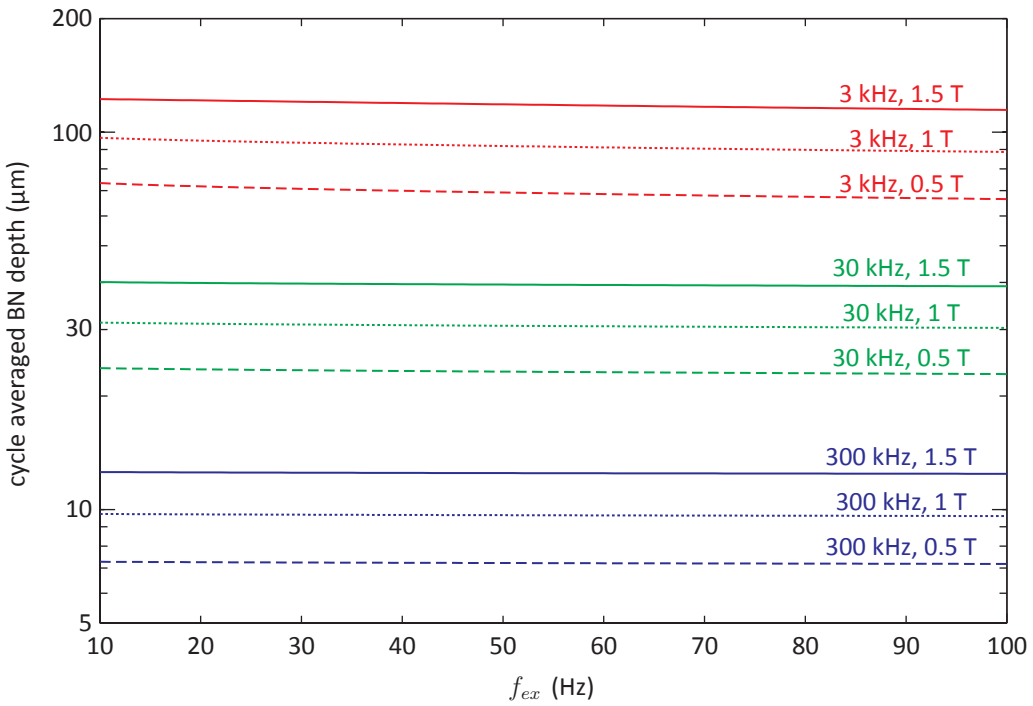

Figure 7.5: BN depth model results for the mean detected BN depth averaged over one excitation cycle as a function of f_{ex}, for f_{bn} values of 3 kHz, 30 kHz and 300 kHz and B_0 values of 1.5 T, 1 T and 0.5 T.

This is because the higher BN frequencies are attenuated sufficiently rapidly that they only represent the near surface field.

In this model, varying f_{ex} changes the penetration of the excitation field, and thus changes the temporal and spatial conditions for BN generation. Figure 7.5 shows the cycle-averaged BN depth (computed by taking the mean detected BN depth and weighting with respect to the BN envelope) as a function of f_{ex} for three f_{bn} values and three B_0 values. The cycle averaged BN depth is shown to decrease with increasing f_{ex}, but this decrease is negligible in comparison with the effects of varying B_0 or f_{bn}.

The above result indicates that so long as B_0 is reproduced, similar BN results will be obtained for f_{ex} values between 10 Hz and 100 Hz. The model indicates that BN

depth sensitivity can be increased by increasing B_0. In a practical BN NDE system, this means increasing B_{FT} (the flux through the feedback coils), or increasing f_{ex} (while keeping B_{FT} constant) and relying on flux conservation to increase the surface field amplitude. It follows that increasing f_{ex} makes more efficient use of the flux through the feedback coils, as more of the flux is going to the surface region where the detected BN is being generated.

The model presented in this section serves as a guide when attempting to quantify the depth penetration of BN, and thus the volume over which stress-sensitive effects may be measured. With B_0 approaching saturation at 1.5 T, the model predicts a mean detected BN depth over one excitation cycle of 13 µm at 300 kHz up to 120 µm at 3 kHz. The average sensing depth of a measured BN waveform will depend on frequency content of the BN power spectrum, but will likely be between these two values. The model shows that further depth information may be resolved in the future by evaluating the BN envelope as a function of ϕ_0.

7.2 BN Pickup Circuit Model

The typical BN waveform can be considered a superposition of transient pulses with peak to peak amplitude of ~ 1 mV and detectable frequency content up to 300 kHz. A *National Instruments*® PCI-6133 Multifunction DAQ (PCI-6133) [52], with a maximum sampling frequency of 2.5 MHz and 14 bits of resolution across ± 1.25 V, was selected to meet the BN sampling requirements. A low noise preamplifier with ~ 60 dB gain is required to match the coil voltage levels to the ADC input dynamic range.

The pickup coil, the cabling and connectors, and the preamplifier input forms an analog circuit whose transfer function modifies the detected BN power spectrum.

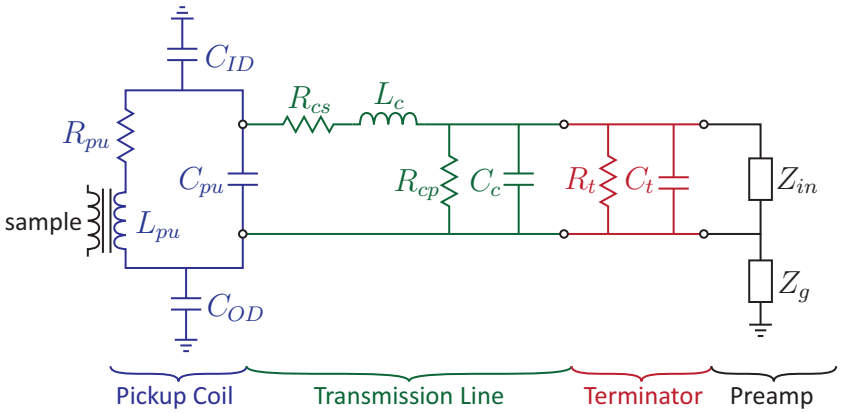

Figure 7.6: The pickup coil electric circuit model. The circuit consists of the pickup coil, a cable with non-negligible capacitance, a terminator, and the preamplifier input impedance.

Table 7.1: Pickup coil electric circuit model component values.

Component	Value	Unit
L_{pu}	$121 \cdot f_{bn}^{-0.0211} - 3i$	µH
R_{pu}	5.4	Ω
C_{pu}	1	pF
R_{cs}	0	Ω
L_c	0.38	µH
C_c	150	pF
R_{cp}	∞	Ω
R_t	50k, 5k, 500, 50	Ω
C_t	0, 1n, 100n, 1µ	F
Z_{in}	1	GΩ

Figure 7.6 shows an electric circuit model for the system, consisting of: the pickup coil (L_{pu}, R_{pu}, C_{pu}, C_{OD} and C_{ID}), cabling modelled as a transmission line (R_{cs}, L_c, C_c and R_{cp}), an optional terminating resistor (R_t), a tuning capacitor (C_t), and the preamplifier input (Z_{in} and Z_g). The pickup coil model and cabling considerations are presented in detail in Appendix E, along with calculations for typical component values. The component values used in this model are summarized in Table 7.1.

The pickup circuit model is evaluated as follows:

- In Section 7.2.1 the transfer function for voltages induced in the pickup coil to the preamplifier impedance is evaluated. A resonance between L_{pu} and the circuit capacitance is identified, and it is shown that R_t can be used to damp the resonance, while C_t can be used to tune the resonant frequency.
- Section 7.2.2 presents grounding considerations for the circuit.
- In Section 7.2.3 the actual component values and grounding configuration used for the measurements in this thesis are provided.

7.2.1 Transfer Function

An ideal voltage measurement requires that an infinite impedance be connected parallel to the device across which the voltage is to be measured. It can be deduced from Figure 7.6 that the BN voltage never 'sees' an open circuit, since C_{pu} and C_c are always in parallel with L_{pu}. Using series and parallel impedance relations, and approximating $R_{cp} = \infty$ and $R_{cs} = 0$ (a lossless cable), the circuit in Figure 7.6 can be reduced to find the total complex impedance (Z_{tot}) seen by a voltage induced within the inductor L_{pu}:

$$Z_{tot} = i\omega L_{pu} + R_{pu} + \cfrac{1}{i\omega C_{pu} + \cfrac{1}{i\omega L_c + \cfrac{1}{\cfrac{R_t + Z_{in}}{R_t Z_{in}} + i\omega\left(C_c + C_t\right)}}}, \tag{7.6}$$

where $\omega = 2\pi f_{bn}$ is the angular frequency.

Since the amplified signal is proportional to the voltage across Z_{in}, Kirchoff's current and voltage laws can be used to find the ratio of the voltage across Z_{in} (V_{in}) to the voltage developed across the inductor windings (V_{bn}), which is the transfer function ($\mathcal{F}$) of the circuit:

$$\mathcal{F} = \frac{V_{in}}{V_{bn}} = \frac{1}{Z_{tot}\left[\left(\frac{R_t+Z_{in}}{R_t Z_{in}} + i\omega\left(C_c + C_t\right)\right)\left(1+\omega^2 L_c C_c\right) - i\omega C_c\right]}. \tag{7.7}$$

$\mathcal{F}$ is often expressed as the gain and phase response of the circuit. The gain ($\mathcal{F}_G$) in dB is defined as:

$$\mathcal{F}_G = 20 \cdot \log_{10}\left(\left(\overline{\mathcal{F}} \cdot \mathcal{F}\right)^{\frac{1}{2}}\right), \tag{7.8}$$

where $\overline{\mathcal{F}}$ is the complex conjugate of $\mathcal{F}$. The phase ($\mathcal{F}_\phi$) is given by:

$$\mathcal{F}_\phi = -\arctan\frac{\Im\{\mathcal{F}\}}{\Re\{\mathcal{F}\}}. \tag{7.9}$$

To minimise distortion of the BN measurement, $\mathcal{F}_G$ and $\mathcal{F}_\phi$ must be approximately constant throughout the BN power spectrum. Using the component values indicated in Table 7.1, $\mathcal{F}$ was evaluated in *Maple™12* from 1 kHz to 10 MHz with various values of R_t and C_t with a $Z_{in} = 1\,\mathrm{G\Omega}$ preamplifier.

Damping (R_t)

Figures 7.7(i) and 7.7(ii) show $\mathcal{F}_G$ and $\mathcal{F}_\phi$ for $C_t = 0\,\mathrm{pF}$ and 4 values of R_t from $50\,\mathrm{k\Omega}$ to $50\,\Omega$. A resonance peak is observed in the transfer function at 1.35 MHz in the $R_t = 50\,\mathrm{k\Omega}$ and $R_t = 5\,\mathrm{k\Omega}$ plots. The 1.35 MHz resonance is that between $\Re\{L_{pu}\}$ and the total distributed parallel capacitance ($C_c + C_{pu} + C_t$). The presence

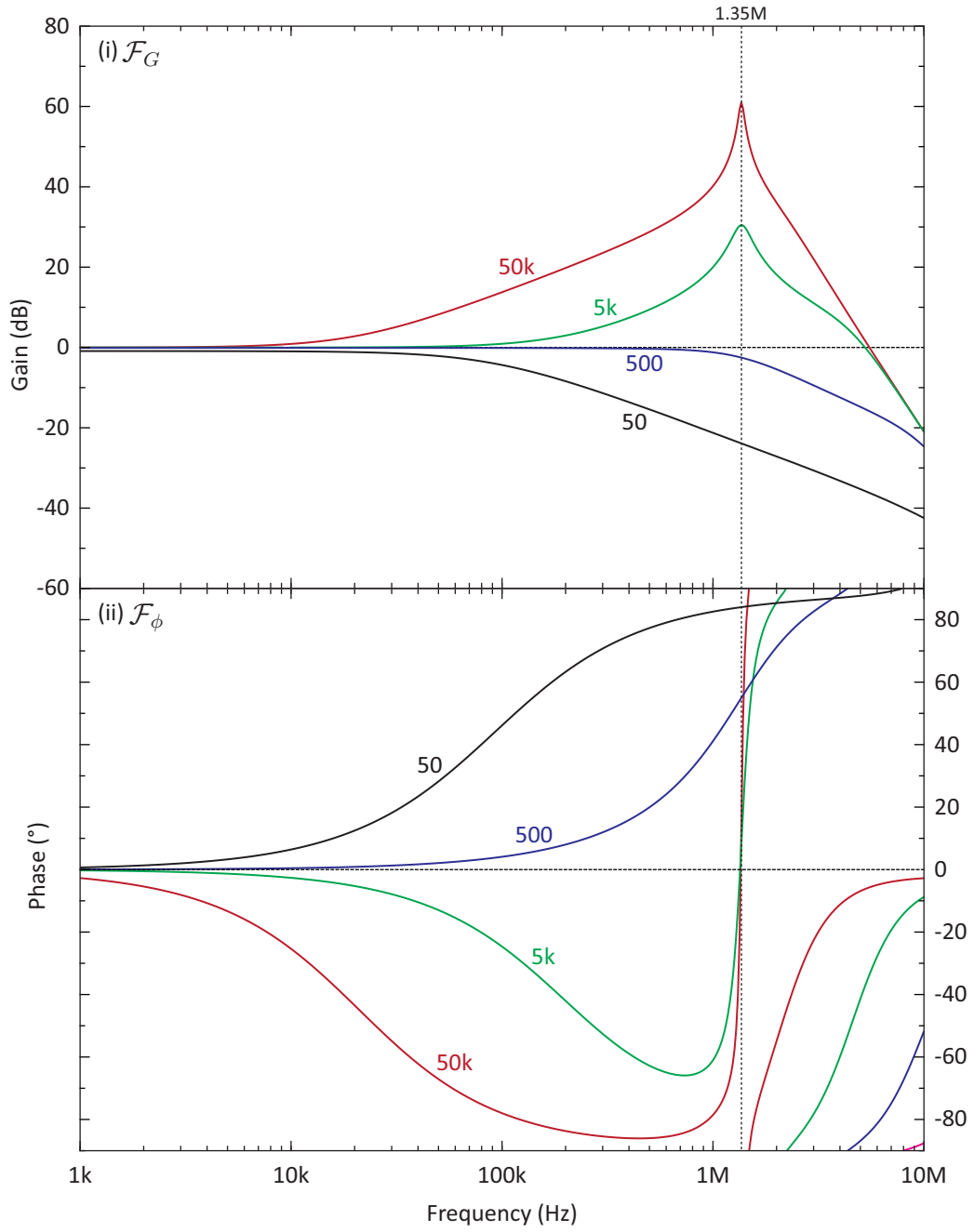

Figure 7.7: Pickup voltage to preamplifier input transfer function (i) gain $\mathcal{F}_G$ and (ii) phase $\mathcal{F}_\phi$ for the component values in Table 7.1 with $C_t = 0\,\mathrm{F}$ and R_t values of $50\,\mathrm{k\Omega}$, $5\,\mathrm{k\Omega}$, $500\,\Omega$ and $50\,\Omega$.

of $\Im\{L_{pu}\}$, R_{pu}, and L_c complicate $\mathcal{F}$, however the approximate resonant frequency (f_0) may be calculated by solving:

$$f_0 = \frac{1}{2\pi\sqrt{\Re\{L_{pu}\} \cdot (C_{pu} + C_c + C_t)}}, \tag{7.10}$$

where L_{pu} is a complex function of frequency. This gives $f_0 = 1.37\,\text{MHz}$ for $C_t = 0\,\text{F}$ and the component values in Table 7.1. R_t may therefore be considered the damping resistor in a parallel RLC circuit.

Figure 7.7 shows that if $R_t \gg 500\,\Omega$ the resonance adds significant gain and distorts the phase between 1 kHz and 1 MHz. Alternatively if $R_t \ll 500\,\Omega$, then $\omega\Re\{L_{pu}\}$ becomes equal to R_t at some frequency significantly below 1 MHz ($\sim 80\,\text{kHz}$ for $R_t = 50\,\Omega$), resulting in significant attenuation of higher frequencies in the BN power spectrum, effectively low-pass filtering the BN waveform. A value of $R_t = 500\,\Omega$ is near the critical damping point, where $\mathcal{F}_G \approx 0\,\text{dB}$ up to $\sim 300\,\text{kHz}$ and $\mathcal{F}_\phi$ is $\sim 0^\circ$ up to $\sim 15\,\text{kHz}$ and increases smoothly through the resonance.

The choice of R_t has a strong influence on the measured BN power spectrum. In cases where the preamplifier bandwidth produces high frequency attenuation, choosing a large R_t and under-damping the resonance may reduce the overall BN distortion. Conversely, if a significant amount of high frequency noise is coupling into the system, choosing a lower R_t may be necessary to damp the noise. In general, for lab work and fundamental studies, choosing R_t to maximally flatten $\mathcal{F}$ across the BN power spectrum is recommended. This is not necessarily the same as critically damping the resonance, particularly when L_{pu} rolls off as in Figure 5.17. Such a roll off may significantly increase f_0, but still result in a non-flat $\mathcal{F}$ for the frequencies of interest.

Note that these calculations were performed with $Z_{in} = 1\,\text{G}\Omega$. Wide-bandwidth

voltage preamplifiers are generally available with high ($> 100\,\mathrm{k}\Omega$) and low ($\sim 50\,\Omega$) Z_{in}. It is recommended that only high Z_{in} preamplifiers be considered, as low Z_{in} preamplifiers will over-damp the resonance and attenuate high frequency content in the BN power spectrum.

Tuning (C_t)

Equation (7.10) indicates that the resonant frequency f_0 is proportional to $\Re\{L_{pu}\}^{-1/2}$ and $(C_c + C_{pu} + C_t)^{-1/2}$. Since C_t may be set to 0, and C_{pu} does not significantly change with the number of pickup coil turns (N_{pu}), f_0 may only be increased significantly by either decreasing L_{pu}, or decreasing C_c. Conversely, once L_{pu} and C_c are set by pickup coil sensitivity and probe access considerations, f_0 may be decreased using a tuning capacitor C_t.

For a given magnetic circuit design, equation (2.54) requires $L_{pu} \propto N_{pu}^2$. Thus, decreasing N_{pu} by a factor of 10 increases f_0 by the same amount. The pickup coil modelled in Section 5.2 and on the SL4P has $N_{pu} = 100\,\mathrm{turns}$. Alignment and structural integrity of small multi-layer pickup coils are non-trivial issues. Thus N_{pu} should be selected to ensure a predictable and robust coil geometry, and sufficiently small that f_0 is above the upper detectable frequencies in the BN power spectrum.

Cable lengths must be selected according to practical access limitations. Since C_c is linearly proportional to the length of cabling used, decreasing cable lengths by a factor of 10 only increases f_0 by a factor of $\sqrt{10}$. Selecting a low-capacitance cable is also an option to maximise f_0. Ideally a wide-bandwidth voltage preamplifier circuit would be integrated into the probe or pickup coil housing to minimize cable lengths, however an integrated preamplifier is beyond the scope of this thesis.

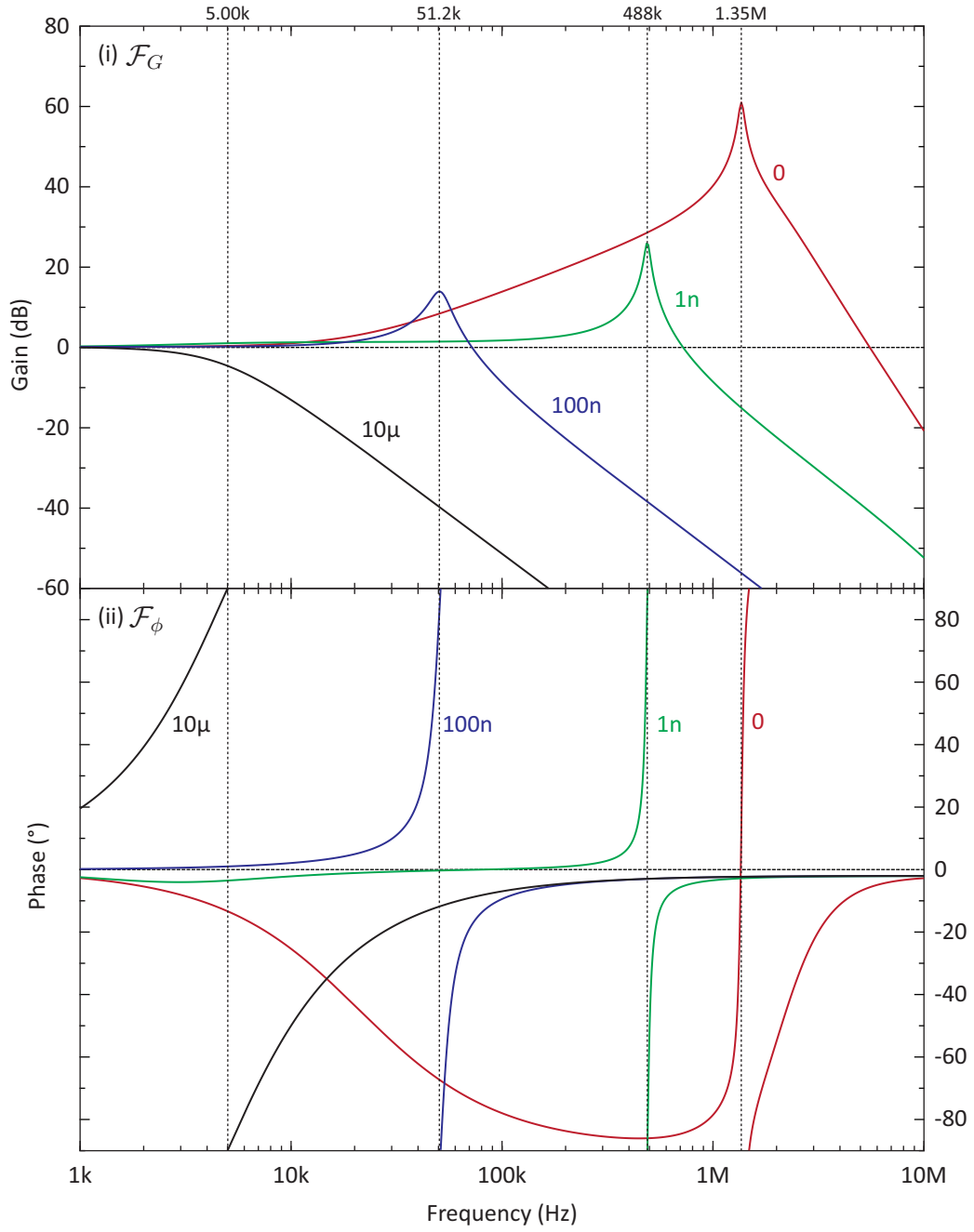

Figure 7.8: Pickup voltage to preamplifier input transfer function (i) gain $\mathcal{F}_G$ and (ii) phase $\mathcal{F}_\phi$ for the component values in Table 7.1 with tuning capacitor (C_t) values of 0 F, 1 nF, 100 nF and 10 µH and $R_t = 50\,\text{k}\Omega$

Figures 7.8(i) and 7.8(ii) show $\mathcal{F}_G$ and $\mathcal{F}_\phi$ for C_t values of 0 F, 1 nF, 100 nF and 10 µH and $R_t = 50\,\mathrm{k}\Omega$ in order to show the tuning effect of C_t. For each value of C_t the resonant frequency is indicated. Values of f_0 in Figure 7.8 are in agreement with equation (7.10) to better than 1%. The decreasing amplitude of the resonant peaks with C_t in Figure 7.8 indicates that the damping requirements of the circuit are reduced with larger C_t. If C_t is used to amplify the BN power spectrum in order to overcome noise, R_t may be increased to as much as desired, or until the preamplifier inputs saturate.

7.2.2 Grounding Considerations

In Figure 7.6 the pickup coil is shown to be capacitively coupled to ground through C_{OD} and C_{ID}. Similarly, the preamplifier is coupled to ground through Z_g. Depending on the type of preamplifier used, the measurement may either be purely differential, in which case $Z_g \approx \infty$, pseudo-differential, where Z_g is finite and specified, or single-ended, where $Z_g \approx 0$. In the case of differential preamplifier configurations, equation (7.7) is likely a sufficient representation of the transfer function. If the amplifier is single-ended however, setting Z_g to zero shorts either C_{OD} (as is the case in Figure 7.6) or C_{ID} to ground, placing an additional parallel capacitance across the circuit.

In most cases, C_{OD} and C_{ID} are comparable to C_{pu} or less, and thus are small compared to the cable capacitance C_c and any tuning capacitor C_t. However, if C_{OD} or C_{ID} are significant, they may decrease f_0 and change the damping requirements of the circuit. The transfer function in equation (7.7) is therefore a good model for differential measurements, and when $C_{OD} \geq C_{ID}$ and $C_{ID} \ll (C_c + C_t + C_{pu})$. To maximise f_0 for single-ended measurements, the pickup coil leads may be connected

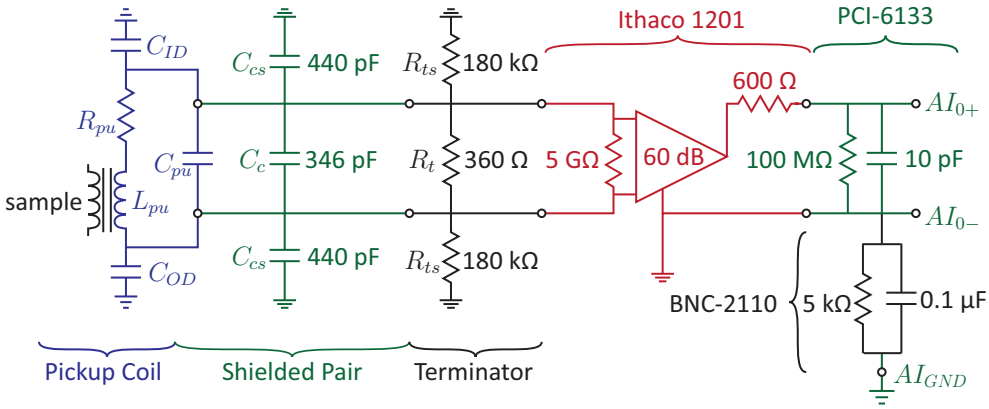

Figure 7.9: Schematic for the pickup coil electric circuit, including the *Ithaco 1201* preamplifier in differential mode, the PCI-6133 DAQ, and the BNC-2110 connector block grounding configuration.

such that the larger of C_{OD} or C_{ID} is shorted to ground.

7.2.3 Pickup Coil Circuit

To meet the preamplifer requirements, an *Ithaco 1201* differential preamplifier with an input impedance (Z_{in}) of 5 GΩ, bandwidth from DC to 400 kHz, input noise of $7\,\mathrm{nV}/\sqrt{\mathrm{Hz}}$, and continuously variable gain from 20 dB to 88 dB was selected to provide the 60 dB gain required [59]. The BN pickup coil circuit is summarized in Figure 7.9, with equivalent circuits for the *Ithaco 1201* in differential mode, the BNC-2110[†] and the PCI-6133 indicated with the appropriate component values.

Cabling between the pickup coil and preamplifier is shown in Figure 7.9 as a lossless shielded twisted pair, with the shield connected to ground and coupled to the pair through capacitors C_{cs}. For the 1.5 m cable used, C_c was measured as 346 pF. Of the 346 pF, 240 pF is the direct coupling between the pair, and the additional 106 pF is attributed to the connectors. Resistors R_{ts} are 180 kΩ, and are required to

[†]A BNC connector block for the PCI-6133 [60].

stabilise the *Ithaco 1201* in differential mode. Cabling between the *Ithaco 1201* and the BNC-2110 is not indicated, and is considered to be included in the *Ithaco 1201* transfer function. The BNC-2110 is configured in the 'floating source' mode, and the PCI-6133 is configured to perform a fully differential measurement at its input terminals AI_{0-} and AI_{0+}. The BNC-2110 internally connects the PCI-6133 AI_{GND} pin as shown.

Using the pickup coil component values in Section E.1 and the pickup coil transfer function in equation (7.7), an optimal value of R_t was found to be $\sim 355\,\Omega$. Using the transfer function in equation (7.7), the combination of $C_c = 346\,\text{pF}$ and $R_t = 355\,\Omega$ gives a pass-band gain of $-0.15\,\text{dB}$ and a $-3\,\text{dB}$ bandwidth of 900 kHz. The total bandwidth of the circuit is limited by the 400 kHz *Ithaco 1201* preamplifier bandwidth.

Chapter 8

BN Analysis Methodology

Pickup coil waveforms consist of broad-band BN bursts combined with low frequency coupling to the magnetic circuit and background noise. Since domains do not form identically during each excitation cycle, the phase distribution of the BN is randomized. This has the consequence that time-based signal averaging reduces both BN and background noise power at similar rates, and requires that BN be analysed using statistical methods.

There is no standard statistical approach for BN analysis. Moreover, with the introduction of the flux-controlled excitation field developed in Chapter 4, and the modelling work in Chapters 5 and 7, there is additional information with regards to the excitation field and the pickup coil response that has not been investigated in previous BN analysis procedures.

This chapter presents the BN analysis approach implemented in *LabVIEW 8.2* for the system developed in this thesis, and serves to define the various BN parameters that are referenced in later chapters.

- In Section 8.1 the raw pickup coil voltage waveforms ($\boldsymbol{V_{bk},_k}$ and $\boldsymbol{V_{(BN+bk)},_k}$)

are analysed in time and frequency space to identify the various signals present in the measured waveforms.

- Section 8.2 presents the filtering operations applied to $\boldsymbol{V_{bk},_k}$ and $\boldsymbol{V_{(BN+bk),k}}$ in order to isolate the BN noise power as a function of frequency and excitation field phase.

- Section 8.3 presents the BN dynamic power spectrum ($\boldsymbol{\mathcal{D}_{BN}}$), which is the result of the filtering operations in Section 8.2.

- In Section 8.4 $\boldsymbol{\mathcal{D}_{BN}}$ is reduced to the RMS BN envelope ($\boldsymbol{BN_{env}}$) and the normalized BN power spectrum ($\boldsymbol{NPS_{BN}}$).

- In Section 8.5, $\boldsymbol{\mathcal{D}_{BN}}$ is further reduced to the BN energy (BN_E) and RMS BN (BN_{rms}) to indicate the total BN power and average BN amplitude, respectively.

- Section 8.6 provides an overview of typical BN measurement uncertainties.

All data shown are from the small feeder bend sample (see Section 9.1 for details) collected using the SL4P.

8.1 Raw Pickup Coil Data

Using the circuit presented in Figure 7.9, for each excitation iteration j the pickup coil voltage ($\boldsymbol{V_{(BN+bk),j}}$) is sampled for f_{ex}^{-1} at 2.5 MHz by the PCI-6133 DAQ. Other than the effects of the cable length and terminating resistor on the transfer function, no analog filtering on the pickup coil voltage is performed. For each iteration that meets the DC current and error thresholding criteria described in Section 4.2,

$\boldsymbol{V_{(BN+bk),j}}$ is stored in the array $\boldsymbol{V_{(BN+bk),k}}$ for $k = 1 \ldots k_{max}$. Prior to each set of BN measurements, the pickup coil voltage is sampled for $k = 1 \ldots k_{max}$ excitation periods in VF mode with 0 V held across all excitation coil channels. This data is stored in the array $\boldsymbol{V_{bk},k}$ and provides a measurement of the background noise in the pickup coil.

This section presents the raw $\boldsymbol{V_{bk},k}$ and $\boldsymbol{V_{(BN+bk),k}}$ waveforms in three ways: the raw voltage waveforms versus time, the power spectrum, and as the dynamic power spectrum. These three visualizations of the BN data are used to identify the various components of the pickup coil signal.

8.1.1 Waveforms

The $\boldsymbol{V_{(BN+bk),k}}$ waveforms are a combination of various noise sources and the magnetic flux rate through the pickup coil. The magnetic flux rate is correlated at low frequencies over multiple excitation cycles to produce a macroscopic field signal, and is uncorrelated at high frequencies to produce BN. Time-averaging $\boldsymbol{V_{(BN+bk),k}}$ over k_{max} excitation cycles according to:

$$\bar{\boldsymbol{V}}_{\boldsymbol{(BN+bk)}} = \frac{1}{k_{max}} \sum_{k=1}^{k_{max}} \boldsymbol{V_{(BN+bk),k}} \tag{8.1}$$

attenuates all noise (including BN) and signals that are not periodic with the excitation field. The $\boldsymbol{V_{bk},k}$ waveforms are measured with a negligible excitation field, and are used to identify signals and noise power that are independent of the magnetic excitation.

Figure 8.1 shows typical $\boldsymbol{V_{bk},k}$, $\boldsymbol{V_{(BN+bk),k}}$, and $\bar{\boldsymbol{V}}_{\boldsymbol{(BN+bk)}}$ waveforms from the

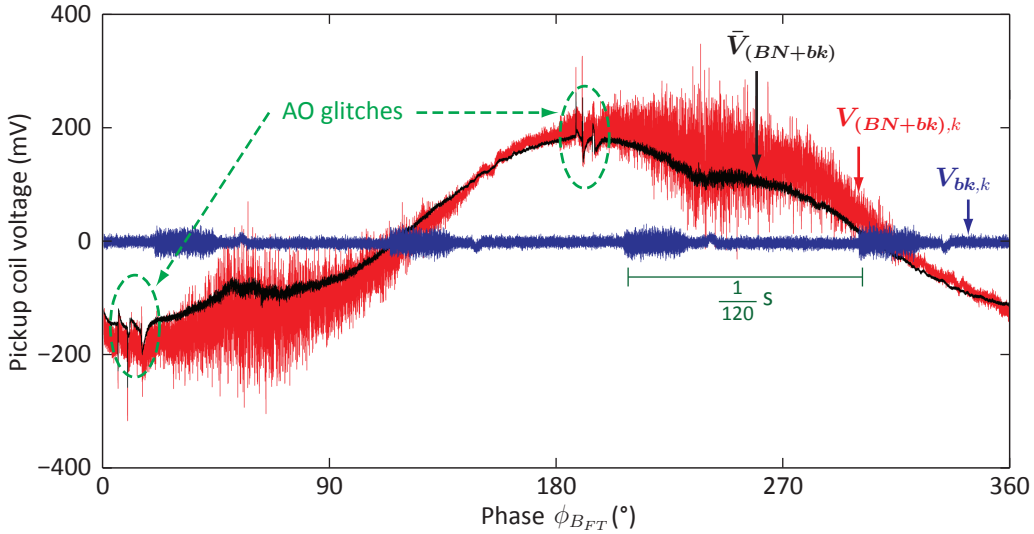

Figure 8.1: Typical background ($\boldsymbol{V_{bk,k}}$), raw ($\boldsymbol{V_{(BN+bk),k}}$), and time-averaged ($\boldsymbol{\bar{V}_{(BN+bk)}}$) pickup coil waveforms, with $f_{ex} = 31\,\text{Hz}$, $B_{FT} = 477\,\text{mT}$, $\theta_T = 45°$ and $k_{max} = 64$. Data are from the SL4P clamped on the small feeder bend.

SL4P mounted to a feeder pipe bend with $f_{ex} = 31\,\text{Hz}$, $B_{FT} = 477\,\text{mT}$, $\theta_T = 45°$, and $k_{max} = 64$. Note that DC offsets were removed from the data in Figure 8.1 as these are attributed to the input offset of the *Ithaco 1201* preamplifier. The typical $\boldsymbol{V_{(BN+bk),k}}$ waveform in Figure 8.1 features two broad-band BN bursts superimposed on a low frequency macroscopic field signal with periodicity matching that of the excitation field. The macroscopic field signal is attributed to misalignment of the pickup coil sensing axis to the sample normal, and to relative matching errors of the feedback coils (i.e., errors in $\mathcal{M}_p$).

Comparing $\boldsymbol{V_{(BN+bk),k}}$ with $\boldsymbol{\bar{V}_{(BN+bk)}}$ in Figure 8.1 illustrates the attenuation of both background noise and BN by time-averaging. At phase ($\phi_{B_{FT}}$) values of $\sim 10°$ and $\sim 190°$ in the $\boldsymbol{\bar{V}_{(BN+bk)}}$ waveform, Figure 8.1 shows 3 to 4 transient pulses that survive time-averaging (indicated as 'AO glitches'). The $\phi_{B_{FT}}$ positions of the pulses are correlated with the zero-crossings of $\boldsymbol{\bar{V}_{ref(p)}}$, which occur at the same time in

every cycle (provided the SL4P lift-off does not significantly change between cycles). The pulses are produced by discharges when the PCI-6229 $AO_{(p-1)}$ channels cross 0 V, and are referred to in *National Instruments* documentation as 'glitches' [61]. To attenuate the power associated with the AO glitches, the $AO_{(p-1)}$ channels are low-pass filtered through R_{ref1} and C_{ref} in Figure 4.1. Further reduction in glitch power may be achieved by decreasing the low-pass filter bandwidth, constructing an active glitch filter, or substituting a DAC without this feature for the PCI-6229.

The typical background noise waveform, $\boldsymbol{V_{bk},_k}$ in Figure 8.1, exhibits a burst of noise every 120^{-1} s with higher power than the during the rest of the cycle. These bursts are attributed to switching transients at double the 60 Hz mains frequency. While Figure 8.1 shows the switching transients clearly in the $\boldsymbol{V_{bk},_k}$ waveform, they are also present in $\boldsymbol{V_{(BN+bk)},_k}$ waveform, though less discernible due to the presence of BN. Ideally, the $\boldsymbol{V_{bk},_k}$ waveforms would have a consistent noise level throughout the cycle, with a low peak-to-peak amplitude compared to the $\boldsymbol{V_{(BN+bk)},_k}$ waveforms.

Using both the *Ithaco 1201* preamplifier and the PCI-6133 in differential mode significantly decreases the switching transient power to the levels shown, which indicates the switching transients have a significant common mode component. The switching transient power is also reduced by grounding the sample. It is expected that further switching transient power reduction may be achieved by improving power supply isolation, such as powering the system with a pure-sinusoid uninterruptible power supply. In order that the switching transients do not occur at the same time in every BN acquisition cycle, f_{ex} values were chosen that do not evenly divide into 120 Hz. This improves the effectiveness of signal averaging.

8.1.2 Power Spectra

Comparison of the $\boldsymbol{V_{(BN+bk),k}}$ and $\bar{\boldsymbol{V}}_{\boldsymbol{(BN+bk)}}$ waveforms in Figure 8.1 shows that time-averaging attenuates both the BN and background noise power. While the phase distributions of both the BN and background noise are randomized, noise power is consistent over many cycles, and can be averaged in frequency space. This allows for precise determination of the average BN and background noise power spectra.

For a given waveform $\boldsymbol{X}_k$, the power spectrum $\boldsymbol{PS}\{\boldsymbol{X}_k\}$ is calculated as [62]:

$$\boldsymbol{PS}\{\boldsymbol{X}_k\} = \mathrm{FFT}\{\boldsymbol{X}_k\} \cdot \overline{\mathrm{FFT}\{\boldsymbol{X}_k\}} \tag{8.2}$$

where $\mathrm{FFT}\{\boldsymbol{X}_k\}$ is the fast-Fourier transform of $\boldsymbol{X}_k$ and $\overline{\mathrm{FFT}\{\boldsymbol{X}_k\}}$ is the complex conjugate of $\mathrm{FFT}\{\boldsymbol{X}_k\}$. If k_{max} cycles are acquired, the average power spectrum is calculated as:

$$\overline{\boldsymbol{PS}}\{\boldsymbol{X}\} = \frac{1}{k_{max}} \sum_{k=1}^{k_{max}} \boldsymbol{PS}\{\boldsymbol{X}_k\}. \tag{8.3}$$

Figure 8.2 shows $\overline{\boldsymbol{PS}}\left\{\boldsymbol{V_{(BN+bk)}}\right\}$, $\overline{\boldsymbol{PS}}\{\boldsymbol{V_{bk}}\}$ and $\boldsymbol{PS}\left\{\bar{\boldsymbol{V}}_{\boldsymbol{(BN+bk)}}\right\}$, acquired for $f_{ex} = 31\,\mathrm{Hz}$, $B_{FT} = 477\,\mathrm{mT}$, $\theta_T = 45°$, and $k_{max} = 64$. Units for the power spectral density (PSD) are $\mathrm{mV}^2_{\mathrm{rms}}/\mathrm{Hz}$. To find the voltage amplitude corresponding to a given frequency bin, the power spectrum value is multiplied by the frequency bin width (in this case, 31 Hz) and the square root is taken to give the amplitude in $\mathrm{mV}_{\mathrm{rms}}$.

By comparing $\overline{\boldsymbol{PS}}\left\{\boldsymbol{V_{(BN+bk)}}\right\}$ and $\boldsymbol{PS}\left\{\bar{\boldsymbol{V}}_{\boldsymbol{(BN+bk)}}\right\}$ in Figure 8.2, the BN frequency band can be identified. Figure 8.2 shows that the majority of power in the $\boldsymbol{V_{(BN+bk),k}}$ waveforms is at $f_{ex} = 31\,\mathrm{Hz}$. Up to $\sim 2\,\mathrm{kHz}$, power is consistent between $\overline{\boldsymbol{PS}}\left\{\boldsymbol{V_{(BN+bk)}}\right\}$ and $\boldsymbol{PS}\left\{\bar{\boldsymbol{V}}_{\boldsymbol{(BN+bk)}}\right\}$, indicating that the majority of signal power below 2 kHz corresponds to the macroscopic field signal. Above 2 kHz,

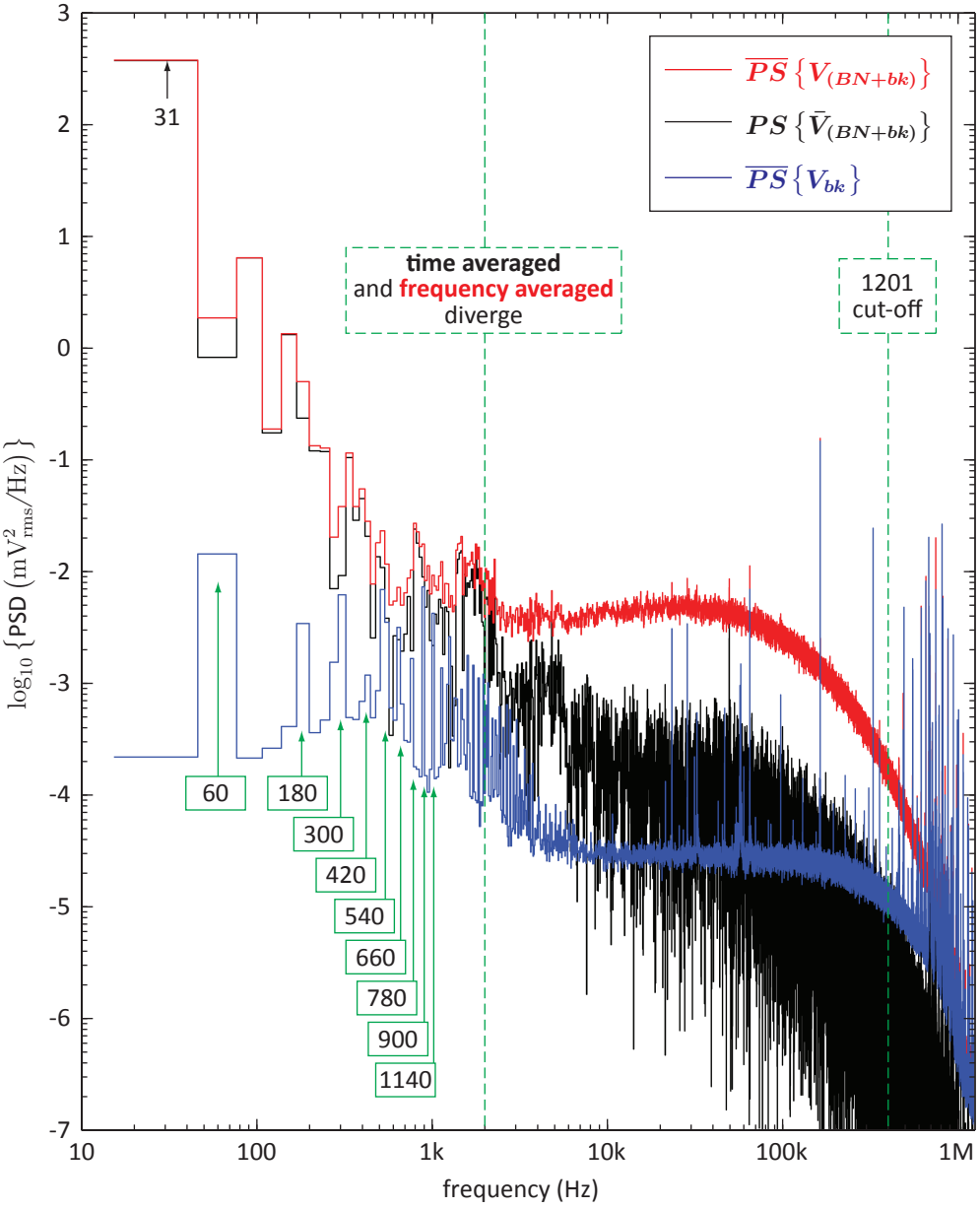

Figure 8.2: Average power spectra for $\boldsymbol{V_{(BN+bk),k}}$ and $\boldsymbol{V_{bk,k}}$ waveforms ($\overline{\boldsymbol{PS}}\{\boldsymbol{V_{(BN+bk)}}\}$ and $\overline{\boldsymbol{PS}}\{\boldsymbol{V_{bk}}\}$ respectively), and the power spectrum for the time-averaged $\bar{\boldsymbol{V}}_{\boldsymbol{(BN+bk)}}$ ($\boldsymbol{PS}\{\bar{\boldsymbol{V}}_{\boldsymbol{(BN+bk)}}\}$). Data were collected with $f_{ex} = 31\,\text{Hz}$, $B_{FT} = 477\,\text{mT}$, $\theta_T = 45°$, and $k_{max} = 64$, with the SL4P clamped on the small feeder bend.

$\boldsymbol{PS}\left\{\bar{\boldsymbol{V}}_{\boldsymbol{(BN+bk)}}\right\}$ decreases, since time-averaging attenuates the background noise and BN power, while $\overline{\boldsymbol{PS}}\left\{\boldsymbol{V}_{\boldsymbol{(BN+bk)}}\right\}$ remains at $\sim 5 \times 10^{-3}\,\mathrm{mV}^2_{\mathrm{rms}}/\mathrm{Hz}$ before rolling off above 50 kHz. This divergence indicates that the BN frequency band begins at $\sim 2\,\mathrm{kHz}$. The roll-off of the BN power above 50 kHz is attributed to the increased attenuation of higher frequencies in the sample. Above 400 kHz, there is additional roll-off associated with the preamplifier bandwidth.

The typical background noise power spectrum ($\overline{\boldsymbol{PS}}\{\boldsymbol{V_{bk}}\}$) in Figure 8.2 is indicated to have peaks at odd harmonics of the power line frequency ($(60 + j120)\,\mathrm{Hz}$, with j being an integer ≥ 0). Power at these mains harmonics decreases up to 6 kHz. Between 6 kHz and 400 kHz a mean noise floor of $3 \times 10^{-5}\,\mathrm{mV}^2_{\mathrm{rms}}/\mathrm{Hz}$ is obtained. Above 6 kHz $\overline{\boldsymbol{PS}}\{\boldsymbol{V_{bk}}\}$ exhibits numerous resonances attributed to the *Ithaco 1201* preamplifier (termed the '1201 signature'), and the switching transients.

The two primary contributors to the $3\times10^{-5}\,\mathrm{mV}^2_{\mathrm{rms}}/\mathrm{Hz}$ noise floor are the thermal noise in the $354\,\Omega$ terminating resistor (R_t), and the *Ithaco 1201* input noise. The PSD of thermal noise in the R_t (PS_{R_t}) may be estimated using:

$$PS_{R_t} = 4 \cdot R_t \cdot k_B \cdot \mathcal{T} \tag{8.4}$$

where $k_B = 1.38 \times 10^{-23}\,\mathrm{J/K}$ is Boltzmann's constant and $\mathcal{T}$ is temperature [63, 64]. At room temperature (293 K) for the $R_t = 354\,\Omega$, equation (8.4) gives $PS_{R_t} = 5.7 \times 10^{-12}\,\mathrm{mV}^2_{\mathrm{rms}}/\mathrm{Hz}$.

The input noise of the *Ithaco 1201* is specified as $7\,\mathrm{nV}/\sqrt{\mathrm{Hz}}$ or $2.5\times10^{-11}\,\mathrm{mV}^2_{\mathrm{rms}}/\mathrm{Hz}$ [59]. Any noise at the *Ithaco 1201* input is then multiplied by the 60 dB gain, leading to an increased PSD by a factor of 10^6. Adding the thermal and input noise in quadrature and multiplying by 10^6 gives a total noise at the amplifier output of

$3.0 \times 10^{-5}\,\mathrm{mV}_{\mathrm{rms}}^2/\mathrm{Hz}$, which is in agreement with the noise floor in Figure 8.2.

Replacing the *Ithaco 1201* with an amplifier that features lower input noise specifications may decrease the noise floor until the thermal noise in R_t becomes the limiting factor. This would require an amplifier with input noise specifications between $0.1\,\mathrm{nV}/\sqrt{\mathrm{Hz}}$ and $1\,\mathrm{nV}/\sqrt{\mathrm{Hz}}$.

8.1.3 Dynamic Power Spectra

The raw waveform data are useful to visualize the structure of the BN waveforms, while the power spectra are useful for estimating the BN frequency band and noise resonances. However, it is difficult using either representation to ascertain which frequencies correspond to specific noise sources. To visualize the pickup coil waveform content in more detail, a plot of the power spectrum as a function of time is useful. Such a plot is the dynamic power spectrum [62].

In order to calculate dynamic power spectrum of a waveform, it is divided into $\mathrm{rnd}\{f_{6229AI}/f_{ex}\}$ arrays centered around equally spaced time intervals, each with $\mathrm{rnd}\{2 \cdot f_{6133AI}/f_{6229AI}\}$ samples, where $\mathrm{rnd}\{\mathrm{x}\}$ rounds x to the nearest integer. Each array is then multiplied by the *LabVIEW 8.2* Hanning window function to reduce time aliasing before the discrete Fourier transform of the array is computed*. A plot of the windowed discrete Fourier transforms versus time (or phase) for the waveform $\boldsymbol{X}_k$ is the dynamic power spectrum ($\boldsymbol{\mathcal{D}}\{\boldsymbol{X}_k\}$). For the pickup voltage waveforms,

*The GUI allows the user both to specify the window width as a ratio of f_{6133AI}/f_{6229AI}, with a default value of 2. In this thesis, 2 is always used. The user also has the choice of a variety of built-in *LabVIEW 8.2* window functions, with the Hanning window being the default.

$\boldsymbol{\mathcal{D}}\left\{\boldsymbol{V_{(BN+bk),k}}\right\}$ and $\boldsymbol{\mathcal{D}}\left\{\boldsymbol{V_{bk,k}}\right\}$ have a time resolution (t_{bin}) of:

$$t_{bin} = \frac{1}{f_{ex} \cdot \text{rnd}\left\{\frac{f_{6229AI}}{f_{ex}}\right\}} \approx \frac{1}{f_{6229AI}} \tag{8.5}$$

and frequency resolution (f_{bin}) of:

$$f_{bin} = \frac{f_{6133AI}}{\text{rnd}\left\{2 \cdot \frac{f_{6133AI}}{f_{6229AI}}\right\}} \approx \frac{f_{6229AI}}{2}. \tag{8.6}$$

The average dynamic power spectrum for k_{max} $\boldsymbol{X}_k$ waveforms is $\bar{\boldsymbol{\mathcal{D}}}\left\{\boldsymbol{X}\right\}$. Each point in $\bar{\boldsymbol{\mathcal{D}}}\left\{\boldsymbol{X}\right\}$ represents the mean PSD in a specific $\phi_{B_{FT}}$ window and frequency range. Since k_{max} dynamic power spectra are calculated, the standard deviation of each point of $\bar{\boldsymbol{\mathcal{D}}}\left\{\boldsymbol{X}\right\}$ in the dynamic power spectrum ($\boldsymbol{st\mathcal{D}}\left\{\boldsymbol{X}\right\}$) is:

$$\boldsymbol{st\mathcal{D}}\left\{\boldsymbol{X}\right\} = \left(\frac{1}{k_{max}-1}\sum_{k=1}^{k_{max}}\left(\boldsymbol{\mathcal{D}}\left\{\boldsymbol{X}_k\right\} - \bar{\boldsymbol{\mathcal{D}}}\left\{\boldsymbol{X}\right\}\right)^2\right)^{\frac{1}{2}}, \tag{8.7}$$

and the standard error ($\boldsymbol{er\mathcal{D}}\left\{\boldsymbol{X}\right\}$) is:

$$\boldsymbol{er\mathcal{D}}\left\{\boldsymbol{X}\right\} = \frac{\boldsymbol{st\mathcal{D}}\left\{\boldsymbol{X}\right\}}{\sqrt{k_{max}}}. \tag{8.8}$$

Figure 8.3 shows $\boldsymbol{\mathcal{D}}\left\{\boldsymbol{V_{bk,k}}\right\}$, $\boldsymbol{\mathcal{D}}\left\{\boldsymbol{V_{(BN+bk),k}}\right\}$, $\bar{\boldsymbol{\mathcal{D}}}\left\{\boldsymbol{V_{bk}}\right\}$ and $\bar{\boldsymbol{\mathcal{D}}}\left\{\boldsymbol{V_{(BN+bk)}}\right\}$ in (a), (b), (c) and (d), respectively, for the SL4P BN data described in the preceding two sections. The primary difference between Figures 8.3a and 8.3b, and figures 8.3c and 8.3d, is the presence of BN, which appears as two broad-band pulses between 0° and 180° and between 180° and 360° in Figures 8.3b and 8.3d. In Figures 8.3b and 8.3d, the AO glitches are visible as bursts of power near 10° and 190° with similar

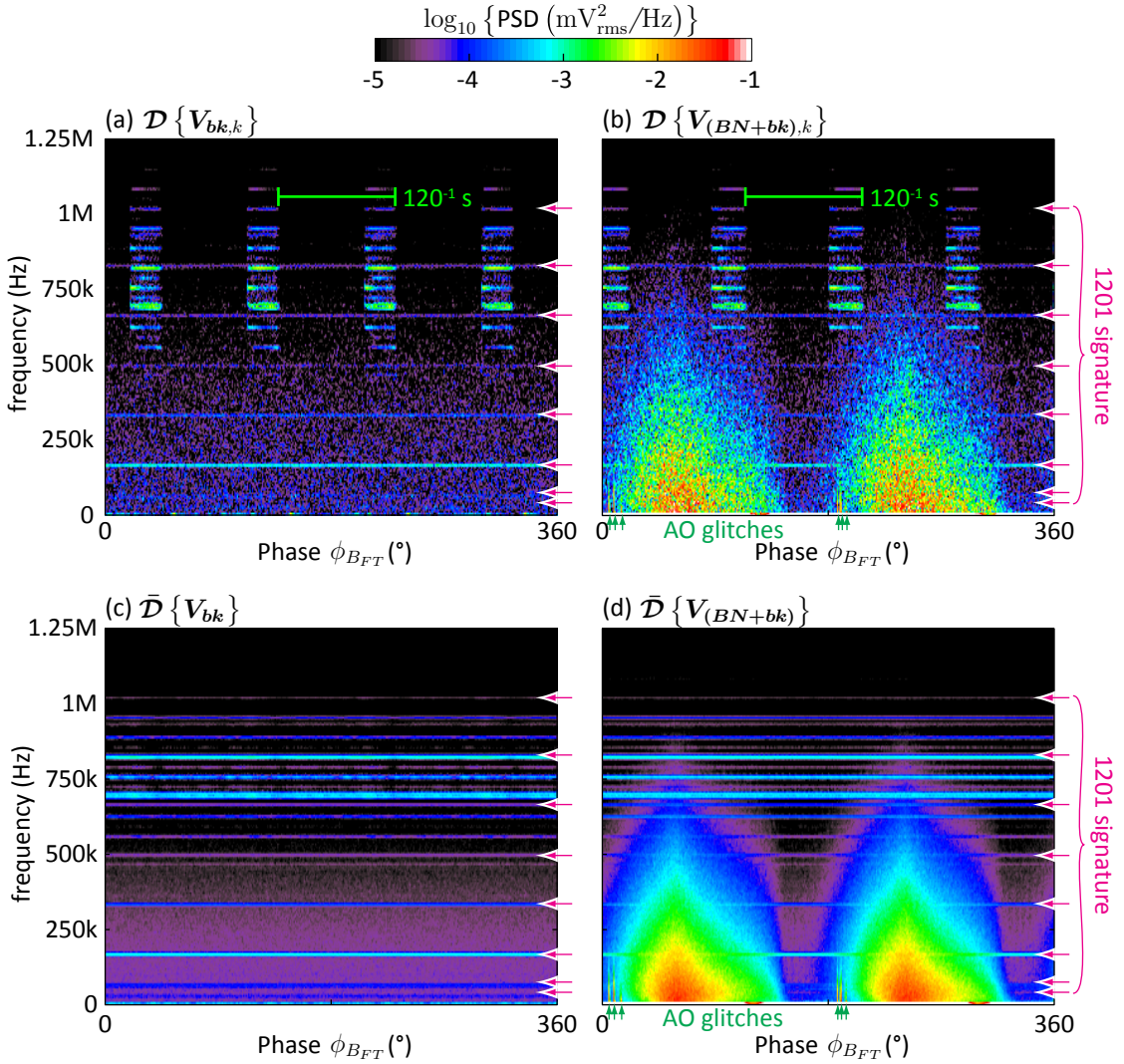

Figure 8.3: Dynamic power spectra for (a) $\boldsymbol{V_{bk,k}}$ and (b) $\boldsymbol{V_{(BN+bk),k}}$, and the averaged dynamic power spectra for $k = 1 \ldots 64$ of (c) $\boldsymbol{V_{bk,k}}$ and (d) $\boldsymbol{V_{(BN+bk),k}}$. Data were collected with $f_{ex} = 31\,\text{Hz}$, $B_{FT} = 477\,\text{mT}$, $\theta_T = 45°$ with the SL4P clamped on the small feeder bend.

spectral content to the BN, but distinctly higher power than the surrounding BN pulse. In Figures 8.3a and 8.3b the power supply switching transients appear as four impulses with evenly spaced harmonics spread 120^{-1} s apart. The *Ithaco 1201* signature appears as horizontal lines of constant power with decreasing power for increasing frequency.

Comparison of Figures 8.3a and 8.3b with Figures 8.3c and 8.3d indicates that averaging the dynamic power spectra significantly decreases the scatter in the images, as is expected from equation (8.8). Since 31 does not evenly divide into 120, the switching transients are smeared across Figures 8.3c and 8.3d, and appear as a consistent (lowered) power level as a function of phase.

The *Ithaco 1201* amplifier bandwidth limits the accuracy to which the BN power spectrum can be estimated above 400 kHz. Figure 8.2 indicates the BN roll-off begins at 50 kHz, and in Figures 8.3b and 8.3d BN power is visible up to 1 MHz, before it goes off-scale. While the 400 kHz preamplifier roll-off is sufficient to avoid aliasing when sampled at $f_{6133AI} = 2.5$ MHz, a higher sampling frequency than 2.5 MHz and a wider-bandwidth preamplifier may yield additional information regarding the BN power spectrum.

Figure 8.3 illustrates that the dynamic power spectrum is as an effective tool for visualizing and differentiating noise sources. An equally effective presentation is to remap $\boldsymbol{V}_{(\boldsymbol{BN+bk}),k}$ to audio frequencies, and play it through speakers. A linear mapping of 1.25 MHz to 22 kHz is recommended. Care should be taken to ensure frequencies below 1 kHz (which maps to 20 Hz) are filtered, as these may have sufficient power to damage speakers. In this format, BN sounds akin to waves on shoreline, the AO glitches are a rapid set of 'clicks' prior to each wave, the switching transients are

periodic 'beeps' like an alarm clock, and the *Ithaco 1201* signature comes through as a constant drone like that of a vacuum cleaner.

8.2 Filtering

In order to derive quantitative BN parameters, it is desirable to isolate the BN from the background noise, macroscopic field signal, AO glitches, *Ithaco 1201* signature, mains harmonics and switching transients. In the present software implementation, BN power is isolated using a combination of an infinite impulse response (IIR) band pass filter, a custom filter for the AO glitches, and background noise power subtraction, presented in sections 8.2.1, 8.2.2, and 8.2.3, respectively.

8.2.1 IIR Band Pass

In Section 8.1.2 it was shown that the macroscopic field signal has significant power at frequencies below 2 kHz, and the mains harmonics have decreasing power between 1 kHz and 6 kHz. Above 600 kHz the switching transients dominate the power spectrum. The BN power spectrum begins at 2 kHz and starts to roll off at 50 kHz. The *Ithaco 1201* preamplifier gain rolls off above 400 kHz, which acts as a low-pass filter. It follows that a band-pass filter between 3 kHz and 600 kHz would effectively attenuate the macroscopic field signal, mains harmonics and switching transients, while preserving the majority of the BN power.

An infinite impulse response (IIR) band-pass filter was implemented in *LabVIEW 8.2* using the built-in filtering coefficients and the zero-phase IIR filter functions. The zero-phase filter is differentiated from a conventional analog filter, in that no phase

distortion is introduced to the filtered waveform. The *LabVIEW 8.2* GUI allows user specification of the filter coefficients as either Bessel, Chebychev, or Butterworth (with Butterworth as default), the filter order (3rd order is default), and the filter cut-offs (3 kHz to 600 kHz by default). The filtering can also be disabled.

Figure 8.4 shows the effect of 3 kHz to 600 kHz band-pass filtering on $\boldsymbol{V_{bk},_k}$ and $\boldsymbol{V_{(BN+bk)},_k}$ using 3$^{\text{rd}}$ order Butterworth coefficients. In Figure 8.4a the f_{ex} signal component extracted from the fast-Fourier transform of $\boldsymbol{V_{(BN+bk)},_k}$ is indicated in green. Since the macroscopic field component signal contains information about possible pickup coil misalignment and flux leakage from the sample, the mean and standard deviation of the f_{ex} component magnitude ($|V_{f_{ex}}|$) and phase ($\phi_{f_{ex}}$) from $\boldsymbol{V_{(BN+bk)},_k}$ for are stored for further analysis.

Comparing Figures 8.4a and 8.4b shows that the switching transients in $\boldsymbol{V_{bk},_k}$ are attenuated, as is the macroscopic field signal in $\boldsymbol{V_{(BN+bk)},_k}$. Without these two signal components, the BN and AO glitches can be seen in Figure 8.4b as the voltage in $\boldsymbol{V_{(BN+bk)},_k}$ above the constant background noise level of $\boldsymbol{V_{bk},_k}$.

Figure 8.5 shows the effects of bandpass filtering on $\bar{\boldsymbol{\mathcal{D}}}\left\{\boldsymbol{V_{(BN+bk)}}\right\}$. Comparison of Figures 8.5a and 8.5b indicates that filtering attenuates the switching transient power, but also attenuates higher frequency content in the BN pulses. Peak BN power in Figure 8.5 is on the order of $10^{-1.5}\,\text{mV}_{\text{rms}}^2/\text{Hz}$, while typical BN power above 600 kHz in Figure 8.5a is $< 10^{-4}\,\text{mV}_{\text{rms}}^2/\text{Hz}$. Thus filtering above 600 kHz does not significantly affect the total BN power in the filtered $\boldsymbol{V_{(BN+bk)},_k}$ waveforms.

The IIR bandpass operation preserves phase information in $\boldsymbol{V_{(BN+bk)},_k}$ and $\boldsymbol{V_{bk},_k}$ waveforms, and thus the filtered waveforms can be used for time-based BN analysis. In BN studies with $f_{ex} < 0.1$ Hz and appropriate sample materials and geometries, it

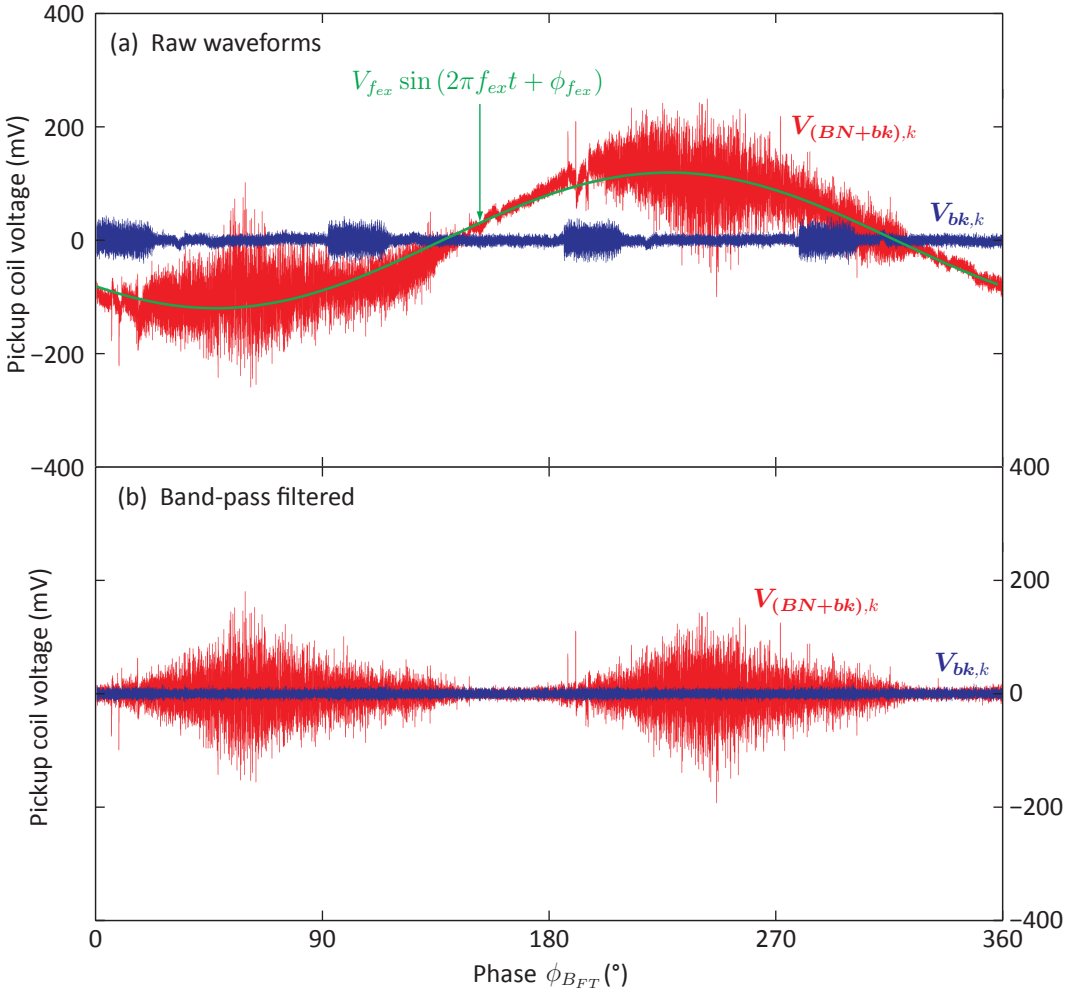

Figure 8.4: The effect of band-pass filtering on $\boldsymbol{V_{bk,k}}$ and $\boldsymbol{V_{(BN+bk),k}}$. (a) Typical $\boldsymbol{V_{bk,k}}$ (blue) and $\boldsymbol{V_{(BN+bk),k}}$ (red) waveforms. The f_{ex} component of $\boldsymbol{V_{(BN+bk),k}}$ is indicated in green. (b) Band-pass filtered $\boldsymbol{V_{bk,k}}$ and $\boldsymbol{V_{(BN+bk),k}}$ between 3 kHz and 600 kHz with 3^{rd} order Butterworth coefficients.

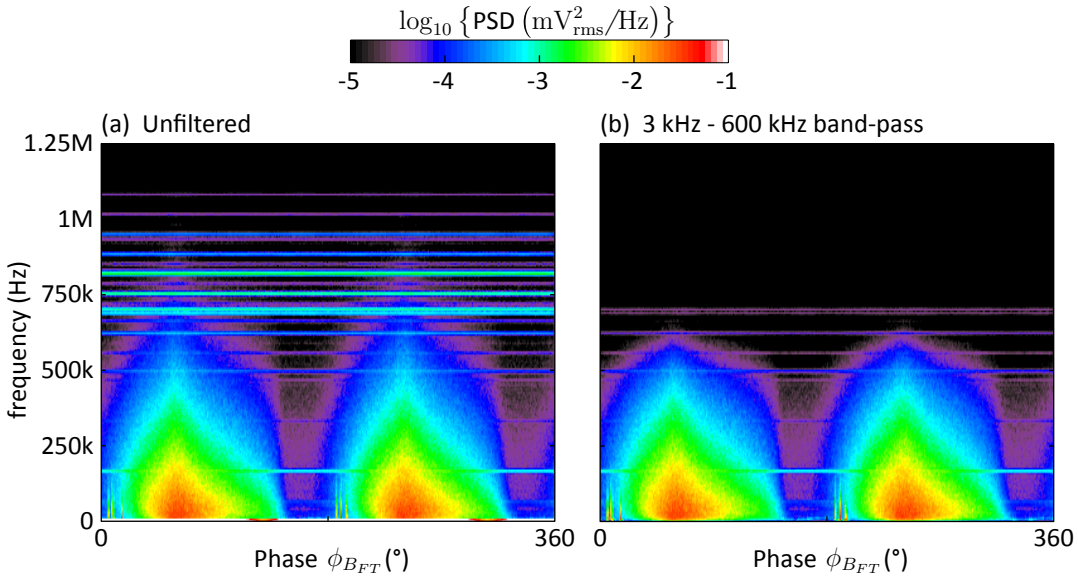

Figure 8.5: The effect of band-pass filtering on the dynamic power spectrum. (a) $\bar{\boldsymbol{\mathcal{D}}}\left\{\boldsymbol{V_{(BN+bk)}}\right\}$ for the unfiltered data, (b) $\bar{\boldsymbol{\mathcal{D}}}\left\{\boldsymbol{V_{(BN+bk)}}\right\}$ after band-pass filtering between 3 kHz and 600 kHz with 3^{rd} order Butterworth coefficients.

is possible to detect individual Barkhausen events [6]. In bulk polycrystalline samples with $10\,\text{Hz} < f_{ex} < 100\,\text{Hz}$, superposition makes it more difficult to distinguish individual events [65]. Point-by-point inspection of the band-pass filtered waveforms from the SL4P and feeders, such as in Figure 8.4b, revealed no individually distinguishable avalanches above background noise levels, though this may be due to corruption of the data by the *Ithaco 1201* signature.

Over the course of this thesis work, several efforts were made to parameterise the BN as a superposition of discrete events with a 'pulse height distribution' and an 'average event' [66]. However, it was determined that such results were primarily dependent on the peak fitting algorithm, and that peak functions were strongly dependent on the pickup coil transfer function. Ultimately it was found that power spectral analysis yielded comparable information to such time-based analysis, and

was considerably easier to relate back to the measured pickup coil voltage waveforms. Time-based analysis was therefore abandoned. The subsequent analysis is based entirely on the band-pass filtered dynamic power spectrum, such as that shown in Figure 8.5b.

8.2.2 AO Glitch Filter

After band-pass filtering (Figure 8.5b), the signal power consists primarily of BN, the AO glitches, the noise floor, and the *Ithaco 1201* signature. In order to remove the AO glitches and better estimate the BN power spectrum, an AO glitch filter was developed. The AO glitch filter assumes that the AO glitches are signals that occur at the same phase each excitation cycle, while the phase distribution of the BN power is randomized.

To identify the AO glitches, the relative standard deviation of the dynamic power spectrum ($\boldsymbol{rst\mathcal{D}}\{\boldsymbol{X}\}$) is calculated as:

$$\boldsymbol{rst\mathcal{D}}\{\boldsymbol{X}\} = \frac{\boldsymbol{st\mathcal{D}}\{\boldsymbol{X}\}}{\bar{\boldsymbol{\mathcal{D}}}\{\boldsymbol{X}\}} \tag{8.9}$$

A value of $\boldsymbol{rst\mathcal{D}}\{\boldsymbol{X}\} = 1$ indicates that the standard deviation and RMS signal power are the same, which is characteristic of random noise such as the BN and the noise floor. For signals that are periodic with f_{ex}, like the AO glitches, $\boldsymbol{rst\mathcal{D}}\{\boldsymbol{X}\} < 1$. For signals that are not periodic with f_{ex}, like the switching transients, $\boldsymbol{rst\mathcal{D}}\{\boldsymbol{X}\} > 1$.

Figure 8.6a shows $\boldsymbol{rst\mathcal{D}}\left\{\boldsymbol{V_{(BN+bk)}}\right\}$ for $B_{FT} = 477\,\text{mT}$, $\theta_T = 45°$, $f_{ex} = 31\,\text{Hz}$, and $k_{max} = 64$ after band-pass filtering. For frequencies $< 600\,\text{kHz}$, Figure 8.6a shows that $\boldsymbol{rst\mathcal{D}}\left\{\boldsymbol{V_{(BN+bk)}}\right\} \approx 1$ for all phase and frequency values, except at the AO glitches and *Ithaco 1201* signature values, where $\boldsymbol{rst\mathcal{D}}\left\{\boldsymbol{V_{(BN+bk)}}\right\} < 1$.

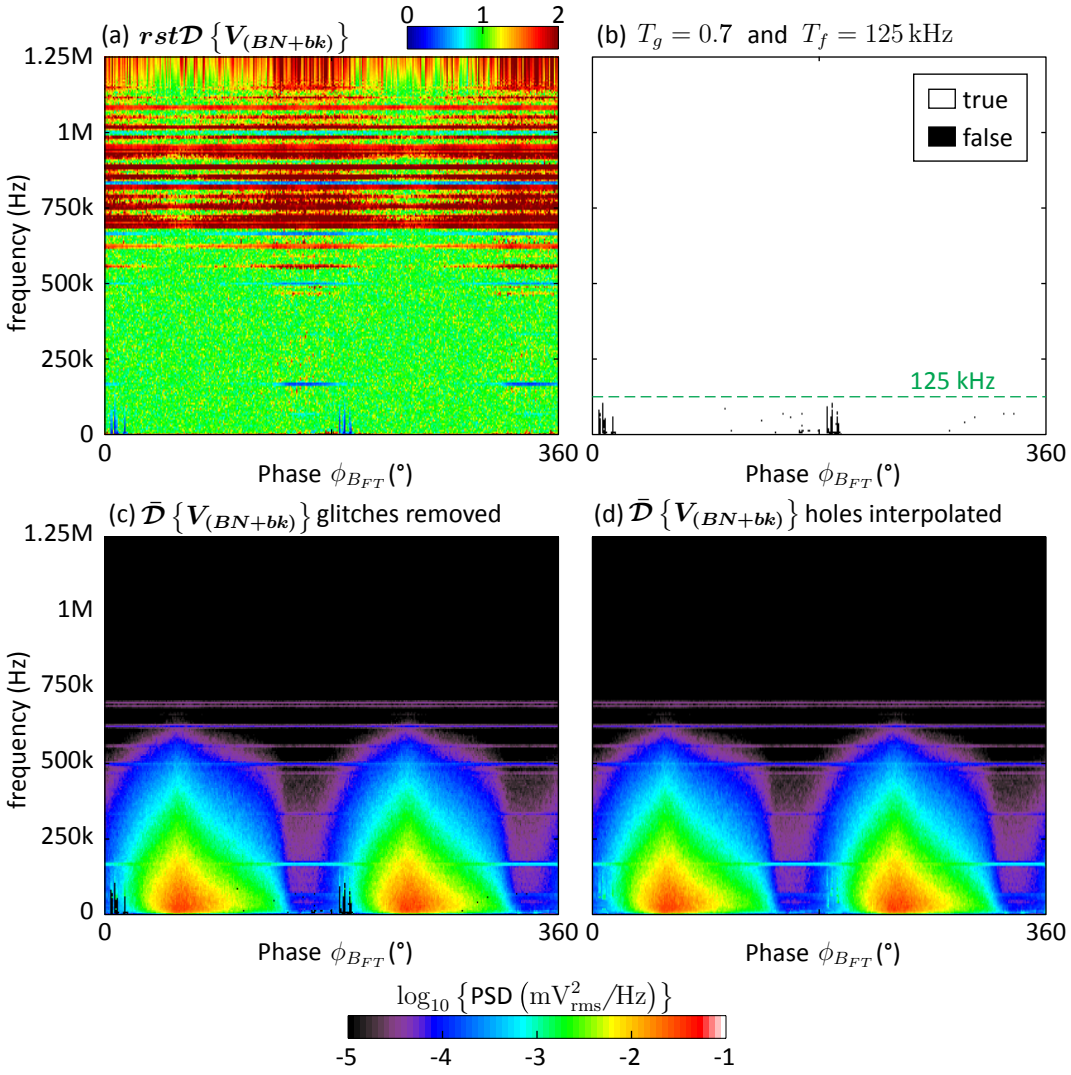

Figure 8.6: AO glitch filtering using the standard deviation of the dynamic power spectrum. (a) The ratio of $\boldsymbol{st\mathcal{D}}\{\boldsymbol{V_{(BN+bk)}}\}$ to $\bar{\boldsymbol{\mathcal{D}}}\{\boldsymbol{V_{(BN+bk)}}\}$ is calculated and (b) thresholded below 0.7 and 125 kHz. (c) Values below the threshold are removed from $\bar{\boldsymbol{\mathcal{D}}}\{\boldsymbol{V_{(BN+bk)}}\}$, and (d) linear interpolation across $\phi_{B_{FT}}$ is used to replace the removed data.

In Figure 8.6b, the phases and frequencies of AO glitches are isolated by selecting $\boldsymbol{rst}\boldsymbol{\mathcal{D}}\left\{\boldsymbol{V_{(BN+bk)}}\right\} < T_g$, for frequencies less than $T_f = 125\,\text{kHz}$, where T_g and T_f are the glitch threshold and cut-off frequency, respectively. Note that some scattered BN and noise floor points are also below the thresholding criteria in Figure 8.6b, due to the limited number of periods averaged.

To filter the AO glitches, data points that fall below T_g and T_f are omitted from $\bar{\boldsymbol{\mathcal{D}}}\left\{\boldsymbol{V_{(BN+bk)}}\right\}$. Linear interpolation across $\phi_{B_{FT}}$ is then used to fill in the omitted data. Figures 8.6c and 8.6d respectively show $\bar{\boldsymbol{\mathcal{D}}}\left\{\boldsymbol{V_{(BN+bk)}}\right\}$ before and after the AO glitch filter was applied with the thresholding criteria in Figure 8.6b.

Comparison of Figures 8.6c and 8.6d indicates some of the higher frequency content of the AO glitches was not successfully omitted. While increasing T_g toward 1 can be used to omit more of the glitch power, in general:

$$T_g < 1 - \frac{1}{\sqrt{k_{max}}}$$

to avoid excessive omission and interpolation of BN power.

8.2.3 Background Power Subtraction

Following band-pass filtering and the AO glitch filter, $\bar{\boldsymbol{\mathcal{D}}}\left\{\boldsymbol{V_{(BN+bk)}}\right\}$ represents the signal power associated with the BN, noise floor, *Ithaco 1201* signature, and some remaining power from the switching transients. In comparison, after band-pass filtering $\bar{\boldsymbol{\mathcal{D}}}\left\{\boldsymbol{V_{bk}}\right\}$ has the same signal components as $\bar{\boldsymbol{\mathcal{D}}}\left\{\boldsymbol{V_{(BN+bk)}}\right\}$, without the BN.

When f_{ex} values are chosen that do not evenly divide into 120 Hz, the switching transients are smeared across the dynamic power spectra over multiple averaged cycles, as shown in Figure 8.7a for $\bar{\boldsymbol{\mathcal{D}}}\left\{\boldsymbol{V_{(BN+bk)}}\right\}$ following band-pass and AO glitch

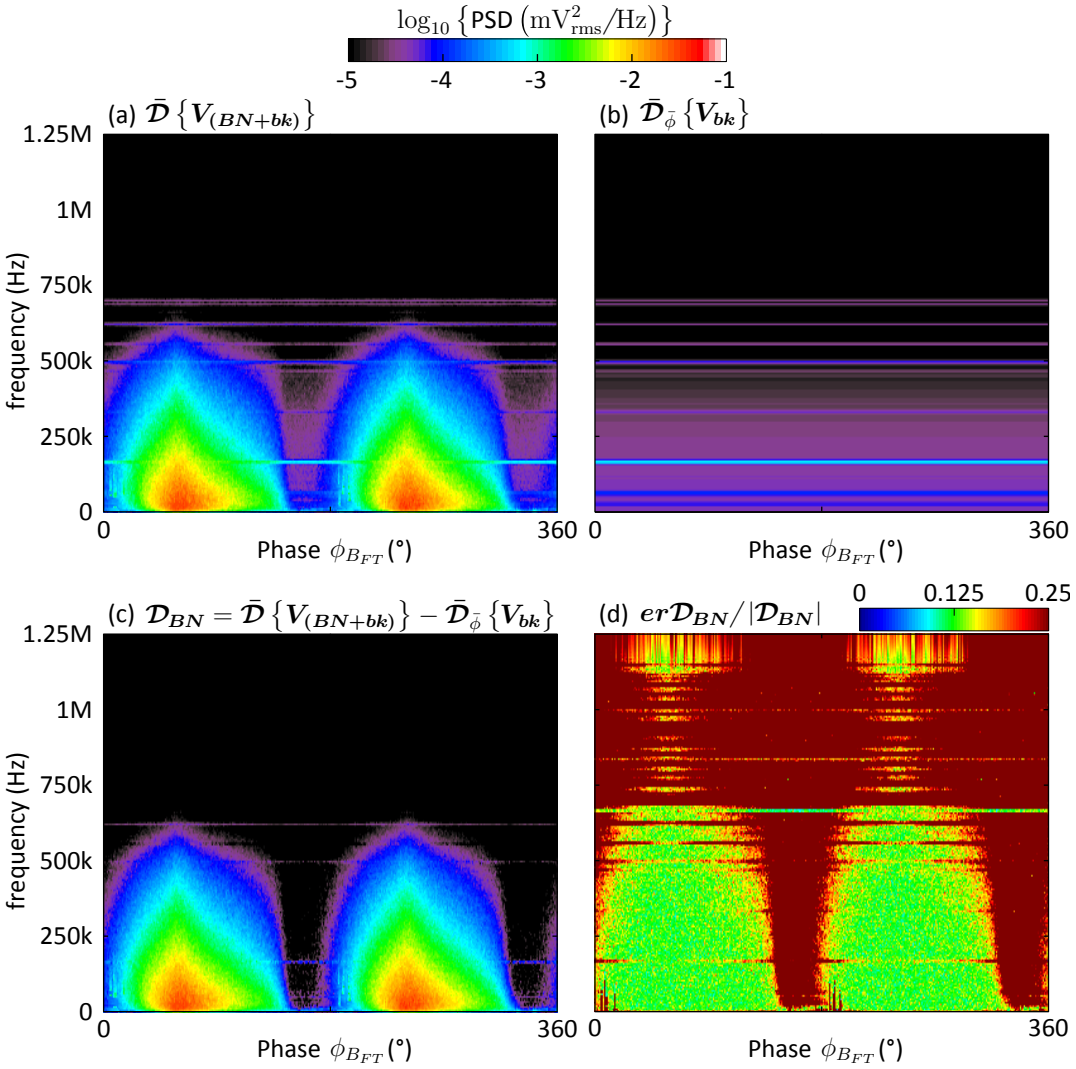

Figure 8.7: Background power spectrum subtraction to produce the BN dynamic power spectrum. (a) $\bar{\mathcal{D}}\{V_{(BN+bk)}\}$ after 3 kHz to 600 kHz band-pass filtering and AO glitch filtering. (b) $\bar{\mathcal{D}}_{\bar{\phi}}\{V_{bk}\}$ after band-pass filtering, and (c) $\mathcal{D}_{BN} = \bar{\mathcal{D}}\{V_{(BN+bk)}\} - \bar{\mathcal{D}}_{\bar{\phi}}\{V_{bk}\}$. (d) The relative error on $\mathcal{D}_{BN}$.

filtering. Provided that k_{max} is sufficiently large, the power in the switching transients averages to a constant background noise power spectrum at all sampled $\phi_{B_{FT}}$ values, as indicated in Figure 8.3c. Further averaging over $\phi_{B_{FT}}$ produces the constant background dynamic power spectrum ($\bar{\boldsymbol{\mathcal{D}}}_{\bar{\phi}}\{\boldsymbol{V_{bk}}\}$), as shown in Figure 8.7b.

Since all power is additive, regardless of phase distribution, subtracting $\bar{\boldsymbol{\mathcal{D}}}_{\bar{\phi}}\{\boldsymbol{V_{bk}}\}$ from $\bar{\boldsymbol{\mathcal{D}}}\left\{\boldsymbol{V_{(BN+bk)}}\right\}$ gives an estimate of the dynamic power spectrum of the BN ($\boldsymbol{\mathcal{D}_{BN}}$):

$$\boldsymbol{\mathcal{D}_{BN}} = \bar{\boldsymbol{\mathcal{D}}}\left\{\boldsymbol{V_{(BN+bk)}}\right\} - \bar{\boldsymbol{\mathcal{D}}}_{\bar{\phi}}\{\boldsymbol{V_{bk}}\}, \tag{8.10}$$

as shown in Figure 8.7c. Comparison of Figures 8.7a and 8.7c shows that the background subtraction effectively attenuates the noise floor, *Ithaco 1201* signature and switching transient power.

For each point in $\boldsymbol{\mathcal{D}_{BN}}$, the standard error ($\boldsymbol{er\mathcal{D}_{BN}}$) is calculated as:

$$\boldsymbol{er\mathcal{D}_{BN}} = \left(\frac{\left(\boldsymbol{st\mathcal{D}}\left\{\boldsymbol{V_{(BN+bk)}}\right\}\right)^2}{k_{max}} + \frac{\sum_{\phi}\left(\boldsymbol{st\mathcal{D}}\{\boldsymbol{V_{bk}}\}\right)^2}{k_{max}\cdot \mathrm{rnd}\left\{\frac{f_{ex}}{f_{6229AI}}\right\}} \right)^{\frac{1}{2}}. \tag{8.11}$$

The ratio of $\boldsymbol{er\mathcal{D}_{BN}}$ to $|\boldsymbol{\mathcal{D}_{BN}}|$ is shown in Figure 8.7d. Note that $\boldsymbol{er\mathcal{D}_{BN}}/|\boldsymbol{\mathcal{D}_{BN}}|$ values are $\sim k_{max}^{-0.5}$ for BN, and $> k_{max}^{-0.5}$ in regions where the background noise sources dominate the power spectrum.

Due to the subtraction operation in equation (8.10), non-physical negative values for $\boldsymbol{\mathcal{D}_{BN}}$ may occur when the background noise power is significantly greater than the BN power (i.e., $\bar{\boldsymbol{\mathcal{D}}}_{\bar{\phi}}\{\boldsymbol{V_{bk}}\} > \bar{\boldsymbol{\mathcal{D}}}\left\{\boldsymbol{V_{(BN+bk)}}\right\}$). Typically $\boldsymbol{er\mathcal{D}_{BN}} > |\boldsymbol{\mathcal{D}_{BN}}|$ for all points where $\boldsymbol{\mathcal{D}_{BN}} < 0$. In Figure 8.7c negative $\boldsymbol{\mathcal{D}_{BN}}$ values were set to $10^{-14}\,\mathrm{mV}^2_{\mathrm{rms}}/\mathrm{Hz}$ in order to render $\boldsymbol{\mathcal{D}_{BN}}$ on a log scale.

8.3 BN Dynamic Power Spectrum

Using band-pass filtering to attenuate the macroscopic field and switching transient signals, the AO glitch filter to omit and interpolate data related to the AO glitches, and subtracting the average background noise spectrum yields the BN dynamic power spectrum, $\boldsymbol{\mathcal{D}_{BN}}$.

Due to the broad-band power of the BN, absolute quantitative analysis of $\boldsymbol{\mathcal{D}_{BN}}$ is limited to frequencies where the system transfer function (pickup coil → *Ithaco 1201* → PCI-6133 → IIR filter) is quantitatively known. From the *Ithaco 1201* to the IIR filter, the transfer function gain is flat between 3 kHz and 400 kHz. However, since the pickup coil transfer function varies with L_{pu}, it is impossible to measure the transfer function independently of the sample.

Under similar magnetisation conditions it is reasonable to assume that the voltage waveform induced in the pickup coil by BN is comparable between circuit configurations. Thus comparison of $\boldsymbol{\mathcal{D}_{BN}}$ for different circuit configurations yields the change in transfer function associated with a given circuit component, and can be used to verify various transfer function models. Once sufficient confidence in a transfer function model is acquired, the model can be used to select the appropriate terminators to linearize the pickup coil transfer function. However, provided that circuit components remain fixed, the transfer function remains constant and the relative variation of $\boldsymbol{\mathcal{D}_{BN}}$ can be attributed to variations of the sample magnetic properties and pickup coil coupling.

The effect of the pickup coil transfer function on the BN response is illustrated in Figure 8.8, which shows $\boldsymbol{\mathcal{D}_{BN}}$ for various terminating resistor (R_t) and tuning capacitor (C_t) values. In Figure 8.8a, $R_t = 354\,\Omega$ was chosen, as this provides a flat

gain response to 400 kHz with a −3 dB roll-off at 1.05 MHz according to the modelled transfer function in equation (7.7). In Figure 8.8b no termination is used. In Figure 8.8c $R_t = 50\,\Omega$, and in Figure 8.8d $R_t = 354\,\Omega$ and $C_t = 43\,\text{nF}$, which decreases the modelled f_0 to 78 kHz. When R_t is removed in Figure 8.8b, the damping on the interaction between L_{pu} and C_c is decreased relative to Figure 8.8a, which increases the signal power at higher frequencies. The damping is increased relative to Figure 8.8a when $R_t = 50\,\Omega$, as in Figure 8.8c, which attenuates higher frequencies. In Figure 8.8d, the addition of $C_t = 43\,\text{nF}$ decreases f_0 to $81 \pm 3\,\text{kHz}$, which is in agreement with the theoretical value of 78 kHz to within a 95% confidence interval[†]. Since R_t was not adjusted to compensate for the resonance in Figure 8.8d, power increases for frequencies up to f_0 and decreases for frequencies greater than f_0.

To illustrate how the BN power spectrum changes during the excitation cycle $\boldsymbol{\mathcal{D}_{BN}}$ can be shown as line plots for selected $\phi_{B_{FT}}$ (vertical strips) or frequency (horizontal strips) values. Figure 8.9 shows line plots from the $\boldsymbol{\mathcal{D}_{BN}}$ plots in Figure 8.8 for $\phi_{B_{FT}}$ values of 60°, 90° and 120°. Comparison of subplots in Figure 8.9 gives an alternative view of the transfer function changes described for Figure 8.8. Frequency axes are limited to 600 kHz to show the *Ithaco 1201* gain roll-off at 400 kHz, which is most visible in Figures 8.9a and 8.9b.

Comparison across $\phi_{B_{FT}}$ values in Figure 8.9 shows that the change in BN power with $\phi_{B_{FT}}$ produces a multiplicative scaling of the power spectrum (a vertical shift on a log axis). Were L_{pu} to vary significantly with $\phi_{B_{FT}}$, f_0 would vary as $L_{pu}^{-1/2}$, and would affect the damping requirements of the circuit at different $\phi_{B_{FT}}$ values. In Figure 8.9d, no significant change of f_0 is seen between the three phase values. The lack in significant change in the power spectrum as a function of $\phi_{B_{FT}}$ is also

[†]The uncertainty on the measured f_0 is the frequency bin-width of $\boldsymbol{\mathcal{D}_{BN}}$.

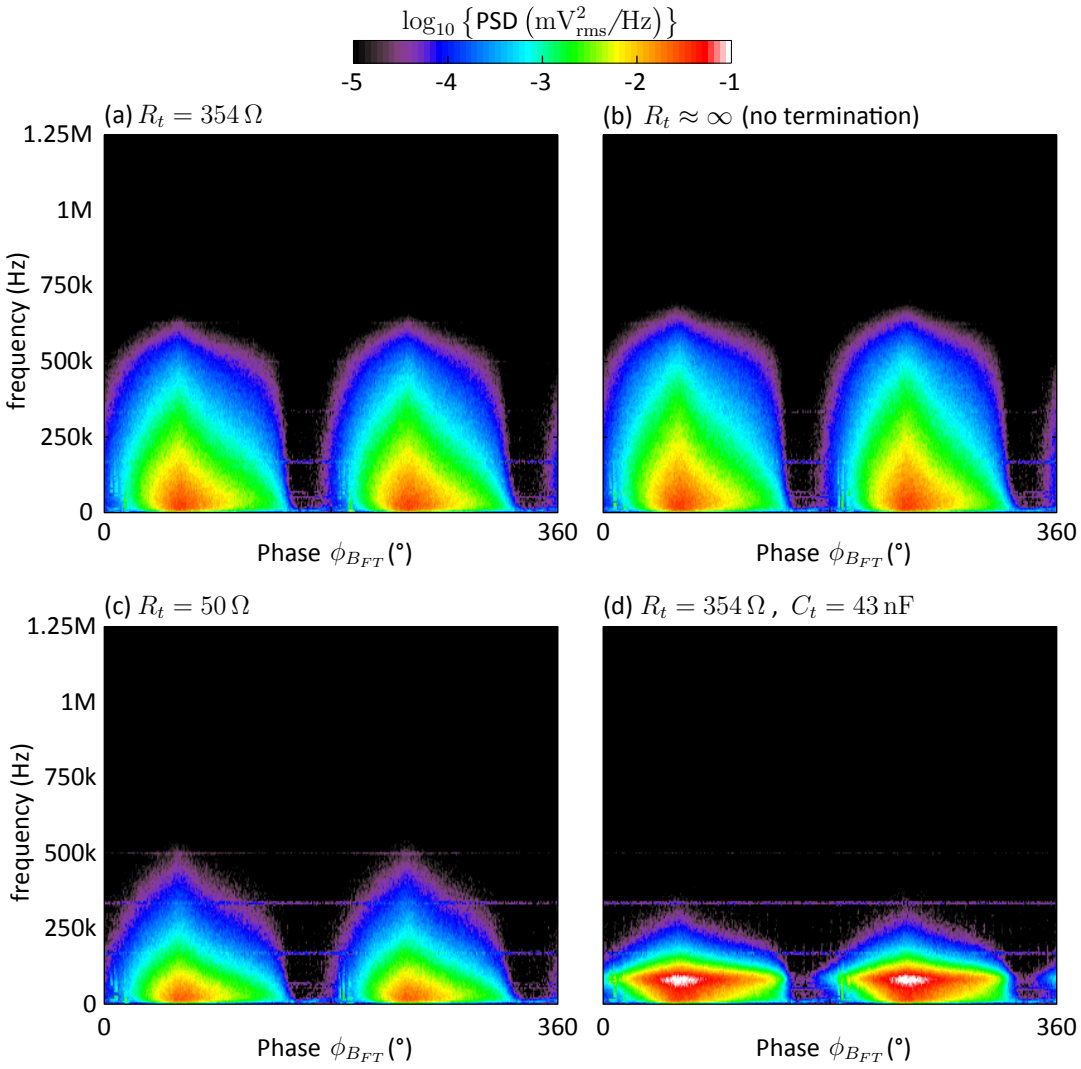

Figure 8.8: The effects of R_t and C_t on $\boldsymbol{\mathcal{D}_{BN}}$, with $f_{ex} = 31\,\mathrm{Hz}$, $B_{FT} = 477\,\mathrm{mT}$, $\theta_T = 45°$, and $k_{max} = 64$. (a) $R_t = 354\,\Omega$, (b) no termination, (c) $R_t = 50\,\Omega$, and (d) $R_t = 354\,\Omega$ and $C_t = 43\,\mathrm{nF}$.

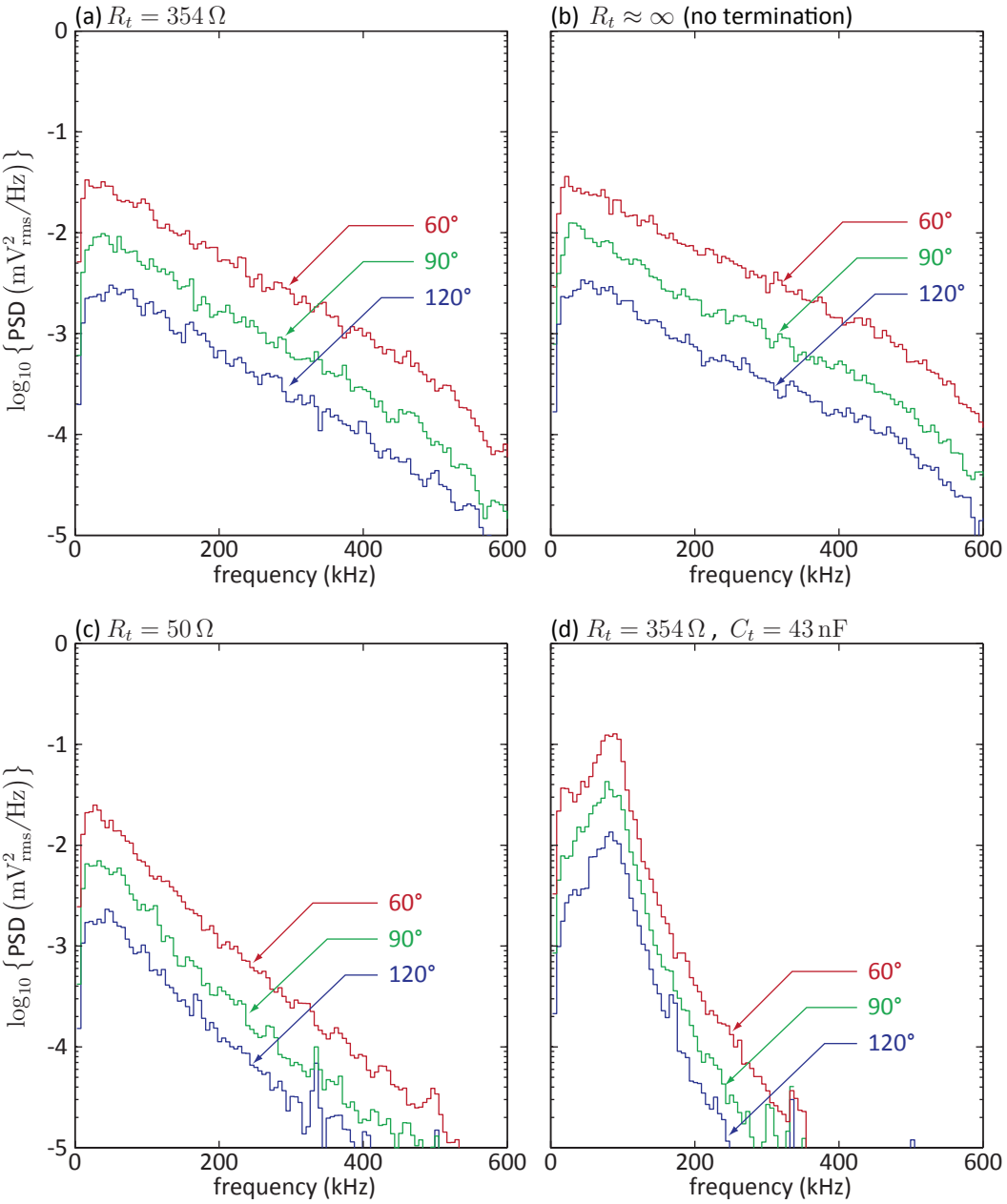

Figure 8.9: Phase dependence of the BN power spectrum for $\phi_{B_{FT}}$ values of 60°, 90° and 120°, with $f_{ex} = 31\,\mathrm{Hz}$, $B_{FT} = 477\,\mathrm{mT}$, $\theta_T = 45°$, and $k_{max} = 64$. (a) $R_t = 354\,\Omega$ (b) no termination, (c) $R_t = 50\,\Omega$, and (d) $R_t = 354\,\Omega$ and $C_t = 43\,\mathrm{nF}$. Subplots (a), (b), (c), and (d) correspond to lines of constant $\phi_{B_{FT}}$ in the respective subplots of Figure 8.8.

consistent with the BN depth model predictions in Figure 7.4b.

8.4 BN Envelope and Normalized Power Spectrum

Since there is little significant change in the BN frequency content as a function of $\phi_{B_{FT}}$, for a given excitation cycle, BN is well-described by the normalized BN power spectrum over all $\phi_{B_{FT}}$ values ($\boldsymbol{NPS_{BN}}$):

$$\boldsymbol{NPS_{BN}} = \frac{1}{f_{bin}} \frac{\sum_{\phi} \boldsymbol{\mathcal{D}_{BN}}}{\sum_{f} \sum_{\phi} \boldsymbol{\mathcal{D}_{BN}}}, \tag{8.12}$$

and the rms BN envelope ($\boldsymbol{BN_{env}}$):

$$\boldsymbol{BN_{env}} = \left(f_{bin} \sum_{f} \boldsymbol{\mathcal{D}_{BN}} \right)^{\frac{1}{2}}. \tag{8.13}$$

Figures 8.10a and 8.10b show $\boldsymbol{NPS_{BN}}$ and $\boldsymbol{BN_{env}}$, respectively, for the R_t and C_t values used in Figures 8.8 and 8.9. Figure 8.10a shows that $\boldsymbol{NPS_{BN}}$ varies strongly with R_t and C_t due to the associated change in the pickup coil transfer function. Figure 8.10b shows $\boldsymbol{BN_{env}}$ on a log scale, whereby any multiplicative scaling factor is represented by a vertical shift of the envelope.

In Figure 8.10b, $\boldsymbol{BN_{env}}$ is shown to vary only with a multiplicative scaling factor between the various circuit configurations. This indicates that while the total BN power varies with $\phi_{B_{FT}}$, currents in the pickup coil do not induce sufficient BN events in the sample to alter the relative shape of $\boldsymbol{BN_{env}}$. Figure 8.10b shows that $\boldsymbol{BN_{env}}$ for $C_t = 43\,\text{nF}$ is greater than for the other circuit configurations. This indicates the system is maximally sensitive to BN when there is an under-damped resonance in

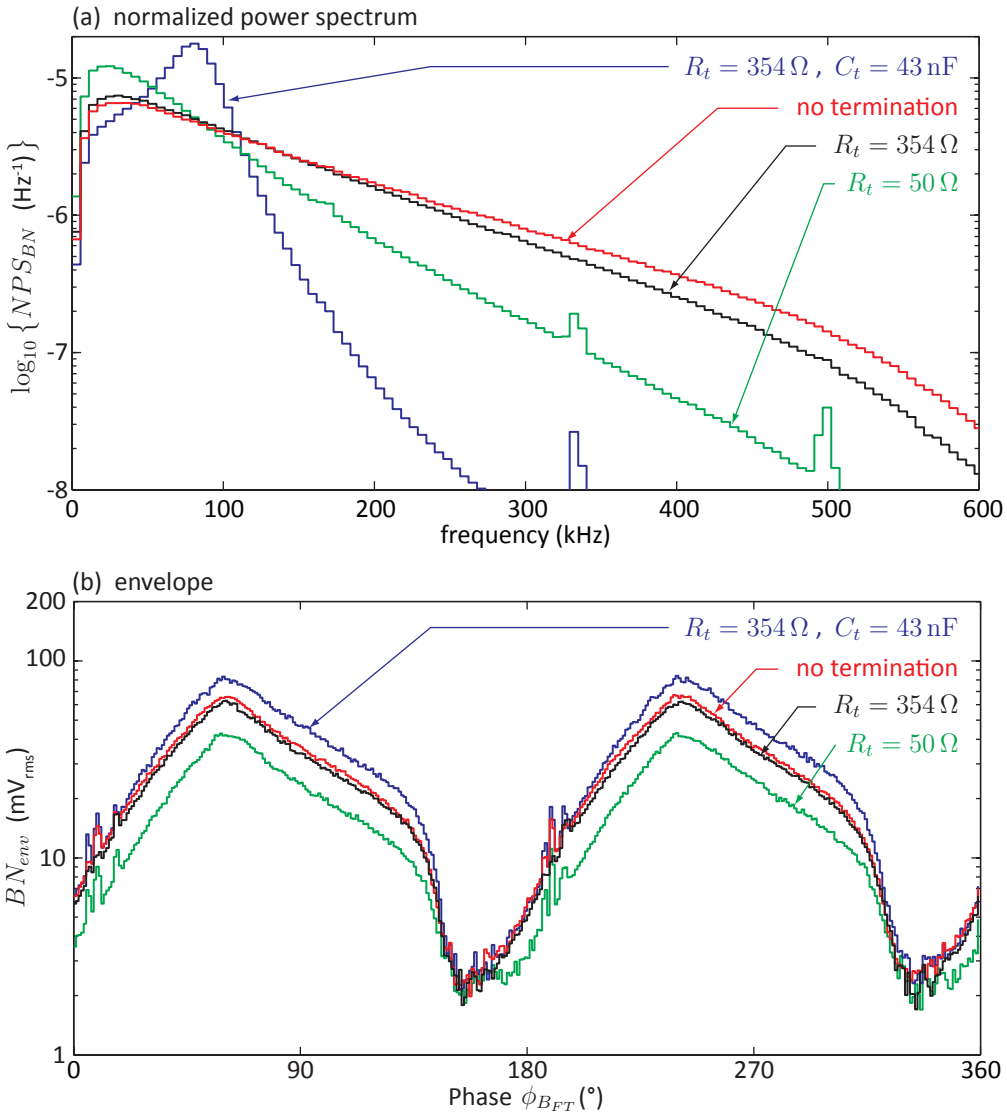

Figure 8.10: (a) The normalized average BN power spectrum ($\boldsymbol{NPS_{BN}}$) and (b) the BN envelope ($\boldsymbol{BN_{env}}$) for $f_{ex} = 31\,\mathrm{Hz}$, $B_{FT} = 477\,\mathrm{mT}$, $\theta_T = 45°$, and $k_{max} = 64$, and the R_t and C_t values used in Figures 8.8 and 8.9.

the BN power spectrum. Over-damping with $R_t = 50\,\Omega$ decreases $\boldsymbol{BN_{env}}$ and BN sensitivity compared to the other configurations.

The choice of termination for relative NDE measurements is therefore arbitrary. If minimal distortion of the BN power spectrum is desired, then detailed characterisation of the circuit transfer function is required and attempts to flatten the power spectrum are justified. Otherwise, the BN power is maximized relative to the background noise power by increasing C_t to produce a resonant frequency within the BN power spectrum. This finding is particularly valuable when long cable runs cannot be avoided. So long as calibration procedures are performed with the same pickup coil, cabling, termination, and amplifier, relative BN power measurements will yield useful results.

Since the pickup coil transfer function model from Section 7.2.1 successfully predicts f_0, it was assumed that the selection of $R_t = 354\,\Omega$ provides close to critical damping for, or at worst over-damps, the resonance at 900 kHz. While the transfer function was not exhaustively tested, an over-damped circuit is sufficient to indicate the relative changes in $\boldsymbol{NPS_{BN}}$ and $\boldsymbol{BN_{env}}$ across the 3 kHz to 400 kHz bandwidth.

8.5 BN Energy and RMS BN

While the $\boldsymbol{\mathcal{D}_{BN}}$, $\boldsymbol{BN_{env}}$ and $\boldsymbol{NPS_{BN}}$ provide a detailed representation of the BN as a function of phase or time, they require a significant time investment to interpret and compare. To further simplify presentation and facilitate interpretation, two more BN parameters are introduced: the BN energy (BN_E), and the RMS BN (BN_{rms}).

BN_E is the integral over 1 excitation cycle of all the power in $\boldsymbol{\mathcal{D}_{BN}}$:

$$BN_E = \sum_{\phi} \sum_{f} \boldsymbol{\mathcal{D}_{BN}} \cdot f_{bin} \cdot t_{bin}, \tag{8.14}$$

with the statistical uncertainty:

$$erBN_E = f_{bin} \cdot t_{bin} \cdot \left(\sum_{\phi} \sum_{f} \boldsymbol{er\mathcal{D}^2_{BN}} \right)^{\frac{1}{2}}. \tag{8.15}$$

BN_E is representative of the total energy emitted during one 'lap' around the sample hysteresis loop for the specified excitation field. BN_E has units of $\mathrm{mV}^2 \cdot \mathrm{s}$.

BN_{rms} is given by:

$$BN_{rms} = \left(f_{ex} \sum_{\phi} \sum_{f} \boldsymbol{\mathcal{D}_{BN}} \cdot f_{bin} \cdot t_{bin} \right)^{\frac{1}{2}}, \tag{8.16}$$

with the statistical uncertainty:

$$erBN_{rms} = \frac{f_{ex} \cdot f_{bin} \cdot t_{bin}}{2\sqrt{BN_{rms}}} \left(\sum_{\phi} \sum_{f} \boldsymbol{er\mathcal{D}^2_{BN}} \right)^{\frac{1}{2}}. \tag{8.17}$$

BN_{rms} is therefore representative of the average BN amplitude over the excitation cycle. Comparison of equations (8.14) and (8.16) shows that $BN_{rms} = (f_{ex} \cdot BN_E)^{1/2}$. It follows that at a given f_{ex}, relative comparison of BN_E and BN_{rms} yields no useful information.

8.6 BN Uncertainties

In order to estimate the number of cycles (k_{max}) and sampling procedures for BN measurements, this section presents a general discussion of the BN measurement uncertainties. Uncertainty in BN measurements using the SL4P on feeders come from a variety of sources, which can be differentiated into two groups: those that contribute to the statistical variation of BN during a measurement when the probe clamped to the sample, and those that contribute to the uncertainty associated with coupling the probe to the sample.

8.6.1 Statistical Variation

When the SL4P is clamped to the sample, the statistical variation of the BN between cycles gives rise to $\boldsymbol{er\mathcal{D}_{BN}}$, as calculated in equation (8.11). This uncertainty is propagated through the summations for $\boldsymbol{NPS_{BN}}$, $\boldsymbol{BN_{env}}$, BN_E and BN_{rms} to yield their respective statistical uncertainties. As can be seen in Figure 8.7d, the ratio of $\boldsymbol{er\mathcal{D}_{BN}}$ to $\boldsymbol{\mathcal{D}_{BN}}$ is approximately $k_{max}^{-1/2}$ (0.125 in Figure 8.7d, since $k_{max} = 64$ for the measurement shown). It follows that $\boldsymbol{er\mathcal{D}_{BN}}$ and the uncertainties of all parameters derived from $\boldsymbol{\mathcal{D}_{BN}}$ can be reduced by increasing k_{max}.

BN_E is often used as a rapid means of detecting changes in the BN response, thus an estimate of the error on the mean BN_E for k_{max} cycles is useful to determine what constitutes a significant change in the BN. It has been observed over many measurements that typical $erBN_E$ values are approximately $\pm 0.015 BN_E/\sqrt{k_{max}}$. Assuming the BN_E statistics follow a normal distribution, then the statistical variation of BN_E measurements is $\pm 0.015 \cdot BN_E$ within a 68% confidence interval. In order for the glitch filtering described in Section 8.2.2 to be effective, and for switching transients to be

adequately signal averaged, k_{max} values ≥ 16 are required. Thus, typical statistical uncertainties on BN_E are $\pm 0.4\%$ (or smaller for $k_{max} > 16$).

8.6.2 Coupling Uncertainties

Coupling uncertainties are estimated from the variance of multiple measurements with large k_{max} at the same position, with the probe removed and reattached between measurements. Coupling uncertainties include the effects of variation in the pickup coil coupling, variation in electromagnet coupling, and positioning errors of the probe with respect to the sample surface. For all measurements in this thesis, the SL4P was positioned by hand, which lead to estimated errors in the SL4P orientation of $\pm 10°$, errors in X-Y or Axial-Hoop positioning of ± 1.5 mm.

The spring-loaded pickup coil and short core assemblies of the SL4P design reduce pickup coil coupling uncertainties and air gap variation, respectively. Coupling uncertainties from SL4P data have an excitation field dependence that varies from $\pm 0.02 BN_E$ to $\pm 0.07 BN_E$, with the higher relative errors occurring at lower B_{FT}. Several measurements at each position should therefore be taken to reduce the error on the mean and give an estimate of the variance.

Since manually repositioning the SL4P on the feeder surface is time consuming, coupling uncertainties combined with positioning errors dominate the measurement uncertainty when scanning the surface of a pipe. If the SL4P is clamped to the surface and only the excitation field control parameters are varied, the coupling and positional uncertainties produce a systematic bias for any one data set. However, the BN variation with the excitation field can be analysed with relative accuracies limited by the statistical variation.

Chapter 9

SA-106 Grade B BN Testing

This chapter presents BN testing results from three SA-106 Grade B samples using the FCS and SL4P, and the BN analysis procedures described in Chapter 8. The three samples are the small feeder bend (SFB), the three-point bending rig (3PBR), and sample T01-5, and are described in detail in their respective sections.

- In Section 9.1, data from the SFB are used to detail the typical BN excitation field response from SA-106 Grade B steel. SL4P measurement uncertainties are estimated from repeated measurements at a given position with varying pickup coil and electromagnet pole lift-off.

- The 3PBR was used to isolate the effects of elastic strain on the BN response of SA-106 Grade B piping. The stress rig was instrumented with strain gauges so that BN versus elastic strain calibration curves could be generated, and the resulting data are presented in Section 9.2.

- AECL provided several bent feeder pipes for BN testing purposes. Sample T01-5 was arbitrarily selected from these samples for a preliminary BN measurement

study. Data from T01-5 are presented in Section 9.3.

9.1 Small Feeder Bend (SFB) Studies

The small feeder bend (SFB), pictured in Figure 9.1, was the first feeder pipe sample provided for study, and was used as a reference sample for BN measurements. It is a $\sim 24\,\text{cm}$ long feeder pipe with a 73° bend. The axial position at the mid-point of the extrados was denoted $(0\,\text{cm}, 0°)$ in (axial, hoop) coordinates. There is a groove around the circumference of the pipe at the bend center (an axial position of 0 cm) with markings every 15°. At an axial position of $-7\,\text{cm}$ there is groove around the circumference of the pipe, and a black band of either tape or paint. During preliminary BN measurements in 2004, the right cheek (hoop position of 90°) was polished to a mirror finish with 1200 grit sandpaper [22], as were a region in the middle of the left cheek centered at $(0\,\text{cm}, -90°)$ and $(8\,\text{cm}, -90°)$. As can be seen in Figure 9.1, some rust accumulation is now evident in the polished regions, and an even finish of oxidation coats the rest of the pipe surface.

9.1.1 BN Excitation Field Response

The SFB was used to characterise the BN excitation field response in feeder pipe steel. A straight section of the SFB at an axial position of $(8 \pm 1)\,\text{cm}$ and a hoop position of $(-90 \pm 10)°$ was selected as a region with low plastic deformation, and the SL4P was mechanically clamped to the SFB. Without changing the SL4P position, B_{FT} and f_{ex} were then varied in order to establish the BN response to a sinusoidal excitation flux in the feedback coils. With the SL4P clamped rigidly to the sample surface, the

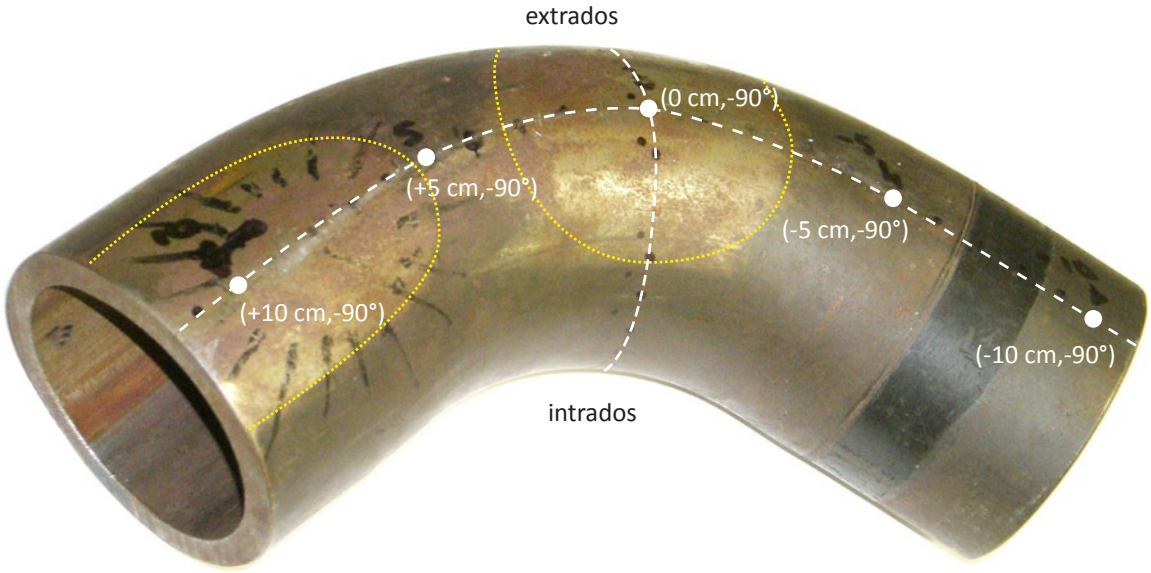

Figure 9.1: Photograph of the small feeder bend sample. (axial, hoop) coordinates are indicated in white. Visible polished regions are enclosed by yellow dotted lines.

relative uncertainties between measurements were limited by the statistical variation of the BN and the flux control system precision. Absolute uncertainties on the measurements presented in this section are predominantly coupling uncertainties, which may introduce a systematic error to all measurements.

Excitation Field Amplitude (B_{FT}) Response

For a given f_{ex} and θ_T, varying B_{FT} changes the total flux through the sample. As B_{FT} is increased, higher sample magnetisations are produced until saturation is achieved. Figure 9.2 shows the change in (a) the normalized BN power spectrum ($\boldsymbol{NPS_{BN}}$) and (b) the BN envelope ($\boldsymbol{BN_{env}}$) for five B_{FT} values from 95 mT to 1145 mT, with $f_{ex} = 31$ Hz and $\theta_T = 45°$. Figure 9.2a shows that as B_{FT} increases, the BN power shifts to higher frequencies. Figure 9.2b shows that $\boldsymbol{BN_{env}}$ consists of two pulses which increase in amplitude with B_{FT}. The peak of each pulse narrows

and shifts to lower $\phi_{B_{FT}}$ with increasing B_{FT}.

For the BN depth model in Section 7.1, peak detected BN emissions were modelled to occur when $\mu_d \cdot |\mathrm{d}B_{ex}/\mathrm{d}t|$ was a maximum within the pickup coil sensing volume. This normally occurs when excitation field phase at the surface (ϕ_0) has values of 90° and 270°. Since ϕ_0 leads the average phase of the flux through the feedback coils by $\sim 45°$ (as indicated by the tetrapole FEM in Section 5.1), the first BN peak is expected to occur for $45° < \phi_{B_{FT}} < 90°$. In Figure 9.2b, the peaks are broad for $B_{FT} = 95\,\mathrm{mT}$ and the first peak occurs for $\phi_{B_{FT}} > 90°$. As B_{FT} increases, the peak narrows, and shifts to $45° < \phi_{B_{FT}} < 90°$, as predicted by the models.

The behaviour observed in Figure 9.2 for increasing B_{FT} is explained as follows:

1. For small B_{FT}, the majority of domain wall motion is elastic and little or no BN occurs.

2. As B_{FT} increases, irreversible magnetisation processes begin to occur late in the magnetisation cycle, and the peak BN occurs for $\phi_{B_{FT}}$ values between 90° and 180°, as in Figure 9.2b for $B_{FT} = 95\,\mathrm{mT}$.

3. Once B_{FT} is sufficiently large, BN is present for the majority of the excitation cycle, as in Figure 9.2b for $B_{FT} > 191\,\mathrm{mT}$.

4. As B_{FT} increases further, the amplitude of $\boldsymbol{BN_{env}}$ increases since the same BN processes must occur in less time (i.e., $\mathrm{d}B/\mathrm{d}t$ increases as B_{FT} increases). This results in increased high frequency content in Figure 9.2a, and a narrowing of the $\boldsymbol{BN_{env}}$ peaks in Figure 9.2b.

5. As the sensing volume nears saturation the number of domains is reduced and less BN occurs. The flux increasingly couples deeper into the sample, which

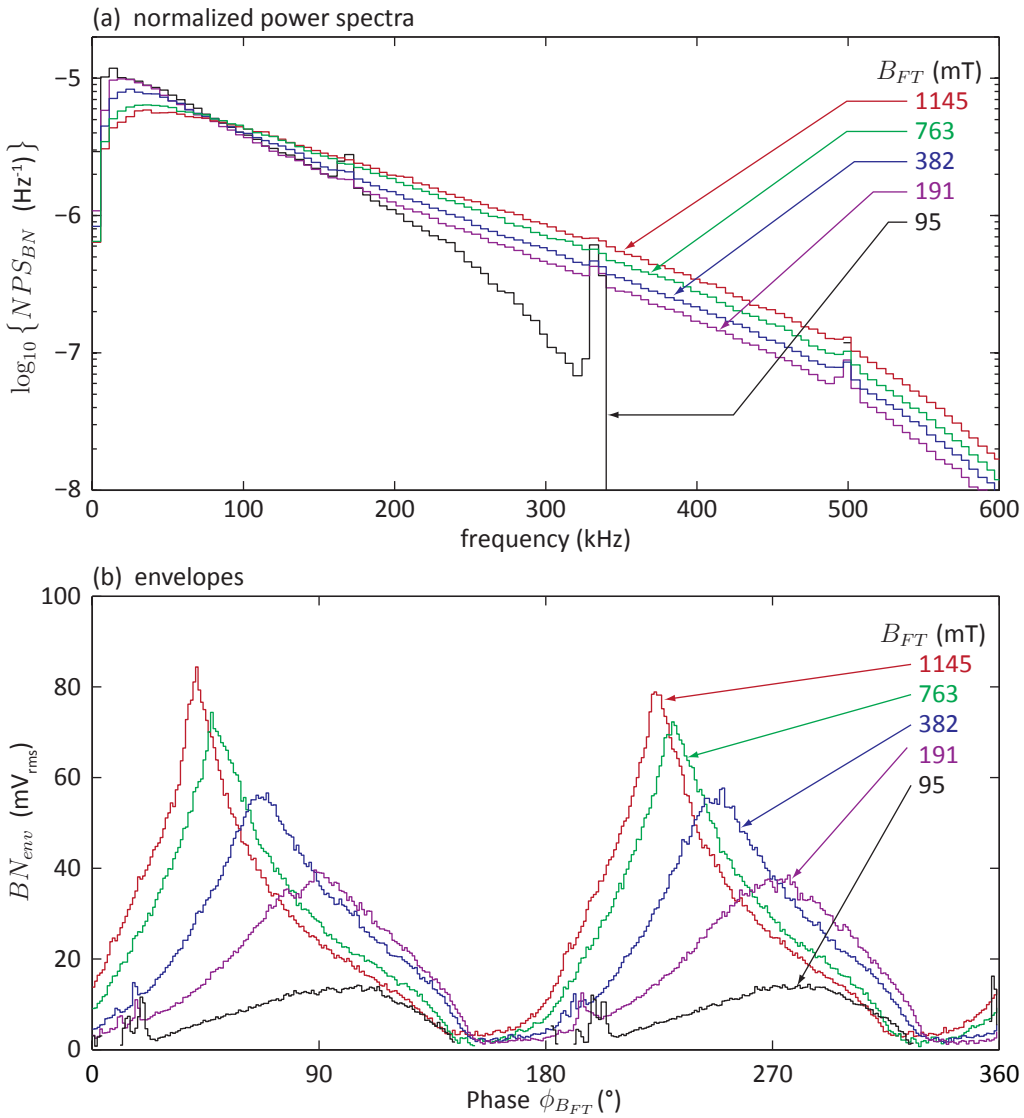

Figure 9.2: BN power spectrum and envelope dependence on excitation field amplitude. (a) $\boldsymbol{NPS_{BN}}$ and (b) $\boldsymbol{BN_{env}}$ for $f_{ex} = 31\,\text{Hz}$, $\theta_T = 45°$ for the SL4P clamped to the SFB with a variety of B_{FT} values.

increases the phase-lead of the field at the sample surface and shifts the peaks in $\boldsymbol{BN_{env}}$ to lower $\phi_{B_{FT}}$ values. Higher frequency content also propagates further in the sample due to the decreased μ_d at flux densities near saturation.

Figures 9.3a and 9.3b show BN_E and $|V_{f_{ex}}|$, respectively, as a function of $\sqrt{2}B_{Frms}$* for $f_{ex} = 31\,\text{Hz}$ and $\theta_T = 45°$. Figure 9.3a shows that BN_E is negligible below $\sim 75\,\text{mT}$ (indicated in green) where magnetisation processes are reversible. Above 75 mT, BN_E increases rapidly with $\sqrt{2}B_{Frms}$ as the surface magnetisation levels increase. Near 250 mT the sample surface begins to saturate. With fewer domains at saturation, $\text{d}BN_E/\text{d}B_{Frms}$ decreases but stays positive. BN_E is always increasing with B_{Frms} because the surface μ_d decreases with saturation. As μ_d at the surface decreases, the BN attenuation length (δ_{bn}) increases and BN from deeper in the sample propagates to the surface and is detected. Thus BN depth sensitivity increases with B_{FT}, and BN from deeper in the sample is detected at $\phi_{B_{FT}}$ values following the peaks in $\boldsymbol{BN_{env}}$.

Figure 9.3b shows that $|V_{f_{ex}}|$ increases with B_{Frms}. If the sample magnetic impedance was a constant, Figure 9.3b would show a straight line through the origin. Instead, Figure 9.3b shows that for low B_{FT}, when the magnetisation processes are reversible and little BN occurs, $\text{d}\,|V_{f_{ex}}|\,/\text{d}B_{Frms}$ is greater than its average value (indicated by a straight line fit through the origin) due to the higher sample impedance associated with elastic domain wall motion. Once into the irreversible regime and BN_E is increasing, the sample impedance and $\text{d}\,|V_{f_{ex}}|\,/\text{d}B_{Frms}$ decrease. When entering the saturation regime, $\text{d}\,|V_{f_{ex}}|\,/\text{d}B_{Frms}$ again increases with the increasing magnetic

*For sinusoidal flux waveforms, $\sqrt{2}B_{Frms} \approx B_{FT} \approx B_{Fpk}$. $\sqrt{2}B_{Frms}$ is calculated using all the points in the $\boldsymbol{B_{F(p),j}}$ waveforms, and thus preferred to B_{Fpk} (which is more sensitive to noise because it only uses a single measured point) and B_{FT} (which is not an actual measurement but the set control parameter).

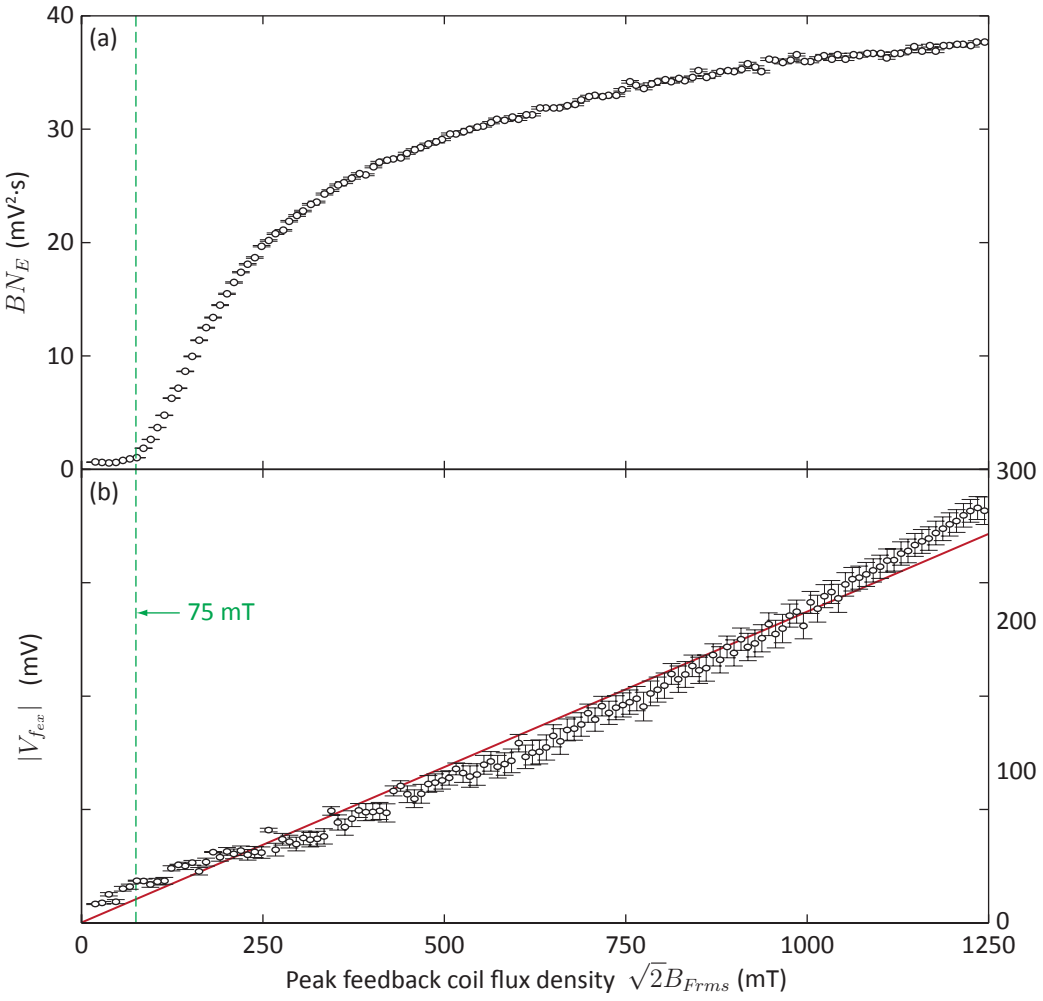

Figure 9.3: Excitation field amplitude (B_{Frms}) dependence of (a) BN energy (BN_E) and (b) the excitation frequency pickup coil signal component ($|V_{f_{ex}}|$) for $f_{ex} = 31\,\text{Hz}$, $\theta_T = 45°$ for the SL4P mounted on the small feeder bend. Error bars indicate a 68% confidence interval. The transition between reversible and irreversible magnetisation processes is indicated by a vertical dashed line. In (ii), a linear fit is shown in red.

impedance. Figure 9.3b confirms that the sample is exhibiting saturation effects at higher B_{FT} values, and demonstrates the type of information that can be resolved from the low frequency data in the pickup coil waveform.

Excitation Frequency (f_{ex}) Response

For a given B_{FT} and θ_T, varying f_{ex} changes the excitation field skin depth (δ_{ex}) and $\mathrm{d}\vec{B}/\mathrm{d}t$. With δ_{ex} decreasing with increasing f_{ex} (see equation (7.1)), it follows from flux conservation that the flux density at the sample surface increases with f_{ex}. Figures 9.4a, 9.4b and 9.4c show BN_E, BN_{rms}, and $|V_{f_{ex}}|$, respectively, as a function of B_{Frms} for f_{ex} values of 11 Hz, 31 Hz, 51 Hz, and 71 Hz.

Figure 9.4a shows that below 250 mT, BN_E increases with f_{ex}. This indicates that the transition between reversible and irreversible magnetisation processes occurs at lower B_{Frms} values for higher f_{ex}. Saturation effects are also seen at lower B_{Frms} for higher f_{ex}. Both of these phenomena support the theory that the combination of a smaller δ_{ex} and flux conservation increases the flux density at the sample surface with increasing f_{ex}. As a result, more domain activity in the sensing region occurs, and BN_E increases.

Above 500 mT, Figure 9.4a shows that BN_E decreases with f_{ex}. The BN depth model in Chapter 7 indicates a slight increase in BN penetration depth occurs with decreasing f_{ex} (see Figure 7.5). This results in a larger sensing volume, and an increased BN_E with decreasing f_{ex} at high B_{FT} values. Destructive superposition of incoherent Barkhausen events may also decrease BN_E with increasing f_{ex}, though this would need to be tested in fundamental BN studies.

Figures 9.4b and 9.4c show that BN_{rms} and $|V_{f_{ex}}|$ increase with f_{ex}. This is due

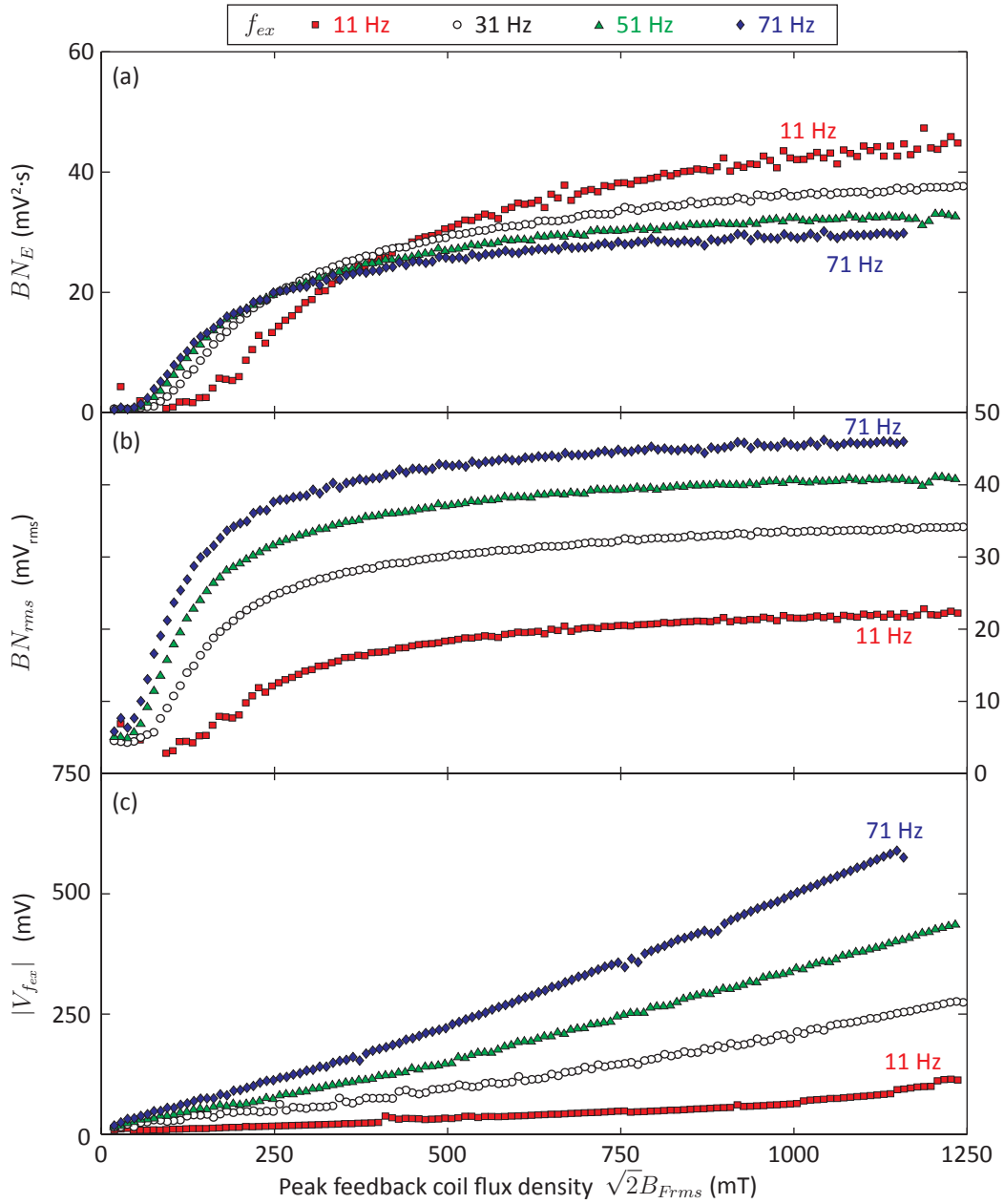

Figure 9.4: Excitation frequency (f_{ex}) dependence of (a) BN energy (BN_E),(b) the rms BN (BN_{rms}), and (c) the excitation frequency pickup coil signal component ($|V_{f_{ex}}|$) with varying B_{Frms} for $\theta_T = 45°$ for the SL4P on a feeder pipe sample.

to the increased $\mathrm{d}\vec{B}/\mathrm{d}t$ through the pickup coil with f_{ex}. Since the background noise levels remain constant, the ratio of BN_{rms} to the RMS background noise increases with f_{ex}. It follows that with higher f_{ex}, the relative error associated with separating BN and background noise power is reduced.

The preceding analysis indicates that surface magnetisation levels increase with f_{ex} for the same B_{FT}. This means that more of the total BN response can be produced by increasing f_{ex} in a current-limited[†] system. In a given period of time, the number of BN cycles that can be collected and analysed increases with f_{ex}. BN voltage levels also increase with f_{ex}, making them easier to isolate from other noise sources at higher f_{ex}. At large B_{FT} and low f_{ex}, there is evidence that BN depth penetration is increased, due to the higher BN_E in these configurations. This depth increase is predicted to be minor by the BN depth model (see Figure 7.5). Henceforth, an f_{ex} value of 51 Hz was used to allow larger k_{max} and reduced data processing times, compared to $f_{ex} = 31$ Hz or lower.

9.1.2 Lift-Off Compensation

Coupling uncertainties were identified in Section 8.6 as being the dominant source of error for scanning BN measurements. In addition to positional variation of the sample magnetic properties, the coupling uncertainties include the effects of both pickup coil lift-off and electromagnet lift-off. To quantify the performance of the SL4P's lift-off compensation features, the pickup coil lift-off and electromagnet lift-off sensitivities were estimated on the SFB. A discussion of these two separate lift-off effects follows.

[†]Power supplies are current limited at low f_{ex}, and voltage limited at high f_{ex} when driving inductive loads. Excitation coils may overheat with too much current.

Table 9.1: BN_E variation with pickup coil lift-off for different excitation field settings.

Lift-off (mm)	0.00	0.43	0.86	1.72
Excitation	BN_E (mV^2s)	fraction of BN_E at 0.00 mm (%)		
31 Hz, 477 mT	30.49 ± 0.09	-	$(10.9 \pm 0.5)\%$	$(3.4 \pm 0.2)\%$
51 Hz, 239 mT	18.09 ± 0.06	$(24.7 \pm 0.4)\%$	$(11.9 \pm 0.2)\%$	-
51 Hz, 477 mT	28.36 ± 0.08	$(24.7 \pm 0.3)\%$	$(11.2 \pm 0.1)\%$	-
51 Hz, 955 mT	36.61 ± 0.10	$(25.2 \pm 0.2)\%$	$(10.8 \pm 0.1)\%$	-

Pickup Coil Lift-Off

To estimate the SL4P pickup coil lift-off sensitivity, a magic marker was used to indicate a point on the SFB in the region used in Section 9.1.1. The SL4P pickup coil was placed directly on top of the marked point, and 25 measurements were taken for several excitation field configurations, removing and replacing the SL4P between each measurement. One, two or four layers of 0.43 mm thick vinyl tape were then affixed to the bottom of the pickup coil, and the procedure was repeated.

Table 9.1 shows the mean BN_E without any tape between the pickup coil and the sample (i.e., for 0.00 mm lift-off), and the fraction (in percent) of BN_E detected after the coil is lifted off, for four excitation field configurations. This data indicates that the introduction of a non-permeable gap between the pickup coil and the sample has a scaling effect on the measured BN_E that is similar for all excitation conditions. With 0.43 mm of tape, $\sim 25\%$ of the BN_E detected at the surface reaches the coil. Only $\sim 11\%$ of the BN_E is detected 0.86 mm from the sample, and 3.4% is detected at 1.72 mm.

The loss of 75% of the BN_E within the first 0.43 mm from the sample surface is problematic for absolute measurements of BN on surfaces with variable finish, since a relatively small variation in the surface finish may lead to a significant variation in the measured BN power. Any scanning BN measurement on a surface should therefore

be accompanied by a scan in a region of the sample that includes the whole range of surface conditions to ascertain the typical BN variance with surface condition. Such measurements will also include contributions from the variation of the sample magnetic properties. The variation in pickup coil coupling, combined with the magnetic property variability, limits the precision to which any other parameter that changes BN (e.g., strain) can be resolved.

Electromagnet Pole Lift-Off

When attached to a feeder pipe, the SL4P poles 1 and 3 are aligned to the hoop axis, while poles 2 and 4 are aligned to the axial direction. Since feeders have a larger degree of curvature along the hoop axis than along the axial direction and the SL4P poles are flat, poles 1 and 3 are significantly less coupled to the sample than poles 2 and 4. Furthermore, the variation in curvature due to the bending process is expected to differ along the axial and hoop axes. It follows that electromagnet coupling uncertainties in the axial direction are different from those in the hoop direction.

To measure the hoop electromagnet lift-off response, a point on the SFB was marked[‡]. With 0.43 mm non-magnetic gaps between each pole and the sample[§] and $f_{ex} = 51\,\text{Hz}$, $k_{max} = 64$ and $\theta_T = 0°$, B_{FT} was varied from 95 mT to 955 mT to trace out the BN response to B_{FT}. The B_{FT} response was measured 8 times, removing and re-positioning the SL4P over the marked point for each measurement, in order that the data could be averaged to compensate for pickup coil coupling uncertainties. The gap under pole 1 was then increased to 1.29 mm (with 0.43 mm gaps under the other

[‡]The same point as used to measure pickup coil coupling.

[§]Gaps were introduced by affixing 0.43 mm thick vinyl tape between the poles and the sample.

three poles), and the B_{FT} response was measured 8 times as described above. The gaps under both poles 1 and 3 were then set to 1.29 mm, and the B_{FT} response was measured again. This procedure is similar to that used in [50], but has the added complication that the pickup assembly is repositioned with the SL4P, which required the B_{FT} responses to be averaged.

Figure 9.5 shows the B_{FT} responses for the three different lift-off configurations. In Figure 9.5a, the mean BN_E for the 8 measurements is plotted against the mean RMS excitation current in poles 1 and 3 (I_{Xrms}), with horizontal error bars indicating the difference between the current in excitation coils 1 and 3. In Figure 9.5b, the mean BN_E is plotted against the mean RMS flux density in feedback coils 1 and 3 (B_{Fxrms}), with the horizontal error bars representing the difference in flux density between the two coils. Vertical error bars for both plots are the standard error on the mean BN_E.

Note that Figures 9.5a and 9.5b show exactly the same BN_E data plotted against different excitation field parameters. Figure 9.5a shows the relatively weak correlation between the excitation current and BN_E under variable lift-off conditions. As the total lift-off increases, so too must the average current in order to reproduce the same BN_E. When pole 1 had a gap of 1.29 mm and pole 3 was at the default 0.43 mm, significantly more current was required through excitation coil 1 than through excitation coil 3 in order to compensate for the reduced coupling. This demonstrates that the excitation current is an inappropriate means of reproducing the sample BN response under variable electromagnet coupling conditions.

Figure 9.5b shows that when 1.29 mm of lift-off was present beneath both poles, the B_{FT} response was consistent with the default 0.43 mm lift-off configuration. The consistency of B_{FT} response with equal gaps under the poles in the hoop direction

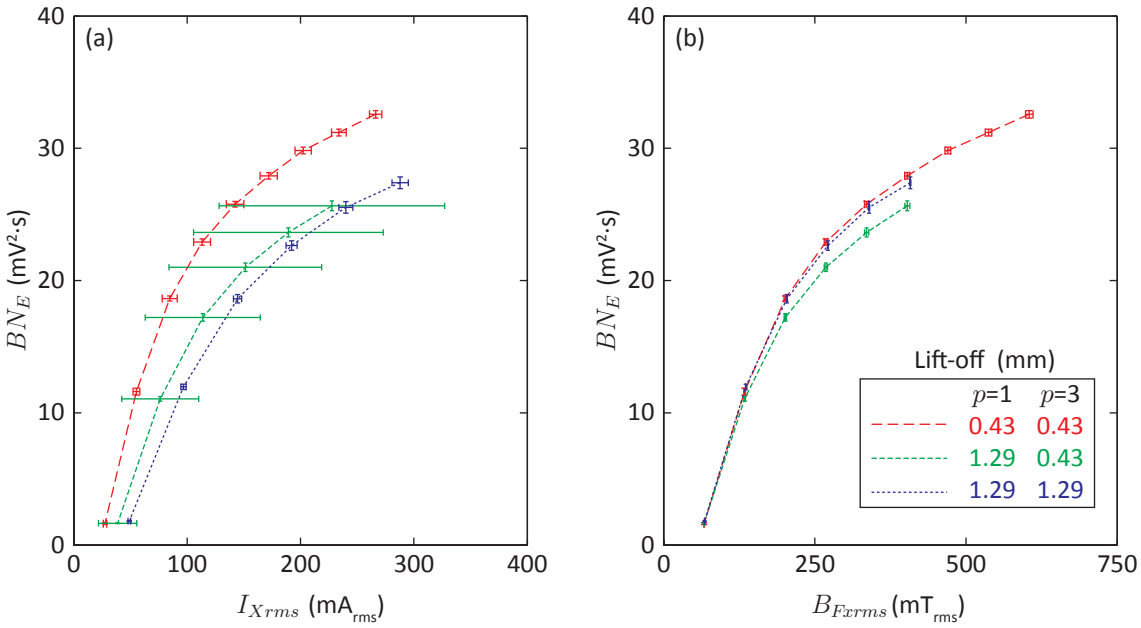

Figure 9.5: Hoop axis tetrapole lift-off sensitivity, showing the BN_E variation with (a) the mean RMS current in excitation coils 1 and 3 (I_{Xrms}), and (b) the mean RMS flux density in feedback coils 1 and 3 (B_{Fxrms}), for the SL4P on the SFB with variable lift-off configurations. Lift-off values for poles 1 and 3 are indicated in the legend in mm. Horizontal error bars show the difference in either current or flux density in poles 1 and 3. Vertical error bars are a 68% confidence interval for the error on the mean BN_E. Lines are to guide the eye.

shows that the flux conservation approximation is effective at reducing sensitivity of lift-off along the hoop axis. However, when only the gap under pole 1 was increased to 1.29 mm, the lift-off was non-uniform, and BN_E values are shown to decrease by $8 \pm 2\%$, which is inconsistent with the default B_{FT} response.

The above procedure for estimating the electromagnet lift-off response was repeated for poles 2 and 4 along the axial direction, with $\theta_T = 90°$. Figure 9.6 shows the B_{FT} response for the three different lift-off configurations. BN_E is plotted against the mean RMS current in excitation coils 2 and 4 (I_{Yrms}) in Figure 9.6a, and against the mean RMS flux density in feedback coils 2 and 4 (B_{Fyrms}) in Figure 9.6b. Figure 9.6a,

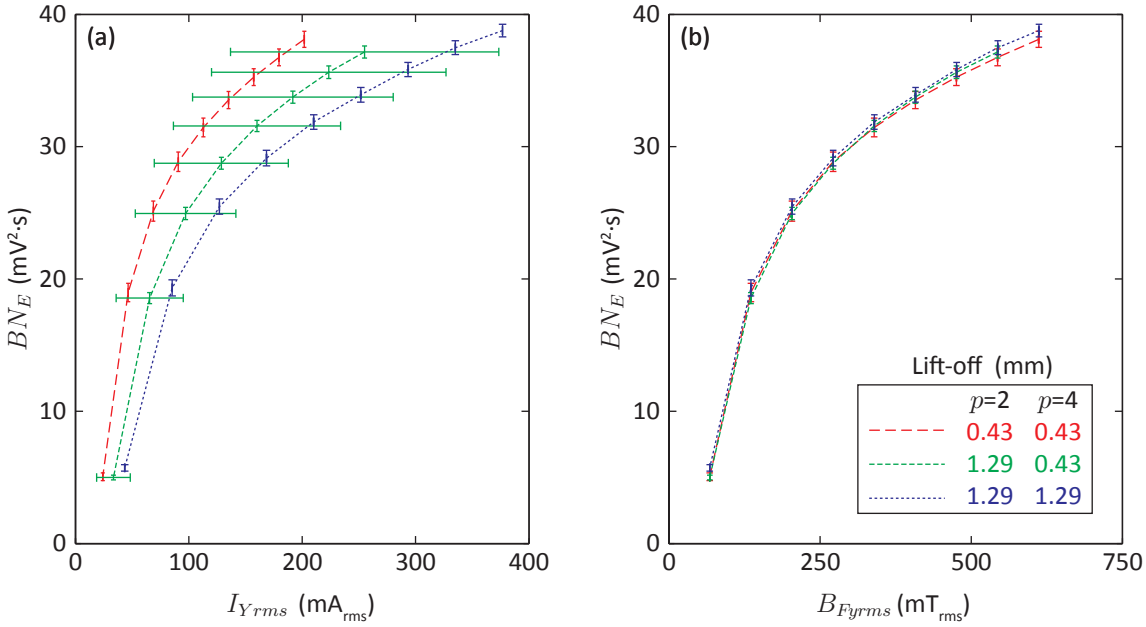

Figure 9.6: Axial direction tetrapole lift-off sensitivity, showing the BN_E variation with (a) the mean RMS current in excitation coils 2 and 4 (I_{Yrms}), and (b) the mean RMS flux density in feedback coils 2 and 4 (B_{Fyrms}), for the SL4P on the SFB with variable lift-off configurations. Lift-off values for poles 2 and 4 are indicated in the legend in mm. Horizontal error bars show the difference in either current or flux density in poles 2 and 4. Vertical error bars are a 68% confidence interval for the error on the mean BN_E. Lines are to guide the eye.

like Figure 9.5a, shows the relatively weak correlation between the excitation current and BN_E under different lift-off configurations. In Figure 9.6b, the BN response is consistent with respect to the average flux density for all three lift-off configurations.

Comparison of Figure 9.5b with Figure 9.6b shows that the consistency of the BN response with the flux density in the feedback coils along the axial direction is superior to the hoop direction. This is because the SL4P coupling is stronger along the axial direction, so flux conservation in the magnetic circuit is a better approximation. In order to improve the performance along the hoop axis, coupling must be increased by reducing the average gap between the short core poles and the feeder pipe. This can be

achieved by shaping the short core poles to better conform to the hoop curvature. It has been confirmed with the core manufacturing company *MK Magnetics* that cutting U-cores to accommodate the feeder hoop curvature is possible, "if the tolerances for the angles and/or pole radii are not critical" [67].

For the existing SL4P design, electromagnet coupling effects on the BN response are minimized when the SL4P is mounted such that the coupling for poles 1 and 3 are equal. Provided equal coupling of poles 1 and 3 is maintained, the BN response to B_{FT} is consistent along both axial and hoop directions for lift-off up to at least 1.29 mm under any one pole. This implies that the FCS and SL4P can be used to make measurements at a variety of positions on a bent feeder pipe with confidence that variation in the electromagnet coupling is not responsible for changes in the measured BN.

9.2 Three-Point Bending Rig (3PBR) Studies

The three-point bending rig (3PBR) was constructed in order to measure correlations between BN and strain in SA-106 Grade B steel.

- Section 9.2.1 presents a description of the 3PBR components and operation.
- Section 9.2.2 presents the strain and BN measurement procedure, so that strain hysteresis effects due to plastic deformation can be readily identified in later analyses.
- Section 9.2.3 discusses the effects of strain on the BN_E at various excitation field amplitudes (B_{FT}).

- Section 9.2.4 demonstrates BN_E anisotropy measurements using the SL4P on the 3PBR for the data presented in Section 9.2.3.
- Section 9.2.5 presents axial BN_E vs. strain calibration data for $f_{ex} = 51\,\text{Hz}$.
- Section 9.2.6 shows the effects of large tensile and compressive strains on $\boldsymbol{BN_{env}}$.
- Section 9.2.7 shows the correlations between $|V_{f_{ex}}|$, which is sensitive the macroscopic field coupling, and strain.
- Section 9.2.8 presents a summary of the results from the 3PBR.

9.2.1 3PBR Sample Details

The 3PBR, illustrated in Figure 9.7, consists of a 3.18 m long, 63.5 mm nominal diameter Schedule 80 SA-106 Grade B pipe, purchased from Russell Metals in Kingston, suspended above a wide flange steel I-beam, using three 6 ton bottle jacks. The top of the pipe directly above the middle jack is denoted $(0\,\text{cm}, 0°)$ in (axial, hoop) coordinates. In the 'tensile' configuration (as illustrated) the pipe is strapped to the outer two bottle jacks, and the middle bottle jack is raised to introduce a tensile axial strain ($\varepsilon_a > 0$) on the top of the pipe. In the 'compressive' configuration (not shown), the pipe is strapped to the middle jack, and the outer jacks are raised to introduce a compressive axial strain ($\varepsilon_a < 0$) on the top of the pipe. As the 3PBR bends to produce an axial strain, Poisson effects result in an opposing hoop strain (ε_h).

The pipe is instrumented with four *Vishay*® general purpose 350 Ω strain gauges, with a gauge factor of $2.100 \pm 0.5\%$ at 24 °C and a transverse sensitivity of $0 \pm 0.2\%$. Two gauges oriented in the axial direction are centered at $(9.1\,\text{cm}, 0°)$ and $(30.2\,\text{cm}, 0°)$. The other two gauges are oriented in the hoop direction and centered

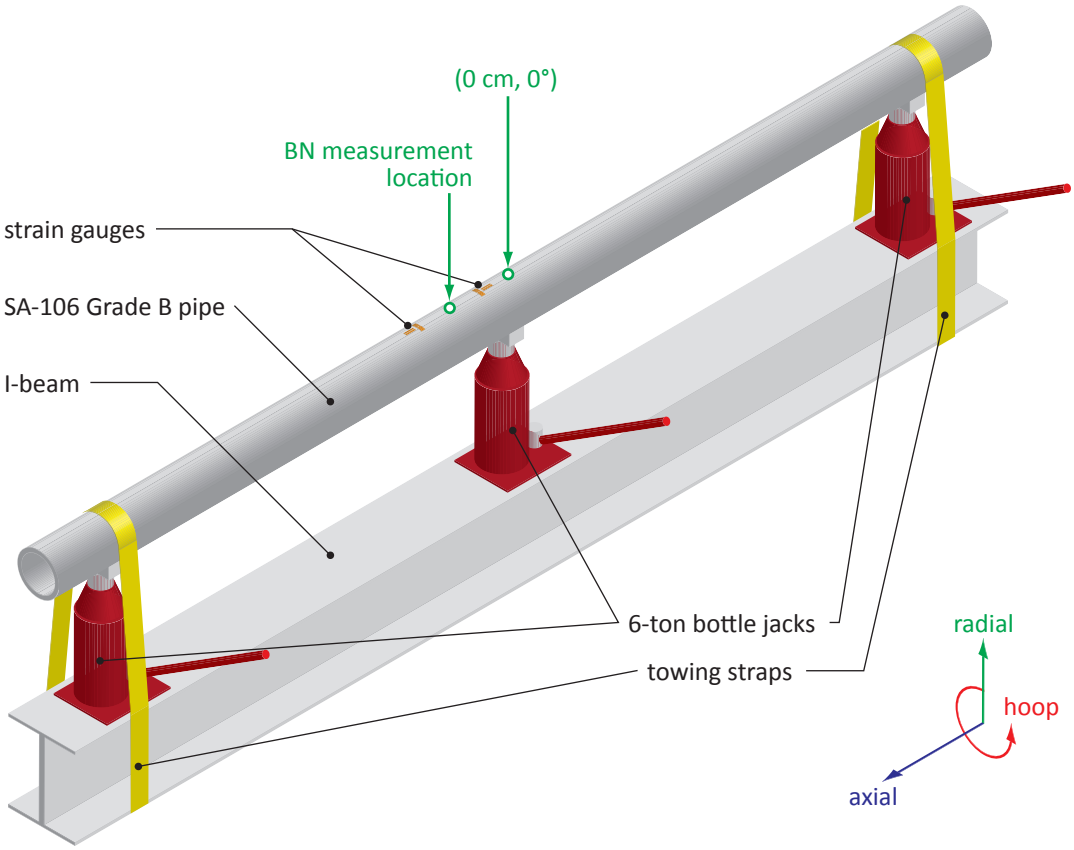

Figure 9.7: Schematic of the three-point bending rig in the tensile configuration. The pipe surface origin is labeled $(0\,\text{cm}, 0°)$ in (axial, hoop) co-ordinates, with the positive axial and hoop directions indicated by arrows. Not to scale.

at $(11.5\,\text{cm}, 0°)$ and $(28.5\,\text{cm}, 0°)$. The surface of the pipe immediately surrounding and between the gauges was sanded to a smooth finish using 600 grit sandpaper to allow proper mounting of the strain gauges. Linear interpolation was used as a first-order approximation for ε_a and ε_h at any point between the two gage pairs.

The minimum specified yield strength for SA-106 Grade B piping is 240 MPa, with an elastic modulus (Y) of 202.7 GPa at 21 °C, and a Poisson ratio (ν) of 0.3 [17]. Using the generalized form of Hooke's law for an isotropic material (equation (1.3))

in cylindrical coordinates gives the axial stress (σ_a) as:

$$\sigma_a = \frac{Y}{1+\nu}\left[\varepsilon_a + \frac{\nu}{1-2\nu}\left(\varepsilon_a + \varepsilon_h + \varepsilon_r\right)\right], \tag{9.1}$$

and the hoop stress (σ_h) as:

$$\sigma_h = \frac{Y}{1+\nu}\left[\varepsilon_h + \frac{\nu}{1-2\nu}\left(\varepsilon_a + \varepsilon_h + \varepsilon_r\right)\right], \tag{9.2}$$

where ε_r is the radial strain. To calculate σ_a and σ_h from the above equations requires a value for ε_r, which was shown to be small compared to ε_a and ε_h in neutron diffraction studies [24], and was therefore set to 0.

It was found from preliminary strain measurements on the 3PBR that the introduction of an axial strain ε_a produced a hoop strain:

$$\varepsilon_h = -(0.291 \pm 0.001)\varepsilon_a. \tag{9.3}$$

This is close to $\nu = 0.3$, and indicates approximately uniaxial loading at the top of the pipe where BN and strain measurements were performed. To determine the operating range for BN experiments, equation (9.3) was substituted into equation (9.1), and solved for $\sigma_a = 240\,\text{MPa}$. This gave $\varepsilon_a = 1028\,\mu\varepsilon$ at the specified yield stress, where $\mu\varepsilon = 10^{-6}$ is 'microstrain.'

9.2.2 Measurement Procedure

To investigate BN-strain relationships in SA-106 Grade B steel, the SL4P was clamped to the 3PBR halfway between the strain gauges at an (axial, hoop) position of ((20.0±

$0.5)\,\text{cm}, (0 \pm 5)^\circ$). The four gauges were balanced to $0\,\mu\varepsilon$ and the estimated $(\varepsilon_a, \varepsilon_h)$ at the SL4P position was varied in the following sequence:

1. initial configuration: $(0, 0)\,\mu\varepsilon$
2. axial compression: $(-914, 261)\,\mu\varepsilon$
3. release: $(9, 4)\,\mu\varepsilon$
4. axial tension: $(911, -263)\,\mu\varepsilon$
5. release: $(1, 5)\,\mu\varepsilon$.

At each strain configuration described above, the following BN measurements were made with $f_{ex} = 51\,\text{Hz}$:

(A) With $\theta_T = 90^\circ$ (along the axial direction), B_{FT} was varied from 19 mT to 955 mT in 19 mT increments. These data are used to show the effect of B_{FT} on correlations between BN and strain in section 9.2.3.

(B) With B_{FT} values of 191 mT, 382 mT and 764 mT, θ_T was varied from 0° to 360° in 10° increments. These θ_T sweeps were used to measure BN anisotropy changes due to strain in section 9.2.4.

To measure the BN-strain response in more detail, the 3PBR was then cycled in the following sequence:

1. increasing from $(5, 5)\,\mu\varepsilon$ to $(902, -260)\,\mu\varepsilon$,
2. decreasing from $(716, -260)\,\mu\varepsilon$ to $(-936, 269)\,\mu\varepsilon$,
3. increasing from $(-565, 174)\,\mu\varepsilon$ to $(1273, -370)\,\mu\varepsilon$,

4. and decreasing from $(921, -266)\,\mu\varepsilon$ to $(-7, 9)\,\mu\varepsilon$,

with an average ε_a increment size of $110\,\mu\varepsilon$. At each strain configuration, the axial BN was measured for B_{FT} values of 191 mT, 382 mT, 573 mT and 764 mT, with $f_{ex} = 51$ Hz and $\theta_T = 90°$. This data is presented in Section 9.2.5 as BN_E vs. strain calibration curves, and used in Section 9.2.6 to show the effect of strain on $\boldsymbol{BN_{env}}$. This data is also used in Section 9.2.7 to show the correlations between strain and the macroscopic field component ($|V_{f_{ex}}|$).

9.2.3 Excitation Amplitude and Strain

The flux control system and the SL4P allows the operator to explore a large variety of excitation field configurations. In principle, this facilitates optimization of the excitation field amplitude (B_{FT}) and frequency (f_{ex}) to maximize BN correlations with strain and/or stress. To simplify data collection and analysis, only B_{FT} considerations are presented here, with $f_{ex} = 51$ Hz. BN_E is an efficient estimate of the total BN power, and is therefore used for this analysis.

Figure 9.8a shows the axial BN response to B_{Frms} for various strain configurations, with the configuration sequence indicated in the legend. Comparing the data sets for $(-914, 261)\,\mu\varepsilon$ and $(0, 0)\,\mu\varepsilon$ shows the BN_E increasing with axial compression for most B_{Frms} values, except for a small decrease for $\sqrt{2}B_{Frms} < 250$ mT. When the axial compression is released to $(9, 4)\,\mu\varepsilon$, the BN_E increases further. This suggests that plastic deformation occurred when the pipe was in compression, establishing a new reference strain state with a tensile residual stress. When the pipe was released from compression, it elastically returned to the new reference at $(9, 4)\,\mu\varepsilon$, and the BN_E increased. This indicates that BN_E decreases with elastic compression, and

increases with residual tension. Note however, that the BN_E increased with the residual tension, even when elastic compression was present.

Figure 9.8a shows a significant increase in BN_E from the relaxed $(9, 4)\,\mu\varepsilon$ state to the axial tension state at $(911, -263)\,\mu\varepsilon$. After relaxation from axial tension, the $(1, 5)\,\mu\varepsilon$ BN_E is decreased relative to the $(9, 4)\,\mu\varepsilon$ BN_E, indicating that plastic deformation occurred under axial tension, leading to a compressive residual stress at $(1, 5)\,\mu\varepsilon$ relative to $(9, 4)\,\mu\varepsilon$. Thus BN_E increases with elastic tension, and decreases with residual compression.

Figure 9.8b shows the difference in BN_E between the $(911, -263)\,\mu\varepsilon$ and $(1, 5)\,\mu\varepsilon$ states to show the change in BN_E with tension, and the difference between the $(-913, -261)\,\mu\varepsilon$ and $(9, 4)\,\mu\varepsilon$ states to show the change in BN_E with compression. In general, Figure 9.8b shows that the introduction of strain changes the BN_E at all excitation field amplitudes where BN is produced. Above $\sqrt{2}B_{Frms} = 300\,\mathrm{mT}$, the change in BN_E due to strain is approximately constant as a function of B_{Frms}, with a maximum sensitivity to tension at $B_{Frms} \approx 500\,\mathrm{mT}$. This suggests that the majority of BN variation with tensile strain occurs at low sample magnetisations, at or near the coercive field, which is consistent with previous results [68]. Comparing the difference in BN_E between the $(-914, 261)\,\mu\varepsilon$ and $(9, 4)\,\mu\varepsilon$ states with the difference between the $(911, -263)\,\mu\varepsilon$ and $(1, 5)\,\mu\varepsilon$ states indicates that BN_E is approximately 4.5 ± 0.4 times more sensitive to elastic tension than to elastic compression.

9.2.4 BN Anisotropy and Strain

Since the 3PBR introduces an axial strain due to the loading and a hoop strain via Poisson's effect, a variation in the BN_E with θ_T at the different strain configurations

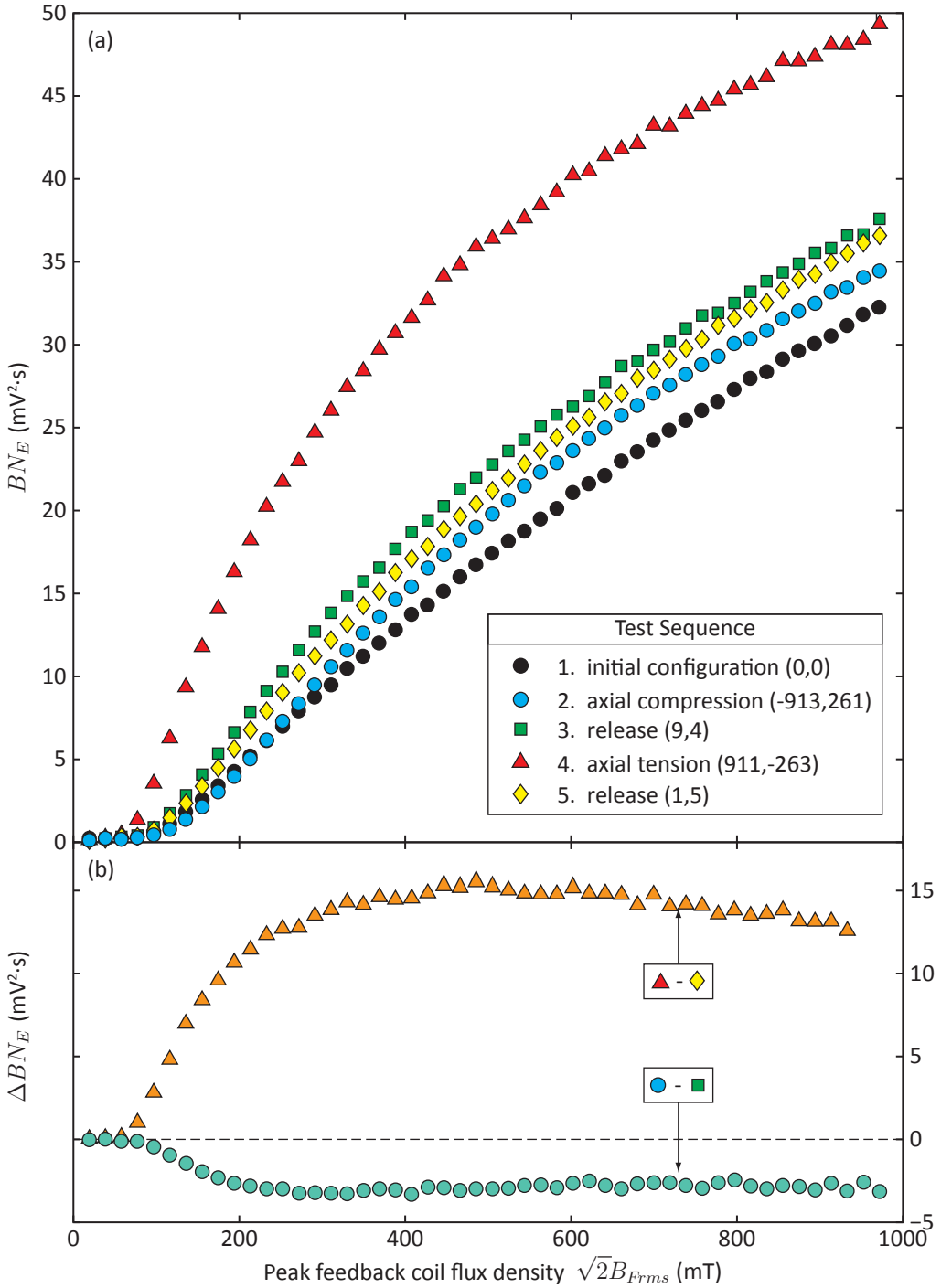

Figure 9.8: Axial BN excitation field amplitude dependence in the 3PBR, with $f_{ex} = 51\,\text{Hz}$ and $\theta_T = 90°$, (a) for five load configurations in sequence. (b) Differences between sequences 2 and 3, and sequences 4 and 5.

is expected. For the same strain configuration sequence presented in Section 9.2.3, Figures 9.9a, 9.9b, and 9.9c show BN_E anisotropy measurements, produced with field superposition by varying θ_T, at B_{FT} values of 191 mT, 382 mT and 764 mT, respectively.

Comparing the BN_E along the axial direction in Figure 9.9 shows the same trends as indicated in Figure 9.8: from the initial reference configuration, plastic deformation from axial compression resulted in residual tension, and plastic deformation from axial tension resulted in residual compression. At the end of the test sequence, there was a net increase in axial tension from the initial reference condition.

Figure 9.9 also shows that in the $(-914, 261)\,\mu\varepsilon$ state, the hoop BN_E is elevated with the tensile hoop strain due to Poisson's effect. When the axial compression was released, since the hoop stress was below the yield stress, the sample elastically returned to the reference state. In the $(911, -263)\,\mu\varepsilon$ configuration, Figure 9.9a shows the hoop BN_E decreasing due to Poisson's effect, though this decrease is not visible in Figures 9.9b and 9.9c. When the axial tension was released, the hoop strain again returned to reference levels. Thus little plastic deformation occurred in the hoop direction over the testing sequence.

Note that Figure 9.9 demonstrates that the SL4P combined with the FCS is capable of BN anisotropy measurements on feeders. However, there is some evidence that the superposition is nonlinear, which leads to artifacts. In Figure 9.9a, the $(0, 0)\,\mu\varepsilon$, $(9, 4)\,\mu\varepsilon$, and $(1, 5)\,\mu\varepsilon$ configurations all exhibit increased BN_E along the axial and hoop directions, which are coincidentally the orientations of the SL4P cores. This biaxial pattern does not appear in Figure 9.9b with $B_{FT} = 382$ mT, and at 764 mT in Figure 9.9c, appears to be inverted with peaks in the BN_E at $\pm 45°$ and

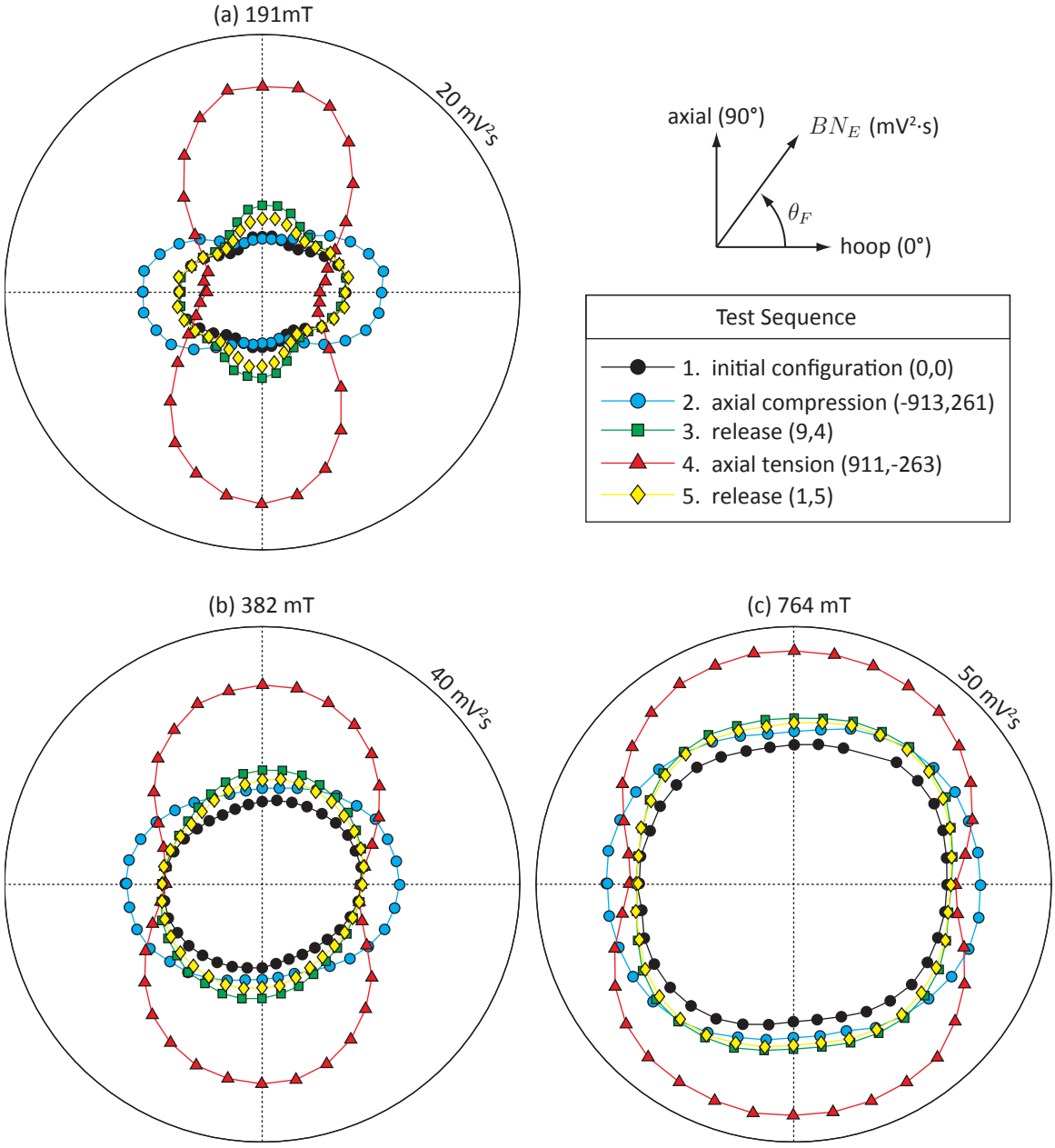

Figure 9.9: Angular BN measurements in near-yield and relaxed strain configurations from the 3PBR with $f_{ex} = 51$ Hz and B_{FT} values of (a) 191 mT, (b) 382 mT and (c) 764 mT. Data in the legend are indicated in sequence, and lines are to guide the eye.

$\pm 135^\circ$ to the hoop axis.

Since the SL4P was not designed to be rotated on feeders, no tests have been able to confirm whether the biaxial patterns seen in Figure 9.9a are purely an artifact of nonlinear superposition, or whether they also indicate texture and/or residual strain along the axial and hoop directions of the pipe. There is also the possibility that pickup coil misalignment contributes to the measured anisotropy. Testing for these effects on a similarly thick isotropic flat surface with negligible edge effects is recommended for future study.

Despite these potential issues, Figure 9.9 shows the SL4P and θ_T rotation are effective at measuring relative changes in anisotropy due to strain. Moreover, the SL4P system offers considerable time-savings and decreased probe wear over the traditional rotational measurement due to the lack of moving parts. In addition, the pickup coil coupling is unchanged during the measurement. This allows relative angular measurements to be performed with higher precision than can be achieved using a mechanically rotated electromagnet, where the pickup coil coupling changes for each angular position.

9.2.5 Axial BN Calibration Curves

In Section 9.2.3, it was shown that BN_E is 4.5 ± 0.4 times less sensitive to compression than to tension. It follows that the relationship between BN_E and strain is non-linear. By incrementally increasing the strain in the 3PBR and performing BN measurements, elastic calibration curves can be generated. This was done in the second strain configuration sequence described in Section 9.2.2, and Figure 9.10 shows the resulting BN_E vs axial strain plots. The top axis in Figure 9.10 indicates the

approximate axial stress, calculated by substituting the measured strain gauge values into equation (9.1), with $\varepsilon_r = 0$, $Y = 202.7\,\text{GPa}$ and $\nu = 0.3$ [17].

Figure 9.10 shows that the initial increase in tension (circles) results in a smoothly increasing BN_E at all excitation field amplitudes. After the initial increase in tension, the BN_E decreases with the strain (squares), tracking the initial increasing data to the relaxed state at $5\,\mu\varepsilon$, where the BN_E is shown to be on average 1.3% lower than the initial BN_E. This suggests only minor plastic deformation occured at the near-yield tension, resulting in a small amount of residual compression.

As the 3PBR was taken further into compression (squares), Figure 9.10 shows all four data sets decreasing to $\sim -500\,\mu\varepsilon$. Below $-500\,\mu\varepsilon$, BN_E is seen to increase for decreasing strain, except for $B_{FT} = 191\,\text{mT}$, where the BN_E is seen to reach a constant value of 70% of the initial BN_E. As the compressive strain is again increased (triangles), the BN_E follows a new curve, suggesting that plastic deformation occurred during compression. The 3PBR was then cycled up to $1273\,\mu\varepsilon$ (triangles), estimated as 304 MPa or 1.3× the yield stress, and relaxed (diamonds) to a resting state of $-7\,\mu\varepsilon$, suggesting tensile plastic deformation occured, resulting in residual compression.

The average statistical error for all BN_E data in Figure 9.10 is $erBN_E/BN_E = \pm 0.21\%$. These errors are smaller than the points on the plot, and therefore are not shown. This precision was obtained with $k_{max} = 64$, and is possible because the pickup coil was fixed in the same position for all the measurements described in this section (i.e., Section 9.2). The calibration curves in Figure 9.10 therefore represent the best case scenario for correlations between BN_E and strain and/or stress. For residual stress measurements, the relative error on BN_E is closer to ±2% to ±7% due

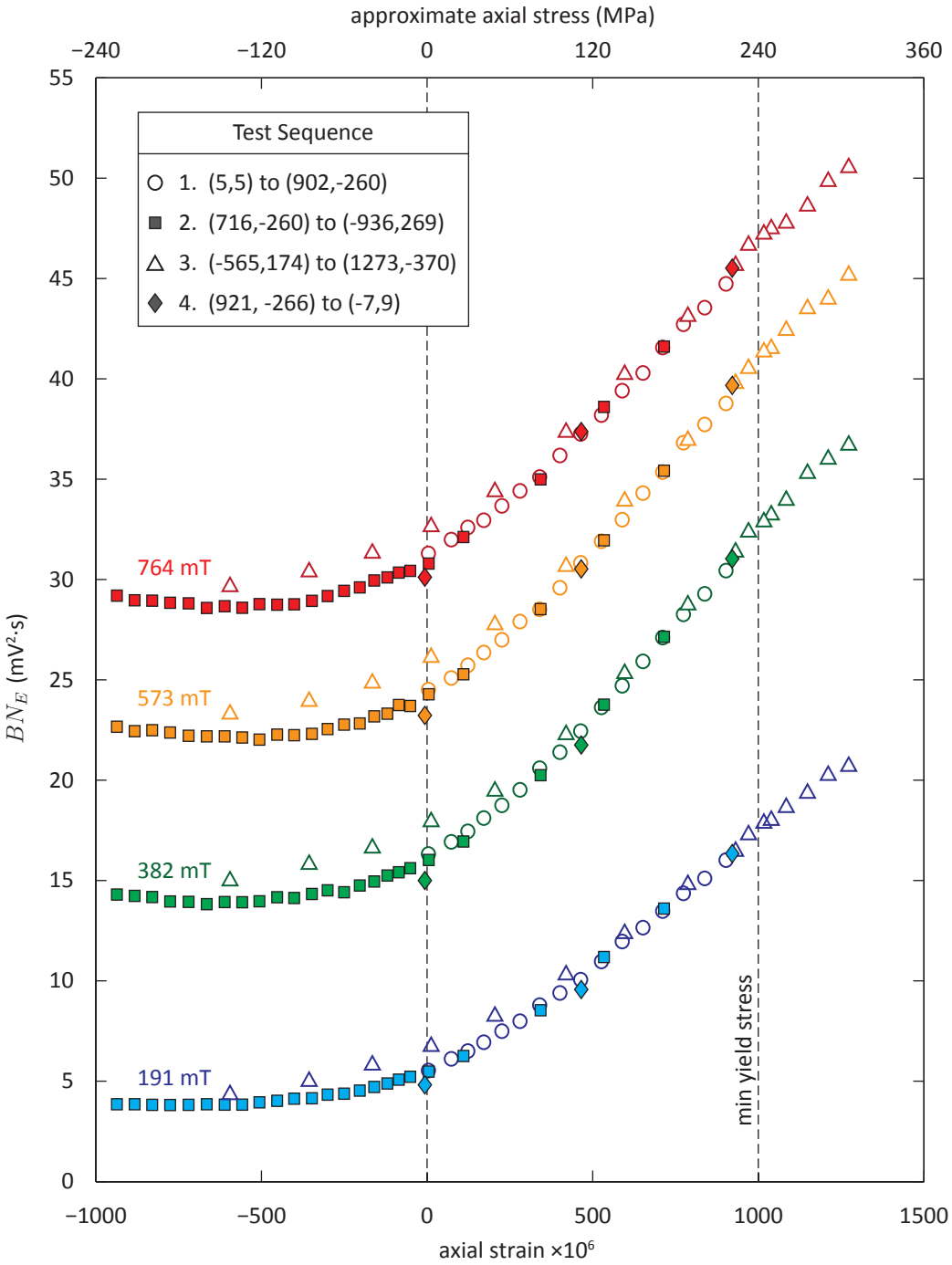

Figure 9.10: Axial BN energy strain response from the 3PBR, for $f_{ex} = 51\,\text{Hz}$, $\theta_T = 90°$ and the indicated B_{FT} values. The test sequence is indicated in the legend.

to pickup coil coupling uncertainties, as described in Section 8.6.2.

A $\pm 7\%$ BN_E uncertainty is not problematic for measuring tensile stresses. For $B_{FT} = 191\,\text{mT}$, Figure 9.10 shows a $\sim 250\%$ increase in the BN_E between $0\,\mu\varepsilon$ and the minimum yield strain of $\varepsilon_a = 1000\,\mu\varepsilon$. This gives a tensile measurement resolution of $\pm 30\,\mu\varepsilon$ within a 65% confidence interval. Converted to stress this gives a measurement resolution of $\sim 7\,\text{MPa}$, which is within the specified 25 MPa resolution in Section 1.6. Typically, the relative coupling error decreases as B_{FT} increases, with $\sim 2\%$ errors at $B_{FT} = 800\,\text{mT}$. Using a 2% error with the 764 mT data in Figure 9.10 gives an estimated resolution of 9 MPa.

The BN_E sensitivity to compression is more difficult to estimate than for tension, due to the hysteresis of BN_E from plastic deformation, and the relatively small correlation between BN_E with compressive strains. Though there is some evidence that the BN_E correlation with compressive strains is increased for $B_{FT} < 382\,\text{mT}$, when combined with coupling uncertainties the sensitivity of BN_E to compression may be considered negligible. This is supported in Figures 9.9b and 9.9c, where compressive strains are shown to have negligible effects on the BN_E in the hoop direction.

9.2.6 BN Envelope and Strain

The preceding analysis makes use of the BN_E parameter, which was shown in section 9.2.4 to have good sensitivity to tension, but poor sensitivity to compression. To see why this occurs in more detail, Figure 9.11 shows, for each of the B_{FT} values used in Figure 9.10, the $\boldsymbol{BN_{env}}$ data for three strain configurations:

- the initial reference configuration at $+5\,\mu\varepsilon$,
- the peak tensile configuration from the first test sequence at $+902\,\mu\varepsilon$,

- the lowest compressive configuration at $-936\,\mu\varepsilon$.

Figure 9.11a (with $B_{FT} = 191\,\text{mT}$) shows that the introduction of tensile strain produces an increase in $\boldsymbol{BN_{env}}$ at all $\phi_{B_{FT}}$ values, while a compressive strain produces a comparatively smaller decrease in $\boldsymbol{BN_{env}}$. However, as B_{FT} increases, Figures 9.11b, 9.11c and 9.11d show that change in $\boldsymbol{BN_{env}}$ with strain is local to the peaks in $\boldsymbol{BN_{env}}$. As B_{FT} increases, the peaks shift to lower $\phi_{B_{FT}}$ values, and the area changes associated with strain remain approximately constant. According to the BN depth model in Section 7.1, the peaks in $\boldsymbol{BN_{env}}$ correspond to times when $B_{ex} \approx 0$ at the sample surface. This suggests that the peak values of $\boldsymbol{BN_{env}}$ are most sensitive to changes in strain at the highest magnetisation rates near the coercive point.

The cause of the increasing BN_E with large compressive strains can be seen most clearly in Figures 9.11c and 9.11d, where $\boldsymbol{BN_{env}}$ for $\varepsilon_a = -937\,\mu\varepsilon$ rises above $\boldsymbol{BN_{env}}$ for $\varepsilon_a = +5\,\mu\varepsilon$ and $\varepsilon_a = +902\,\mu\varepsilon$ after the initial peak. This occurs at later $\phi_{B_{FT}}$ values when the sample surface is saturating, and implies that large compressive strains result in an increase in BN power at near-saturation flux densities

In order to achieve maximum sensitivity to tension and compression using an integrated parameter such as BN_E or BN_{rms}, the optimal B_{FT} will be one that ensures the area change in $\boldsymbol{BN_{env}}$ associated with strain is maximised. Using this criteria, Figure 9.11 indicates the maximum strain sensitivity is for $B_{FT} \approx 500\,\text{mT}$, which is supported by Figure 9.8b. While it may be possible to construct a parameter from $\boldsymbol{BN_{env}}$ with stronger compressive strain correlation than BN_E, ultimately, the BN sensitivity to compressive strain in SA-106 Grade B steel is significantly less than the BN sensitivity to tensile strain.

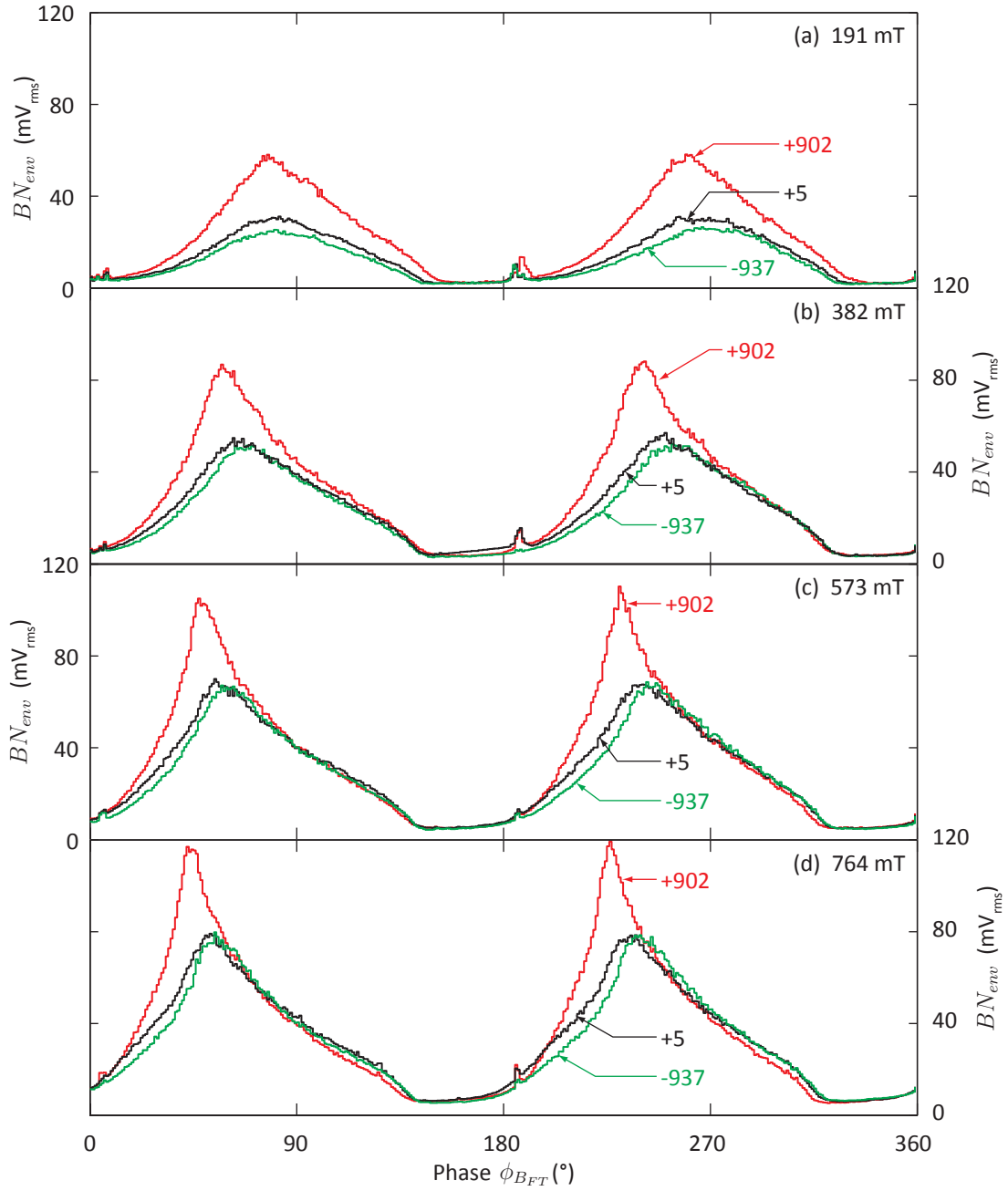

Figure 9.11: Strain effects on the BN envelope from the 3PBR, for $f_{ex} = 51\,\text{Hz}$, $\theta_T = 90°$ and the indicated B_{FT} and axial strain values.

9.2.7 Macroscopic Coupling and Strain

While the BN sensitivity to compression is small (as discussed above), compressive strain does have an effect on the macroscopic field coupling to the sample. From the FCS and SL4P data, macroscopic field coupling can be estimated using either the excitation coil inductances ($L_{ex(p)}$), which is a measurement of the magnetic impedance of the excitation circuit, or pickup coil macroscopic field component ($|V_{f_{ex}}|$) which is analogous to a radial AC flux leakage measurement¶. In this section $|V_{f_{ex}}|$ is used, since it was found to have a stronger variation with strain ($\sim 30\%$) than $L_{ex(p)}$ ($\sim 4\%$). Figure 9.12 shows $|V_{f_{ex}}|$ for the measurements in Figure 9.10.

For a given B_{FT}, $|V_{f_{ex}}|$ may change with the pickup coil coupling, the SL4P pole lift-off, and the sample magnetic impedance. The change in the pipe curvature due to strains in the 3PBR is expected to produce variations in the pickup coil coupling and pole lift-off. However, these geometrical effects are only expected to change the coupling by a factor comparable to the strain, which is between -0.1% and 0.15% in the axial direction, and $+0.03\%$ to -0.5% in the hoop direction. Therefore, the 30% variation in $|V_{f_{ex}}|$ in Figure 9.12 is primarily attributed to changes in the sample magnetic impedance.

Figure 9.12 shows that $|V_{f_{ex}}|$ increases with compressive axial strain, and for increasing tensile strain above $\sim 400\,\mu\varepsilon$. For $\varepsilon_a < 0\,\mu\varepsilon$, the compressive axial strain causes the permeability in the axial direction to decrease, preventing flux from coupling into the sample. Since the flux through the feedback coils is conserved, a reduced sample permeability results in increased flux above the sample surface, which increases $|V_{f_{ex}}|$. For $0 < \varepsilon_a < 400\,\mu\varepsilon$ the sample axial permeability increases with

¶Ideally, this would be accomplished with axial and hoop flux leakage measurements.

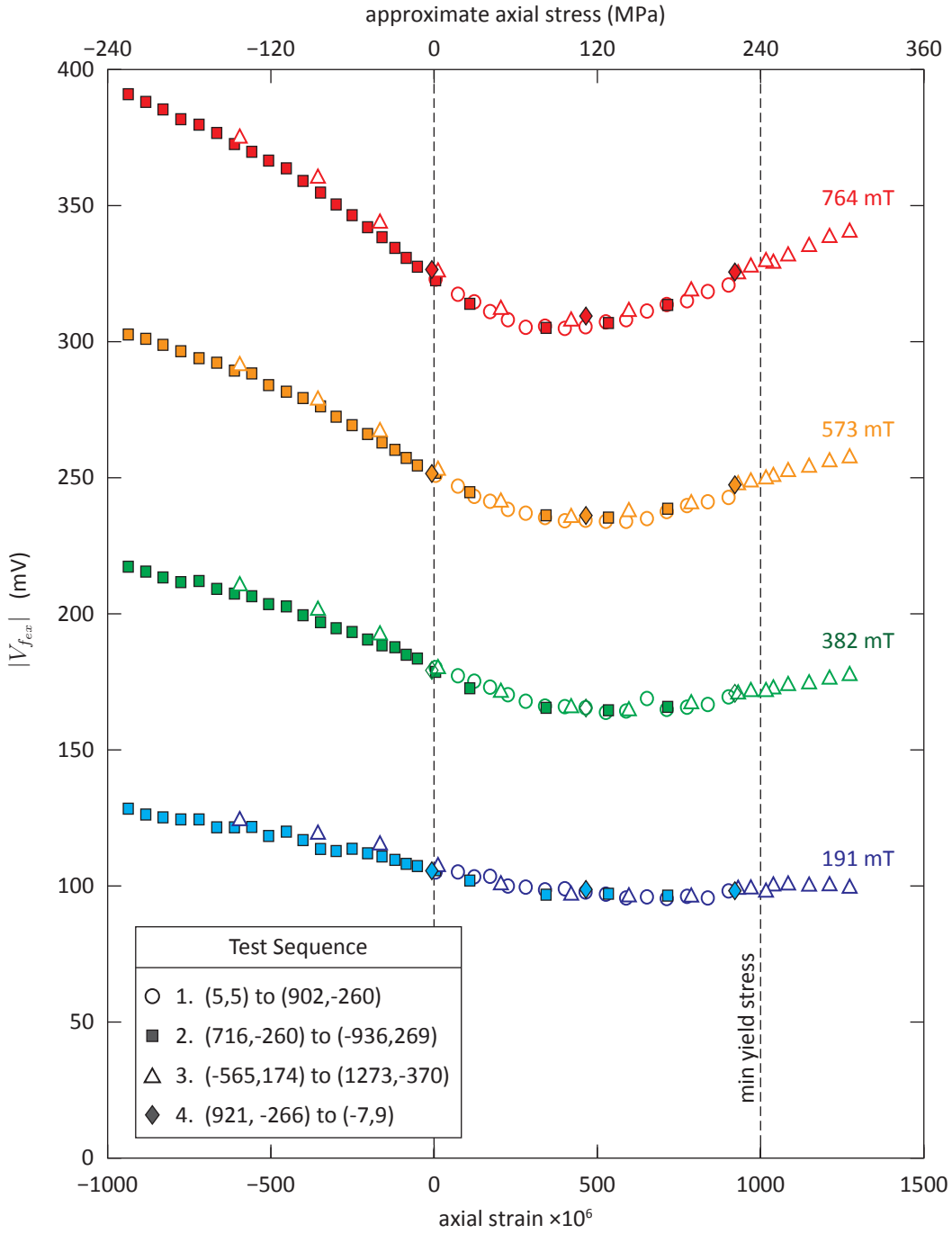

Figure 9.12: Axial macroscopic field component ($|V_{f_{ex}}|$) strain response from the 3PBR, for $f_{ex} = 51\,\text{Hz}$, $\theta_T = 90°$ and the indicated B_{FT} values. The test sequence is indicated in the legend.

tension, causing more flux to couple into the sample and decreasing $|V_{f_{ex}}|$.

For $\varepsilon > 400\,\mu\varepsilon$ Figure 9.12 shows that $|V_{f_{ex}}|$ increases, which is counter to the preceding argument. This is explained by considering that Poisson's effect results in a magnetic hard axis in the hoop direction with large uniaxial ε_a. As shown in the tetrapole finite element models (e.g., Figure 5.11a), the flux is not confined in the hoop direction when it enters the sample under axial magnetisation conditions, and therefore tends to diverge. If the hoop permeability is decreased, the flux is confined to the axial direction, which drives the axial magnetisation to saturation more rapidly, and causes increased flux leakage [69].

Figure 9.12 indicates that macroscopic field coupling measurements are strongly sensitive to compression, while Figure 9.10 indicates BN is strongly sensitive to tension. It follows that a combination of the two magnetic measurements would provide a larger range of strain measurement capability than either measurement individually. This is the case in BN measurements where the excitation current or voltage is controlled as opposed to the feedback coil flux, where an increase in the sample impedance with compressive strain decreases the flux in the sample, and hence decreases the BN produced [50].

On feeder pipes however, flux control is required in order to compensate for the large variation in macroscopic field coupling associated with the varying feeder pipe curvature. As a result, measurements of $L_{ex(p)}$ or $|V_{f_{ex}}|$ from scanning measurements on feeders are dominated by curvature effects and coupling variations, and are not useful for estimating compressive residual strain. If a macroscopic field coupling measurement were devised that effectively compensated for variations in curvature, the magnetic sensitivity to compression demonstrated in Figure 9.12 could be exploited

for feeder pipe measurements.

9.2.8 3PBR Summary

In summary, data from the 3PBR indicate that BN is sensitive to strain for SA-106 Grade B steel. BN sensitivity to strain was shown to be dependent on the excitation field amplitude, with the majority of the BN strain sensitivity occurring for $B_{FT} < 300\,\text{mT}$, and peak sensitivity to tension at $B_{FT} \approx 500\,\text{mT}$ with $f_{ex} = 51\,\text{Hz}$. While an exhaustive calibration has not been performed for all excitation frequencies, BN_E residual measurements at $f_{ex} = 51\,\text{Hz}$ have been estimated to have tensile stress resolution between 7 MPa and 9 MPa for B_{FT} values between 191 mT and 764 mT, respectively, and negligible sensitivity to compression. However, more sophisticated analysis of $\boldsymbol{BN_{env}}$ or $\boldsymbol{\mathcal{D}_{BN}}$ may yield better sensitivity to compression than the integrated BN_E parameter.

Data from the 3PBR also showed strong correlations between compressive strain and macroscopic field coupling parameters such as $|V_{f_{ex}}|$. For the SL4P sensor design on feeder pipes, these macroscopic field coupling parameters are dominated by variations in feeder curvature, and are not useful for residual stress estimation.

9.3 Sample T01-5 Studies

Sample T01-5, pictured in Figure 9.13, is one of several bent feeder pipe samples provided by AECL for BN testing. It is $\sim 60\,\text{cm}$ long, with a 73° bend. The axial position at the mid-point of the extrados was denoted $(0\,\text{cm}, 0°)$ in (axial, hoop) coordinates. T01-5 was provided with a laser-etched grid around the bend from an

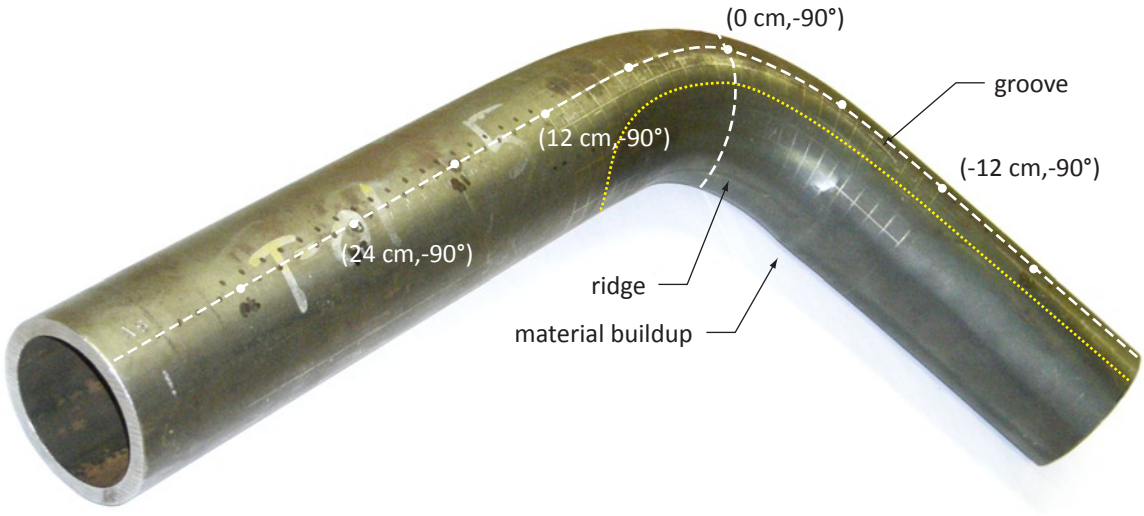

Figure 9.13: Sample T01-5. (axial, hoop) coordinates are indicated in white. The heat treated region is enclosed by the yellow dotted curve.

axial position of $-12\,\text{cm}$ to $12\,\text{cm}$, with $\sim 1\,\text{cm}$ axial spacing and 15° hoop spacing. The grid was marked prior to bending the pipe, which introduced significant plastic deformation and ovality. Thus there is significant variation in the grid spacing from point-to-point, and coordinates refer to those on the un-bent pipe.

Additional features of T01-5 include a ridge along the intrados at the middle of the bend, presumably from the bending die, and a groove centered at $(-6\,\text{cm}, -105°)$. There is some buildup of material on the intrados at an axial position of $-8\,\text{cm}$. Discolouration from heat treatment is visible on the intrados from $+11.5\,\text{cm}$ to $-24\,\text{cm}$ (the pipe extent), and from 90° to 270° around hoop axis. The outer surface finish on the heat-treated intrados region is black and smooth, while the extrados and straight sections of pipe feature are oxidized. There is an increased amount of rust on the cheeks.

There was some concern on inspection of T01-5 about the laser etched grid around the bend affecting BN measurements. Before BN measurements were performed on

the rest of the pipe, BN measurements were performed in a small region on and off the grid. This data, which is presented in Section 9.3.1, confirms that the grid has a significant effect on the BN response. Despite the effect of the grid, several axial and hoop BN scans were performed on T01-5, and are presented in section 9.3.2. BN scans were performed with $f_{ex} = 51\,\text{Hz}$ and $B_{FT} = 477\,\text{mT}$, as this was shown in Figure 9.8b to have the peak sensitivity to tensile strain.

9.3.1 T01-5 Grid

Effects of the T01-5 grid on the BN response were tested with a series of BN measurements on and off the grid around the (axial, hoop) position of $(12\,\text{cm}, 90°)$ with $f_{ex} = 51\,\text{Hz}$, $B_{FT} = 477\,\text{mT}$, for θ_T values of 0° (along the hoop axis) and 90° (along the axial direction). Figure 9.14 shows the axial and hoop $\boldsymbol{BN_{env}}$ data recorded for the series of points.

Figure 9.14 shows that data off the grid, which includes plots at $(11.5\,\text{cm}, 82.5°)$ and $(10.5\,\text{cm}, 82.5°)$, share a similar $\boldsymbol{BN_{env}}$ structure to those shown in earlier $\boldsymbol{BN_{env}}$ plots, such as Figures 9.2b and Figure 9.11, with each BN burst having a single sharp peak. The other four points in Figure 9.14 are on the grid, and show a broadening and flattening of the $\boldsymbol{BN_{env}}$ peaks, resulting in increased BN at later $\phi_{B_{FT}}$ values. Plots at $(12\,\text{cm}, 82.5°)$ and $(11\,\text{cm}, 82.5°)$ also show increased difference between axial and hoop $\boldsymbol{BN_{env}}$ functions, indicating increased anisotropy.

These changes in the $\boldsymbol{BN_{env}}$ on and off the grid bear little resemblance to the effects of elastic stress shown in Figure 9.11. It is hypothesized that the $\boldsymbol{BN_{env}}$ changes are due to a combination of pickup coil coupling variation due to changes in surface geometry, with a change in the local magnetic properties introduced by

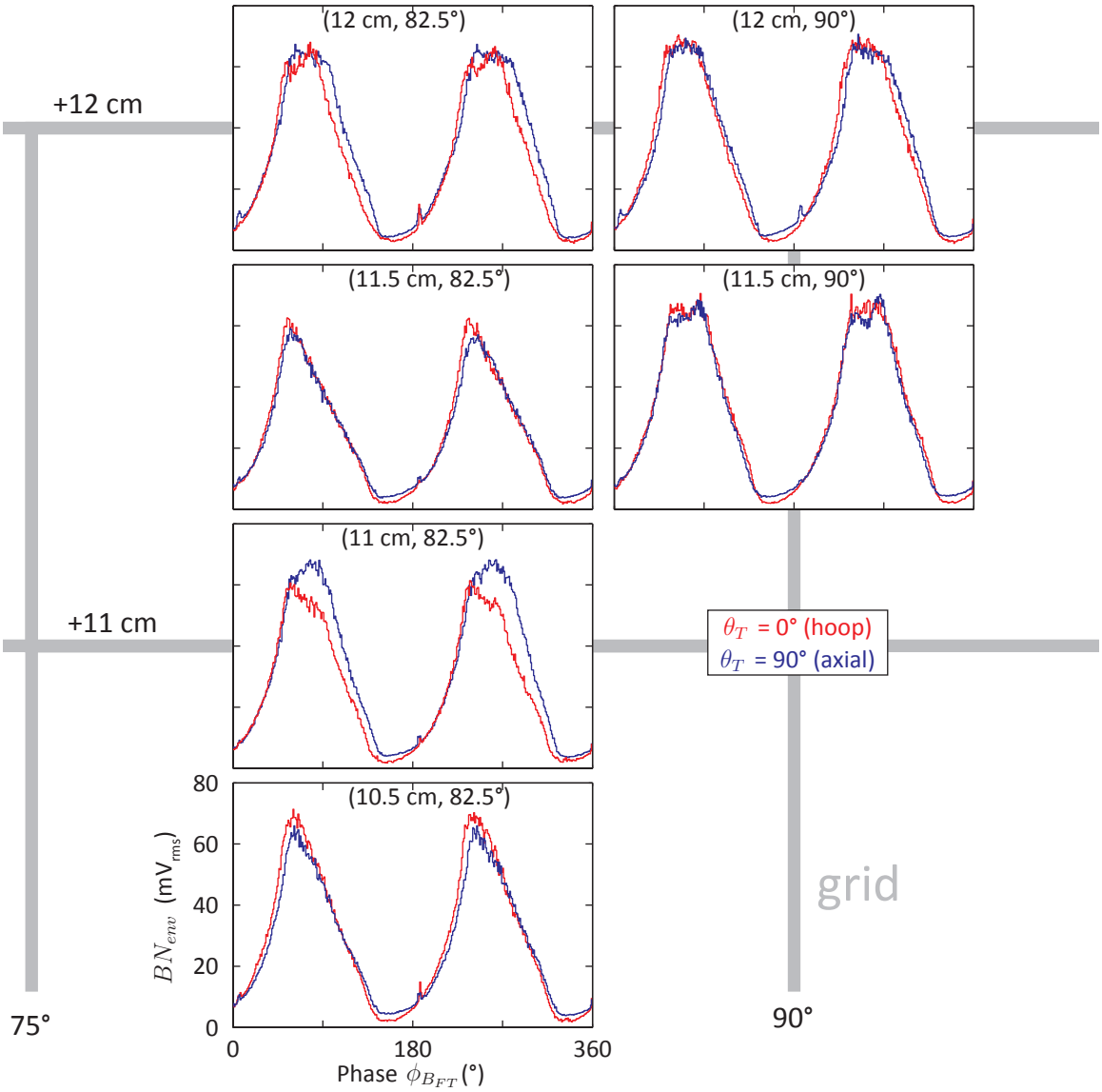

Figure 9.14: T01-5 laser etched grid effects on the BN envelope for $f_{ex} = 51\,\text{Hz}$, $B_{FT} = 477\,\text{mT}$, and θ_T values of 0° and 90°. Plots are labeled by their grid coordinates, and plot axes are all equal. Grid lines are indicated in gray (not to scale).

the laser etching process. It is therefore concluded that the laser etching process compromises BN studies.

9.3.2 T01-5 Axial and Hoop Scans

This section presents axial and hoop scan BN data from sample T01-5. It follows from the analysis of the $\boldsymbol{BN_{env}}$ data on and off the grid in Section 9.3.1 that the BN_E calibration curves in Figure 9.10 cannot be used to correlate on-grid BN_E results from T01-5 to residual stress. To compensate for this, scans were performed with the SL4P centered between grid lines. Measurements were performed with $f_{ex} = 51\,\text{Hz}$, $B_{FT} = 477\,\text{mT}$, and θ_T values of 0° and 90° to measure hoop and axial BN_E, respectively.

To identify regions of interest, axial scans were performed along the extrados and the left cheek, with hoop positions of −7.5° and −82.5°, respectively. The resulting data is shown in Figure 9.15.

The extrados scan in Figure 9.15a shows the axial and hoop BN_E to be approximately equal for axial positions $> 12\,\text{cm}$. This indicates low levels of plastic deformation in the straight sections of the pipe away from the bend. From $-17.5\,\text{cm}$ to $12\,\text{cm}$, Figure 9.15a shows elevated BN_E in both axial and hoop directions, with larger axial BN_E. A steep transition is evident between positions of $11.5\,\text{cm}$ and $12.5\,\text{cm}$, suggesting the grid may be partially responsible for the elevated BN_E. However, in the negative axial direction, BN_E levels return to their reference levels for axial positions $< -19.5\,\text{cm}$, which is $7.5\,\text{cm}$ from the last grid line. It is therefore likely that plastic deformation contributes to the BN_E changes. It follows that the elevated axial and hoop BN_E in Figure 9.15a from $-17.5\,\text{cm}$ to $11.5\,\text{cm}$ may indicate the presence of tensile axial and tensile hoop stresses at the extrados surface (i.e.,

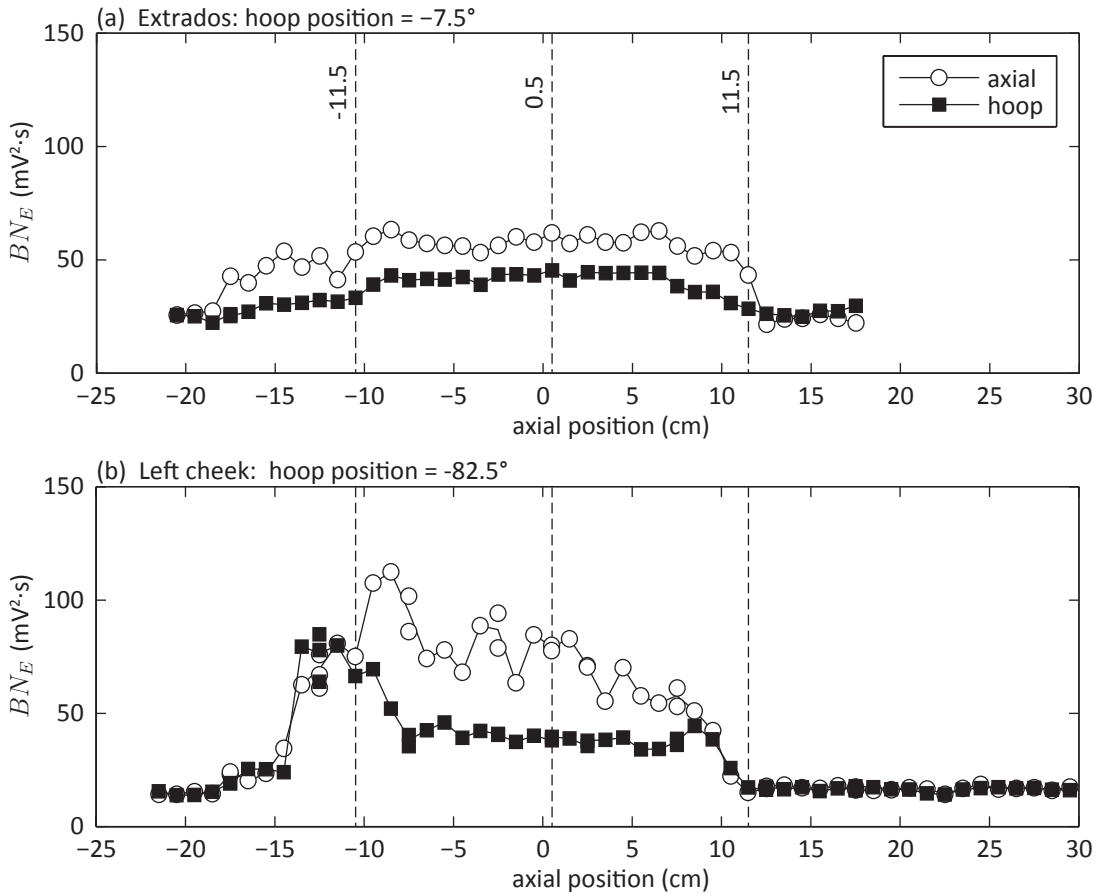

Figure 9.15: T01-5 axial BN scans along (a) the extrados, and (b) the left cheek, with $f_{ex} = 51\,\text{Hz}$, $B_{FT} = 477\,\text{mT}$, and θ_T values of 0° (hoop) and 90° (axial). Lines are to guide the eye, and the dashed lines indicate hoop scan positions.

biaxial tension on the extrados). A neutron diffraction study of 'warm bent' feeder pipes indicated a similar trend, with elevated axial and hoop stresses at the extrados surface [19].

Like Figure 9.15a, the left cheek scan in Figure 9.15b shows equal axial and hoop BN_E for axial positions $> 12\,\text{cm}$. Both axial and hoop BN_E levels are elevated around the bend, however there is a significant increase in the scatter and amplitude of the axial BN_E in Figure 9.15b compared to Figure 9.15a. The increased scatter

of the axial BN_E is likely due to either pickup coil coupling errors associated with the increased rust on the cheeks, or to stress gradients along the cheeks associated with non-uniform plastic deformation. Figure 9.15b also shows large increases in the axial BN_E between $-10\,\text{cm}$ and $-6.5\,\text{cm}$, and the hoop BN_E between $-14.5\,\text{cm}$ and $-9.5\,\text{cm}$. This region corresponds to the start of the bend, and is also near the groove centered at $(-6\,\text{cm}, -105°)$.

To further investigate T01-5, hoop scans were performed with 15° spacing at axial positions of 11.5 cm (in the straight region of the pipe), 0.5 cm (the bend center), and $-11.5\,\text{cm}$ (the start of the bend, with high signal levels in Figure 9.15). The resulting BN_E plots are shown in Figure 9.16.

The scan at 11.5 cm, shown in Figure 9.16a, shows relatively small variation in the BN_E around the circumference of the pipe, with small increase in axial BN_E near the extrados. This is consistent with the axial scans in Figure 9.15, which show the axial and hoop BN_E at 11.5 cm diverging at the extrados, but consistent on the left cheek.

Figure 9.16b shows that at an axial position of 0.5 cm, in the middle of the bend, there is increased axial BN_E relative to the hoop BN_E between $-82.5°$ and 82.5°. The largest anisotropy occurs at hoop positions of approximately ±75°. Figure 9.16b is also consistent with Figure 9.15, which shows elevated anisotropy at the left cheek compared to the bend center.

Figure 9.16c shows significantly more anisotropy than the other two hoop scans, and a large increase in hoop BN_E between 97.5° and 142.5°, accompanied by a drop in the axial BN_E. This suggests the presence of a tensile hoop stress. Diametrically opposite, at positions between $-97.5°$ and $-37.5°$, there are increases in both axial

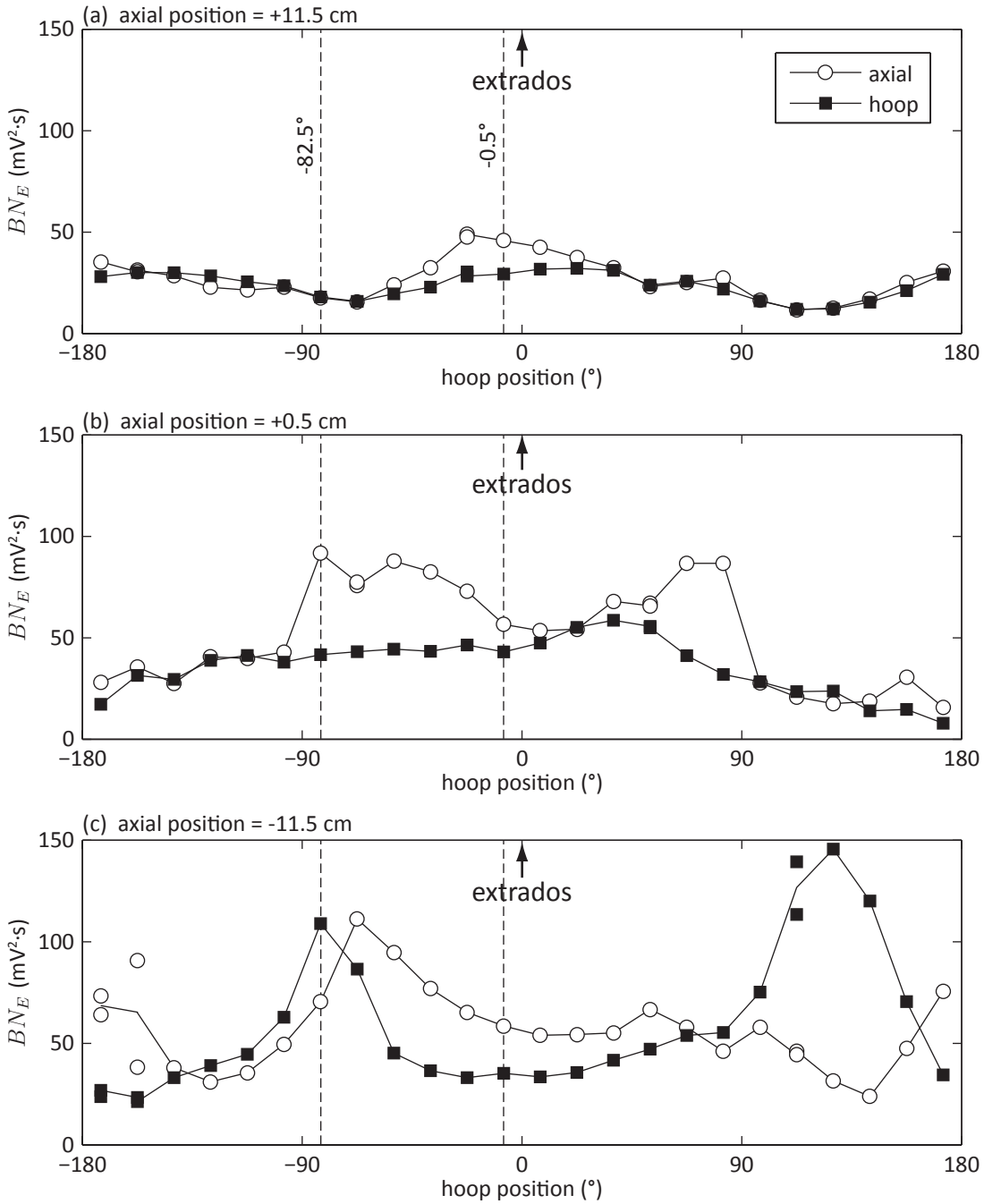

Figure 9.16: T01-5 hoop BN scans at axial positions of (a) 11.5 cm, (b) 0.5 cm, and (c) −11.5 cm, with $f_{ex} = 51$ Hz, $B_{FT} = 477$ mT, and θ_T values of 0° (hoop) and 90° (axial). Lines are to guide the eye, and the dashed lines indicate axial scan positions.

and hoop BN_E, as was shown in Figure 9.15b.

In summary, if BN_E is taken to be directly correlated with tensile residual stresses in T01-5, then the axial and hoop scans presented in Figures 9.15 and 9.16, respectively, show maximum tensile stresses near the start of the bend at axial positions of $\sim -12\,\text{cm}$. This suggests that the accumulation of material at the start of the bend was due to a compressive forces during the bending process, which lead to tensile residual stress. While surface stresses may be highest in this region, the material accumulation has likely increased pipe strength and prevented cracking. The BN data also indicates surface stress gradients are largest in the bend cheeks, which is historically where intrados feeder cracking has been found. Stresses on the extrados are tensile and elevated throughout the bend, and taper off in the straight sections of the pipe. BN_E values from the intrados were generally smaller than from the extrados, suggesting either compressive or negligible stress concentrations.

Chapter 10

Summary & Conclusions

The objective of this thesis was to develop a magnetic Barkhausen noise system to measure residual stresses in CANDU® feeder pipe bends. To compensate for the variable curvature and limited clearances of the feeder pipe geometries, significant modifications to conventional BN testing systems were required. While the models, systems, and experimental approach developed for this thesis were tailored to the feeder pipe geometry, they have significant implications for BN NDE not only for feeders, where BN measurements are now possible, but for all testing geometries.

10.1 Flux Control

The most generally applicable of these developments is the flux source concept and the associated flux control system (FCS). Using the approximation that the electromagnet circuit is a series of unknown reluctive loads, it was shown in Chapter 3 that flux conservation ensures that the sample magnetisation is repeatable when the magnetic flux in the circuit is reproduced. The use of a flux source allows BN measurements

to be performed with confidence that the measurement sensitivity to changes in the surface geometry is significantly reduced. Changes in the BN response can then be attributed to changes in sample properties or BN sensor coupling. While both active and passive approaches to flux source design are possible, it was shown that only an active flux source is feasible for the feeder geometry.

Active flux source designs were investigated, and an approach that combines high gain analog feedback from encircling coils with digital feedback was selected. Encircling coils were chosen as the flux feedback sensor, since the voltage across an encircling coil is proportional to both the flux rate and the excitation voltage by way of transformer coupling, and voltage amplifiers were found to be significantly easier to design than current amplifiers for large inductive loads. To stabilize the DC response of the circuit, direct feedback of the excitation voltage was used, which introduced an error in the feedback coil flux. An iterative digital feedback system was then implemented in *LabVIEW 8.2* to reduce the error. This combination of analog and digital feedback was shown to provide rapid convergence compared to purely digital feedback algorithms, and enhanced stability and precision over purely analog solutions.

With electromagnet coupling compensation achieved via the flux control, flux conservation in the sample was extended to flux superposition. A tetrapole electromagnet was proposed as a means of achieving field orientation rotation in the sample with no moving parts, thereby reducing the mechanical systems required within the feeder clearances to achieve BN anisotropy measurement. Magnetic circuit analysis of the tetrapole revealed coupling between adjacent poles, requiring a minimum of three flux sources to determine the sample flux density. For reasons of symmetry and enhanced control opportunities, a four flux source solution was selected, and it was this design

choice that led to the four channel FCS implementation.

While the FCS was designed for BN testing and the SL4P, it can provide flux control to any (four) appropriately designed excitation and feedback coil pair(s). Since the location of the feedback coil in the magnetic circuit is arbitrary, the FCS can be used to drive the flux within the sample for fundamental BN studies, as in Figure 3.3a. The system also outputs both the excitation and feedback coil waveforms, thus it can also be used for permeability and inductance measurements on a variety of magnetic circuits. For example, the FCS was used to measure the permeability of SA-106 Grade B steel in Appendix B.

Applications of flux control outside of materials testing are also possible. In any system that makes use of applied magnetic fields, flux control can be used to locally correct for nonlinearities due to eddy currents and ferromagnets.

10.2 Tetrapole Development

To better visualize the magnetic fields produced by the tetrapole magnet geometry, two tetrapole configurations with flux feedback were modelled in 3D using the finite element method in *Infolytica MagNet*. These models identified saturation limitations with ferrite cores, which could be avoided by using high saturation flux core materials, such as Supermendur. The models also showed that the introduction of a non-magnetic gap between the poles and the sample would improve field uniformity in the sample by preventing flux concentration at the sample-pole interface, and indicated that the field superposition was maximally uniform within a 2.5 mm radius from the center of the sample surface for the orthogonal U-core geometry.

Finite element models were then used to design a pickup coil assembly with a 90%

sensing radius $< 2.5\,\text{mm}$ at $30\,\text{kHz}$. This was achieved by the introduction of a ferrite core to lower the magnetic impedance at the center of the coil, a ferrite sheath to complete the pickup coil magnetic circuit at the target radius, and a brass shield to attenuate fields from outside the coil assembly (the CSS configuration). The models were also used to confirm the skin depth equations for the pickup coil sensitivity, and calculate the complex inductance of the pickup coil assembly.

Based upon the finite element model results, the SL4P was implemented with orthogonal Supermendur U-cores and a pickup coil in the CSS configuration. To ensure consistent pickup coil and electromagnet coupling, the pickup shield and short core were spring-loaded, with sufficient travel to accommodate feeder curvature as well as flat plates. The SL4P is therefore a suitable probe for any sample geometry with sufficient access, and equal or lesser curvature than feeders.

The combined performance of the flux source circuit and the SL4P was then tested. The circuit voltage dividers and shunt resistors were matched between the four channels to within 0.3% and 0.6% respectively, and the SL4P feedback coils were matched to within 0.3% with a 2% systematic uncertainty. The electromagnet control system performance was then characterised in terms of convergence and RMS error for the excitation frequency range of interest. It was shown that for feedback coil flux densities $> 400\,\text{mT}$ and excitation frequencies $\geq 50\,\text{Hz}$, the digital error correction (DEC) flux mode has equivalent error performance to the circuit in voltage following (VF) mode.

10.3 BN Depth Penetration

Since X-ray diffraction was already abandoned for feeder pipe analysis due to its penetration depth of $< 10\,\mu m$, a meaningful estimate of the BN penetration depth in feeders was required. A model was developed using the approximation that frequencies in the BN band (f_{bn}) are much greater than the excitation frequency (f_{ex}). Under this approximation, the excitation field (B_{ex}) as a function of depth (z) and the excitation field phase at the sample surface (ϕ_0) was treated as static with respect to the BN fields. Using the skin depth equations, and approximating the BN emission strength as the product of the dynamic permeability, $\mu_d\{z, \phi_0\}$, with the flux rate, $|\mathrm{d}B_{ex}/\mathrm{d}t|\{z, \phi_0\}$, it was shown that the excitation field modulates the mean detected BN depth.

The BN depth model showed that peak BN emissions are detected from within the first $4\,\mu m$ to $50\,\mu m$ for f_{bn} values of $300\,kHz$ and $3\,kHz$, respectively. Peak BN emissions were shown to occur when the surface flux density is $\sim 0\,T$, at ϕ_0 values of 90° and 270°. As the surface of the sample saturates, it becomes increasingly transparent to BN from deeper in the sample, with mean penetration depths from $100\,\mu m$ to $500\,\mu m$ possible under surface saturation conditions. The BN emission depth is therefore a function of ϕ_0 and the surface excitation field amplitude (B_0).

The OUC-P finite element model showed that as f_{ex} increases, B_0 increases relative to the peak flux density sensed by the feedback coils (B_{Fpk}) (see Figures 5.4 and 5.5). Since the BN depth penetration increases with B_0 but is significantly smaller than δ_{ex}, the combination of the OUC-P result with the BN depth model indicates that BN depth sensitivity increases with f_{ex} for the same B_{FT}. This is particularly convenient, since measurements at higher f_{ex} require less measurement time and generate higher

amplitude BN emissions due to the increased flux rate. The tetrapole models also showed that ϕ_0 tends to lead the phase of the flux in the feedback coils ($\phi_{B_{F(p)}}$), due to flux conservation of the directly coupled excitation field. BN envelope data from feeders indicated that this phase lead varied as a function of the excitation field amplitude. The phase lead variation may be reproducible in time-harmonic finite element models, though such model solutions were not investigated.

The combination of the BN depth model with tetrapole finite element models was shown to demonstrate the large-scale features of the BN envelope. This combination predicts the BN excitation field response from feeders, without the need for sophisticated domain models. The success of this approach implies that much of the structure of the BN response is due to macroscopic magnetic behaviour. With appropriate control of the excitation field and selective frequency analysis of the BN, improved depth estimates from thick samples may be possible in the future. Note that the BN depth model applies to any sample significantly thicker than δ_{ex}, as it does not model reflections of the excitation field.

10.4 Pickup Coil Transfer Function

In order to ensure that the pickup coil measurement sufficiently characterises the broad-band nature of BN, an electric circuit model from the pickup coil to the preamplifier input was constructed. The transfer function for voltages induced within the pickup coil was calculated using the complex pickup coil inductance estimated with the pickup coil finite element model. The transfer function identified a resonance between the pickup coil and cabling, and provided restrictions on the preamplifier input impedance (Z_{in}) to values $> 500\,\Omega$. Since the *Ithaco 1201* preamplifier used

had $Z_{in} \gg 500\,\Omega$, the model was used to estimate the appropriate value for the terminating resistor R_t.

BN data from feeder pipes confirmed the resonance condition predicted by the transfer function model. It was shown that variation of R_t and a terminating capacitor C_t could significantly distort the measured BN power spectrum. The BN data also showed that variations in the transfer function had a scaling effect on the BN envelope. This indicated that absolute BN power spectrum analysis was not possible without transfer function calibration, although BN measurements could be compared, provided the transfer function was consistent between measurements. Pickup coil coupling to the sample also affects the transfer function, and was shown to be the dominant contributor to the BN measurement uncertainty. A recent paper has demonstrated a method for transfer function calibration that may reduce pickup coil coupling uncertainties [65].

10.5 BN Analysis

In order to relate BN to the excitation field, a set of BN measurement and analysis procedures was developed. Using a combination of time, frequency and power analysis, the BN dynamic power spectrum ($\boldsymbol{\mathcal{D}_{BN}}$) was isolated from the background noise power and a variety of other phenomena that contribute to the pickup coil voltage. $\boldsymbol{\mathcal{D}_{BN}}$ was then summed over frequency and time space to produce the BN envelope ($\boldsymbol{BN_{env}}$) and normalized BN power spectrum ($\boldsymbol{NPS_{BN}}$), respectively. The total BN power was also estimated as the BN energy (BN_E), and was related to the RMS BN amplitude (BN_{rms}). These various parameters, particularly $\boldsymbol{BN_{env}}$ and BN_E, allow rapid characterisation of the BN excitation field response.

10.6 BN, Stress, and Feeders

Correlations between elastic strain and BN were investigated using the three point bending rig (3PBR). Results showed that tensile strains produced a significant increase in BN_E, while compressive strains resulted in a small, if not negligible, decrease in BN_E. Assuming reasonable pickup coupling uncertainties, BN_E could be calibrated to measure tensile stress with resolution of $\pm 7\,\mathrm{MPa}$ to $\pm 9\,\mathrm{MPa}$, depending on the excitation field configuration. Anisotropy measurements using field superposition were shown to indicate Poisson's effect, demonstrating the capability for measuring multiple components of strain. Hysteresis of the BN_E with respect to the surface strain, after yield-strength tensile and compressive stresses were applied to the 3PBR, indicated correlations between BN and residual stresses that could not be resolved with the surface-mounted strain gauges.

Analysis of $\boldsymbol{BN_{env}}$ variations with strain showed that BN_E correlations with strain were primarily associated with the peaks in $\boldsymbol{BN_{env}}$. As B_{FT} was increased, the $\boldsymbol{BN_{env}}$ peaks shifted to lower $\phi_{B_{FT}}$ values, and the envelopes at different strains were shown to increasingly overlap, leading to an offset in the BN_E, but no additional strain-correlated variation. At $f_{ex} = 51\,\mathrm{Hz}$, peak BN sensitivity to tensile strain was measured at $B_{FT} \approx 500\,\mathrm{mT}$.

Using the 3PBR, the macroscopic field coupling parameter $|V_{f_{ex}}|$ was shown to have strong correlation with compressive strain. However, due to the large variation in macroscopic field coupling with feeder pipe curvature, this response was not useful for estimating residual stresses in feeders with the present sensor design.

The SL4P was then used to measure the axial and hoop BN_E response from the T01-5 feeder bend sample. The sample featured a laser-etched grid around the bend,

which was shown to modify $\boldsymbol{BN_{env}}$ compared to BN measurements from the SFB and the 3PBR. Measurements were therefore performed with the SL4P pickup coil centered between grid lines. Axial scans along the extrados and left cheek of T01-5 were performed, as well as three hoop scans at the start, middle and end of the bend. Scans showed increased BN_E around the bend, with larger BN_E variation and anisotropy along the cheeks, and peak BN_E at the start of the bend.

10.7 Conclusions

BN testing has yet to achieve the widespread use of other NDE technologies such as ultrasonic or eddy current testing. In part, this is because BN testing only applies to ferromagnetic materials, limiting the range of applications and the opportunities for development. However, BN testing has also been plagued by an abundance of sensitivity to various phenomena, with a lack of specificity. This has led to BN being generally perceived as an unreliable measurement technique, and has limited its use primarily to laboratory settings.

Feeders, with their variable curvature, thick walls, and limited clearances, could be considered a challenging geometry for BN testing, requiring lift-off compensation, high flux densities, and a compact probe. Using the FCS and SL4P, BN measurements on feeders can now be performed with confidence that the observed changes in the BN response are due to changes in the sample magnetic properties, as opposed to changes in the feeder pipe curvature. Correlations between strain and the BN response from feeder pipe geometries were demonstrated on the 3PBR, and measurements on T01-5 showed that significant changes in the BN response occur around feeder pipe bends. Additional progress was made to specify the pickup coil sensing area, transfer

function, and model the BN depth sensitivity and excitation field dependence.

In designing a BN testing system capable of feeder pipe measurement many of the issues affecting BN measurement repeatability have been addressed. The modelling, engineering, and procedures developed for this BN testing system provide an improved basis for the future advancement of BN testing, both of feeders and other geometries, and ferromagnetic testing in general.

Chapter 11

Future Work

The FCS and SL4P enable BN testing over an unprecedented parameter space that exceeds the scope of this thesis. In its present configuration, the SL4P can be used to probe a wide variety of material geometries, and the FCS can be adapted for many more. This raises a number of topics for future investigation:

- Section 11.1 presents additional considerations for BN NDE on feeder pipes that are not addressed by the design and/or the measurements described in this thesis.
- Section 11.2 presents topics for future BN NDE research.
- Section 11.3 presents engineering suggestions for a next generation BN system.

11.1 Feeder Pipe NDE

The data presented in this thesis were used to demonstrate correlations between BN and strain in SA-106 Grade B piping, and to outline the types of qualification

procedures required for BN testing to be a repeatable measurement. However, the data collected are by no means an exhaustive calibration. There are several additional investigations required in order to calibrate and use BN as an *in situ* measurement.

11.1.1 Residual Stress Standards

While data from the 3PBR demonstrated stress/strain calibration for BN is possible using elastic rigs, the BN_E calibration curves and $\boldsymbol{BN_{env}}$ response are specifically correlated with the approximately uniaxial three-point bending configuration. However, three-point bending differs from the various bending processes used for feeders, which are known to produce biaxial stresses [18, 19].

To calibrate BN for residual stress measurements, it is recommended that a series of bent feeder pipes be produced with known residual stress distributions. These stress distributions should be evaluated using neutron diffraction, as this is the only standardized [70] residual stress measurement technique able to replicate (and exceed) the depth penetration and resolution of BN technique.

11.1.2 Depth Estimation

The BN depth model showed that the phase of the BN response is correlated with the mean detected BN depth. An experimental procedure should therefore be developed to confirm that the depth penetration of the BN response follows the BN depth model. Since the BN from the sample surface is the least attenuated, near-surface results dominate integrated BN parameters like BN_E. If near-surface BN results are insufficient for effective NDE on feeders, BN analysis with respect to the excitation waveform phase may be required to resolve stress variation at the depths of interest.

11.1.3 Temperature Effects

Magnetic properties change significantly with temperature, and thus the BN response from feeders may be temperature dependent. Under shut-down conditions feeder pipe temperatures may range from 35 °C to 42 °C [21]. Since inspections may occur over a period of several days, it is likely that the temperature would vary between BN measurements. The effect of temperature on the BN response should therefore be evaluated to indicate whether temperature calibration is required. All the measurements in this thesis were performed at $\sim 20\,^{\circ}\mathrm{C}$.

11.1.4 Texture Effects

Magnetic properties are also affected by crystallographic texture, specifically along the $\langle 100 \rangle$ directions. Both the extrusion process used to produce seamless SA-106 Grade B piping and the plastic deformation introduced to feeders may have significant effects on texture and the BN response. Whether texture has a significant effect on the BN response of feeders remains to be determined.

11.1.5 Magneto-Acoustic Emission

Ultimately, BN testing on feeders is limited by the penetration depth of electromagnetic waves at BN frequencies. Domain reconfiguration processes also produce acoustic waves due to magnetostriction (magneto-acoustic emission or MAE), which may be detected using ultrasonic testing apparatus. Ultrasonic waves have significantly higher depth penetration in steel than electromagnetic waves, and may therefore be used to detect stress-sensitive signals from as deep as the excitation field can generate MAE. The enhanced depth penetration of MAE comes with the complication of

reflections. The precise excitation field control provided by the FCS and SL4P should provide the same enhancements to MAE as they to do for BN testing.

11.1.6 Macroscopic Magnetic Coupling

In Section 9.2.7 it was shown that the macroscopic magnetic field coupling changes significantly with compressive strain in feeders. The SL4P was specifically designed to produce maximum field uniformity in the sample region of interest for BN anisotropy measurements via superposition. With minimal design changes to the SL4P pole and connector design, it would be possible to incorporate pickup coils with sensing axes along the axial and hoop directions (as opposed to radial for the current BN sensor) to produce an AC flux leakage instrument for feeders.

Alternatively, a magnetic sensor could be designed to directly measure changes in the sample magnetic impedance. This would involve smaller cores than the SL4P with sharpened or hemispherical poles that would couple similarly for all feeder pipe curvatures. The excitation coil inductance (preferably calibrated using flux control) would then vary with the bulk magnetic impedance.

Both of the above solutions would have depth penetration on the scale of δ_{ex}, and may therefore be capable of through-wall measurements.

11.2 General NDE

The combination of the FCS and SL4P can accommodate any sample with curvature less than or similar to the feeder geometry. The system can therefore be used for conventional BN testing on a wide variety of samples. However, since the FCS can

generate arbitrary flux waveforms, there is an extensive range of flux control schemes that may be considered.

11.2.1 Conventional BN Testing

The precise excitation field control of the FCS and SL4P now permits BN measurements to be performed in such a way that they can be directly compared between materials. However, due to the interaction between geometry and the excitation field, comparisons should be restricted to those having similar geometries. Since feeder pipes are thick compared to δ_{ex}, the phase of the excitation field is correlated to the BN response from various depths in the material. This is not the case for samples that are thin compared to δ_{ex}.

In the thin sample limit, the flux through the sample is directly coupled to the feedback coil flux, and uniform throughout the sample thickness. Thin samples can therefore be used to investigate the BN response at different magnetisations. It follows that variations in the BN response from thin samples having similar geometries can be linked to changes in material composition. For example, Figure 11.1 shows the BN response, measured using the FCS and SL4P, from four steel plates with varying composition: increasing carbon from Figures 11.1a to 11.1c; and the introduction of silicon in 11.1d. Plates are also the ideal geometry for isolating specific influences on the BN response, such as stress and texture.

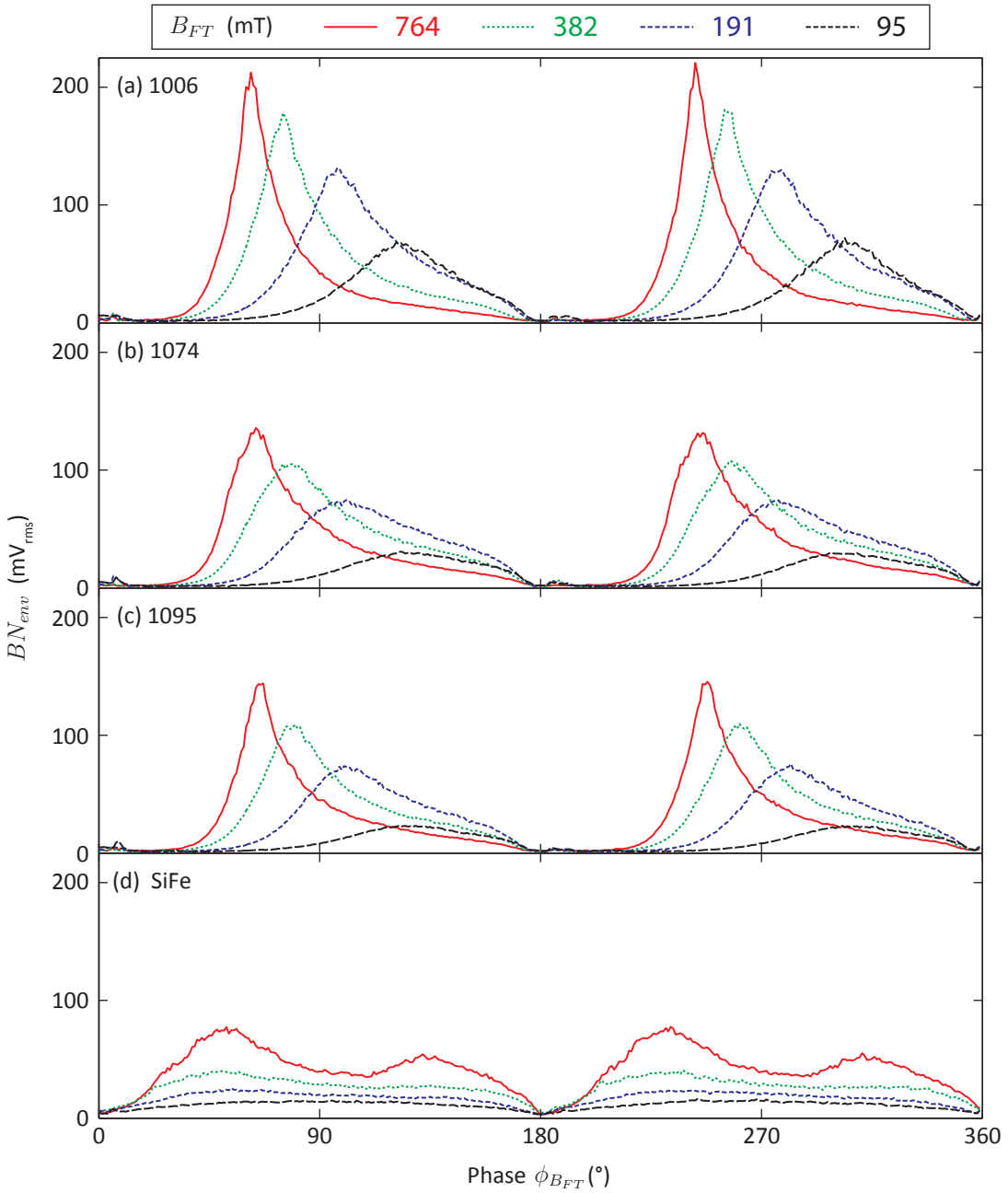

Figure 11.1: BN response from four flat plates consisting of (a) 0.625 mm thick 1006-1020 steel, (b) 0.65 mm thick 1074 steel, (c) 0.64 mm thick 1095 steel, and (d) 0.50 mm thick SiFe steel cut from a transformer. B_{FT} values are are listed in the legend, and $f_{ex} = 51$ Hz.

11.2.2 Novel Flux Control

In this thesis, BN measurements were performed using single-frequency flux waveforms configured so as to imitate the fields used in conventional BN anisotropy measurements. This was also done to facilitate single-frequency analysis of the excitation field. However, since the flux control system allows specification of arbitrary periodic waveforms, the excitation field is not constrained to pure sinusoids. Figure 11.2 shows two alternate excitation fields that may be of some interest.

Figure 11.2ai shows that the FCS can drive the excitation field at a constant flux rate of 47.7 T/s through the feedback coils, producing the triangular flux waveform in Figure 11.2aii. While the data in Figure 11.2a was generated using the SL4P, if the measurement were performed using feedback from thin wound samples, then the flux in the sample would be uniform and directly controlled. Since BN is correlated with the flux rate, this kind of excitation field control could be used to reduce the effects of flux rate modulation on the BN response.

Figure 11.2b shows an alternate means of excitation field control for BN anisotropy measurement. This field configuration produces a constant surface field rotating at f_{ex}, allowing a direct mapping between $\phi_{B_{FT}}$ and the field orientation θ. Flipping the sign of the field in poles 2 and 4 would cause the field to rotate in the opposite direction, and allow estimation of the phase lead at the sample surface. This type of field control could be used for rapid BN anisotropy measurement, requiring only two BN measurements (field rotation clockwise and counterclockwise) with large k_{max}. This could lead to considerable time savings for inspections where BN anisotropy measurements are of interest.

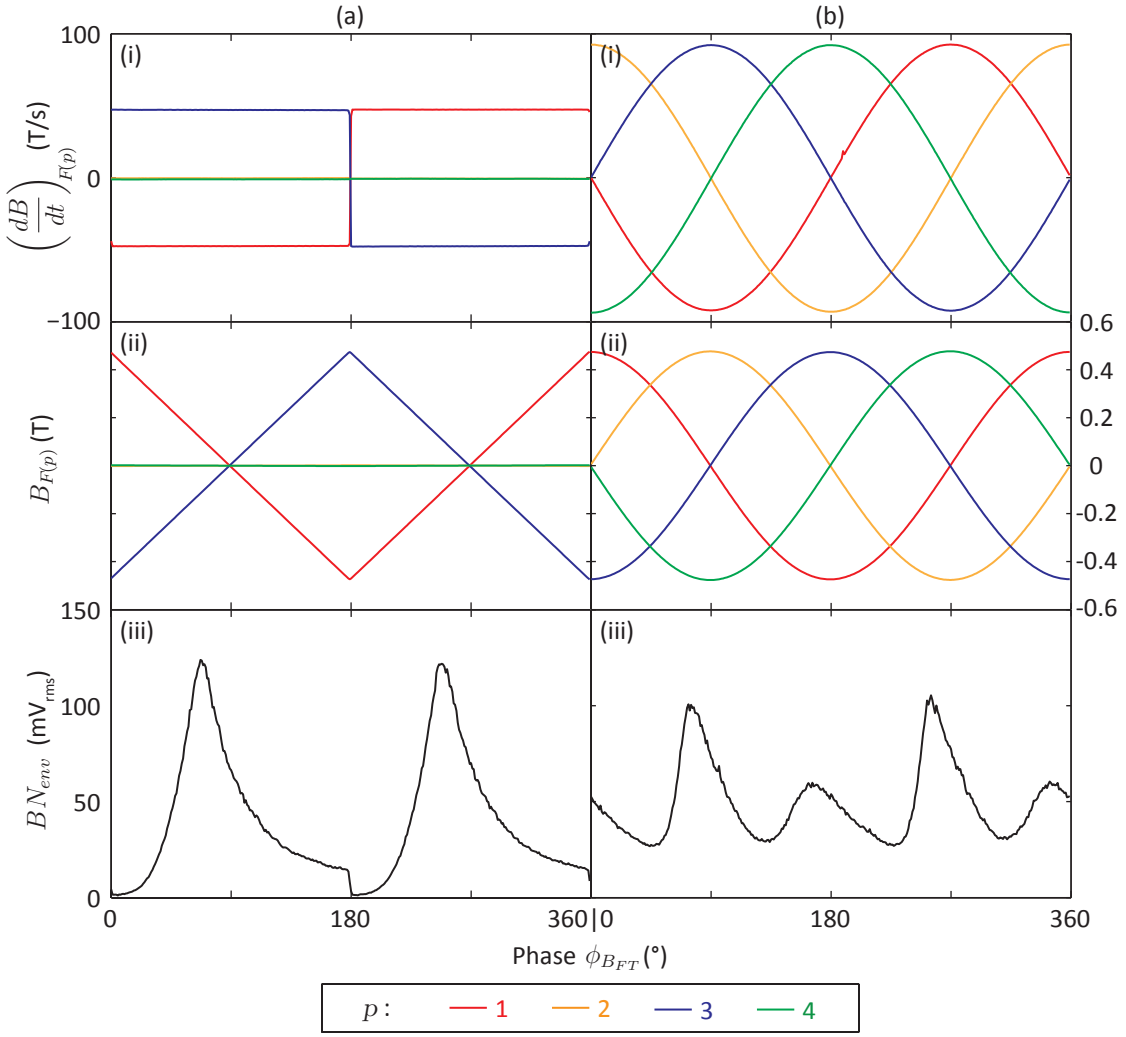

Figure 11.2: Alternate excitation field configurations with corresponding BN data from a 0.625 mm thick 1006-1020 steel plate sample: (a) Magnetising with a constant flux rate of 47.7 T/s up to a peak flux of 477 mT, (b) Rotating surface field at $f_{ex} = 31$ Hz with $B_{FT} = 477$ mT.

Other flux waveforms are also possible and have been tested, such as high frequency modulation, DC current offsets, and driving poles with common mode flux (i.e., driving all poles to magnetic north at the same time) with the SL4P's four pole flux control. Such novel magnetisation schemes combined with the appropriate signal processing may lead to more rapid BN testing procedures that are not possible with a single core electromagnet.

11.3 Next Generation System

The BN testing system developed for this thesis has several limitations that should be addressed in future designs. In this section, these limitations are identified, and possible solutions are discussed.

11.3.1 Flux Control System

The first recommendation for FCS improvement is the removal of R_{F2} from Figures 3.4 and 4.1. R_{F2} was originally included in the FCS circuit in order to stabilize the circuit response. This additional stability comes from the reduction of the feedback coil time constant in RTA and DEC modes by the inclusion of a large series resistance with L_F. However, R_{F2} has the unintended consequence of changing the calibration for $V_{F(p)}$, resulting in different matching criteria ($\mathcal{M}_p$) for $V_{F(p)}$ between VF mode and the RTA and DEC modes. Removing R_{F2} and increasing R_{F1} produces* the same stability gains, without the additional matching problems.

In general, the flux control circuit could benefit from further electrical engineering. The present system was built on a printed circuit board (PCB) designed by the author

*This has been tested.

that had to be significantly modified to produce the working circuit in Figure 4.1. As a result, the layout is not optimum and some connections are not robust. The PCB design also does not have sufficient room for power amplifier cooling, and it is possible to drive the LM4701 amplifiers into thermal protection during measurements with large currents. Other recommendations include using terminal blocks and pin headers for off-board connections, designing each PCB for a single channel to make a modular system, and improving connections to the chassis.

The present software design requires a minimum of 3 cycles per iteration. This is because cross-talk between the PCI-6229 and PCI-6133 is present when excitation and pickup waveforms are sampled simultaneously, and because the present algorithm waits for all the data before performing error correction calculations. It is hypothesized that cross-talk could be reduced by adding buffer amplifiers between the flux source circuit and the PCI-6229, thereby allowing simultaneous measurement and reducing the iteration time to 2 cycles. The iteration time could conceivably be reduced further by performing error correction calculations during the measurement.

The PCI-6229 DAC produces analog output glitches that propagate through the circuit into the pickup coil waveform. It is recommended that the 4 channel analog-output design of a next generation system be free from such artifacts to simplify BN analysis. If a suitable 4 channel analog-output card cannot be found, a custom DAC design with an associated computer interface may be required.

The external sources of common mode transients complicate the measurement, constraining the selection of excitation frequencies. Measurements made while visiting AECL had lower noise levels when the system was powered using a pure-sinusoidal uninterruptable power supply. It is recommended that such a supply be added to the

system in the future.

11.3.2 SL4P Improvements

There are several features of the SL4P design that could be improved in future designs:

- The spring-loading mechanisms for the pickup coil and short core assembly were intended for only vertical travel, but have significant horizontal play. This increases the pickup coil coupling uncertainty, and makes it more difficult to correctly align the SL4P on a bent surface.

- The pickup coil shield should be machined from copper as opposed to brass, to enhance its function as an electromagnetic shield.

- Since the Supermendur cores are conductive, it is possible to develop shorts between coils, particularly if they are abraded on the relatively sharp corners of the U-cores. Treating the corners is quite difficult (laminations may easily be separated), so it is suggested that cores should be coated with an insulator prior to assembly in order to limit the possibility of such shorts.

- The AWG 36 excitation and feedback coil leads travel from the coils to the pin header within the long core housing. This poor cable management likely increases the capacitive coupling between coils, and increases the strains on individual wires. A custom PCB for the interior of the long core housing could better manage the impedance, guarding, connections, and stresses on the wires.

- The pin-header connector was selected for the SL4P as it allows a relatively large number of connections per unit area. This unshielded connector can produce

a significant strain on the SL4P, and there are likely better options available. When investigating connectors, consider that the excitation coil cabling should be twisted and separated from the feedback and pickup coil cabling to limit inductive and capacitive coupling (it is in the present implementation). The leads for each coil should be twisted pairs, with electrostatic shields used where appropriate.

- At present, connections to the FCS are made via banana plugs through a steel chassis. If banana plugs are used in the future, these should be set in plastic to avoid coupling to eddy currents in the chassis.

- If the short core frame could be machined from a non-conductive material, then the long core housing and bottom plate could be conductive and grounded. This would better shield internal cabling, and potentially reduce noise.

11.3.3 BN Preamplifier

The present system uses an *Ithaco 1201* preamplifier with differntial inputs for the pickup coil voltage with 400 kHz of bandwidth at 60 dB of gain, and a $7\,\mathrm{nV}/\sqrt{\mathrm{Hz}}$ noise floor. The *Ithaco 1201* also has the undocumented noise floor resonances every 165 kHz. This set of specifications is sufficient to measure BN up to 400 kHz, though data from the BN system indicates BN may have significantly higher bandwidth. The noise floor resonances may also obscure fine detail in the BN waveform, and are difficult to remove with signal processing due to their narrow bandwidth.

Frequencies > 300 kHz represent power from only the first few μm of the sample surface, and are therefore of little interest in NDE applications. However, such frequencies may contain useful information for research. Moreover, the obscuring of fine

detail by the noise floor resonances is undesirable.

In the present system, the *Ithaco 1201* is a 'drop in' solution, and can easily be replaced. If a new preamplifier solution is desired, consider the following specifications:

- A gain of 60 dB is required. Variable gain is also useful.
- The bandwidth should be DC to $> 400\,\mathrm{kHz}$. A maximum bandwidth of DC to 10 MHz is likely sufficient.
- The input impedance must be $> 500\,\Omega$ in order that BN not be significantly damped.
- A low noise floor is desired, though the noise floor is limited by thermal noise from the terminating resistor when $< 1\,\mathrm{nV}/\sqrt{\mathrm{Hz}}$.
- A differential input is preferred to a single-ended input to improve common mode rejection.

Any new preamplifier should be thoroughly tested for undocumented features.

Bibliography

[1] M.T. Hutchings, P.J. Withers, T.M. Holden, and T. Lorentzen. *Introduction to the Characterization of Residual Stresses by Neutron Diffraction.* Taylor & Francis Group, 2005.

[2] Pierre Weiss. L'hypothèse du champ moléculaire et de la propriété ferromagnétique. *J. de Physique*, 6:661–690, 1907.

[3] James P. Joule. On a new class of magnetic forces. *Sturgeon's Annals of Electricity*, 8:219, 1842.

[4] E. Villari. Ueber die aenderungen des magnetischen moments, welche der zug und das hindurchleiten eines galvanischen stroms in einem stabe von stahl oder eisen hervorbringen. *Annalen der Physik*, 202(9):87–122, 1865.

[5] Heinrich Barkhausen. Zwei mit hilfe der neuen verstarker entdeckte erscheinugen. *Zeitschrift für Physik*, 20:401–403, 1919.

[6] Gianfranco Durin and Stefano Zapperi. *The Barkhausen effect.* arXiv:cond-mat/0404512v1, April 2004.

[7] F. Bitter. On inhomogeneities in the magnetization of ferromagnetic materials. *Physical Review*, 38(10):1903–1905, 1931.

[8] H.J. Williams and W. Shockley. A simple domain structure in an iron crystal showing a direct correlation with the magnetization. *Physical Review*, 75(1):178–183, 1949.

[9] R.W. Leep. The Barkhausen effect and its application in nondestructive testing. In *Proceedings of the Symposium on Physics and Nondestructive Testing*, pages 439–453. Gordon and Breach, 1967.

[10] R.L. Pasley. Barkhausen effect: An indication of stress. *Materials Evaluation*, 28(7):157–161, 1970.

[11] Seppo I. Tiitto. *US Patent #4,634,976: Barkhausen noise method for stress and defect detecting in hard steel*, 1987.

[12] V.L. Vengrinovich and V.L. Tsukerman. Stress and texture measurement using Barkhausen noise and angular scanning of driving magnetic field. In *16th WCNDT 2004 World Conference on NDT*, Montreal, 2004.

[13] C.B. Scruby, D.J. Buttle, F.A. Ravenscroft, C.G. de Michelis, M. Gori, and G. Antonelli. *US Patent #5,828,211: Determining stress in ferromagnetic materials from measurements of magnetic anisotropy and magnetic permeability*, 1998.

[14] D.J. Buttle. *US Patent #6,850,055 B2: Measurement of the variation of a material property with depth in a ferromangetic material*, 2005.

[15] D.J. Buttle. *US Patent #6,854,336 B2: Measurement of stress in a ferromagnetic material*, 2005.

[16] D.J. Buttle, W. Dalzell, and P.J. Thayer. *US Patent #7,053,606 B2: Measurement of residual and thermally-induced stress in a rail*, 2006.

[17] *2004 ASME Boiler and Pressure Vessel Code, Sections IIA and IID.* American Society of Mechanical Engineers, 2006.

[18] M. Yetisir, R. Rogge, and R. Donaberger. The effect of manufacturing process on residual stresses of pipe bends. In *Proceedings of PVP2005, 2005 ASME Pressure Vessels and Piping Division Conference*, Denver, CO, 2005.

[19] M. Yetisir, R. Donaberger, and R. Rogge. Residual stresses in CANDU feeder bends - effect of bend radius. In *Proceedings of PVP2005, 2006 ASME Pressure Vessels and Piping Division Conference*, Vancouver, BC, 2006.

[20] J.C. Jin, A. Blahoianu, and T.Vigalsky. Service induced degradations of candu feeder piping - fac wall thinning and cracking. In *Material Degradation and Related Managerial Issues at Nuclear Power Plants, Proceedings of a Technical Meeting, Vienna, 15-18 February 2005.* International Atomic Energy Agency, 2006.

[21] Hélène Hébert. Private correspondence, 2007-2008. AECL.

[22] G. Thompson. Small tube MBN investigations. Queen's AMG internal report, 2004.

[23] B. Lucht. Magnetic flux leakage for evaluation of residual stress in CANDU feeder tubes - proof of concept. Queen's AMG internal report, 2005.

[24] Ronald Rogge. Private correspondence, 2009. National Research Council.

[25] J. C. Maxwell. On physical lines of force. *Philosophical Magazine*, 1861.

[26] J. C. Maxwell. A dynamical theory of the electromagnetic field. *Philosophical Transactions of the Royal Society of London*, 1865.

[27] David J. Griffiths. *Introduction to Electrodynamics Third Edition*. Prentice Hall, 1999.

[28] P. J. Nahin. *Oliver Heaviside The Life, Work and Times of an Electrical Genius of the Victorian Age*. JHU Press, Baltimore, MD, 2002.

[29] M. J. Crowe. *A History of Vector Analysis*. Dover Publications, Mineola, NY, 1994.

[30] B.D. Cullity. *Introduction to Magnetic Materials*. Addison-Wesley, 1972.

[31] Etienne du Trémolet de Lacheisserie. *Magnetostriction: Theory and Applications of Magnetoelasticity*. CRC Press, Inc., 1993.

[32] Y. Yu, T.W. Krause, P. Weyman, and D.L. Atherton. Tensor magnetic hysteresis loop measurements of a steel cube. *Journal of Magnetism and Magnetic Materials*, 166:290–296, 1997.

[33] W. Heisenberg. Mehrkörperproblem und resonanz in der quantenmechanik. *Zeitschrift für Physik*, 38:411–426, 1926.

[34] P.A.M. Dirac. On the theory of quantum mechanics. *Proceedings of the Royal Society of London, Series A*, 112:661–677, 1926.

[35] E.R. Callen and H.B. Callen. Anisotropic magnetization. *Journal of Physics and Chemistry of Solids*, 16:310–328, 1960.

[36] Amikam Aharoni. Magnetostatic energy calculations. *IEEE Transactions on Magnetics*, 27(4):3539–3547, 1991.

[37] W. F. Brown. *Magnetostatic principles in ferromagnetism*. Interscience Publishers, New York, 1962.

[38] D.C. Jiles. Dynamics of domain magnetization and the Barkhausen effect. *Czechoslovak Journal of Physics*, 50(8):893–988, 2000.

[39] D. J. Buttle, G. A. D. Briggs, J. P. Jakubovics, E. A. Little, and C. B. Scruby. Magnetoacoustic and Barkhausen emission in ferromagnetic materials. *Philosophical Transactions of the Royal Society of London A*, 320:363–378, 1986.

[40] B. Augustyniak, M. J. Sablik, F. J. G. Landgraf, D. C. Jiles, M. Chmielewski, L. Piotrowski, and A. J. Moses. Lack of magnetoacoustic emission in iron with 6.5% silicon. *Journal of Magnetism and Magnetic Materials*, 320:2530–2533, 2008.

[41] ASTM Standard E1004-02. *Standard Practice for Determining Electrical Conductivity Using the Electromagnetic (Eddy-Current) Method*. ASTM International, West Conshohocken, PA, 2002.

[42] ASTM Standard D257-99. *Standard Test Methods for DC Resistance or Conductance of Insulating Materials*. ASTM International, West Conshohocken, PA, 1999.

[43] Stuart Craig. Private correspondence, 2007-2008. AECL.

[44] Mark Green. Private correspondence, 2007. Applications Engineer for Sypris Magnetics.

[45] B. Kulke, R. Frye, and F. Penko. Effects if irradiation on hall probe sensitivity. In *13th Particle Accelerator Conference*, Chicago, IL, 1989.

[46] A.V. Karpukhin, V.M. Lachinov, V.K. Makoveev, N.I. Zamiatin, I.A. Bolshakova, M.M. Bolshakov, A.O. Matkovski, and T.A. Moskovets. Influence of neutron irradiation on magnetic field sensors. *IEEE Transactions on Applied Superconductivity*, 10(1):1407–1409, 2000.

[47] V.K. Makoveev, M.M. Filatov, V.P. Goncharov, A.V. Karpukhin, V.M. Lachinov, A.V. Leonov, and V.N. Mordkovich. Influence of neutron irradiation on the parameters of field hall plates. *IEEE Transactions on Applied Superconductivity*, 12(1):1672–1674, 2002.

[48] I. Ďuran, L. Viererbl, V. Klupák, I. Bolshakova, and R. Holyaka. Investigation of stability of iter candidate hall sensors under neutron irratdiation. *Czechoslovak Jouranl of Physics*, 56:B54–B60, 2006.

[49] S. Zurek, P. Marketos, T. Meydan, and A.J. Moses. Use of novel adaptive digital feedback for magnetic measurements under controlled magnetizing conditions. *IEEE Transactions on Magnetics*, 41(11):4242–4249, 2005.

[50] S. White, T. Krause, and L. Clapham. Control of flux in magnetic circuits for Barkhausen noise measurements. *Measurement Science and Technology*, 18:3501–3510, 2007.

[51] National Instruments Corporation, www.ni.com. *NI 622x Specifications*, 2006.

[52] National Instruments Corporation, www.ni.com. *NI 6132/6133 Specifications*, 2006.

[53] National Semiconductor Corporation, www.national.com. *LM4701 Overture^{TM}Audio Power Amplifier Series 30W Audio Power Amplifier with Mute and Standby Modes*, 2004.

[54] Fairchild Semiconductor Corp, www.fairchildsemi.com. *Photo FET Optocouplers*, 2003.

[55] *Fair-Rite Product's Catalog Part Data Sheets, 3078990831 and 3067990831.* Fair-Rite Products Corp., www.fair-rite.com, PO Box J, One Commercial Row, Wallkill, NY 12589-0288, 2008.

[56] *2005/2006 Powdered Cores Catalog.* Magnetics Inc., www.mag-inc.com, 110 Delta Drive Pittsburgh, PA 15238-0422, 2004.

[57] *M20 Material.* National Magnetics Group, Inc., www.magneticsgroup.com, 1210 Win Dr. Bethlehem, PA 18017-7061, 2008.

[58] Harold A. Wheeler. Simple inductance formulas for radio coils. *Proceedings of the IRE*, 16(10):1398–1400, 1928.

[59] DL Instruments, LLC, 233 Cecil A. Malone Drive, Ithaca, N.Y. 14850, www.dlinstruments.com. *Model 1201 Programmable Voltage Preamplifier*, 2008.

[60] National Instruments Corporation, www.ni.com. *BNC-2110 Installation Guide*, 2003.

[61] National Instruments Corporation, www.ni.com. *DAQ M Series, M Series User Manual*, 2008.

[62] R. N. Bracewell. *The Fourier Transform and its Applications*. McGraw Hill, third edition edition, 2000.

[63] J.B. Johnson. Thermal agitation of electricity in conductors. *Physical Review*, 32:97–109, 1928.

[64] H. Nyquist. Thermal agitation of electric charge in conductors. *Physical Review*, 32:110–113, 1928.

[65] V. S. Augutis, Z. Nakutis, and R.Ramanauskas. Advances of Barkhausen emission measurement. *IEEE Transactions on Instrumentation and Measurement*, 58(2):337–341, 2009.

[66] S. White, T. Krause, and L. Clapham. Quantitative analysis of surface Barkhausen noise measurements. In *Review of Progress in Quantitative Nondestructive Evaluation, AIP Conference Proceedings*, volume 27.

[67] Bill Jahnke. Private correspondence, 2009. Technical Director, MK Magnetics Inc.

[68] C. Mandache, T. W. Krause, and L. Clapham. Investigation of optimum field amplitude for stress dependence of magnetic Barkhausen noise. *IEEE Transactions on Magnetics*, 43(11):3976–3983, 2007.

[69] T. W. Krause, K. Mandal, C. Hauge, P. Weyman, B. Sijgers, and D. L. Atherton. Correlation between magnetic flux leakage and magnetic Barkhausen noise: Stress dependence in pipeline steel. *Journal of Magnetism and Magnetic Materials*, 169:207–219, 1997.

[70] ISO/TS 21432:2005. *Non-destructive testing – Standard test method for determining residual stresses by neutron diffraction.* British Standards Institute, 2006.

[71] NAM Acquiring Corporation. *Wound Magnetics.* Magnetic Metals, www.magmet.com, 2001.

[72] *Hyperco®50 HS Alloy Data.* Carpenter Technologies, www.cartech.com, 1995.

[73] *Soft Magnetics Application Guide.* Arnold®group of SPS Technologies, February 2003.

[74] *Technical Data Booklet.* MWS Wire Industries www.mwswire.com, 2005.

[75] A. Massarini and M.K. Kazimierczuk. Self capcitance of inductors. *IEEE Transactions on Power Electronics*, 12(4):671–676, 1997.

[76] *2006 Belden Master Catalog.* Belden Inc., www.belden.com, 2006.

Appendix A

Flux Control System Details

This appendix presents the flux control system (FCS) algorithm and timing implementation in sections A.1 and A.2, respectively. FCS channel matching procedures are presented in section sec:FCSmatch.

A.1 FCS Algorithm

Figures A.1, A.2 and A.3 are flow charts for the FCS algorithm for single excitation frequency flux and voltage waveforms. A brief overview for the steps in each flow chart are described below.

Figure A.1 shows the initialization sequence for the FCS algorithm. Upon initialization, the FCS switches to voltage following (VF) mode and 0 V is written to the PCI-6229 $AO_{(0...3)}$ channels to ensure the voltage across the excitation coil outputs is small. User-specified excitation parameters are then read and used to calculate the various initialization parameters. To ensure exact periodicity of the excitation field, f_{ex} is rounded to an integer division of the analog output frequency (f_{6229AO}). A

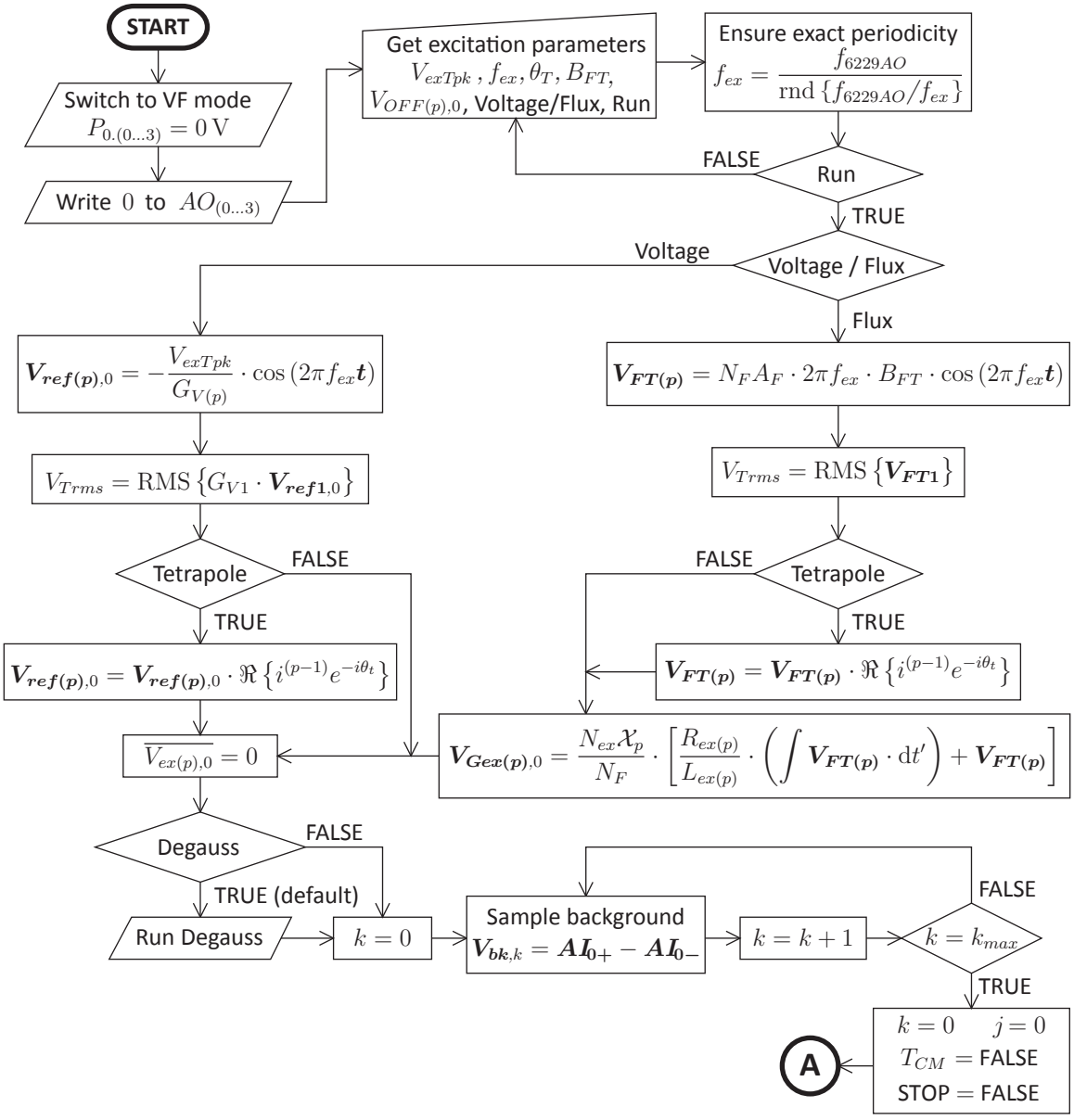

Figure A.1: Flow chart for FCS algorithm initialization. See Figures A.2 and A.3 for the rest of the algorithm.

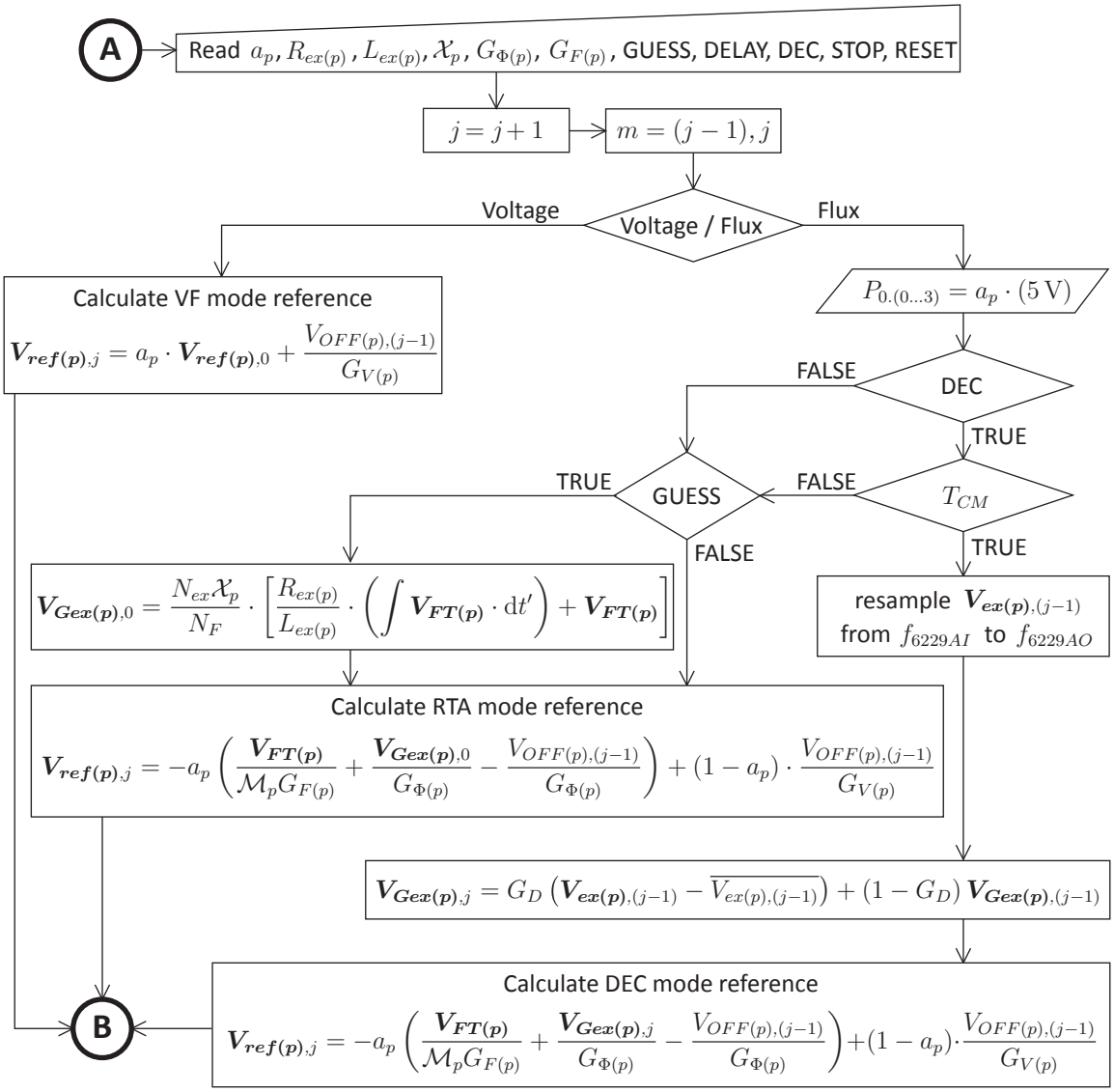

Figure A.2: Flow chart for FCS algorithm reference voltage calculation. See Figures A.1 and A.3 for the rest of the algorithm.

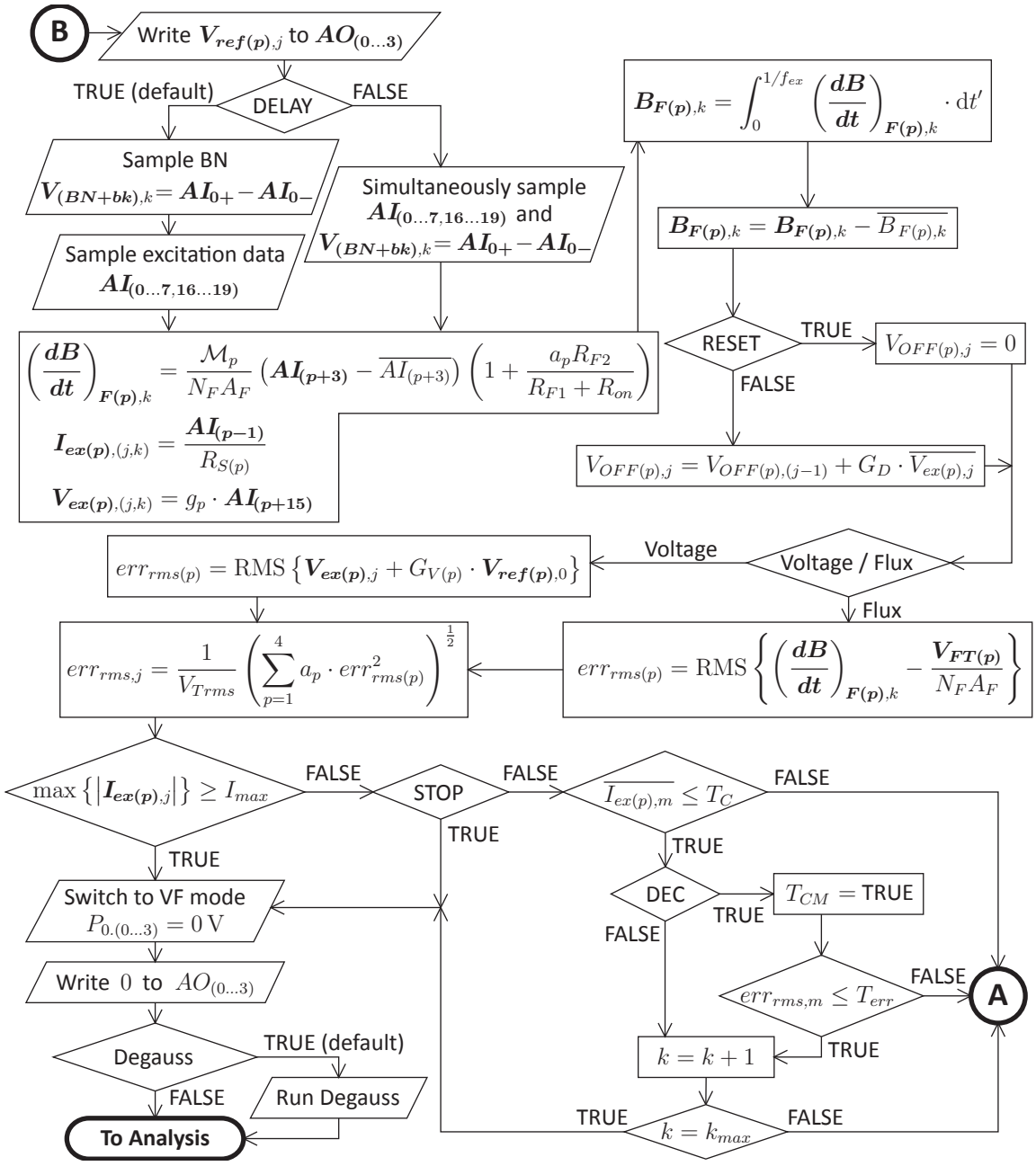

Figure A.3: Flow chart for FCS algorithm sampling and threshold testing. See Figures A.1 and A.2 for the rest of the algorithm.

degaussing algorithm is then run to zero the initial flux density, and the background noise in the pickup coil ($\boldsymbol{V_{bk},_k}$) is sampled for k_{max} cycles.

Figure A.2 shows the calculation procedure for the reference voltage ($\boldsymbol{V_{ref(p)},_j}$) within the feedback loop. At the start of each iteration, a_p is read and specifies which poles are active, with $a_p = 1$ and $a_p = 0$ for active and inactive poles, respectively. $R_{ex(p)}$, $L_{ex(p)}$, $\mathcal{X}_p$, $G_{\Phi(p)}$ and $G_{F(p)}$ are all read within the loop, and are used to optimize $\boldsymbol{V_{ref(p)},_j}$ in RTA and DEC modes. The calculation of $\boldsymbol{V_{ref(p)},_j}$ in RTA and DEC modes differs only by whether the guess excitation is calculated from the user-specified parameters as $\boldsymbol{V_{Gex(p)},_0}$, or from the measured $\boldsymbol{V_{ex(p)},_{(j-1)}}$ as $\boldsymbol{V_{Gex(p)},_j}$. DEC calculations are only performed when T_{CM} is 'TRUE.' Since f_{6229AO} is not equal to PCI-6229 analog input frequency (f_{6229AI}), $\boldsymbol{V_{ex(p)},_{(j-1)}}$ must be re-sampled to calculate $\boldsymbol{V_{Gex(p)},_j}$ in DEC mode.

Figure A.3 starts with the writing of $\boldsymbol{V_{ref(p)},_j}$ to the PCI-6229 $AO_{(0...3)}$ channels. This is a continuous write process that will keep writing $\boldsymbol{V_{ref(p)},_j}$ until the loop is stopped. Each time the write action is called with a new $V_{ref(p),j}$ the buffer is updated and the write process continues with the new waveforms. $\boldsymbol{V_{(BN+bk)},_k}$ and $\boldsymbol{AI_{(0...7,16...19)}}$ are then sampled on the PCI-6133 and PCI-6229, respectively, with a delay between them by default to prevent cross-talk. The $\boldsymbol{AI_{(0...7,16...19)}}$ data are then used to calculate the various excitation waveforms, DC offsets ($V_{OFF(p),j}$), the RMS error for each channel ($err_{rms(p)}$), and the aggregate error for iteration ($err_{rms,j}$).

Once $err_{rms,j}$ is calculated, Figure A.3 shows that any the control loop is terminated if the maximum excitation current exceeds I_{max}, the user-specified 'STOP' parameter is set to 'TRUE,' or k_{max} cycles are acquired. Data are saved in VF and

RTA modes when the DC excitation current ($\overline{I_{ex(p),m}}$) is less than the current threshold (T_C) for two successive cycles ($m = (j-1), j$). In DEC mode, data is saved when both the current threshold is met, and $err_{rms,j} \leq T_{err}$.

A.2 Timing and Triggering

The relative timing and triggering between the PCI-6229 and PCI-6133 during FCS system operation is controlled using the digital real-time system integration (RTSI) bus.

Figure A.4 shows a timing diagram with the relevant PCI-6229, PCI-6133, and RTSI channels. A degauss cycle is implemented before and after each measurement in order to reduce residual magnetisation effects. After the initial degauss cycle, background noise in the pickup coil is sampled on the PCI-6133 $AI_{0+} - AI_{0-}$ channel for k_{max} cycles at $f_{6133AI} = 2.5\,\text{MHz}$. Before entering the digital feedback loop, $P.0.(0 \ldots 3)$ is switched to 5 V for RTA and DEC modes, or left at 0 V for VF mode. A continuous $AO_{(0\ldots3)}$ write process auto-starts following $P_{0.(0\ldots3)}$ switching.

Continuous $AO_{(0\ldots3)}$ write processes only output a single start trigger pulse on the first iteration ($j = 0$), which is routed to $RTSI_3$. To provide timing for subsequent cycles a PCI-6229 digital clock process with a frequency f_{ex} and a 25% duty cycle is routed to $RTSI_0$ and triggered to start on the rise of $RTSI_3$.

The PCI-6229 read $AI_{(0\ldots7,16\ldots19)}$ is triggered to start on the fall of $RTSI_3$, and routs its start trigger to $RTSI_1$. The PCI-6133 read $AI_{0+} - AI_{0-}$ process starts on the rise of $RTSI_1$. Thus both 6229 read and 6133 read processes are initialized by the same $RTSI_0$ pulse. To remove cross-talk, the 6229 read process is delayed by f_{ex}^{-1} following the start trigger.

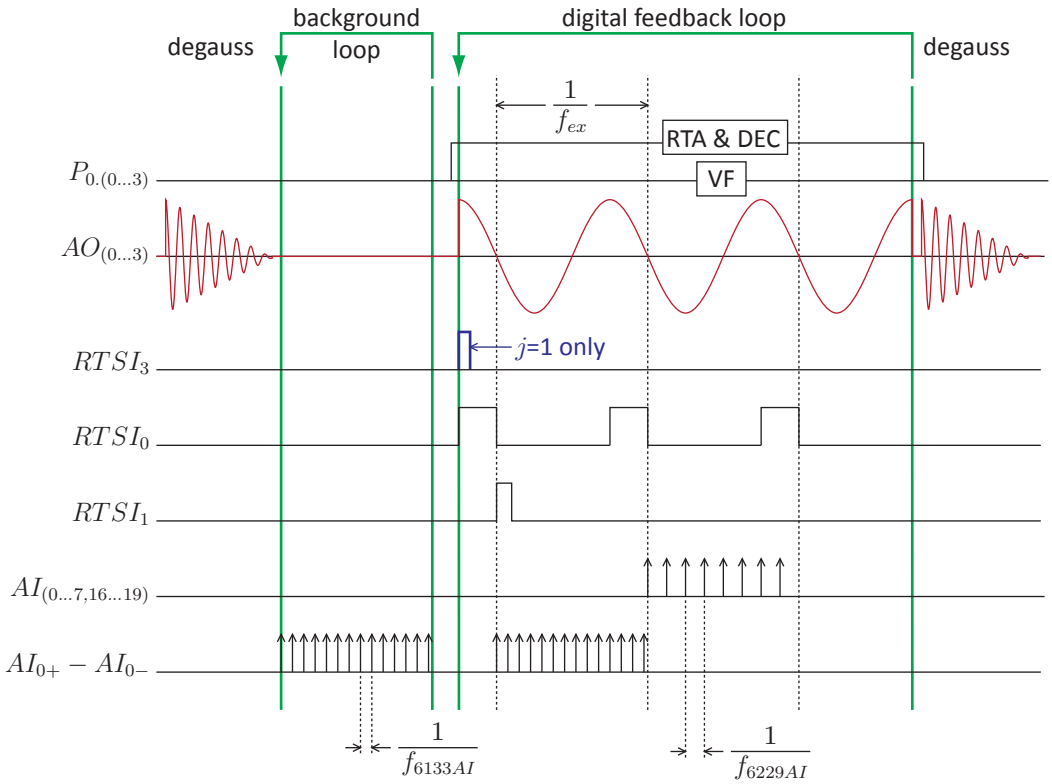

Figure A.4: FCS timing diagram.

The time between digital feedback iterations is an integer multiple of f_{ex}^{-1} due to the time required to trigger, sample, correct the reference waveforms, and trigger on the next excitation cycle. Iterations typically occur every 3 (as is shown in Figure A.4) to 5 times f_{ex}^{-1}, depending on f_{ex}, f_{6229AO}, f_{6229AI}, and the feedback mode calculation time. Due to the delay, the theoretical minimum number of cycles per iteration is 3.

A.3 FCS Channel Matching

Each excitation iteration j, the FCS outputs four excitation voltage waveforms ($\boldsymbol{V_{ex(p),j}}$), measured across voltage dividers with ratios g_p, and four excitation current waveforms ($\boldsymbol{I_{ex(p),j}}$), measured using shunt resistors $R_{S(p)}$. Matching procedures for g_p and $R_{S(p)}$

are described in sections A.3.1 and A.3.2, respectively.

Prior to the calibration procedures described below, all cables were disconnected from the PCI-6133 DAQ and PCI-6229 DAQ, and the self-calibration routines were run from within *National Instruments® Measurement and Automation Explorer*. At the time of the measurements in this thesis, both DAQs were ~ 3 years from their last external calibration.

A.3.1 Voltage Divider Ratios (g_p)

Voltage divider ratios (g_p) were measured using the circuit configuration shown in Figure A.5. Excitation and feedback coils were disconnected from the circuit, and $AI_{(p+3)}$ was shorted to the amplifier output. $AI_{(p+3)}$ was configured to operate between $\pm 10\,\mathrm{V}$, and $P_{0.(p-1)}$ was set to $0\,\mathrm{V}$ across all channels to place the circuit in voltage following mode. Analog output channels were then driven with waveforms $\boldsymbol{AO_{(p-1)}}$ according to:

$$\boldsymbol{AO_{(p-1)}} = -V_0 \cdot \sin\left(2\pi f_{ex} \boldsymbol{t}\right) \tag{A.1}$$

for $p = 1 \ldots 4$, with $V_0 = 1\,\mathrm{V}$ and f_{ex} taking values of $(1, 3, 10, 30, 100, 300, 1000)\,\mathrm{Hz}$. $AI_{(p+3)}$ and $AI_{(p+15)}$ were sampled at $30\,\mathrm{kHz}$ for 128 cycles.

The voltage divider ratios g_p were then evaluated as:

$$g_p = \frac{\mathrm{RMS}\left\{\boldsymbol{AI_{(p+3)}}\right\}}{\mathrm{RMS}\left\{\boldsymbol{AI_{(p+15)}}\right\}}, \tag{A.2}$$

for each of the 128 cycles, where $\boldsymbol{AI_n}$ is the voltage waveform from channel n for one excitation period. The typical standard deviation of the 128 measurements of g_p at a given given frequency was $\pm 0.003\%$, however the standard deviation of g_p

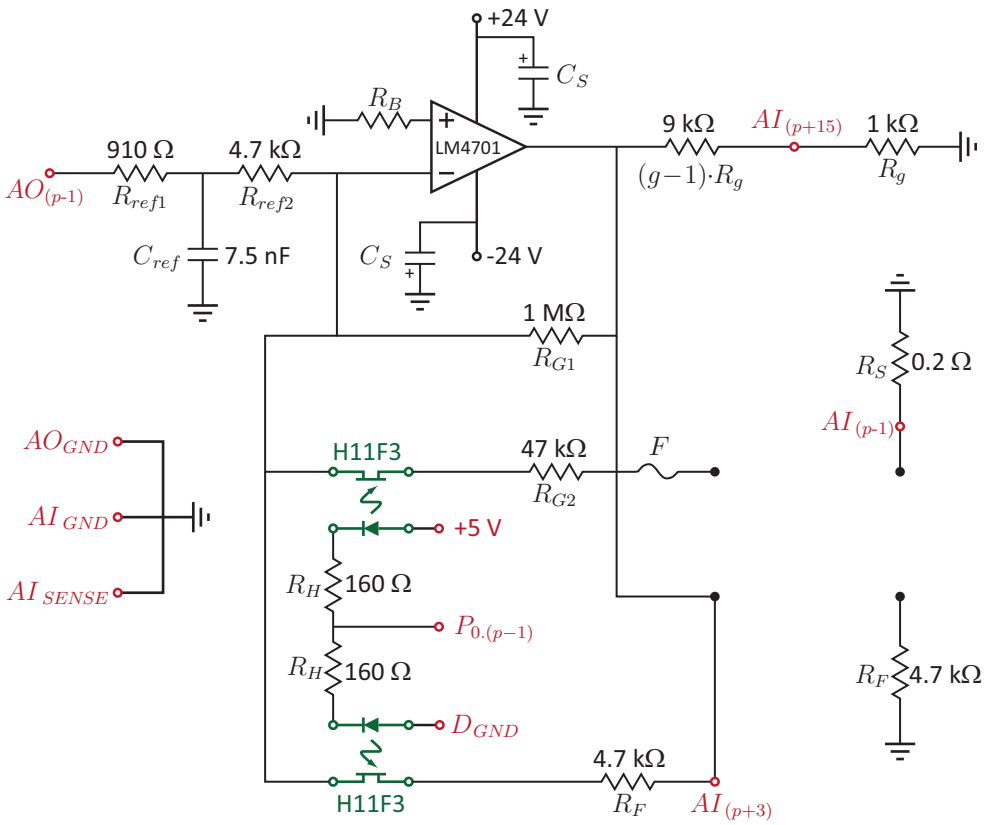

Figure A.5: Circuit configuration for evaluation of g_p, $G_{V(p)}$, and $G_{F(p)}$.

with frequency was ±0.009% to 0.03%. Other than random variation, no significant frequency dependence was observed. The mean and standard deviation of g_p over the measured frequency range are presented in Table A.1.

Uncertainties on g_p values in Table A.1 represent the precision to which g_p values were consistent over the measured frequency range. The systematic uncertainty of the g_p values depends on the accuracy of the $\boldsymbol{AI_{(p+3)}}$ waveforms in the ±10 V range and the $\boldsymbol{AI_{(p+15)}}$ waveforms in the ±5 V range. Using the absolute accuracy at full scale* values of ±3.1 mV and ±1.6 mV, for the ±10 V and ±5 V ranges, respectively, gives a systematic uncertainty of ±0.032 (0.3%) for all values of g_p.

*From the PCI-6229 specifications [51].

Table A.1: Flux control circuit matching parameters. Systematic uncertainty for g_p is given as ± 0.032.

Pole p	g_p (± 0.032)	$R_{S(p)}$ (Ω)
1	10.289 ± 0.003	0.2192 ± 0.0012
2	10.2493 ± 0.0009	0.2180 ± 0.0012
3	10.3458 ± 0.0009	0.2247 ± 0.0015
4	10.4053 ± 0.0010	0.2234 ± 0.0014

A.3.2 Shunt Resistances ($R_{S(p)}$)

Shunt resistance values ($R_{S(p)}$) were measured using the circuit configuration shown in Figure A.6. Excitation and feedback coils were disconnected from the circuit, and a *Hewlett Packard* 34401A digital multimeter was configured as an ammeter and inserted in place of the excitation coil for each channel.

$AI_{(p-1)}$ was configured to operate between ± 1 V sampled at 30 kHz, and $P_{0.(p-1)}$ was set to 0 V across all channels to place the circuit in voltage following mode. The analog output channels were then driven according to equation (A.1), with $V_0 = 0.025$ V, giving an output voltage of ~ 0.19 V across the total circuit resistance. Measurements were performed at f_{ex} values from 10 Hz to 1000 Hz.

The mean value of RMS $\left\{ \boldsymbol{AI_{(p-1)}} \right\}$ was calculated over ~ 10 s of sampling, while the RMS current I_{rms} was measured from the 34401A multimeter. Standard deviations of the mean RMS $\left\{ \boldsymbol{AI_{(p-1)}} \right\}$ over 128 cycles were $\sim 0.1\%$. The 34401A has AC current accuracy specifications in its 3 A range of $\pm(0.15\% + 1.8\,\text{mA})$. Typical I_{rms} values were 125 mA. Therefore I_{rms} values had an uncertainty of ± 2 mA or 1.6%.

$R_{S(p)}$ values were calculated as:

$$R_{S(p)} = \frac{\text{RMS}\left\{ \boldsymbol{AI_{(p-1)}} \right\}}{I_{rms}} \tag{A.3}$$

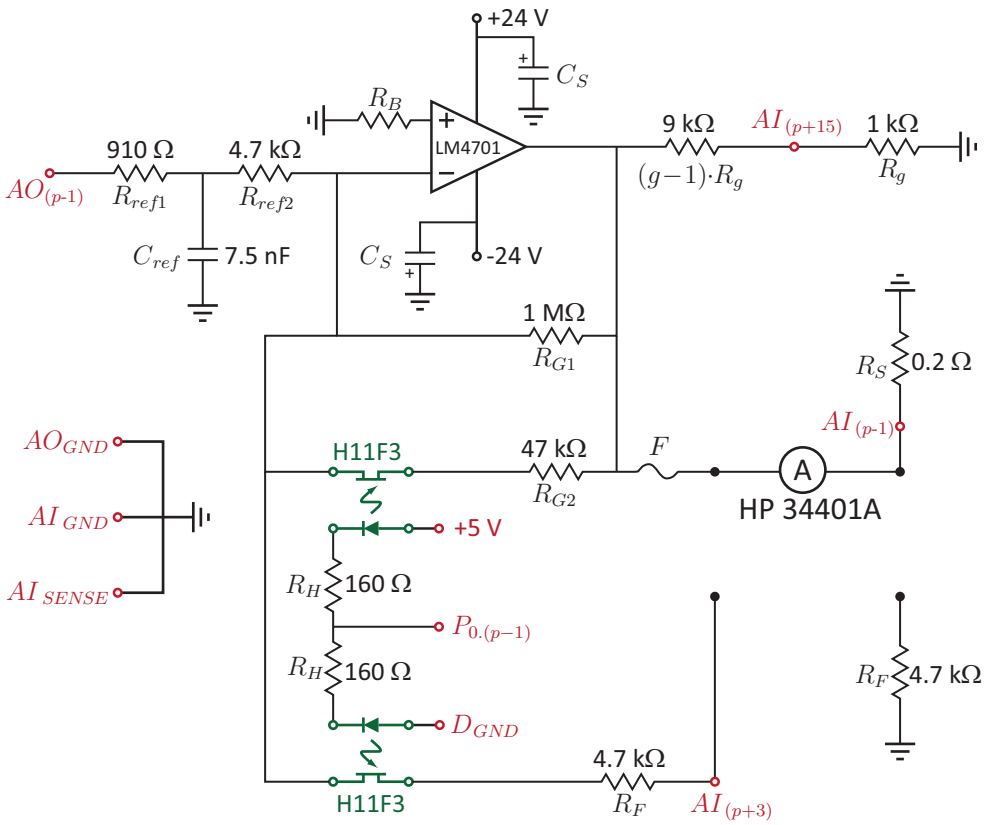

Figure A.6: Circuit configuration for evaluation of $R_{S(p)}$, using a *Hewlett Packard* 34401A multimeter configured as an ammeter.

for each value of f_{ex}, and errors were propagated. The mean and uncertainty of $R_{S(p)}$ weighted with respect to error over all f_{ex} values are shown in Table A.1. Errors on the mean value of $R_{S(p)}$ take into account the systematic uncertainty associated with the 34401A I_{rms} measurement and the precision of the RMS $\left\{\boldsymbol{AI_{(p-1)}}\right\}$ measurement. Absolute accuracy of the RMS $\left\{\boldsymbol{AI_{(p-1)}}\right\}$ voltage measurement is not taken into account, thus $R_{S(p)}$ values are calibrated effective resistances. The relative uncertainty in the $R_{S(p)}$ values is limited to an average of $\pm 0.6\%$ by the accuracy of the 34401A multimeter.

Appendix B

Magnetic Properties of SA-106 Grade B Steel

This appendix presents the measurements that were performed in order to specify the SA-106 Grade B *MagNet* material used in the finite element models in Chapter 5.

Note that the ASME specifications allow for some flexibility in the chemical composition of SA-106 Grade B steel [17]. When CANDU® feeders are ordered, they are tracked through the manufacturing process and have more specific chemistry than the ASME specification requires. The SA-106 Grade B pipe used for these measurements was not provided by AECL, but was purchased from Russell Metals in Kingston, and may not have the exact composition of feeder steel. The magnetic properties of other SA-106 Grade B steel samples may therefore vary from those presented here.

B.1 Theory

In order to make an accurate measure of the magnetic hysteresis of a material, both the auxiliary field ($\vec{H}$) and the flux density ($\vec{B}$) must be known.

When a ferrogmanetic core is wound with an excitation coil, the $\vec{H}$ field generated by the current through the windings produces a force local to the windings on the core domain structure. The domain structure within this local $\vec{H}$ field then magnetises, which then diffuses through the rest of the domain structure, generating free poles at the surfaces of the core. As free poles develop at the core surface, so does $\vec{H}_d$ to ensure continuity. The total $\vec{H}$ field consists of both the field introduced by the excitation current in addition to $\vec{H}_d$.

The only geometry for which $\vec{H}_d$ is negligible is a toroid, since in this geometry the $\vec{H}$ field is always tangential to the surface, and $\vec{J}$ outside the toroid is zero. In the limit that there are no domains with components normal to the surface of the sample $\vec{H}_d = 0$. In this circumstance, $\vec{H}$ may be accurately calculated using only equation (2.31), or approximated using equation (2.34). Note that since the path length on the inner surface of the toroid is shorter than the path length on the outer surface, there is a gradient of $\vec{H}$ as a function of radius.

The most appropriate way to measure $\vec{B}$ within a material is to measure the open circuit voltage on an encircling coil, and find $\bar{B}$ by integrating. This measurement requires that $\mathrm{d}\vec{B}/\mathrm{d}t \neq 0$ however, which means that in a material with a non-zero conductivity (σ_e), eddy currents will form and decrease the measured permeability. Some means must therefore be taken to compensate for the eddy currents.

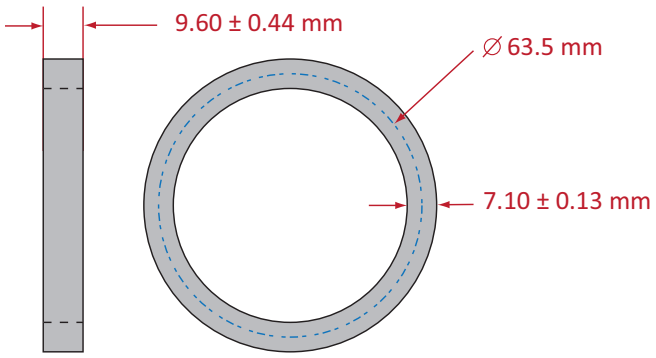

Figure B.1: Scale drawing of the SA-106 Grade B sample used.

B.2 Toroid Specifications

A toroid was formed by cutting a nominal 63.5 mm SA-106 Grade B Schedule 80 pipe normal to the axial direction, to produce a ring, illustrated in Figure B.1. Eight measurements of each the depth and wall thickness were taken evenly spaced around the diameter of the toroid, with the mean and standard deviation indicated.

An excitation coil was wound by hand, consisting of two layers of AWG 30 wire with a total of 1100 ± 50 turns. The second layer of the excitation coil was wound 'back' on the first layer (i.e., with opposite helical pitch) in order to minimize any component of current parallel to the hoop direction, and such that the excitation current entered and left the coil at the same point. An effort was made to wind the coil evenly around the entire diameter of the toroid, so as to minimize measurement delays due to magnetic diffusion processes. The excitation coil has a resistance of $11.1 \pm 0.1\,\Omega$.

A sensing coil was wound by hand on top of the excitation coil, consisting of 200 ± 10 turns. Similar to the excitation coil, the sensing coil was wound back on itself, but only occupies approximately $\pi/3$ along the diameter. The sensing coil has resistance of $3.16 \pm 0.03\,\Omega$.

Both coils were connected to instrumentation via AWG 24 twisted pairs and pin headers rated for a maximum current of 3 A.

B.3 Measurements and Analysis

Measurements were performed using an early version of the flux control system using an open loop amplifier with DC current correction. In order to ensure the impedance associated with eddy currents in the material was constant for any given hysteresis loop, triangular flux waveforms were used (as in Figure 11.2a), with flux rates from 0.5 T/s to 10 T/s.

Figure B.2 shows magnetic hysteresis loops with a peak flux densities (B_{pk}) of 1 T for flux rates of 2 T/s, 5 T/s and 10 T/s. The effect of eddy currents can be seen as the increase in coercivity, decrease in permeability, and increased hysteresis loop area with increasing flux rate

The procedure for estimating a magnetisation curve is shown in Figure B.3. With a fixed $\mathrm{d}B/\mathrm{d}t$, B_{pk} is swept. For each hysteresis loop the peak flux density B_{pk} and peak auxiliary field (H_{pk}) are recorded, forming the initial magnetisation curve. The permeability is then calculated for any point on the magnetisation curve as $\mu_r\mu_0 = B_{pk}/H_{pk}$.

Figure B.4 shows the data collected in order to estimate the DC permeability of the material. $\bar{B}_{pk}$ was varied from 0.100 T to 1.5 T. At each value of B_{pk}, $\mathrm{d}B/\mathrm{d}t$ was varied from 0.5 T/s to 10 T/s in 0.5 T/s steps. 16 hysteresis loops at each combination of B_{pk} and $\mathrm{d}B/\mathrm{d}t$ were stored when DC currents were below 5 mA. The average peak auxiliary field (H_{pk}) was estimated for each set of loops. H_{pk} values for a flux rate of 0 T/s were then calculated as the y-intercept of a cubic polynomial fit to each series

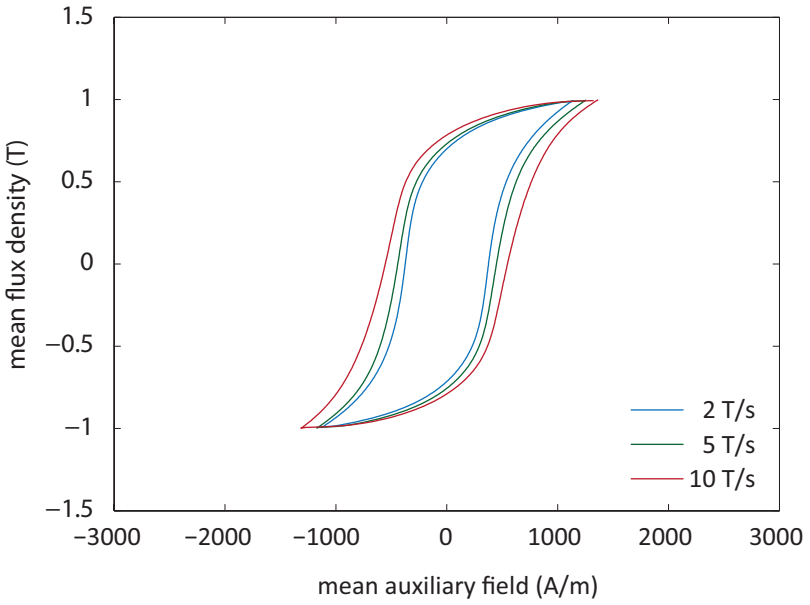

Figure B.2: Magnetic hysteresis loops for the SA-106 grade B toroid with peak mean flux densities of 1 T and flux rates of 2 T/s, 5 T/s, and 10 T/s.

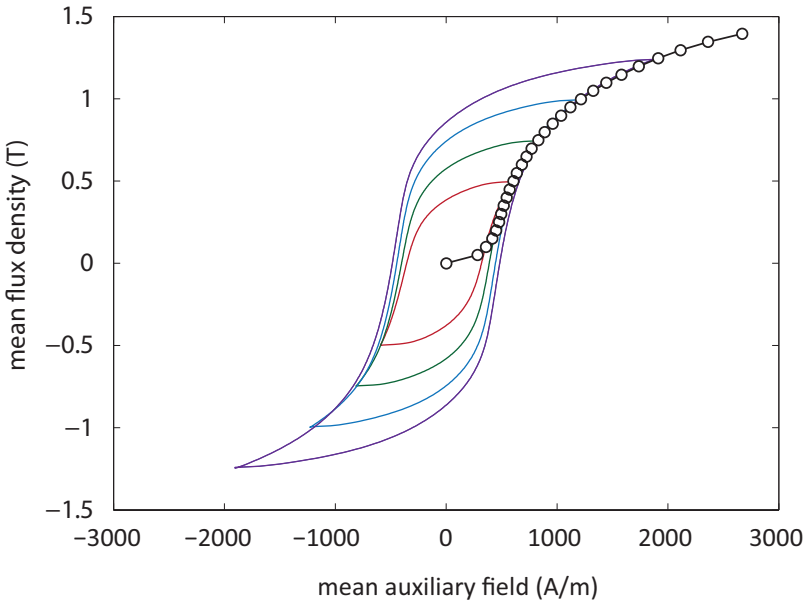

Figure B.3: Magnetic hysteresis loops and the magnetisation curve for the SA-106 grade B toroid with a flux rate of 5 T/s.

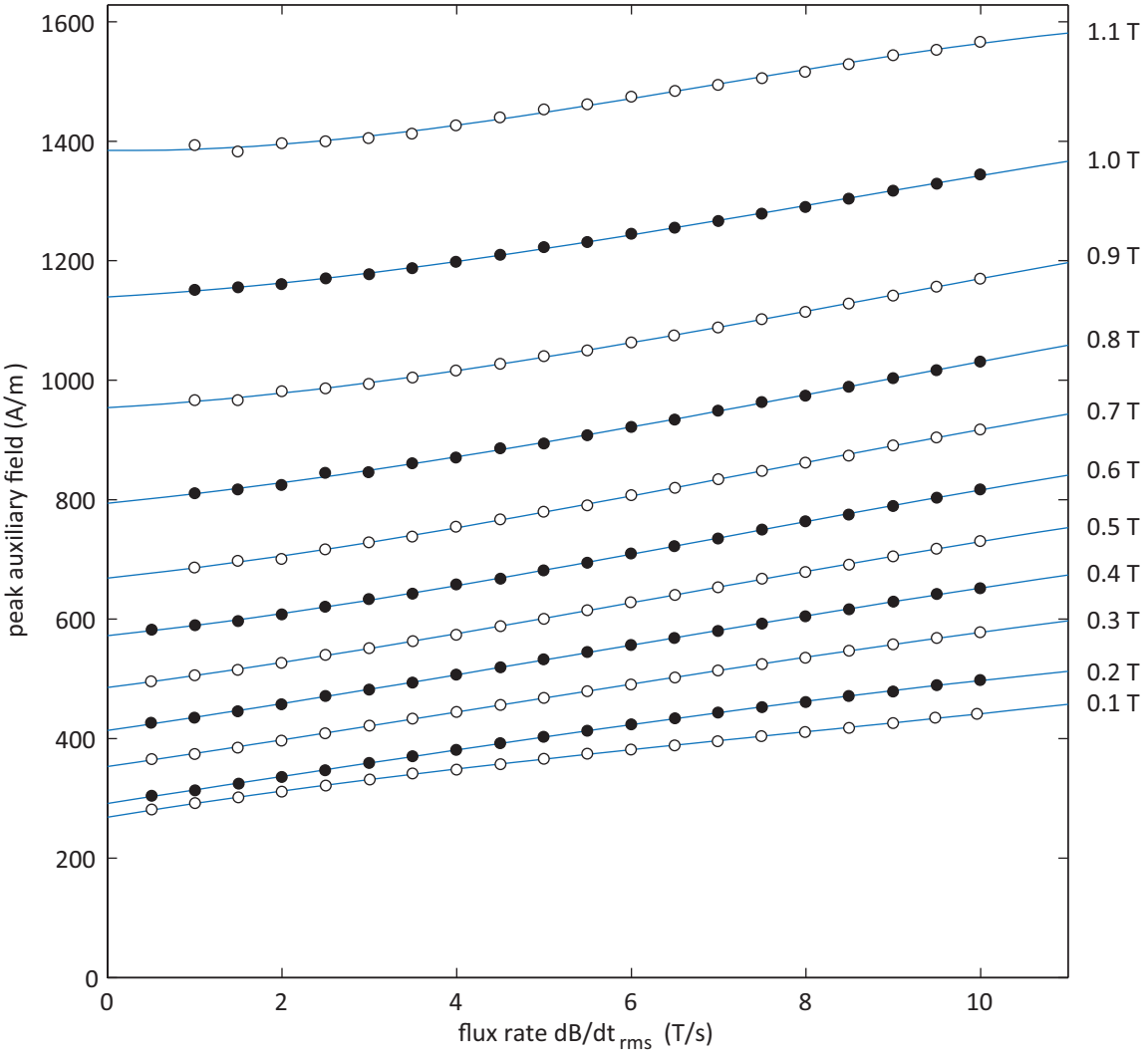

Figure B.4: Peak auxiliary field values as a function of the rms flux rate, for peak flux densities ranging from $0.1 - 1.1\,\mathrm{T}$. For each flux value, data are fit with a cubic polynomial in order to estimate the $0\,\mathrm{T/s}$ intercept.

of H_{pk} vs. $\mathrm{d}B/\mathrm{d}t_{rms}$ with a common B_{pk}. The estimated H_{pk} values for $0\,\mathrm{T/s}$ were then used with the B_{pk} to calculate the DC permeability.

Figure B.5 shows the permeability as a function of auxiliary field for a variety of flux rates and the estimated DC permeability curve. Error bars due to statistical

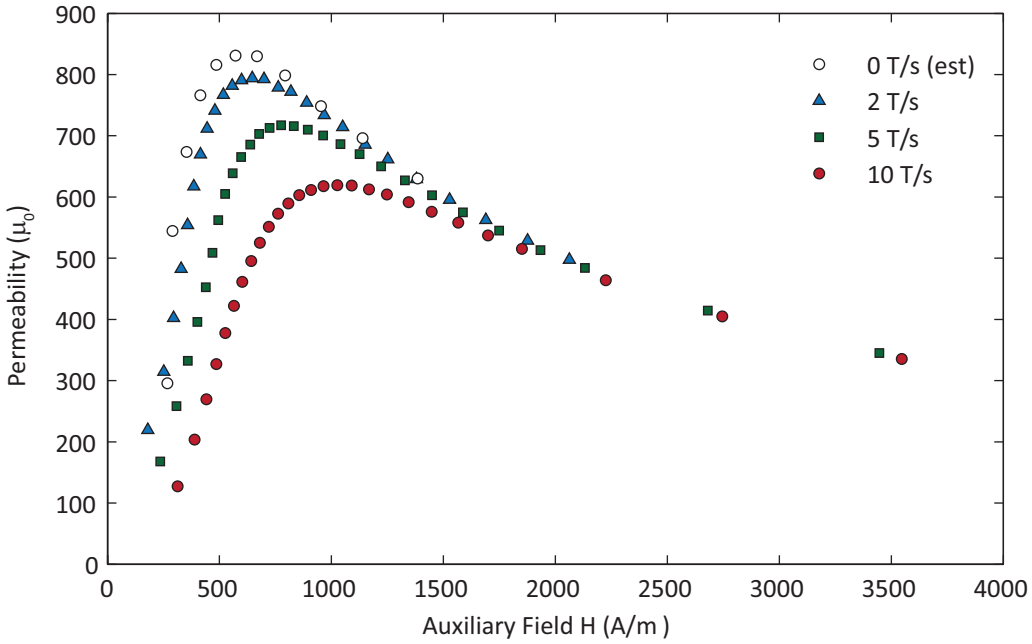

Figure B.5: Permeability as a function of the auxiliary field for flux rates of 2 T/s, 5 T/s and 10 T/s, and the estimated DC (0 T/s) permeability.

variation are too small to be indicated on the figure, however systematic uncertainties in the number of turns place the uncertainty on the estimated permeabilites at approximately 7%. The maximum DC permeability estimated from this data is $830 \pm 60\,\mu_0$.

Appendix C

Tetrapole FEM Details

This appendix presents details for the tetrapole *Infolytica MagNet*® finite element models (FEMs) used to inform the SL4P design in Section 5.1.

C.1 FEM Materials

Three user-defined *MagNet*® materials were used in the CB-P, UC-P, and UC-F models. These are SA-106 grade B steel, R Ferrite, and 0.1 mm thick laminated Supermendur. The relevant *MagNet*® parameters for all three materials are found in Table C.1, with the B-H data for SA-106 Grade B and ferrite in Tables C.2 and C.3 respectively.

Samples were modelled as SA-106 grade B steel in order to approximate the response of feeder steel. The SA-106 grade B specification does not include the magnetic properties of the pipe [17], thus the bulk magnetic properties of a SA-106 grade B pipe were estimated experimentally, and are presented Appendix B. An electrical conductivity value of $5.15 \times 10^6\,(\Omega \cdot \mathrm{m})^{-1}$ was measured and supplied by AECL [43].

Table C.1: User-defined *MagNet* materials

Property	SA-106 grade B	R Ferrite	Supermendur
Conductivity (S/m)	5.15×10^6	0.167	0
Loss at 60 Hz (W/kg)	No	No	$0.490 \cdot B^{1.356}$
Relative Permittivity	1	1	1
Mass Density (kg/m^3)	7880	4800	8120
B-H Curve	Table C.2	Table C.3	Hyperco 50

Table C.2: *MagNet* SA-106 Grade B B-H Curve and differential permeability

H (A/m)	B (T)	μ_d
0	0	-
26.58	0.1995	3620.1
83	0.299	1773.4
211.74	0.4981	1190.9
297.23	0.5981	1152.4
341.8	0.6976	901.0
519.3	0.7973	569.7
676.8	0.8972	468.9
861.9	0.997	415.8
1097.8	1.0965	306.8
1478	1.1976	233.0
1862	1.3	190.4
2410	1.4	142.5
3177	1.5	78.5
6671	1.75	-

Table C.3: *MagNet* R Ferrite B-H Curve

(H A/m)	B (T)
0	0
15.4	0.1
27.825	0.2
52.47	0.3
103.35	0.4
182.85	0.44
1176.6	0.5

Ferrites are a family of low conductivity ceramics with saturation flux densities of $\sim 0.5\,\mathrm{T}$. For small-scale production, ferrites can be shaped using precision grinding methods. The geometrical complexity of the common-backing (CB) core design required that the core material be readily machined, therefore ferrite was used in the CB-P model. The particular ferrite used to generate the user-defined *MagNet* material was 'R power ferrite,' as this was the material used in prototype CB tetrapole cores that were machined by *Hi-Tec Magnetics*.

'Supermendur' is the discontinued product name from *Carpenter Technologies* for a 49% Co - 49% Fe - 2% V alloy, and is similar in composition to their current *Hyperco® 50* product [71, 72]. Of all ferromagnetic alloys, Co-Fe combinations have the highest saturation flux density at 2.4 T. Supermendur is therefore used in applications where the maximum inductance per unit weight and volume is required. Supermendur is a good conductor with $\sigma_e = 3.85 \times 10^7\,(\Omega \cdot \mathrm{m})^{-1}$. To minimize eddy currents, the alloy is rolled to thicknesses of 0.1 mm, slit into strips, coated in an electrical insulator, and wound around a frame of the desired geometry. Cores are then annealed, epoxy-impregnated, and cut to to the desired dimension [73].

Supermendur was used for the tetrapole cores in the OUC-P and OUC-F models to take advantage of its high saturation flux. Supermendur also has a high residual flux density at 2.0 T, which yields a rectangular hysteresis loop. Rather than attempt to experimentally determine the B-H curve for Supermendur, the B-H curve from the pre-defined Hyperco 50 0.006″ *MagNet®* material was used.

Eddy currents in laminated materials are not usually modelled in *MagNet®*. Instead, the manufacturer's specified loss curves are entered, and the user-material has $\sigma_e = 0\,(\Omega \cdot \mathrm{m})^{-1}$. A loss curve for 0.1 mm thick Supermendur at 60 Hz was estimated

from [71], and entered into *MagNet*, see Table C.1.

C.2 CB-P Model

CB-P model dimensions are provided in Figure C.1. Coil voltages and currents from the model solutions shown in Figure 5.2 are provided in Tables C.4 and C.5.

C.3 OUC-P Model

OUC-P model dimensions are provided in Figure C.2. Coil voltages and currents for the model solutions in Figures 5.4 and 5.6 are provided in Tables C.6 and C.7, respectively.

C.4 OUC-F Model

OUC-F model dimensions are provided in Figure C.2. Coil voltages and currents for the model solutions in Figure 5.11 are provided in Table C.8.

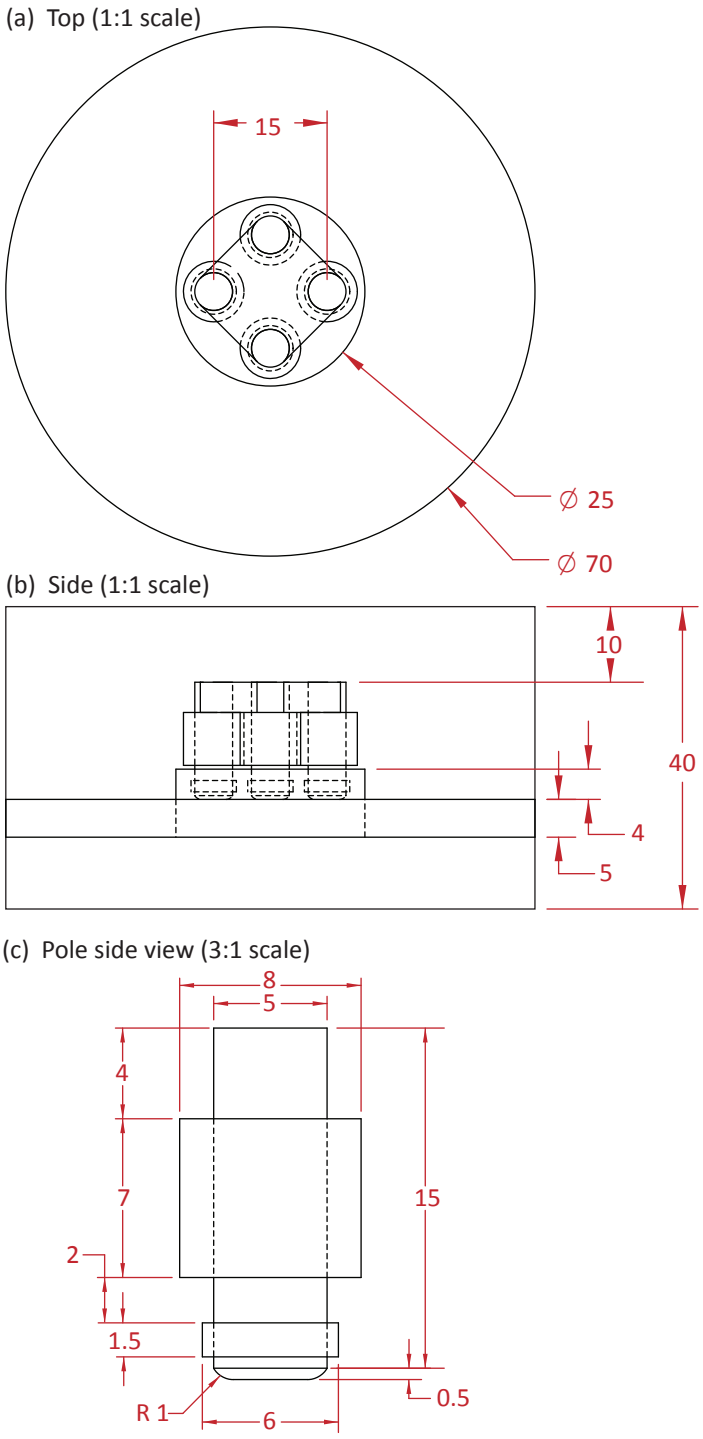

Figure C.1: CB-P model dimensions. (a) Top view, (b) Side view, and (c) pole side view. Units are in mm.

Table C.4: CB-P coil currents and voltagess corresponding to Figures 5.2a, 5.2b, and 5.2c.

	Current		Voltage	
Coil	Magnitude (mA_{rms})	Phase (°)	Magnitude (mV_{rms})	Phase (°)
(a) All poles 0 mm lift-off.				
ex1	8.56	-64.0	250.0	0.0
ex2	0.03	-83.5	0.0	-38.4
ex3	8.51	-64.0	250.0	0.0
ex4	0.03	-84.2	0.0	-38.4
F1	0	-90	39.4	-174.8
F2	0	-90	0.0	102.2
F3	0	-90	39.4	-174.8
F4	0	-90	0.0	-78.5
(b) Poles 1,3,4 with 0 mm lift-off, pole 2 with 0.1 mm lift-off.				
ex1	8.57	-63.9	250.0	0.0
ex2	0.02	-44.5	0.0	156.5
ex3	8.53	-64.0	250.0	0.0
ex4	0.03	-84.2	0.0	-74.2
F1	0	-90	39.3	-174.8
F2	0	-90	0.0	140.9
F3	0	-90	39.4	-174.8
F4	0	-90	0.0	-90.3
(c) Poles 1,2,4 with 0 mm lift-off, pole 3 with 0.1 mm lift-off.				
ex1	7.89	-137.2	225.0	0.0
ex2	9.62	-11.72	0.0	-32.0
ex3	135.52	-80.8	540.0	-45.0
ex4	9.62	-11.74	0.0	-24.9
F1	0	-90	39.8	-176.4
F2	0	-90	3.7	164.9
F3	0	-90	39.3	-175.8
F4	0	-90	3.7	-15.1

Table C.5: CB-P coil currents and voltages corresponding to Figures 5.2d, 5.2e, and 5.2f.

	Current		Voltage	
Coil	Magnitude (mA_{rms})	Phase (°)	Magnitude (mV_{rms})	Phase (°)
(d) All poles 0.1 mm lift-off.				
ex1	75.07	-50.2	371.0	0.0
ex2	0.02	-24.7	0.0	-138.6
ex3	75.06	-50.3	371.0	0.0
ex4	0.02	-19.9	0.0	-116.8
F1	0	-90	39.4	-142.3
F2	0	-90	0.0	160.4
F3	0	-90	39.5	-142.3
F4	0	-90	0.0	-16.5
(e) Poles 1,3,4 with 0.1 mm lift-off, pole 2 with 0.2 mm lift-off.				
ex1	75.06	-50.2	371.0	0.0
ex2	0.01	-11.7	0.0	118.1
ex3	75.06	-50.2	371.0	0.0
ex4	0.02	-23.2	0.0	-72.0
F1	0	-90	39.4	-142.3
F2	0	-90	0.0	160.4
F3	0	-90	39.5	-142.3
F4	0	-90	0.0	-20.0
(f) Poles 1,2,4 with 0.1 mm lift-off, pole 3 with 0.2 mm lift-off.				
ex1	71.13	-54.0	355.0	0.0
ex2	5.68	23.5	0.0	-16.5
ex3	166.83	-50.0	620.0	-17.0
ex4	5.69	23.4	0.0	-50.8
F1	0	-90	39.7	-142.6
F2	0	-90	1.8	-160.4
F3	0	-90	39.5	-142.3
F4	0	-90	1.8	19.5

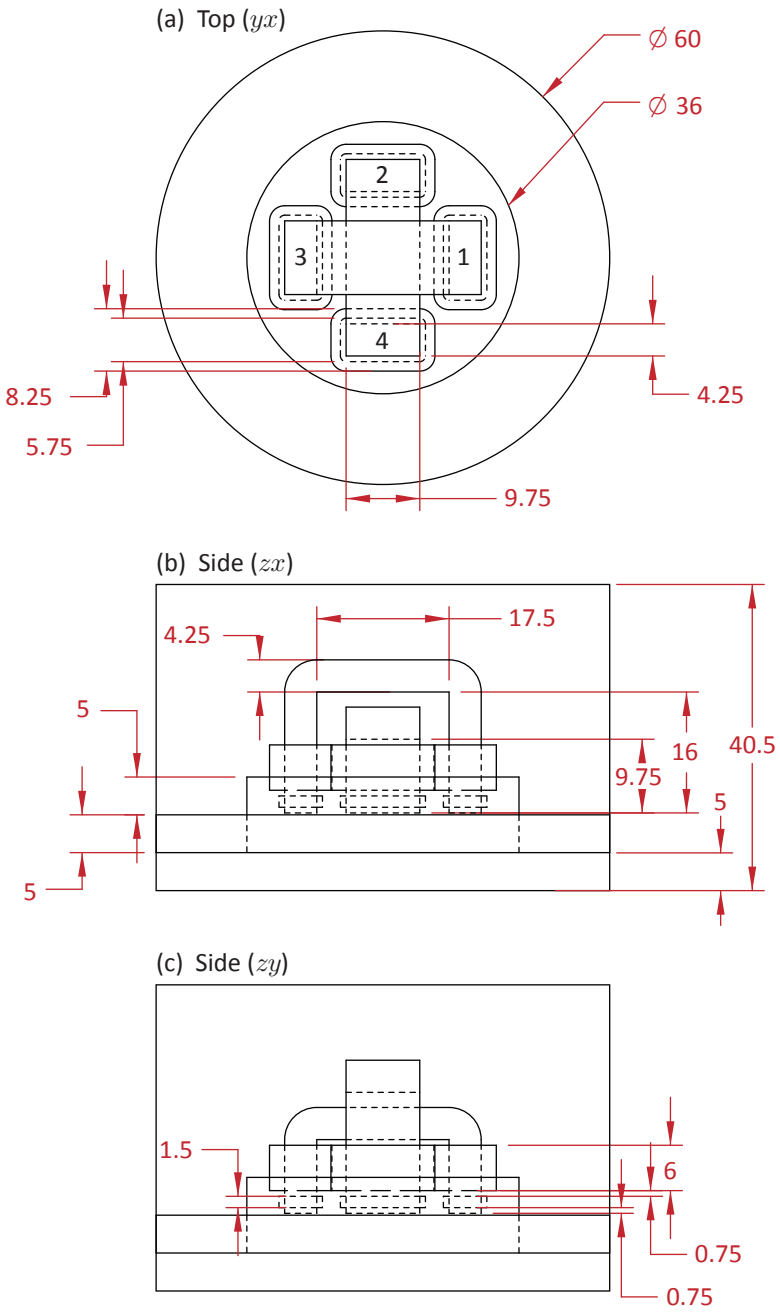

Figure C.2: OUC-P model dimensions at 1:1 scale: (a) Top (xy), (b) side (zx), and (c) side (zy) drawings with dimensions in mm. Pole labels are shown in (a).

Table C.6: OUC-P coil currents and voltages corresponding to Figure 5.4.

	Current		Voltage	
Coil	Magnitude (mA_{rms})	Phase (°)	Magnitude (mV_{rms})	Phase (°)
(a) 10 Hz excitation on poles 1 and 3				
ex1	268	-24.3	5000	0.0
ex2	0	22.8	0	8.7
ex3	268	155.7	5000	180.0
ex4	0	58.2	0	114.6
F1	0	-90	151	64.4
F2	0	-90	0	-140.8
F3	0	-90	151	-115.6
F4	0	-90	0	-121.1
(b) 30 Hz excitation on poles 1 and 3				
ex1	268	-50.7	7500	0.0
ex2	0	-14	0	-68.6
ex3	268	129.3	7500	180.0
ex4	0	-8.9	0	-130.0
F1	0	-90	423	36.7
F2	0	-90	0	169.3
F3	0	-90	423	-143.2
F4	0	-90	0	169.4

Table C.7: OUC-P coil currents and voltages corresponding to Figure 5.6.

	Current		Voltage	
Coil	Magnitude (mA_{rms})	Phase (°)	Magnitude (mV_{rms})	Phase (°)
(b) Driving the Y pole				
ex1	0	72.8	0	159.7
ex2	268	0.0	7511	50.8
ex3	0	69.9	0	18.1
ex4	268	180.0	7504	-129.3
F1	0	-90	0	-105.2
F2	0	-90	424	87.4
F3	0	-90	0	-107.1
F4	0	-90	423	-92.6
(c) Driving the X pole, with the X-pole rotated by 1° about the Y-axis.				
ex1	240	0.0	7136	54.0
ex2	7	-103.1	0	18.9
ex3	570	180.0	11640	-146.8
ex4	7	-103.3	0	-114.5
F1	0	-90	419	88.3
F2	0	-90	6	73.7
F3	0	-90	413	-91.5
F4	0	-90	6	73.4
(d) Driving X and Y poles with a 30.9° superposition field.				
ex1	230	0	6430	50.7
ex2	137	0	3838	50.7
ex3	230	180	6427	-129.3
ex4	137	180	3839	-129.3
F1	0	-90	363	87.4
F2	0	-90	217	87.4
F3	0	-90	362	-92.6
F4	0	-90	217	-92.6

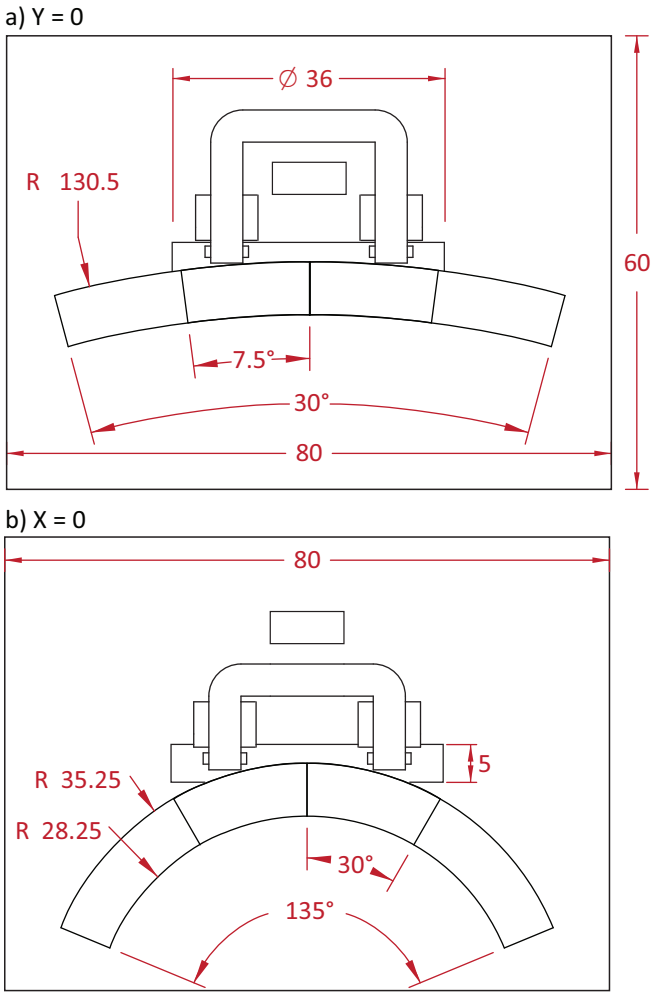

Figure C.3: OUC-F model dimensions at 1:1 scale. (a) looking along the hoop axis and (b) looking along the axial axis, with dimensions in mm. OUC tetrapole dimensions are the same as in Figure C.2.

Table C.8: OUC-F coil currents and voltages corresponding to Figure 5.11.

	Current		Voltage	
Coil	Magnitude (mA_{rms})	Phase (°)	Magnitude (mV_{rms})	Phase (°)
(a) Driving the X-core: $\theta_F = 0°$				
ex1	220	0.0	6245	51.8
ex2	0	69.9	0	108.2
ex3	220	180.0	6240	-128.2
ex4	0	74.2	0	118.6
F1	0	-90	360	88.3
F2	0	-90	0	-108.3
F3	0	-90	359	-91.7
F4	0	-90	0	-101.3
(b) Driving the Y-core: $\theta_F = 90°$				
ex1	0	69.8	0	40.9
ex2	360	0.0	8130	40.9
ex3	0	71.3	0	-110.1
ex4	360	180.0	8118	-139.1
F1	0	-90	0	-107.3
F2	0	-90	365	89.2
F3	0	-90	0	-105.0
F4	0	-90	363	-90.8
(c) Driving both cores: $\theta_F = 45°$				
ex1	156	0.0	4428	52.1
ex2	254	0.0	5735	40.9
ex3	156	180.0	4429	-127.9
ex4	256	180.0	5729	-139.1
F1	0	-90	256	88.6
F2	0	-90	257	89.2
F3	0	-90	256	-91.4
F4	0	-90	256	-90.8

Appendix D

SL4P Details

This appendix presents sub-assembly diagrams, in Section D.1, and CAD drawings, in Section D.2, for the spring-loaded tetrapole prototype (SL4P). The final SL4P assembly is presented in Section 5.3 in the main body of the thesis. Two coil formers were designed in order to manufacture the pickup, excitation and feedback coils of the SL4P, which are presented in Section D.3. Figures appear at the end of the appendix.

D.1 SL4P Assembly

The SL4P consists of three main sub-assemblies: the pickup assembly, the short core assembly, and the long core assembly.

The pickup assembly is shown in Figure D.1. A 0.5 mm thick 100 turn pickup coil was wound from AWG 44 PN bond wire (supplied by *MWS Technologies*) using a 1 mm ID coil former. The coil was slid onto the ferrite core. Leads were made from flexible AWG 32 wire, which were fed through the brass shield. The ferrite sheath was slid over the AWG 32 leads, which were then stripped and soldered to the AWG

44 coil ends. The core and coil were then slid into the ferrite sheath and fixed in place with epoxy after it was verified that coil leads were not shorted to either the brass shield or to each other. Once dry, the shield-sheath-core-coil assembly was slid into the pickup housing.

The short core assembly is shown in Figure D.2. The AWG 32 leads from the pickup assembly were first slid through a hole located in bottom of the frame. The short core was then placed into the frame. The AWG 32 leads were then pushed into the trough in the frame beside the short core, and the four 2-56×0.125″ screws and washers were fastened to hold the short pole and pickup leads in place. Coloured vinyl tape was affixed to the poles to improve the excitation field uniformity, as was modelled in Chapter 5. The four guide screws* were then pushed into the frame, and four 0.12″ × 0.25″ compression springs with a wire diameter of 0.016″ (*Gardner Spring* part 36000G) were slid over the guides.

The long core assembly is shown in Figure D.3. Coloured vinyl tape was affixed to poles of the long core. The long core was placed into the housing, and held in place by the steel plate and two 2-56×0.25″ screws. The electromagnet pin header (*Tyco Electronics* part 4-102973-0-08) was affixed to a pad-per-hole perforated prototype board using super glue, and was placed into the long-pole housing. The pickup pin receptacle (*Tyco Electronics* part 87499-3) was then epoxied to the housing.

An exploded view of the final SL4P assembly is shown in Figure D.4. A compression spring (*Gardner Spring* part 36000G) was placed in the bottom of the short core assembly. The pickup assembly was then fastened to the short core assembly using the four 1-72×0.25″ screws, which spring-loads the shield (and hence the pickup

*The guide screws are 2-56×0.5″ brass screws with threads removed from 7.5 mm along the length.

coil). The short core assembly was then fastened to the housing, which spring-loads the short core assembly. The AWG 32 pickup coil leads were then fed out the left of the housing in Figure D.4, stripped, crimped to connector sockets (*Tyco Electronics* part 102128-1) and snapped into the pickup pin receptacle.

Four 500 turn rectangular excitation coils and four 50 turn rectangular feedback coils were wound using AWG 36 PN bond wire (supplied by *MWS Technologies*) and the rectangular coil former described in Appendix D. Excitation and feedback coils were slid onto the four poles of the long and short cores. Excitation and feedback coil leads were then tinned and soldered to the electromagnet pin header according to the pinout diagram in Figure D.5. Connections were tested, and the excitation and feedback coils were then affixed to the vinyl tape on the poles using rubber cement. The backing plate was then fastened to the housing using the four 2-56×0.25″ screws to protect the electromagnet wiring.

D.2 Custom Parts

Several custom parts were ordered and machined for the SL4P. These include the cores (Figure D.6), pickup shield (Figure D.7), pickup housing (Figure D.8), short core frame (Figure D.9), long core housing (Figure D.10), and the bottom plate (D.11).

The Supermendur U-cores for the SL4P were ordered simultaneously from two companies: *MK Magnetics* and *Magnetic Metals*. Dimensions for the two orders are shown in Figure D.6. At the time of ordering the design for the SL4P was in flux, thus the orders have slightly different dimensions. Note that the tolerances in Figure D.6a are representative of the tolerances for both companies, and are poor compared

to what can be obtained via machining. These tolerances arise from the tape-wound cut-core manufacturing process, and were compensated for when machining the short core frame and the long core housing, shown in Figures D.9 and D.10, respectively.

As is shown in Figure D.6a, the cores were ordered to be cut off-center in order to produce both the long core and short core from a single tape winding. While this was an option from both manufacturers, it was an atypical request, and several erroneously cut cores were received. If such cores are purchased in the future, it is recommended contact with customer service be established to emphasize the cutting requirements.

Note that the pickup shield (Figure D.7), pickup housing (Figure D.8), and short core frame (Figure D.9) are machined from brass. Of these, the conductive properties of the pickup housing and short core frame are unimportant. The author made attempts to machine these parts from Delrin and aluminum, but could not achieve the required rigidity or tolerances with these materials, respectively. Brass was found easier to machine than aluminum, and was therefore used. Brass was also selected for the pickup shield for its ease to machine. However, since the shield attenuates high frequency fields from entering the pickup coil and higher electrical conductivity provides stronger attenuation, aluminum, gold, copper, or silver would be better suited for the pickup shield material than brass.

D.3 Coil Formers

In order to manufacture the SL4P coils, a 1 mm inside diameter pickup coil former and a rectangular excitation and feedback coil former, shown in Figures D.12 and D.13, respectively, were designed. The formers were used with AWG 44 and AWG

36 PN bond wire, which has a self-adhesive coating that dissolves in methyl hydrate. The wire was wound around the steel cores while being whet with methyl hydrate, then dried and removed to form free-standing coils.

While a 1 mm drill blank was used for the pickup coil former, the stainless steel core for the rectangular former was custom machined. In order to remove coils from the rectangular former without damaging them, the core was polished to a mirror finish with 1200 grit sandpaper, and the corners were rounded.

D.4 Feedback Coil Matching ($\mathcal{M}_p$)

The SL4P feedback coils each consist of 50 turns of AWG 36 wire. To produce the desired excitation field using superposition, precise relative matching of the four feedback coils is required. The transfer function of the coils to a flux change may vary due to a number of phenomena including: feedback coil resistor matching, inductive and capacitive coupling of the leads, and misalignment between the core and coil axes. It is assumed in the software implementation that the combination of these phenomena has a linear scaling effect on the feedback coil sensitivity at all frequencies of interest, and may be compensated for by using the matching parameter $\mathcal{M}_p$.

Values for $\mathcal{M}_p$ were determined by matching the flux through the SL4P feedback coils with an external reference coil. A 56 turn reference coil was wound around one pole of an erroneously cut Supermendur core from *Magnetic Metals* (see drawings in Appendix D). The core was then placed to complete the circuit for each pole as shown in Figure D.14, with the reference coil aligned to the pole of interest.

At each pole position the FCS was run in DEC mode with $f_{ex} = 50\,\text{Hz}$, $B_{FT} = 477\,\text{mT}$ and $\theta_T = 45°$ and $a_p = [1, 0, 1, 0]$ for measuring poles 1 and 3, and $a_p =$

Table D.1: SL4P feedback coil matching parameters ($\mathcal{M}_p$) and performance for various target flux density (B_{FT}) values at $f_{ex} = 50\,\text{Hz}$.

	B_{FT}	239 mT	477 mT	954 mT	1430 mT	1910 T
Pole p	$\mathcal{M}_p$	$V_{rms(p)}$(mV)				
1	1.0257	46.43	93.43	188.1	281.4	373.6
2	0.9852	46.45	93.31	188.0	279.9	373.3
3	1.0123	46.39	93.09	188.1	281.6	373.4
4	0.9830	46.42	93.02	187.6	280.3	373.0
$100 \cdot \frac{\text{max}-\text{min}}{\text{mean}}$ (%)	3.76	0.13	0.44	0.27	0.61	0.16

$[0, 1, 0, 1]$ for measuring poles 2 and 4. $G_{\Phi(p)}$ and $G_{F(p)}$ were optimized for best performance at 50 Hz, and $\mathcal{M}_p$ was set to 1 for all channels. The RMS voltage across the reference coil ($V_{rms(p)}$) was measured using a *Tektronix*® TDS 3014 oscilloscope and its 'Cycle RMS' function, averaged over 512 cycles. $\mathcal{M}_p$ was then calculated as:

$$\mathcal{M}_p = \frac{\frac{1}{4}\sum_{p=1}^{4} V_{rms(p)}}{V_{rms(p)}}. \tag{D.1}$$

The resulting $\mathcal{M}_p$ values were then input into the FCS control software, and the procedure was repeated with $B_{FT} = (239, 477, 954, 1430, 1910)$ mT to check the performance of the matching corrections. Table D.1 shows the $\mathcal{M}_p$ values used and the resulting $V_{rms(p)}$ values for the various B_{FT}. The last row in Table D.1 shows the difference between the maximum and minimum values in the column above it, divided by the mean value and scaled to a percentage.

Table D.1 shows that $\mathcal{M}_p$ values vary by 3.76% or $\pm 2\%$, which including matching differences between the feedback resistors (R_{F1} and R_{F2}) as well as varition from the feedback coil manufacturing and mounting process. Note that the mean of the 4 $\mathcal{M}_p$ values was normalized to 1. If it is assumed that the mean sensitivity of the

feedback coils is accurate, the ±2% matching error is representative of the systematic uncertainty of the feedback coil sensivitity. The variation of $V_{rms(p)}$ for the different flux levels suggests that the feedback coils were relatively matched to within ±0.3%. Flux rates calculated from feedback coil voltages are therefore specified to have a systematic uncertainty of ±2% and a relative uncertainty of ±0.3%.

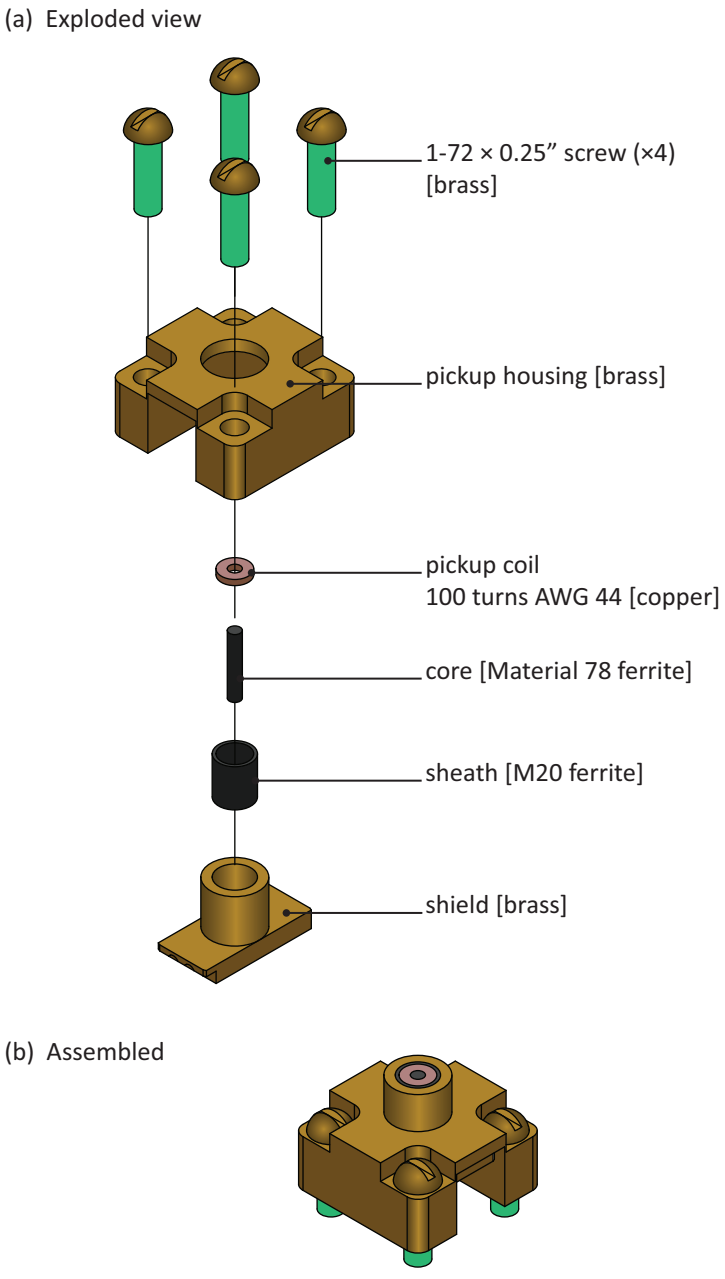

Figure D.1: Pickup assembly (a) exploded view, and (b) fully assembled. Component materials are identified in square brackets. 2:1 scale.

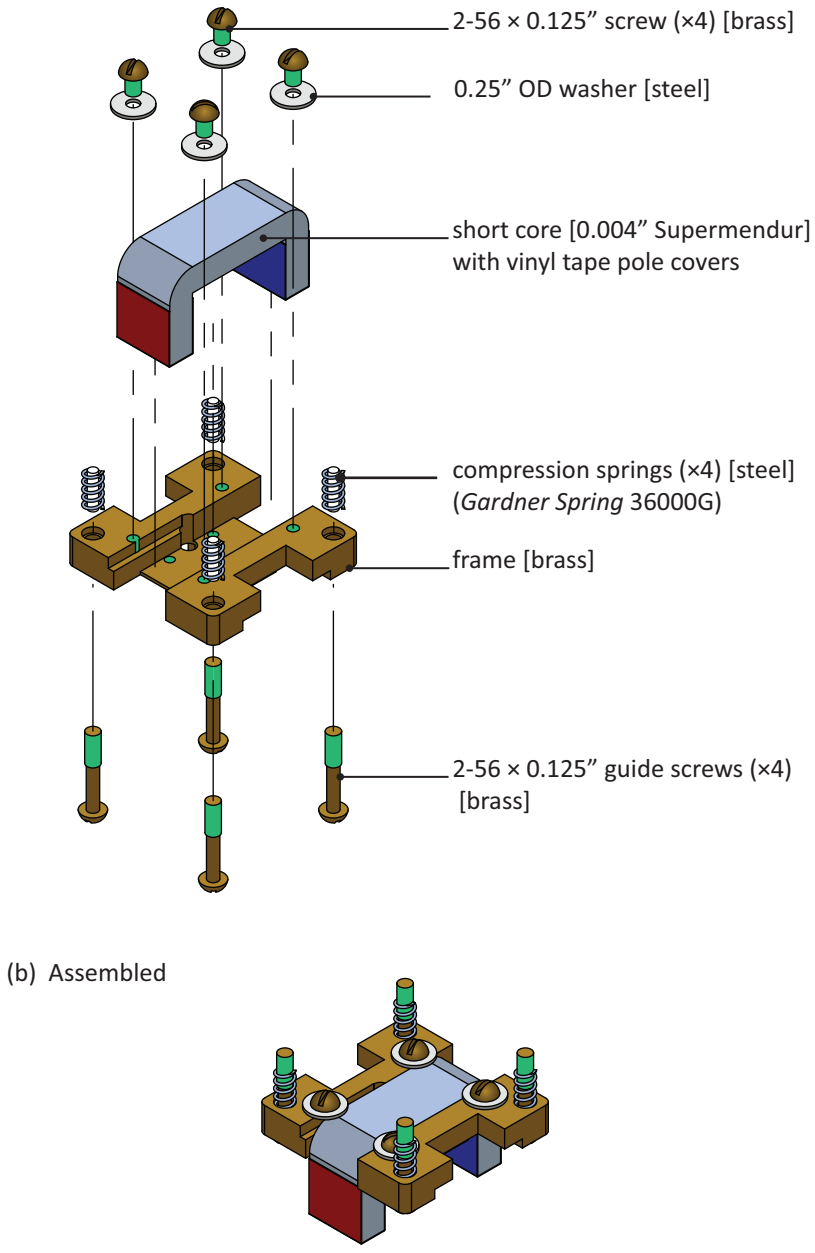

Figure D.2: Short core assembly (a) exploded view, and (b) fully assembled. Component materials are identified in square brackets. 1:1 scale.

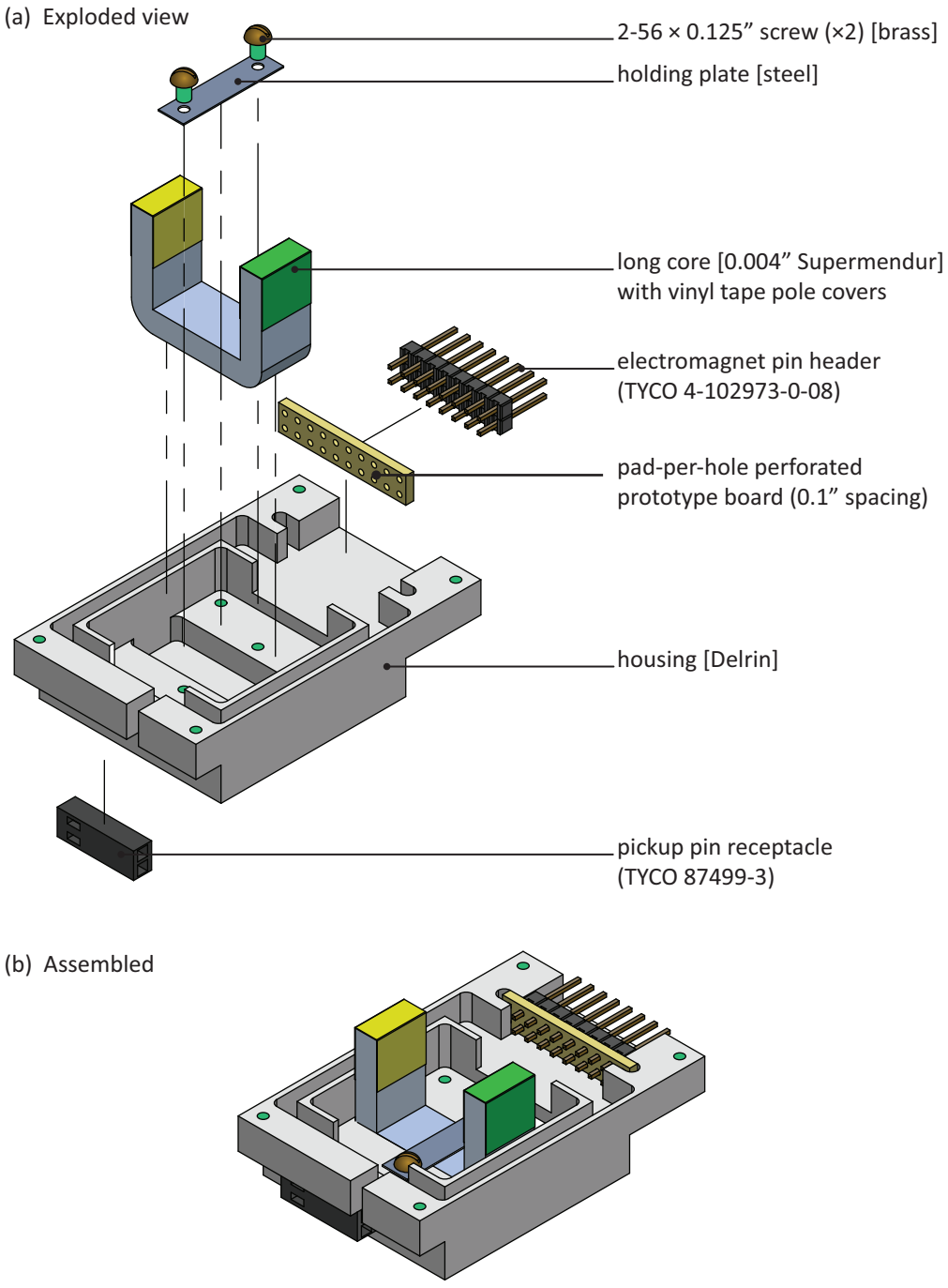

Figure D.3: Long core assembly (a) exploded view, and (b) fully assembled. Component materials are identified in square brackets. 1:1 scale.

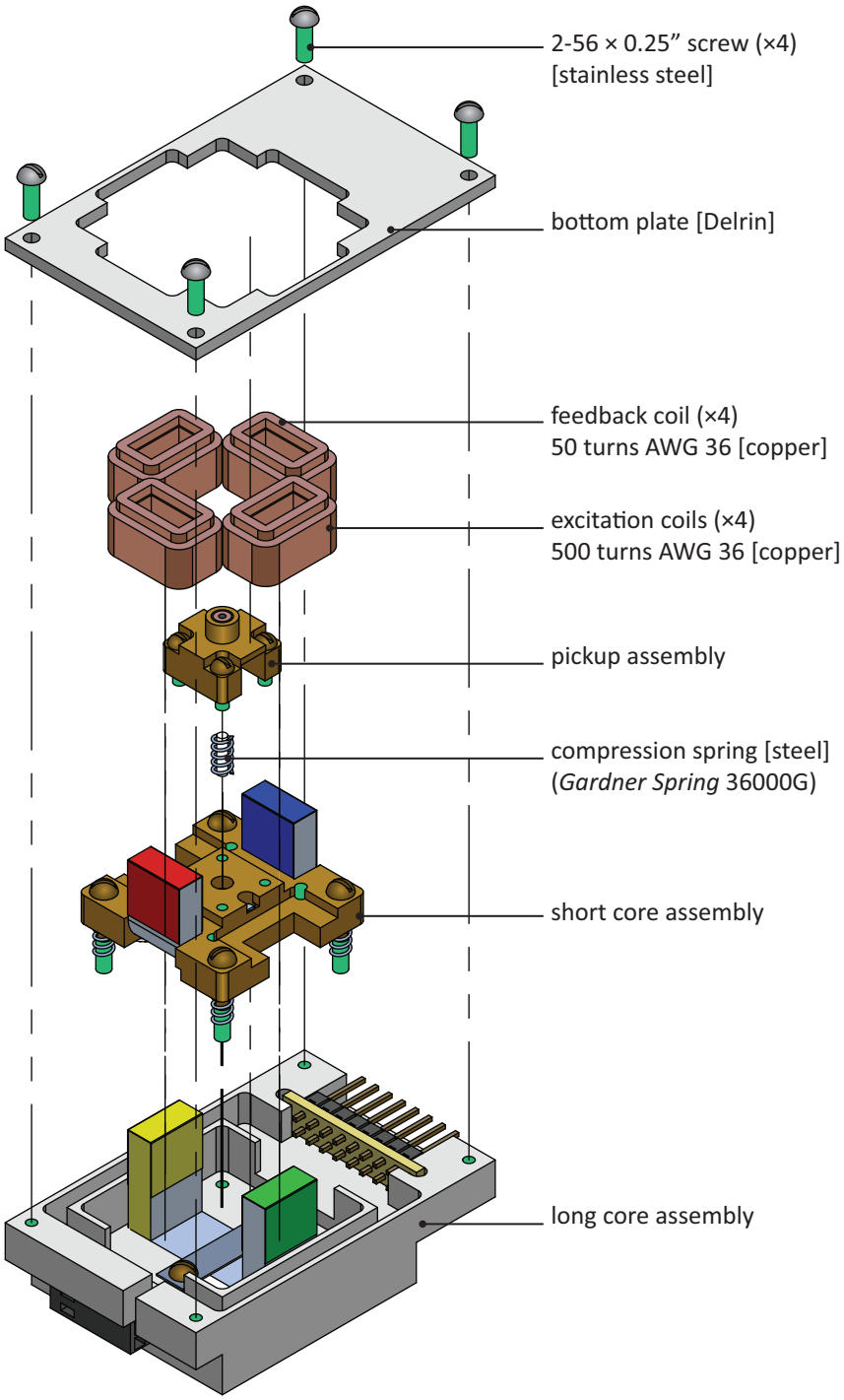

Figure D.4: Exploded view of the SL4P assembly. Component materials are identified in square brackets. 1:1 scale.

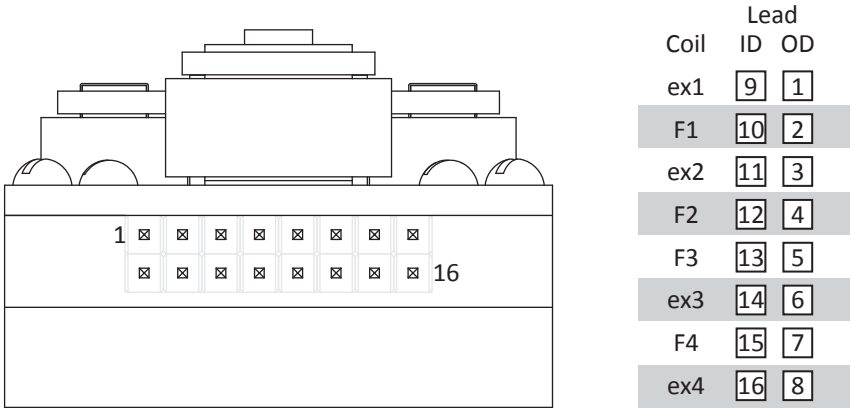

Figure D.5: SL4P electromagnet pinout diagram. Each coil has an inner lead (ID) and an outer lead (OD) that are connected to the electromagnet pin header.

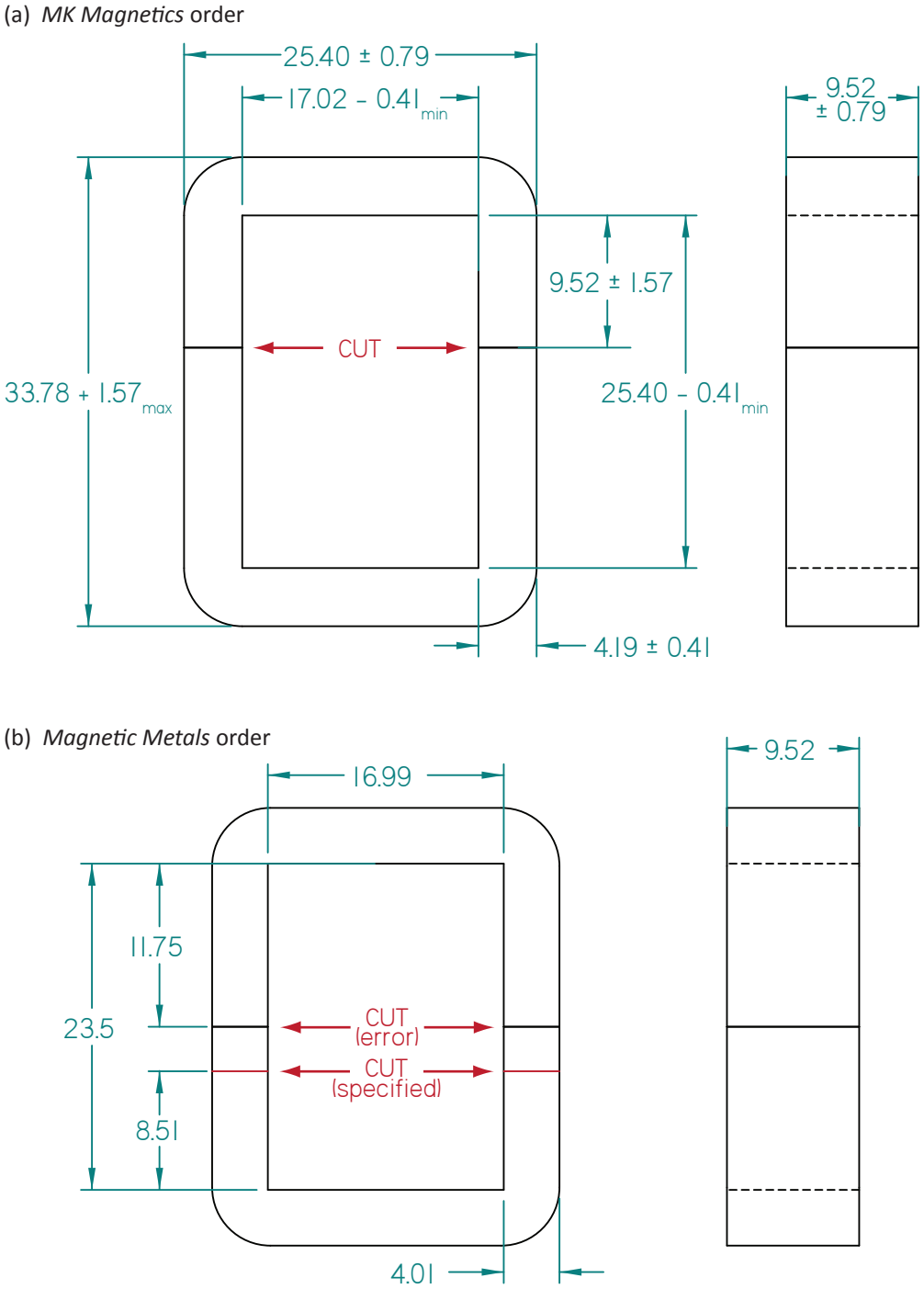

Figure D.6: U-core order dimensions (mm). (a) MK Magnetics order with tolerances. (b) Magnetic Metals order, with specified and erroneous cuts. Material: 0.004" laminated Supermendur. 2:1 scale. ±0.79 mm tolerance on side view in (a) is the maximum tilt.

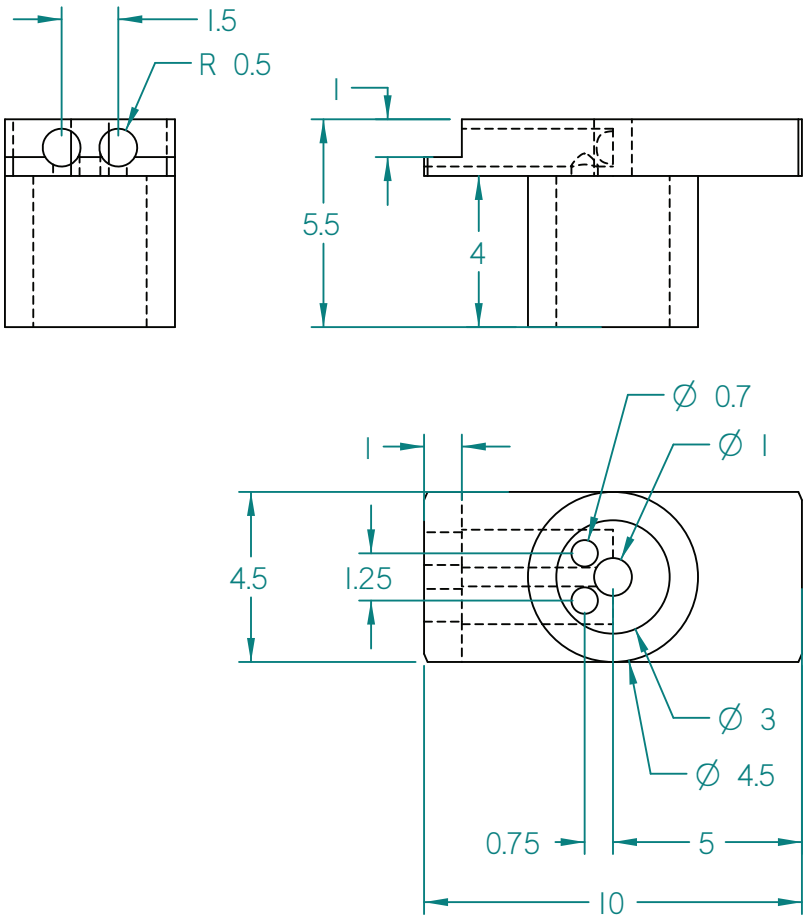

Figure D.7: Pickup shield dimensions (mm). Material: Brass. 5:1 scale.

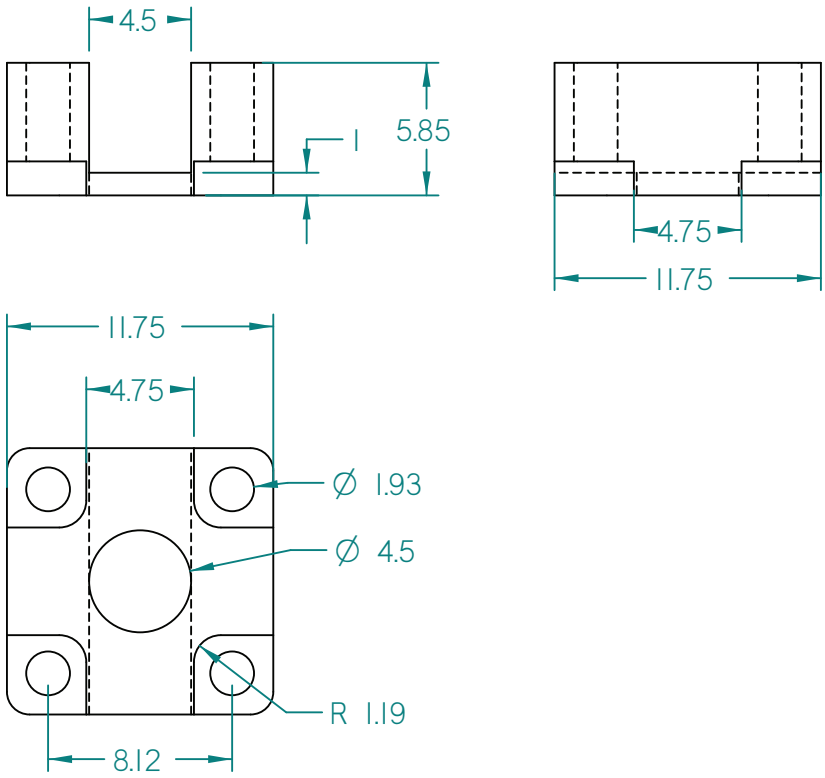

Figure D.8: Pickup housing dimensions (mm). Material: Brass. 3:1 scale.

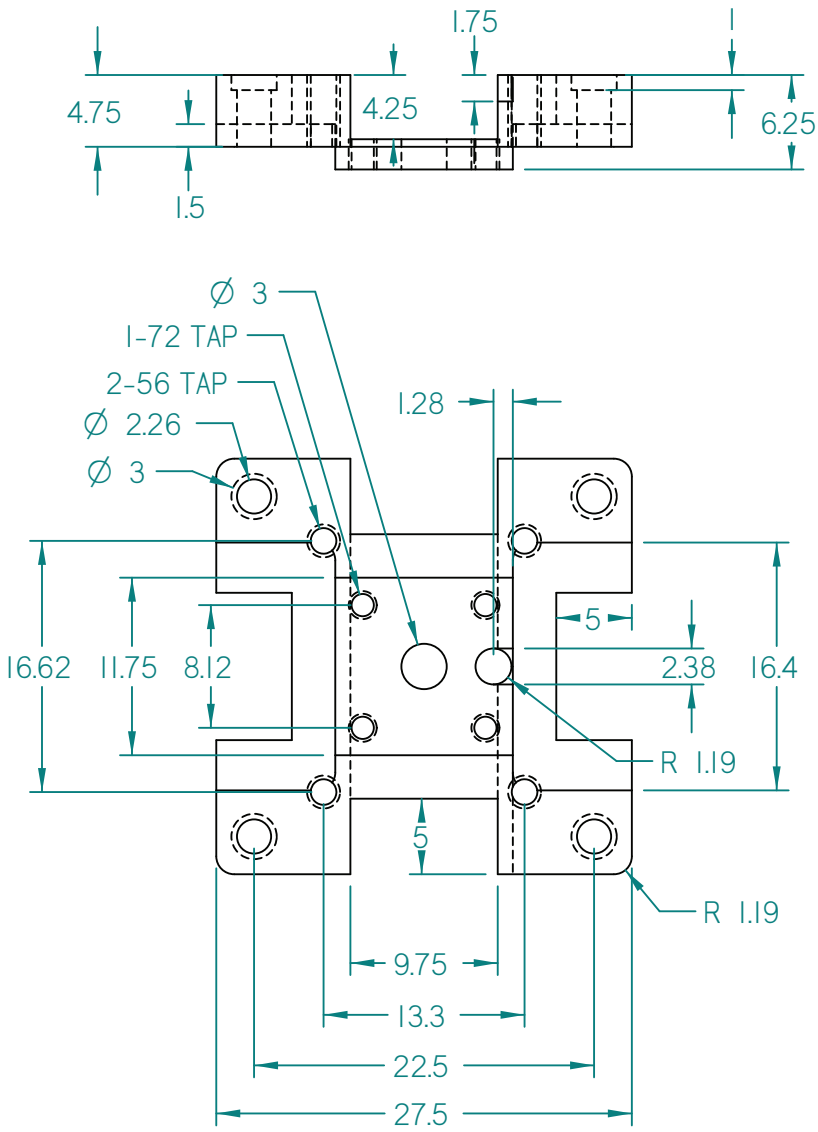

Figure D.9: Short core frame dimensions (mm). Material: Brass. 2:1 scale.

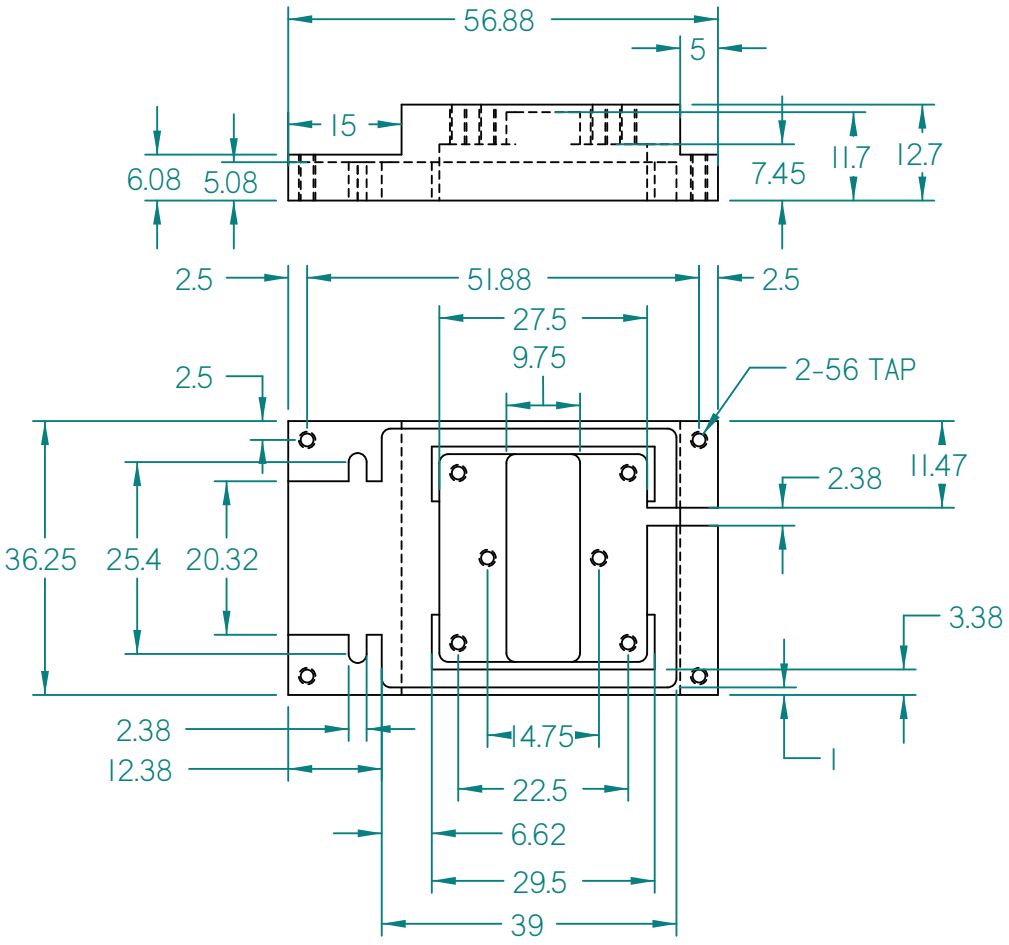

Figure D.10: Long core housing dimensions (mm). Material: Delrin. 1:1 scale.

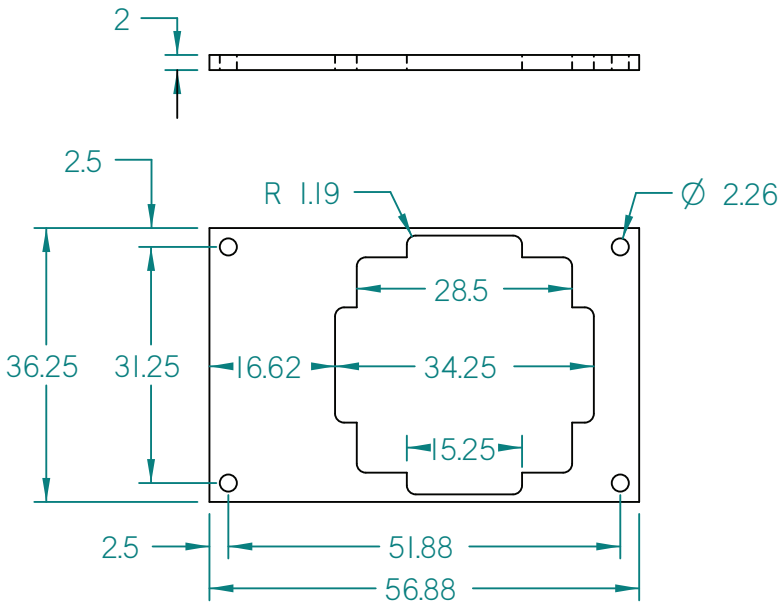

Figure D.11: Bottom plate dimensions (mm). Material: Delrin. 1:1 scale.

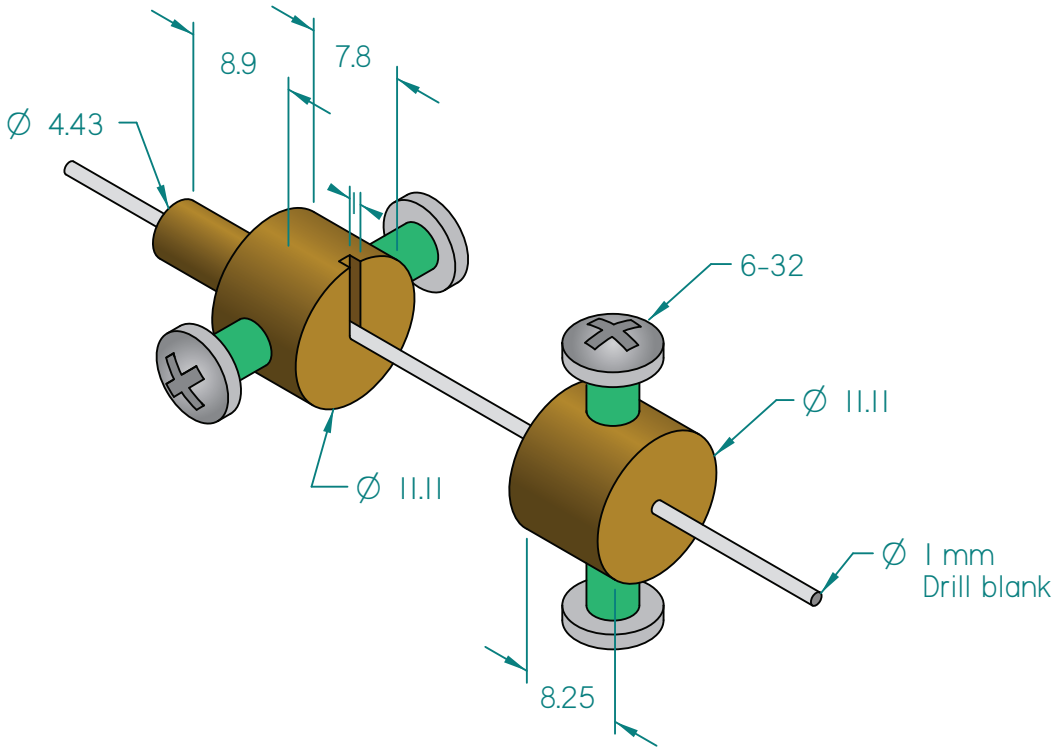

Figure D.12: Pickup coil former dimensions (mm). Materials: Brass and steel. 2:1 scale.

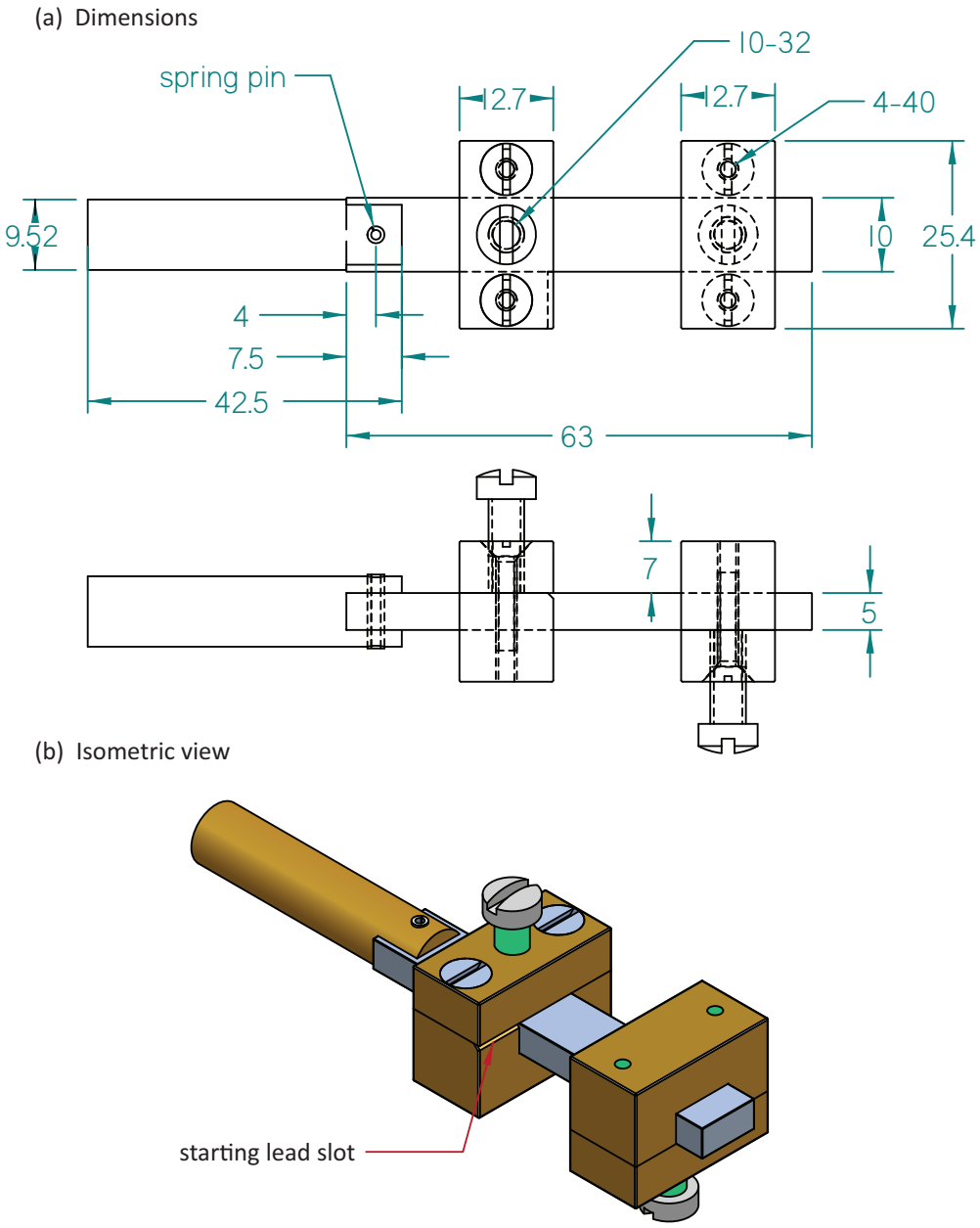

Figure D.13: Excitation coil and feedback coil former (mm). Materials: Brass and stainless steel. 1:1 scale.

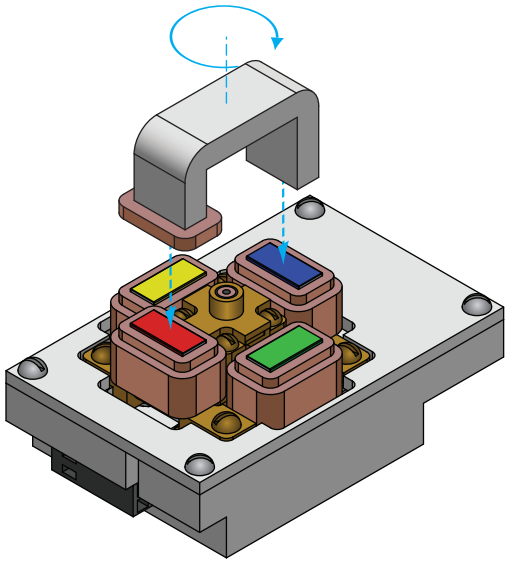

Figure D.14: Physical configuration for measuring $\mathcal{M}_p$ on the SL4P. To measure M_1, a separate U-core with a 56 turn reference coil was placed across poles 1 and 3 with the reference coil aligned to pole 1. Voltages in F1 and the reference coil were compared. The separate core was rotated in increments of 90° to align the reference coil with poles 2 through 4 to estimate M_2 through M_4, respectively.

Appendix E

BN Circuit Components

This appendix presents pickup coil (Section E.1) and cabling (Section E.2) considerations used for the BN transfer function model in Section 7.2.

E.1 Pickup Coil

In Figure 7.6 the pickup coil is modelled as a series resistor (R_{pu}) and inductor (L_{pu}) in parallel with a capacitor (C_{pu}). L_{pu} is shown to be magnetically coupled to the sample. The inside and outside of the coil are capacitively coupled to ground through C_{ID} and C_{OD} respectively.

While the BN flux may only produce a significant EMF on a small number of the pickup coil turns, it must drive current through R_{pu} and L_{pu}. Charge buildup between windings capacitively stores energy in local electric fields. All distributed capacitance of this form is parallel to the series L_{pu} and R_{pu}, and may therefore be modelled as a combined parallel capacitance, C_{pu}.

For a 100 turn coil with a 1 mm ID, a 3 mm OD, and a 0.5 mm thickness, the coil

consists of approximately 16 layers with 6.25 turns per layer. This gives a total length of wire of approximately 0.63 m, and if AWG 44 wire is used at 8.51 Ω/m [74], then $R_{pu} \approx 5.4\,\Omega$.

The complex pickup coil inductance L_{pu} was evaluated using the pickup assembly FEM in Section 5.2.4. For the electric circuit model, the fit to L_{pu} for the pickup coil in the CSS configuration in Figure 5.17 is used. The fit gives $L_{pu} = \left(121 \cdot f_{bn}^{-0.0211} - 3i\right)$ μH between 1 kHz and 1 MHz. If the frequency corresponding to the peak of the complex sample permeability is significantly greater than 600 kHz, this form of L_{pu} may be valid up to 10 MHz.

The value of C_{pu} varies with the winding methods, since capacitance is primarily due to the proximity of the windings. Typically C_{pu} must be measured by finding the self-resonant frequency of the coil . This is complicated by the fact that almost any connector or cabling will have a capacitance larger than C_{pu}.

Models for calculating C_{pu} also exist. In Masserani's paper [75], the capacitance of an inductor is modelled as a distributed capacitance between close-packed windings, with a basic capacitance 'cell' C_{tt} combined over many turns. The total capacitance is then expressed as some fraction of C_{tt}, and it is shown for 2 and 3 layer coils to be on the order of C_{tt}. For a multi-layer 1 mm ID, 3 mm OD coil with a $D_0/D_c = 1.05$, where D_0 is the wire diameter with insulation and D_c is the diameter of the conductor, and an insulation $\epsilon_r = 3$, equation (15) in [75] gives $C_{tt} = 1$ pF. In subsequent calculations, $C_{pu} \approx 1$ pF, and is assumed not to change significantly with the number of pickup coil turns (N_{pu}).

Ideally, C_{ID} and C_{OD} are negligible, however they may vary significantly with the grounding configuration of the pickup coil. In the CSS configuration, the nearest

grounded media are the shield and the sample. Since the outer windings of the coil are closer to the shield than they are to the sample, it is expected that $C_{OD} > C_{ID}$. If the pickup coil is not shielded, it is expected that $C_{ID} \approx C_{OD}$. The effects of C_{ID} and C_{OD} are discussed further in Section 7.2.2.

E.2 Transmission Line

The cabling required to connect the pickup coil to the preamplifier includes at a minimum two leads and a ground conductor. Due to the low amplitude of the BN waveform, shielded cabling, either coaxial cable or a shielded twisted pair, is required to minimise coupling of external $\vec{E}$ and $\vec{B}$ fields into the voltage measurement.

Signals travel along cables at the speed of light: $c = c_0 \cdot (\epsilon_r \mu_r)^{-1/2}$, where c_0 is defined as 299792458 m/s and ϵ_r is the relative permittivity of the insulating material between the conductors. The length of a cable therefore corresponds to a specific wavelength (λ) and frequency (f), related by the wave equation: $c = f\lambda$. Typical ϵ_r values for cable dielectrics range from 1.2 to 4, and μ_r is usually 1. If the maximum BN frequency is 300 kHz, then sampling frequencies should be on the order of 3 MHz, corresponding to minimum wavelengths (λ_{min}) of 50 m to 90 m. As cable lengths approach λ_{min} various resonances and reflections along the cable may distort the BN.

Cables also have distributed parallel capacitance, series inductance and resistance. In coaxial and twisted pair designs, the bulk of the induced magnetic field is near or within the cable and is not at risk of coupling to the pickup coil or the sample. Provided the cable is sufficiently shorter than λ_{min} for the frequencies of interest, the distributed impedance of the transmission line may be modelled as in Figure 7.6.

Cables are usually specified according to their characteristic impedance ($Z_0 =$

$\sqrt{L_c/C_c}$), capacitance per unit length (C_c/ℓ_c) where ℓ_c is the length of the cable, and loss per unit length as a function of frequency in dB/m [76]. The typical range for Z_0 is $50\,\Omega$ to $150\,\Omega$. C_c/ℓ_c is usually between $30\,\text{pF/m}$ and $150\,\text{pF/m}$. Losses per unit length may range from $0.3\,\text{dB/m}$ to $0.01\,\text{dB/m}$. Therefore, for a typical $1.5\,\text{m}$ cable with $Z_0 = 50\,\Omega$, $C_c \approx 150\,\text{pF}$, $L_c \approx 0.34\,\mu\text{H}$. For cable lengths $< 10\,\text{m}$ at $0.01\,\text{dB/m}$, losses are on the order of 1% and may be considered negligible, such that $R_{cp} \approx \infty$ and $R_{cs} \approx 0$.